Studies of Atmospheric Ozone and Related Constituents in the Arctic and at Mid-latitudes

by

Xiaoyi Zhao

A thesis submitted in conformity with the requirements
for the degree of Doctor of Philosophy

Graduate Department of Physics
University of Toronto

Studies of Atmospheric Ozone and Related Constituents in the Arctic and at Mid-latitudes

Xiaoyi Zhao

Doctor of Philosophy

Graduate Department of Physics
University of Toronto

2017

Abstract

Two UV-visible differential absorption spectroscopy (DOAS) ground-based spectrometers (GBSs) were installed at the Polar Environment Atmospheric Research Laboratory (PEARL) in the Canadian High Arctic (80.1° N, 86.4° W). These two instruments have been used to measure stratospheric trace gases since 1999 and 2006 respectively. In 2010 and 2014, two solar-tracking systems were integrated with the GBSs to make tropospheric trace gas measurements.

One goal of this work was to study surface ozone depletion events (ODEs) in the Arctic, using data from the GBSs. The measurements of ozone and BrO, combined with model results, indicate that both high wind/blowing snow and low wind/stable boundary layer are favorable environmental conditions for bromine explosion events, and in some cases, the combination of these two conditions will extend the lifetime of a bromine explosion event. In addition, during a strong surface ODE (ozone VMR < 1 ppbv), BrO concentration can be significantly controlled by the ozone concentration. The HDO depletions observed during two blowing-snow-induced ODEs were found to be weaker than those modelled using pure Rayleigh fractionation. This work provided evidence of a blowing-snow sublimation process, which is a key step in producing bromine-enriched sea-salt aerosol.

This work also evaluated the performance of the recently developed Pandora spectrometer by comparing it with the Brewer world reference triad. Statistical analysis was used to determine the quality of the total colum ozone (TCO), with all Pandora and Brewer instruments shown to meet the Global Atmosphere Watch requirement for a precision better than 1%. However, there is a 1% seasonal difference and a 3% bias between the standard Pandora and Brewer TCO data, which is related to the temperature dependence and difference in ozone cross sections. A statistical model was developed to correct Pandora data, reducing the seasonal difference to 0.25% and the bias to 0.04%.

Acknowledgments

My Ph.D. work has been finished as the most wonderful journey in my life. Thank you to my supervisor Prof. Kimberly Strong. You enrolled me seven years ago as an M.Sc student, and I appreciate the great opportunity you gave to me to explore the Canadian High Arctic. I thank you for all your great support though my Ph.D. work, revising my manuscripts, reports, and slides. I enjoyed the seven years in the group doing research with you. And the trips to the Arctic are highlights in my life. Thank you to my committee members, Prof. Dylan Jones and Prof. Jon Abbatt, your insightful suggestions and questions are the light in my research work. Thank you to Dr. Vitali Fioletov, I learned how to think like a scientist though the collaboration with you. Thank you also to Prof. Kaley Walker, Prof. Jim Drummond, and Dr. Pierre Fogal. Without any of you, I would never have had the great experience in working in the Arctic.

Thank you to Dr. Udo Friess for teaching me about HeiPro and answering all my questions. Thank you to Dr. Xin Yang for providing me modelled BrO data and taking time to have discussions with me. Thank you to Prof. Robin Schofield, Dr. Andreas Richter, Dr. Anne Blechschmidt, Dr. Ja-Ho Koo, Dr. Alexander Cede, Dr. Jonathan Davies, Dr. Gloria Manney, Dr. Luis Millán, Dr. Edwin Eloranta, and Dr. Matthias Schneider for providing me with codes, data, and advice! Thank you also to Prof. William Simpson, Prof. Thomas Wagner, Dr. Olga Puentedura, and Dr. Folkard Wittrock who accepted my invitation to give Noble seminars. Thank you also to Prof. Jochen Stutz for having me visit your group.

Thank you to Dr. Cristen Adams. You trained me in all the instrumental work, and I am glad that you accompanied me for my first trip to Eureka. Thank you to Dr. Sophie Tran. Your helped me in taking care of GBSs during the 2014 ACE campaign and making an extra trip to Eureka in October of that year. Thank you to Orfeo Colebatch for all your technical support. Thank you to everyone who travelled to Eureka with me: Dan Weaver, Joseph Mendonca, Zen Mariani, Rodica Lindenmaier, Felicia Kolongjari, Paul Loewen, Mike Maurice, Volodya Savastiouk, Emily McCullough, Debora Griffin, Lin Dan, and many others who worked in the Eureka weather station! Thank you to all the people in my office, previously and now (Niall Ryan, Keven Roy, Zen Mariani, Joseph Mendonca, Dan Weaver, Jenny Kliever, Sebastien Roche, Paul Jeffery, Tailong He, Kristof Bognar …). All the interesting office discussion and trivia talks are part of my best memory with you. Kristof Bognar, thank you for taking care of the GBSs (I hope they will treat you nicely during your Ph.D. study).

Thank you to Mom and Dad for all your support and as my first teachers. In six years, I earned a degree and two beautiful little ones, without whom I could use maybe only four years. But, I love you my dear Nicole and Naomi. Thank you for coming in to my life. Besides the training in science and academia I learned in Toronto, you two helped me learn more about care, love, responsibility, and of course how to change your diapers. Thank you to Jia, my dear wife, who gave those two precious little ones to me. I am sorry you were the last addressed in our family, but I know you will be the only one in our family who will read this and accompanied me through this six years.

Table of Contents

List of Tables

List of Figures

List of Acronyms

ACE	Atmospheric Chemistry Experiment
AHSRL	Arctic High Spectral Resolution Lidar
AMF	airmass factor
AOD	aerosol optical depth
ATDF	absolute temperature dependence factor
BrT	Brewer reference Triad
BrT-D	Brewer reference Triad-Double
CANDAC	Canadian Network for the Detection of Atmospheric Change
CCD	charge coupled device
CINDI	Cabauw Intercomparison of Nitrogen Dioxide measuring Instruments
CINDI-2	the second Cabauw Intercomparison of Nitrogen Dioxide measuring Instruments
DMP	derived meteorological product
DBM	Daumont, Brion, and Malicet
DOAS	differential optical absorption spectroscopy
DOD	differential optical depth
DOFS	degrees of freedom for signal
DS	direct sun
DSCD	differential slant column density
ECMWF	European Centre for Medium-Range Weather Forecasts
ECC	electrochemical concentration cell
ECCC	Environment and Climate Change Canada
EWS	Eureka Weather Station
FLEXPART	Lagrangian FLEXible PARTicle dispersion model
FOV	field-of-view
FTIR	Fourier transform infrared spectrometer
FTS	Fourier transform spectrometer
FWHM	full width at half maximum
GAW	Global Atmosphere Watch
GBS	Ground-Based Spectrometer
GEOS-5	Goddard Earth Observing System-5
GOME	Global Ozone Monitoring Experiment
GOME-2	Global Ozone Monitoring Experiment-2
GPIB	general purpose interface bin
HDO	hydrogen-deuterium oxide
HDF	Hierarchical Data Format
HeiPro	Heidelberg remote sensing group profile retrieval code
HYSPLIT	Hybrid Single-Particle Lagrangian Integrated Trajectory
LLG	liquid light guide
LUT	look-up table
MANTRA	Middle Atmosphere Nitrogen TRend Assessment

MAX-DOAS	multi-axis differential optical absorption spectroscopy
MERRA	Modern Era Retrospective-analysis for Research and Applications
MLS	Microwave Limb Sounder
MMCR	Millimetre Cloud Radar
MMR	mass mixing ratio
MODIS	Moderate Resolution Imaging Spectroradiometer
MUSICA	MUlti-platform remote Sensing of Isotopologues for investigating the Cycle of Atmospheric water
NDACC	Network for the Detection of Atmospheric Composition Change
NDSC	Network for the Detection of Stratospheric Change
NSIDC	National Snow and Ice Data Center
NSERC	Natural Sciences and Engineering Research Council
ODE	ozone depletion event
OMI	Ozone Monitoring Instrument
OO-SSA	open-ocean sourced sea-salt aerosol
OSIRIS	Optical Spectrograph and Infra-Red Imaging System
PAHA	Probing the Atmosphere of the High Arctic
PEARL	Polar Environment Atmospheric Research Laboratory
PEARL-GBS	Polar Environment Atmospheric Research Laboratory Ground-Based Spectrometer
PSC	polar stratospheric cloud
RSP	Raman scattering probability
PSU	practical salinity units
pTOMCAT	the Cambridge Parallelised-Tropospheric Offline Model of Chemistry and Transport model
PV	potential vorticity
PWV	precipitable water vapour
RCD	reference column density
RIVM	National Institute for Public Health and the Environment (the Netherlands)
RMS	root mean square
RRS	rotational Raman scattering
RTDF	relative temperature dependence factor
SAOZ	System D'Analyse par Observations Zenethales
SCD	slant column density
SI-SSA	sea-ice sourced sea-salt aerosol
sPV	scaled potential vorticity
SSA	sea-salt aerosol
SSF	spot-to-slit fibre
SZA	solar zenith angle
TCO	total column ozone
TCP	Transmission Control Protocol
TOMS	Total Ozone Mapping Spectrometer
TROPOMI	Tropospheric Monitoring Instrument
UDP	User Datagram Protocol

UKCA	United Kingdom Chemistry and Aerosols model
UT-GBS	University of Toronto Ground-Based Spectrometer
VCD	vertical column density
VMR	volume mixing ratio
VSLS	very short-lived substance
VSMOW	Vienna Standard Mean Ocean Water
WMO	World Meteorological Organization
ZS	zenith sky

Chapter 1

1 Introduction

Ozone is one of the most well-known atmospheric trace gases. It was first made in the laboratory in the 1830s (Schönbein, 1837) and identified in the atmosphere in the 1860s (Rubin, 2001). Although monitoring of atmospheric ozone can be traced back to 1926 (Dobson, 1968a), it came into wide public interest in the 1980s when the ozone hole over the Antarctic was discovered (Farman et al., 1985). Ozone is essential to human life as it has several important roles: in the stratosphere, the ozone layer absorbs harmful UV radiation, thus protecting humans, animals, and plants; in the troposphere, ozone is one of the major oxidizing agents to initiate the chemical removal of methane and other hydrocarbons from the lower atmosphere, although its oxidizing properties are harmful to human health. In addition, ozone has important links to climate: tropospheric ozone causes warming through the absorption of long-wave radiation, while stratospheric ozone has a slight cooling effect, as it prevents solar short-wave radiation from reaching the surface (IPCC, 2013). This chapter will describe the general motivation and scientific objectives of this thesis in the context of ozone depletions in both the troposphere and stratosphere.

1.1 Motivation and Scientific Objectives

From 1999 to the present, ozone and related trace gases have been measured by UV-visible spectrometers at Eureka, Nunavut, Canada (80.05°N, 86.41°W). These spectrometers are now part of the Canadian Network for the Detection of Atmospheric Change (CANDAC), which was formed in 2005. CANDAC is a network dedicated to studying the changing atmosphere over Canada, and a suite of instruments are installed at Eureka to measure atmospheric constituents and parameters. CANDAC's research theme, "Arctic Middle Atmospheric Chemistry" (AMAC, 2005-2011), had the goal to improve understanding of the processes controlling the Arctic ozone budget and its future evolution using observations made at Eureka. The UV-visible spectrometers were key instruments for achieving AMAC research objectives.

In 2013, CANDAC started a new research program, "Probing the Atmosphere of the High Arctic" (PAHA), which is funded by the Natural Sciences and Engineering Research Council

(NSERC). A new research project under the PAHA "Composition Measurements" (CM) theme is "Ozone and Related Species" (CM-O3), which has several scientific objectives that provide the foundation for this thesis:

1) To acquire a High Arctic dataset of partial and total column measurements of ozone and ozone-related trace gases, including tropospheric and stratospheric columns of BrO.
2) To unravel the coupled processes controlling Arctic stratospheric composition and quantify the contributions from dynamics, chemistry, and climate change to ozone depletion and recovery.
3) To combine measurements of tropospheric ozone and BrO to investigate the origin and occurrence of bromine explosions and their impact on the surface ozone budget at Eureka.
4) To improve our understanding of chemistry-climate processes by combining the measurements with atmospheric models to facilitate both improved modelling of the atmosphere and the interpretation of the measurements.

In addition to these general scientific objectives, the following sections (1.1.1 and 1.1.2) will describe the motivation of this thesis in the context of specific scientific questions, which will be addressed and answered in Chapters 3, 4, and 5.

1.1.1 Tropospheric Ozone

In the 1980s, around the same time of the discovery of the ozone hole over the Antarctic, severe surface ozone depletion events (ODEs) in the Arctic were discovered (Bottenheim et al., 1986; Barrie et al., 1988). These events have since been linked to extremely high concentrations of bromine and are reviewed by Simpson (2007b; 2015) and Abbatt et al. (2012). After three decades, tropospheric ODEs are still not fully understood. Many aspects of this phenomenon remain open questions. For example, the optimum meteorological conditions for the occurrence of these events remain uncertain. A stable shallow boundary layer and blowing snow conditions have both been proposed. One of the motivations behind this thesis is to better understand the mechanisms generating tropospheric ODEs.

This work focussed on addressing the following scientific questions, using the data collected by the UV-visible spectrometers at Eureka (combined with ozonesondes, radiosondes, lidar, radar, satellite, and modelled data):

- What is the source of the extremely high concentrations of bromine in the polar troposphere? Do we have observations at Eureka that provide evidence that the blowing-snow induced sea-salt aerosol is one of the bromine sources?
- What are the differences between high-wind-condition and low-wind-condition ODEs? What meteorological conditions can enable bromine explosion events at Eureka?
- How well do the satellite measurements of tropospheric BrO agree with ground-based measurements at Eureka?
- Do our current ODE modelling results agree with ground-based measurements at Eureka? How well can models simulate BrO, ozone, and sea-salt aerosol (compared to measurements)?
- The lifetime of reactive bromine is only a few hours in the absence of recycling. Do we have evidence of this recycling over aerosol or blowing-snow/ice particles at Eureka?
- The blowing-snow sublimation process is a key step in producing bromine-enriched sea-salt aerosol. Can we use isotopologue measurements at Eureka to provide evidence of this sublimation process?

These questions are critical to our understanding of reactive bromine sources, and for meaningful prediction/modelling of future halogen activation, boundary-layer ozone depletion, and mercury deposition. In the context of a rapid changing Arctic, these questions are also crucial to environmental change and human health. For example, the decline of the Arctic sea ice extent and thickness has been confirmed (Comiso et al., 2008; Kurtz et al., 2011), however, how this sea-ice melting trend will affect ODEs is not clear (Abbatt et al., 2012). The activated halogenated species in ODEs can remove gas-phase mercury and deposit the product on snow (Calvert and Lindberg, 2004a, 2004b; Steffen et al., 2008; Calvert et al., 2015). The deposited mercury can ultimately reach deep sediments and/or bioaccumulate into wildlife and eventually into humans (Simpson et al., 2007b). Studies show that 40-320 tons of mercury can be deposited to the Arctic over a period of one year due to ODEs (Ariya et al., 2004; Skov et al., 2004; Dastoor et al., 2008; Durnford et al., 2012; Dastoor et al., 2015). However, without knowledge to predict ODEs in the rapid changing Arctic, meaningful prediction of mercury deposition is difficult. The multi-year dataset (17 years of zenith-sky and seven years of multi-axis scattered sunlight measurements) acquired at Eureka, can contribute to determining the ODE trends in the Arctic, improving ODE modelling, validating satellite ODE observations, and facilitating studies related to rapid environmental change in the Arctic region.

1.1.2 Stratospheric Ozone

Another scientific focus of this thesis is related to stratospheric ozone. This thesis evaluates the performance of total column ozone (TCO) (mainly stratospheric ozone) measurements from the recently developed Pandora spectrometer by comparing it with the Brewer world reference triad. Stratospheric ozone has been an important scientific topic since the 1970s and became a matter of intense interest with the discovery and subsequent studies of the Antarctic ozone hole (Farman et al., 1985; Solomon et al., 1986; Stolarski et al., 1986) and ozone depletion on the global scale (Stolarski et al., 1991; Ramaswamy et al., 1992). To improve their accuracy and to automate the TCO measurements, the Brewer spectrophotometer was developed in the early 1980s (Kerr et al., 1981; 1988), and was designated as the World Meteorological Organization (WMO) Global Atmosphere Watch (GAW) standard for total column ozone measurement in 1988. By 2014, there were more than 220 Brewer instruments installed around the world, with most still in operation today. The Pandora system was developed at NASA's Goddard Space Flight Center and first deployed in the field in 2006. Pandora instruments are suitable candidates for both direct-sun (DS) and zenith-sky (ZS) measurements of total column ozone and other trace gases (Herman et al., 2009; Tzortziou et al., 2012). By 2015, several long-term Pandora sites had been established in the United States and worldwide (including Austria, Canada, Canary Islands, Finland, and New Zealand).

The ground-based TCO measurements from Brewer and Pandora instruments have been used for satellite validation (Balis et al., 2007; Antón et al., 2009; Loyola et al., 2011; Tzortziou et al., 2012; Labow et al., 2013) and modelling/trend analysis work (Bojkov et al., 1995; Fioletov et al., 2002; Austin and Wilson, 2006; Austin et al., 2010), for example, to predict stratospheric ozone recovery (IPCC, 2013; WMO, 2014). However, it has been found that Pandora TCO data have a bias relative to Brewer TCO data (Tzortziou et al., 2012). It is important to understand and evaluate the difference between the TCO datasets from these two generations of ozone monitoring networks. Using the co-located TCO measurements from two Pandora instruments and the Brewer world reference triad (six Brewer instruments in total) in Toronto, the following scientific questions were addressed in this thesis:

- What is the cause of the difference between Brewer and Pandora TCO measurements?

- What are these instruments' measurement precisions and accuracies? How do the differences between the Brewer and Pandora instruments (optical design, retrieval algorithm, etc.) affect the precision and accuracy of their TCO measurements?
- Are the TCO measurements by Brewer and Pandora meeting the GAW requirement?
- Can the Pandora TCO data quality be improved in a way that makes it comparable to Brewer TCO data (given that the Brewer is designed to produce high-quality TCO data)?

These questions are important, as answering them is needed to evaluate the quality of the TCO datasets generated from both instruments. For instance, our statistical analysis indicates the quality of the TCO, with all Pandora and Brewer instruments meeting the GAW requirement for a precision better than 1%. However, there is a 1% seasonal difference and a 3% bias between the standard Pandora and Brewer TCO data. Thus the users who need TCO datasets from these instruments to perform other scientific studies (for example, ozone recovery trends, satellite validation, etc.) must take these findings/differences into account.

To maintain the measurement stability and characterize each individual Brewer instrument, the Brewer network uses a calibration transfer scheme. In general, each field instrument needs to be regularly calibrated against the travelling standard reference instrument. Then the travelling standard itself is calibrated against the Brewer world reference triad (three Brewer single spectrometers, known as the old reference triad). Individual Brewer instruments of the triad are independently calibrated at Mauna Loa, Hawaii every 2-6 years (Fioletov et al., 2005).

The performance of the old reference triad was last reported ten years ago using data to 2004 (Fioletov et al., 2005). A new reference triad (three Brewer double spectrometers) for MKIII Brewer instruments has also been in operation since the 1990s. Thus, this thesis also provides a new assessment of the performance of both the old and new Brewer world reference triads in recent years.

The following sections in this chapter review tropospheric and stratospheric ozone depletion, with a focus on current understanding and open scientific questions. The ozone remote sensing monitoring networks are also described. Finally, the outline of the thesis and scientific contributions are given in the last section.

1.2 Tropospheric Ozone Depletion

In the 1980s, it was discovered that Arctic surface ozone concentrations occasionally drop from typical levels of 30-40 ppbv to below 10 ppbv, or even below the detection limit (Bottenheim et al., 1986; Oltmans and Komhyr, 1986; Barrie et al., 1988). These episodes of ODEs can last for periods of several hours to several days. Bottenheim et al. (1986) first reported strong ODEs at Alert without being able to explain these observations. Two years later, Barrie et al. (1988) found a strong negative correlation between surface ozone and “filterable bromine” (f-Br) data in spring 1986 at Alert (see Figure 1.1), and hypothesised that the ozone depletion involves a bromine-catalyzed chain reaction.

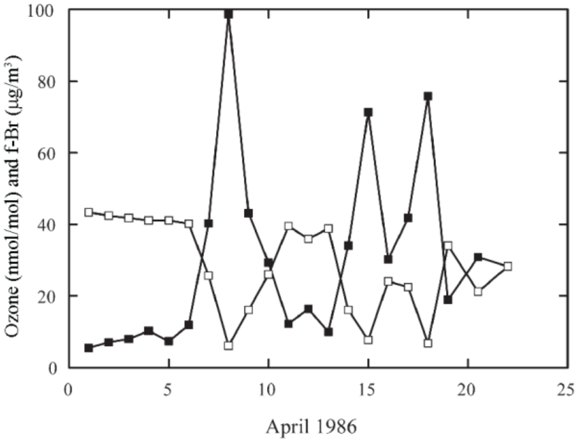

Figure 1.1: The first published observation of the anticorrelation between surface ozone and filterable bromine, measured at Alert. Filled squares show filterable Br (f-Br) in µg/m^3, from 24 h filter packs, and open squares show daily averaged ozone in nmol/mol (ppbv). (Figure adapted from Simpson et al. (2007b), which reprinted the original figure of Barrie et al. (1988)).

Later on, many field campaigns were carried out in the Arctic and Antarctic dedicated to studying the ODEs, e.g., (Bottenheim et al., 1990; Yokouchi et al., 1994; Platt and Lehrer, 1996; Hopper et al., 1998; Bottenheim et al., 2002; Beine et al., 2003; Domine et al., 2004; Jones et al., 2008; Frieß et al., 2011). Large-scale observations of ODEs began in 1997 with the launch of the Global Ozone Monitoring Experiment (GOME) aboard the European ERS-2 satellite (Richter et al., 1998; Burrows et al., 1999). With the help of satellite observations, it became clear that the ODEs are frequent phenomena in both hemispheres in polar spring, covering large areas mainly over sea ice and along the coasts (Wagner et al., 2001; Hollwedel et al., 2004; Simpson et al., 2007b). It is now clear that bromine photochemistry has the central role in ODEs, and that halogen activation causes chemical destruction of surface ozone and changes the oxidising capacity of the troposphere. The activated halogenated species in ODEs can remove and deposit gas-phase mercury, and affect the oxidation of organic gases (Simpson et al., 2007b).

Simpson et al. (2007b) reviewed the relationship between active halogen and ODEs in the polar boundary layer. Abbatt et al. (2012) reviewed the issue with a focus on a molecular level description of the role that ice and snow substrates play in promoting the formation and transformations of reactive halogenated species in the troposphere. Following Simpson et al. (2007b), the key chemical reactions and reaction cycles involved in ODEs are described briefly here. The initial release of bromine radicals from ions

$$\mathrm{HOBr} + \mathrm{Br}^-_{\mathrm{aq}} + \mathrm{H}^+_{\mathrm{aq}} \overset{\mathrm{mp}}{\rightarrow} \mathrm{Br_2} + \mathrm{H_2O} \tag{R1}$$

$$\mathrm{Br_2} \overset{hv}{\rightarrow} 2\mathrm{Br} \tag{R2}$$

$$\mathrm{Br} + \mathrm{O_3} \rightarrow \mathrm{BrO} + \mathrm{O_2} \tag{R3}$$

(where mp indicates a multiphase reaction) can be followed by self-reaction (BrO + BrO), cross reaction (BrO + IO/ClO), and catalytic cycles involving HO_2 and CO (Simpson et al., 2007b). However, these three reaction pathways do not increase the abundance of the BrO_x family (Br + BrO), and thus do not speed up the depletion of ozone. The widely accepted mechanism for the bromine explosion cycle proceeds via the reaction

$$\mathrm{BrO} + \mathrm{HO_2} \rightarrow \mathrm{HOBr} + \mathrm{O_2}. \tag{R4}$$

Combining reactions R1-R4 gives the net reaction

$$\mathrm{Br} + \mathrm{Br}^-_{\mathrm{aq}} + \mathrm{H}^+_{\mathrm{aq}} + \mathrm{O_3} + \mathrm{HO_2} \xrightarrow{\mathrm{mp},hv} 2\mathrm{Br} + 2\mathrm{O_2} + \mathrm{H_2O}. \tag{R5}$$

Followed by rapid ozone depletion in some conditions, this cycle can result in the conversion of particle-phase inactive bromide (Br^-) to gas-phase reactive bromine (BrO_x), thus further speeding up the cycle. This is the widely known bromine explosion reaction sequence (Fan and Jacob, 1992; McConnell et al., 1992; Wennberg, 1999). In addition, the reaction of gas-phase reactive bromine (BrO_x) with gas-phase elemental mercury can lead to toxic mercury deposition in polar ecosystems (Schroeder et al., 1998; Calvert and Lindberg, 2004b; Steffen et al., 2008).

The Br atoms resulting from R5 will cycle between the atomic form and its oxides via the reactions

$$\mathrm{Br} + \mathrm{O_3} \rightarrow \mathrm{BrO} + \mathrm{O_2} \tag{R6}$$

$$\mathrm{BrO} \overset{hv}{\rightarrow} \mathrm{Br} + \mathrm{O}. \tag{R7}$$

The typical conversion time via R6 is on the order of 1 s at 40 ppbv O_3, and the photodissociation rate of R7 (in typical springtime Arctic daytime) is ~4×10^{-2} s^{-1} (Simpson et al., 2007). Thus the partitioning of BrO_x is controlled by a balance between R6 and R7. Modeling studies have revealed that ODEs have a highly non-linear nature (Simpson et al., 2007b), and the partitioning of BrO_x and Br_y (total inorganic Br) plays a key role in speeding up or slowing down ODEs (Evans et al., 2003; Sander et al., 2003; Simpson et al., 2007b; Piot and von Glasow, 2008; Piot and Von Glasow, 2009; Toyota et al., 2011a; Fernandez et al., 2014; Toyota et al., 2014). In general, during the day and at high ozone concentrations (> 10 ppbv), BrO is the prevalent BrO_x species; however, at low ozone concentrations (< 1 ppbv), Br is more abundant than BrO (Simpson et al., 2007). For example, Evans et al. (2003) used a photochemical box model to investigate this partitioning as a function of ozone concentration in a simulation initialized on April 15 at 73°N, at local noon at 100 m altitude. Figure 1.2 shows the evolution of the concentrations of halogen species as the ozone concentration decreases. Note that the ozone scale in the figure is from 0.1 to 100 ppbv, but the simulation only extends from 0.8 to 40 ppbv, which represents the typical range of ozone surface concentrations in the Arctic. This figure illustrates the highly non-linear nature of BrO_x and Br_y partitioning as a function of ozone concentration.

Although bromine explosion events have been extensively studied over the past three decades, many questions remain. Figure 1.3 demonstrates the physical nature and composition of different substrates upon which halogen activation may occur in the polar boundary layer, as summarised by Abbatt et al. (2012). In general, studies of the surface on which reaction R1 proceeds have suggested that this surface may be sea salt deposited on the snowpack and ice (McConnell et al., 1992; Simpson et al., 2007a; Dibb et al., 2010; Pratt et al., 2013), acidified background sea-salt aerosol (Vogt et al., 1996), brines concentrated on frost flowers that form on young sea ice (Rankin et al., 2002; Kaleschke et al., 2004), and bromine in blowing snow (Yang et al., 2008; Jones et al., 2009). Brines concentrated on frost flowers are no longer considered as a pathway for bromine activation primarily due to their high pH, which is not favourable for Br_2 formation (Abbatt et al., 2012; Pratt et al., 2013; Wren et al., 2013). The optimum meteorological conditions for the occurrence of bromine explosion events also remain uncertain. A stable shallow boundary layer (Wagner et al., 2001; Frieß et al., 2004; Lehrer et al., 2004) and blizzard conditions (Yang et al., 2008; Jones et al., 2009; Frieß et al., 2011) have both been proposed. These different meteorological conditions can lead to different transport patterns for the low-ozone airmass, thereby changing the oxidative capacity of the Arctic troposphere.

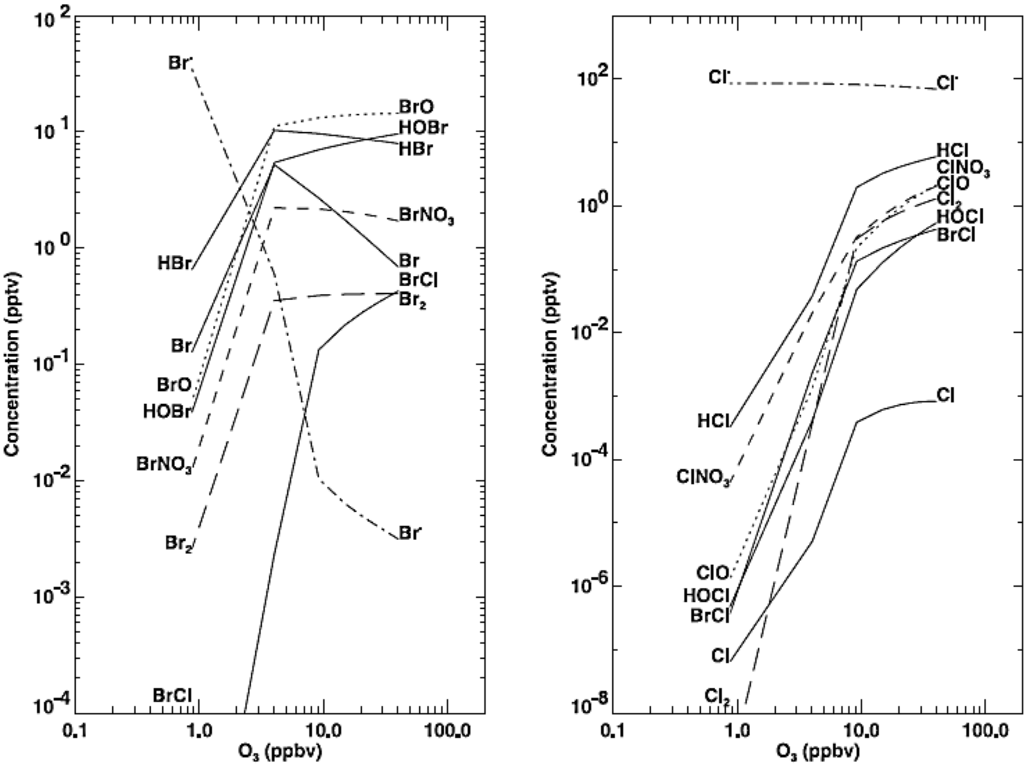

Figure 1.2: Modelled evolution of halogen concentrations for a simulation with 43 pptv of initial bromide, as a function of the ozone concentration. Figure adapted from Evans et al. (2003).

1.2.1 High-Wind ODE

In blowing snow (wind speed > 12 m s^{-1}), the salty snow that is aloft in the air could produce sea-salt aerosol (SSA) through sublimation. The bromine-enriched SSA is thought to act as both source and substrate for bromine chemistry (Yang et al., 2008; Abbatt et al., 2012). In addition, May et al. (2016) report that sea-salt mass concentrations increased in the presence of nearby leads and wind speeds greater than 4 m s^{-1}. SSA produced from leads has the potential to alter cloud formation (May et al., 2016), as well as the chemical composition of the tundra snowpack (Simpson et al., 2005; Pratt et al., 2013). Given the thinning of Arctic sea ice and decreasing multiyear sea ice extent (Cavalieri and Parkinson, 2012; Stroeve et al., 2012), wind-driven production of SSA from blowing snow and leads could further increase the frequency of wind-driven surface ODEs in polar spring. On the other hand, assuming the complete loss of sea ice will result in a large surface ozone increase in spring, also attributed mainly to bromine chemistry (Voulgarakis et al., 2009). While the connections between the presence of sea ice and halogen chemistry are not yet fully understood and it is unlikely that all sea ice will disappear in the springtime, Abbatt et al. (2012) point out that a decrease in ice and snow has the potential to alter atmospheric composition. As another complication, Maslanik et al. (2007) found that in addition to less multi-year sea ice overall in the Arctic, the fraction of younger and thinner sea ice has increased. In general, the changing of sea ice cover or character in the Arctic will impact halogen chemistry, which can further impact atmospheric oxidation and may impact the lifetime of pollution transported to the Arctic regions (Abbatt et al., 2012).

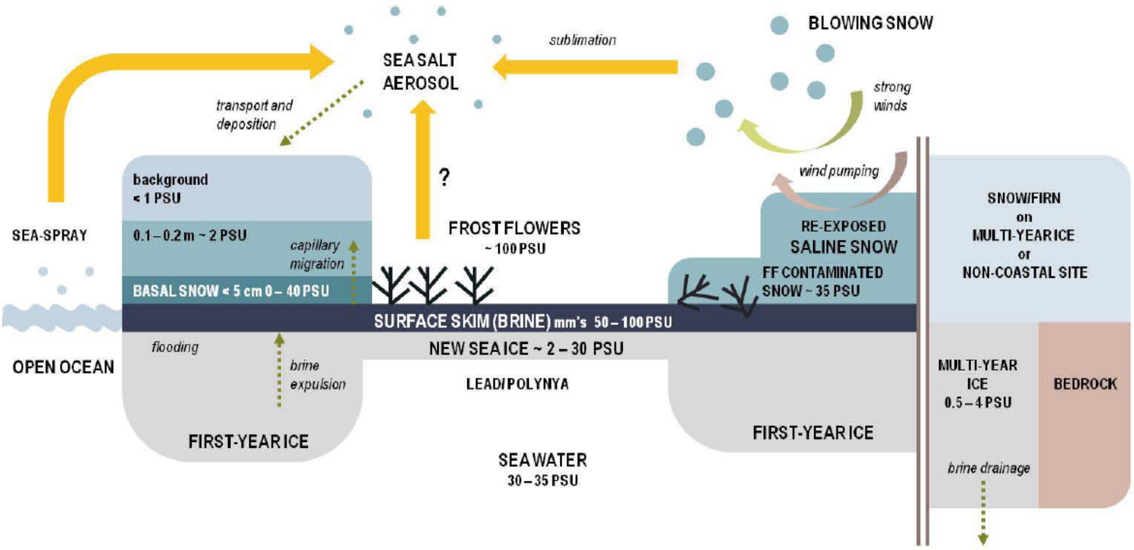

Figure 1.3: Sources of halides in the polar boundary layer. A range of salinity values is indicated: frost flowers (Rankin et al., 2002), brine, new ice (Ehn et al., 2007), multi-year ice (Timco and Weeks, 2010), basal snow (Toyota et al., 2011b), snow < 0.2m (Toyota et al., 2011b), background snow (Massom et al., 2001), frost flower (FF) contaminated snow (Obbard et al., 2009). Figure adapted from Abbatt et al. (2012).

To understand the high-wind ODE mechanism, measurements of SSA are important. However, direct observation of the aerosol in blowing snow is challenging due to the meteorological conditions (strong winds and low visibility). Lidar measurements provide a means of looking through the ice clouds and aerosol layer and can provide important particle information, for example, size, density, and vertical profile. Examples of using lidar and radar measurements for high-wind ODEs are described in Chapter 3 (radar only) and 4 (lidar and radar).

In addition to aerosol measurements, isotopologue measurements can be a useful proxy to identify the lifetime of the airmass and aerosol. Measurements of atmospheric hydrogen-deuterium oxide (HDO), which is heavier than H_2O, contain information about the history of the airmass. Simultaneous observations of tropospheric water isotopologues can provide information on processes related to moisture uptake, exchange, cloud formation, transport/mixing, and temperature upwind of the detected airmass (Schneider et al., 2016). An airmass from the open ocean surface typically contains more HDO than an airmass from the frozen ice-covered ocean at high latitude. For example, in Eureka, from February to April, airmasses with low HDO content are usually from the ice-coved Arctic Ocean, whereas airmasses with high HDO content are usually from ice-free region of the Atlantic Ocean. Thus the transportation history of the airmass can be evaluated by its water isotopologue ratio. In general, the water isotopologue ratios are typically expressed in the δ notation, which relates the observed ratio to the standard ratio of ocean water. For instance, the HDO/H_2O ratio is normally expressed as the relative deviation (δD) from the HDO content of the Vienna Standard Mean Ocean Water (VSMOW) (Craig, 1961), as shown in Eq. (1.1)

$$\delta\mathrm{D} = \left(\frac{R_m}{R_{\mathrm{VSMOW}}} - 1\right) \times 1000‰ \,, \tag{1.1}$$

where R is the HDO/H_2O ratio, subscript m denotes the measurement, and R_{VSMOW} (0.00031152) (Craig, 1961) is the HDO/H_2O ratio in Vienna Standard Mean Ocean Water.

In the polar regions, ice cloud formation and precipitation can change the HDO/H_2O ratio. As with the formation of liquid clouds, when ice cloud form, HDO is condensed into the ice more efficiently than H_2O, and the air becomes HDO depleted. Thus the scavenging of HDO (removing of the ice condensate) leaves the air depleted in HDO (low δD values) and provides information about the ice cloud formation (Rayleigh process) (Rayleigh and Ramsay, 1894). In addition, blowing snow events can contribute to atmospheric δD change.

During blowing snow events, large numbers of snow particles may get into the air. If the air is not saturated, water can sublime from the particles (dependent on wind speed, temperature, relative humidity, snow type, etc.) (Déry and Yau, 1999, 2001), which reduces their size and eventually leads to the formation of SSA. Yang et al. (2008) parameterised the production of SSA, through this process, as a function of the amount of sublimation, snow salinity, and a few other factors, including snow age. The sublimation process is normally considered as a nonfractionation process and does not change δD. This is because of a low coefficient of self-diffusion of water molecules in ice. When sublimation from ice/snow crystals happens layer by layer, the sublimated molecules have the same δD as when they were frozen in the snow/ice crystals. However, sublimation of blowing snow can change the atmospheric δD through mixing. For example, in Eureka, the monthly mean precipitation δD in March is -265‰ (2005-2013, data provided by F. A. Michel and X. Feng, personal communication), while the monthly mean atmospheric δD is -442‰ (see Section 4.3.1). Thus, mixing of the sublimed HDO-enriched water vapour from blowing-snow particles (-265‰) with tropospheric background water vapour (-442‰) can increase the atmospheric HDO content, thus contributing to the change in atmospheric δD; and high atmospheric δD (compared to Rayleigh fractioning model, see Section 4.1.2) should be expected when observing blowing-snow SSA. This process is similar to the phenomenon that δD of water vapour entering the tropical tropopause layer (TTL) is higher than that suggested by Rayleigh model (Moyer et al., 1996; Smith et al., 2006; Blossey et al., 2010). This enrichment of HDO in the TTL is associated with deep convection and sublimation of δD-enriched ice from the lower troposphere (Blossey et al., 2010). In summary, the water isotopologue ratio can be used to study SSA formation and transport, and to facilitate the study of blowing-snow ODEs.

Case studies of ODEs initiated from cyclones in the Beaufort Sea are presented in Chapters 3 and 4. The δD measurements show that HDO was also depleted during those ODEs. HDO depletion observed during these two blowing-snow ODEs is found to be weaker than that simulated by pure Rayleigh fractionation. Thus, this thesis provides evidence support for a blowing-snow sublimation process, which is a key step in producing bromine-enriched SSA.

1.3 Stratospheric Ozone Depletion

The effort to understand the ozone vertical profile in the atmosphere started in the early 1910s (see Platt and Stutz, 2008; Calvert et al., 2015). By late 1920s, it was well established that column ozone levels were several mm and that most of the ozone was located in the stratosphere. The first explanation of the presence of the stratospheric ozone layer was made by Chapman (1930). The Chapman cycle comprises a set of oxygen-only (atom oxygen, oxygen molecules, and ozone) reactions, starting with the photolysis of oxygen molecules by UV photons. The cycle was found to significantly over-predict ozone concentrations in the lower stratosphere. Deficiencies in the Chapman cycle include the neglect of further catalytic cycles and other chemicals. Later research identified ozone-destroying catalytic cycles via hydrogen, nitrogen, and halogen species (chlorine, bromine, and iodine) (Bates and Nicolet, 1950; Crutzen, 1970; Johnston, 1971; Molina and Rowland, 1974; Wofsy et al., 1975; Yung et al., 1980; Solomon et al., 1994).

1.3.1 Chemical and Dynamical Ozone Change

The amount of ozone, more specifically TCO, is controlled by both chemical and dynamical process. TCO declined over most of the globe during the 1980s and early 1990s, by about 2.5% in the global mean, but has remained stable since 2000. There are indications of an increase in global-mean TCO over 2000–2012, consistent with model predictions (WMO, 2014). However, a TCO increase that would be attributable to restrictions on the emissions of ozone-depleting substances decreases has not yet been observed (WMO, 2014).

Ozone loss in the middle stratosphere is dominated by reactive nitrogen. A common catalytic cycle involves the following reactions:

$$\mathrm{X} + \mathrm{O_3} \rightarrow \mathrm{XO} + \mathrm{O_2}\ , \tag{R8}$$

$$\mathrm{XO} + \mathrm{O} \rightarrow \mathrm{X} + \mathrm{O_2}\ . \tag{R9}$$

The net effect of these two reactions is

$$\mathrm{O_3} + \mathrm{O} \rightarrow 2\mathrm{O_2}\ \ . \tag{R10}$$

Examples of catalysts X in the stratosphere are nitric oxide (NO), chlorine (Cl), bromine (Br), and hydroxyl radical (OH). The catalytic cycle is terminated when these catalysts are converted to unreactive reservoir species, such as dinitrogen pentoxide (N_2O_5), nitric acid (HNO_3), hydrochloric acid (HCl), chlorine nitrate ($ClONO_2$), and hydrobromic acid (HBr). More serious ozone loss in the polar regions is due to reaction with chlorine monoxide (ClO). This involves the formation of polar stratospheric clouds (PSCs), which remove reactive nitrogen from the gas phase but also activate chlorine, which destroys ozone more effectively than NO_x (NO and NO_2). For example, exceptionally low Arctic ozone levels were observed in the spring of 2011 coincident with evidence of PSCs over Eureka (Adams et al., 2012a; Lindenmaier et al., 2012).

There are two major dynamical processes that govern Arctic ozone variability. The first is the Brewer-Dobson circulation, named after Alan Brewer (Brewer, 1949) and Gordon Dobson (Dobson, 1956), which involves an upward motion of the airmasses from the troposphere into the stratosphere at low latitudes, poleward motion in the lower stratosphere of each hemisphere, and a slow descent back into the troposphere in the middle and high latitudes (Andrews, 2010). Although the Brewer-Dobson circulation is now used to describe the transport structure of ozone, it was first inferred by Brewer from observations of water vapour and helium over southern England. Brewer found that the helium content was constant up to 20 km but water content dropped rapidly just above the tropopause. He proposed that the observed distributions could be explained by the existence of a circulation in which air enters the stratosphere at the equator, where it is dried by condensation, travels in the stratosphere to temperate and polar regions, and sinks into the troposphere (Brewer, 1949). Dobson linked the circulation proposed by Brewer to ozone. From observations of ozone distribution (although ozone is mainly formed in the equatorial stratosphere, significant amounts of ozone are found at high latitudes), Dobson inferred that the transportation of ozone-rich airmasses from low latitudes to high latitudes must occur through meridional circulation in the stratosphere (Dobson, 1956). In general, the Brewer-Dobson circulation increases the ozone concentrations in the winter polar stratosphere (Butchart et al., 2006; Tegtmeier et al., 2008; Andrews, 2010). The second important dynamical process is related to the polar vortex, which is formed in polar winter due to lack of sunlight and strong meridional temperature gradient. At the edge of the strong temperature gradient, a westerly jet develops in the stratosphere. The low-pressure area inside the jet is called the polar vortex, which isolates the polar stratospheric airmass from its surroundings. In the Arctic, the accumulated ozone (through the Brewer-Dobson circulation in the polar winter) starts to decline when sunlight returns in spring. The extent of Arctic winter-spring ozone depletion in any one year is dominated by the very large meteorological variability exhibited by the Northern Hemisphere polar vortex (WMO, 2014).

In general, ozone loss in the Arctic is a combination of both chemical and dynamical processes (Tegtmeier et al., 2008). For example, the remarkably low ozone levels in 2011 were due to anomalously persistent low temperatures and a strong, isolated polar vortex in the lower stratosphere during spring 2011 that led to a large chlorine- and bromine-induced chemical ozone depletion, and also to weak transport of ozone-rich airmasses into the vortex from lower latitudes (Manney et al., 2011; WMO, 2014).

1.3.2 Ozone Remote Sensing Monitoring Networks

The earliest remote sensing network observations of TCO can be traced back to 1926 when Dobson deployed five Féry photographic spectrometers in Europe (Dobson, 1968a). Later, Dobson developed a new photometric instrument, now called the Dobson Ozone Spectrophotometer, which was made commercially available in the 1930s. There are still approximately 100 of these instruments being used by the WMO/GAW network. Measurement of ozone by the Dobson instrument requires on-site operation. Thus to automate the TCO measurements and also to remove the SO_2 dependence (when the atmospheric SO_2 amount is high, the Dobson instrument will show artificially increased TCO measurements) (Kerr et al., 1981), the Brewer Ozone Spectrophotometer was developed in the early 1980s (Brewer, 1973). In 1988, the Brewer instrument was designated (in addition to the Dobson instrument) as the WMO/GAW standard for TCO measurements. Due to the well-known stray light issue in the UV region (Bais et al., 1996; Fioletov et al., 2000), the MkIII Brewer (double Brewer) was introduced in 1992. The double Brewer has two spectrometers in series, significantly improving UV response and measuring global UV spectral irradiance, O_3, SO_2, and aerosol optical depth. The World Ozone and Ultraviolet Radiation Data Centre (WOUDC) operated by Environment and Climate Change Canada (ECCC) on behalf of the WMO, shows 62 stations reporting Dobson data and 48 reporting Brewer data by 2008 (McElroy and Fogal, 2008). By 2014, there were more than 220 Brewer instruments installed around the world, with most in operation today.

To reduce the cost and improve the accuracy of multi-trace-gas remote sensing, the Pandora system was developed at NASA's Goddard Space Flight Center and first deployed in the field in 2006. Pandora instruments are based on a commercial spectrometer with stability and stray light characteristics that make them suitable candidates for both direct-sun and zenith-sky measurements of total column ozone and other trace gases (Herman et al., 2009; Tzortziou et al., 2012). Pandora instruments have been tested and deployed in multiple scientific measurement campaigns around the world. These include the Cabauw Intercomparison Campaign of Nitrogen Dioxide measuring Instruments (CINDI) in the Netherlands in 2009 (Roscoe et al., 2010) and four NASA DISCOVER-AQ campaigns since 2011 (Tzortziou et al., 2012). The Pandora instruments have been used for validation of satellite ozone (Tzortziou et al., 2012) and NO_2 (Herman et al., 2009; Tzortziou et al., 2012) measurements. By 2015, several long-term

Pandora sites had been established in the United States and worldwide (including Austria, Canada, Canary Islands, Finland, and New Zealand). A comparison of Pandora and Brewer TCO datasets is presented in Chapter 5.

The most accurate ozone data products of Dobson, Brewer, and Pandora instruments are from their direct sun (DS) measurements. However, in addition to DS measurements, these instruments can also derive TCO from zenith sky (ZS) scattered sunlight measurements. While DS measurements are more accurate, ZS measurements are necessary for generating long-term ozone time series unbiased by meteorological conditions and for the validation of satellite algorithms for cloudy scenes (Fioletov et al., 2011). Another major ozone monitoring network which focuses on ZS observation is the international Network for the Detection of Atmospheric Composition Change (NDACC) UV-VIS Working Group (UVVIS-WG) (Van Roozendael and Hendrick, 2009). NDACC has several working groups, which include Dobson, Brewer, Fourier transform infrared spectrometer (FTIR), lidar, microwave, satellite, sondes, and UV-VIS. The NDACC is composed of more than 70 high-quality, remote-sensing research stations for observing and understanding the physical and chemical state of the stratosphere and upper troposphere and for assessing the impact of stratosphere changes on the underlying troposphere and global climate. The NDACC UVVIS-WG consists of about ten research institutes and university labs that operate more than 30 UV-visible spectrometers deployed worldwide. With an emphasis on the long-term evolution of the ozone layer, these instruments have provided more than two decades of regular measurements of total column amounts of ozone retrieved from ZS scattered sunlight differential optical absorption spectroscopy (DOAS) observations (Vaughan et al., 1997; Van Roozendael et al., 1998). Two UV-VIS DOAS instruments, the University of Toronto Ground-based Spectrometer (UT-GBS) and the Polar Environment Atmospheric Research Laboratory GBS (PEARL-GBS) have been deployed in Eureka since 1999 and 2006 respectively, and they are part of the NDACC UVVIS-WG. Further details (instrumentation and characterization) about these instruments are provided in Chapter 2.

1.4 Thesis Outline and Scientific Contributions

The thesis has six chapters. This first chapter covers the scientific background and other chapters are organized as follows.

Chapter 2 describes the instrumentation and data analysis and has four parts. The first part is a review and update of the UT-GBS and PEARL-GBS status. I have been responsible for the GBSs since 2011, which involved four visits to Eureka and one campaign at Cabauw. During each field campaign, I performed standardised laboratory testing for the GBSs, following methodologies developed by a previous post-doctoral fellow and three Ph.D. students (Matt Bassford, Elham Farahani, Annemarie Fraser, and Cristen Adams). In 2015, I upgraded UT-GBS from ZS-DOAS to multi-axis (MAX-) DOAS operation and also implemented negative elevation viewing geometry for PEARL-GBS MAX-DOAS measurements. In 2016, I upgraded PEARL-GBS from 1-D MAX-DOAS to 2-D MAX-DOAS viewing for the second Cabauw Intercomparison of Nitrogen Dioxide measuring Instruments (CINDI-2) campaign. The UT-Suntrackers used by the GBSs to perform MAX-DOAS measurements were first developed by Clive Midwinter and colleagues. The tracking software was primarily developed by Cristen Adams (until Trax2.4, passive tracking) and Jonathan Franklin (until Trax6.3, active tracking). The UT-Suntracker #1 was deployed by Cristen Adamas at Eureka in 2008, and the UT-Suntracker #2 was deployed by Sophie Tran at Eureka in 2014. The second part of Chapter 2 includes brief methodology of ZS-, MAX-, and DS-DOAS, along with introduction of profile retrieval codes used in this work. The third part of Chapter 2 includes descriptions of the Canadian Arctic ACE/OSIRIS Validation Campaigns. During each of the campaigns (2011, 2012, 2013, and 2015), I spent about three weeks working intensively with other researchers at the PEARL Ridge Lab in Eureka. I was responsible for calibration and operation of GBSs, as well as the set-up and operation of a guest instrument, the Système D'Analyse par Observations Zénithales (SAOZ) from France (Hendrick et al., 2011). Sophie Tran helped me work on the GBSs during the 2014 campaign, and she travelled to Eureka again in October 2014 to assemble the UT-Suntracker #2 and a new housing (developed by Orfeo Colebatch) for PEARL-GBS. The Eureka GBS zenith-sky ozone and NO_2 columns were submitted to the NDACC archive in NASA Ames format in 2013. GBS data in Hierarchical Data Format (HDF) will be updated and submitted to the NDACC archive in early 2017 by Kristof Bognar. The last part of Chapter 2 describes the CINDI-2 campaign (September 2016) that Kristof Bognar and I participated in and some preliminary aerosol optical depth (AOD) and NO_2 profile comparison results. Kristof and I worked together for about two months to prepare the PEARL-GBS for the CINDI-2 campaign. Kristof was in charge of the hardware and organised shipping logistics. With help from Orfeo Colebatch, Kristof refurbished the cooling box used by UT-GBS in the MANTRA campaigns and arranged the installation of PEARL-GBS and the UT-Suntracker #3. I was mainly in charge of upgrading the software to match the data acquisition sequences defined for the campaign and enabling/testing the active tracking. During the campaign, Kristof and I deployed the instrument together. Kristof was responsible for the production of O_4 and NO_2 dSCD data, while I was responsible for profile retrievals. The NO_2 lidar data were provided by Dr. Stijn Berkhout from National Institute for Public Health and the Environment (RIVM), the Netherlands.

Chapter 3 presents a case study of a transported bromine explosion event (BEE) in 2011. Ozone depletion events in the polar troposphere have been linked to extremely high concentrations of bromine. However, as addressed in Sections 1.1 and 1.2, the optimum meteorological conditions for the occurrence of these events remain uncertain. On 4-5 April 2011, a combination of both blowing snow and a stable shallow boundary layer was observed during an ODE at Eureka. Measurements made by PEARL-GBS were used to retrieve BrO profiles and partial columns. During this event, the near-surface BrO volume mixing ratio (VMR) increased to ~20 parts per trillion by volume (pptv), while ozone was depleted to ~1 parts per billion by volume (ppbv) from the surface to 700 m. Cristen Adams and I acquired the GBS data together. Prof. Robin Schofield provided an optimal estimation code that I used to retrieve stratospheric BrO profiles. Dr. Xin Yang performed a model simulation for this case using a chemical-climate model, which has the blowing snow scheme included. Dr. Andreas Richter and Dr. Anne Blechschmidt provided the Global Ozone Monitoring Experiment-2 (GOME-2) tropospheric BrO column data for the comparison work. The optimal estimation code that I used to retrieve tropospheric aerosol and BrO profiles was provided by Dr. Udo Friess. Dr. Ja-Ho Koo helped in performing backward trajectories study. This work has been published in *Journal of Geophysical Research – Atmosphere* (Zhao et al., 2016a). I also contributed GBS data to Blechschmidt et al. (2016), which was a complementary study of the 2011 BEE.

Chapter 4 continues the work of Chapter 3. It focuses on new evidence of cyclone-induced ODE. First, multiple ground-based and satellite datasets were used to identify two similar cyclone-induced surface ozone depletion events in Eureka on March 2007 and April 2011. These two events were coincident with observations of depleted HDO, and indicate the condensation and sublimation process during the transportation of the ozone-depleted airmass. Lidar and radar measured the ice cloud and aerosol when the ozone- and HDO-depleted airmass arrived at Eureka. Two global models were used to simulate the surface ozone depletion. Dan Weaver was responsible for the HDO/H_2O dataset. Dr. Matthias Schneider produced MUSICA δD data. Lidar and radar data were provided by Dr. Edwin Eloranta. Dr. Gloria Manney and Dr. Luis Millán were responsible for the MERRA-2 data. Dr. Xin Yang performed the chemical model simulations (both pTOMCAT and UM-UKCA) for these two cases. Dr. Vitali Fioletov and Dr. David Tarasick from ECCC provided Brewer and ozonesonde data. Dr. Frederick Michel from Carleton University and Dr. Xiahong Feng from Dartmouth College provided Eureka isotopologue precipitation data. This work benefited from discussions with Prof. Dylan Jones and Prof. Jon Abbatt. A manuscript on this work has been completed and will be soon submitted to *Atmospheric Chemistry and Physics*.

Chapter 5 presents a comparison of TCO measurements by Brewer and Pandora instruments. This work evaluates the performance of the recently developed Pandora spectrometers (introduced in 2006, deployed in Toronto in 2013) by comparing it with the Brewer world reference triads, which are composed of three single Brewers (deployed in Toronto in1980s) and three double Brewers (deployed in Toronto in the 1990s). The statistical uncertainty analysis of TCO records from these instruments indicates that the random uncertainty for the Brewer is below 0.6%, while that for the Pandora is below 0.4%. However, there is a 1% seasonal difference and a 3% bias between the standard Pandora and Brewer TCO data, which is related to the temperature dependence and difference in ozone cross sections. A statistical model was developed to remove this seasonal difference and bias. In addition, the stray light performance of both Pandora and Brewer instruments were investigated. In this work, I was responsible for writing the code of the statistical models and performing analysis. The model and analysis work was done under the supervision of Dr. Vitali Fioletov and Prof. Kimberly Strong. Dr. Vitali Fioletov, Dr. Jonathan Davies, and Dr. Alexander Cede provided the Brewer and Pandora datasets. This work has been published in *Atmospheric Measurement Techniques* (Zhao et al., 2016b).

The last chapter summarises the conclusions and presents suggestions for future work. In general, in comparison to the Ph.D. theses by previous students who have worked with the GBSs (Farahani, 2006; Fraser, 2008; Adams, 2012), this thesis presents a broader picture of using UV-visible spectroscopy to measure and monitor atmospheric trace gases. The major contributions include: upgrading UT-GBS to 1-D and PEARL-GBS to 2-D MAX-DOAS instruments, performing trace gas (BrO, NO_2, and O_4) vertical profile retrievals, investigating blowing-snow-induced ODEs, evaluating the Brewer and Pandora TCO measurements, and improving our understanding of the Pandora temperature dependency effect. I also spent time working on studies of the colour index dataset generated by the GBSs and stratosphere-troposphere exchange events (or stratospheric intrusion events) over Eureka, which are not included in this thesis. These studies may lead to future publications.

Chapter 2

2 Instrumentation, Data Analysis, and Campaigns

This chapter describes the technical aspects and the data analysis methodology for the UT-GBS and PEARL-GBS that were used in the bromine explosion study (Chapter 3 and 4). These GBS instruments were first deployed in Eureka in 1999 and 2006 respectively as zenith-sky-viewing DOAS instruments. After more than a decade, these two instruments have been gradually upgraded to ZS/DS/MAX-DOAS instruments with more capabilities to measure both stratospheric and tropospheric species. The standard laboratory calibration procedures for GBSs have been presented in previous Ph.D. theses (Farahani, 2006; Fraser, 2008; Adams, 2012). Thus the current chapter will only address the instrument status from 2011 to 2015 in the context of the GBS standard laboratory calibration. In addition, upgrades that been made during my Ph.D. study are summarised in this chapter.

2.1 UV-visible Spectrometers

2.1.1 Brief History of GBSs

The GBS instruments have been involved in numerous field campaigns, which were summarised in Adams (2012). The GBS measurement history table has been updated to the present (see Table 1) based on Adams (2012). The UT-GBS was assembled by Dr. M. Bassford and Dr. K. Strong in 1998 and was first deployed as one of the ground-based instruments in the MANTRA 1998 balloon campaign in Vanscoy, Saskatchewan (Bassford et al., 2001; Bassford et al., 2005). After that, UT-GBS worked as a travelling instrument and participated in another three MANTRA balloon campaigns, 17 springtime campaigns at Eureka, one springtime campaign at Resolute Bay (2002), and the 2009 CINDI campaign at Cabauw, the Netherlands. When it is not travelling, the UT-GBS takes measurements in the University of Toronto Atmospheric Observatory or stays at the Polar Environment Atmospheric Research Laboratory (PEARL, Fogal et al. (2013)) for extended periods. From 1999 to 2014, the UT-GBS only performed ZS-DOAS measurements, except during the 2009 CINDI campaign, when a suntracker (UT-Suntracker #2) was installed above the UT-GBS to allow MAX-DOAS measurements (Roscoe et al., 2010). In February 2015, the UT-GBS was moved to the PEARL-GBS hatch at the PEARL

Ridge Lab and took over the PEARL-GBS suntracker (UT-Suntracker #1). Since then, UT-GBS has performed ZS- and MAX-DOAS measurements in Eureka.

The PEARL-GBS was a near identical instrument to the UT-GBS made by the same manufacturer (Jobin-Yvon/Horiba). The major improvement on this instrument is an integrated filter wheel in its optics. It was assembled by Annemarie Fraser and permanently installed at PEARL Ridge Lab in August 2006 and has been taking measurements during the sunlit part of the year since then. The NDACC UV-VIS Working Group has established a series of criteria to ensure consistency in NDACC certified UV-visible instruments. These standards are described on the NDACC website (NDACC, 2017). The PEARL-GBS was granted NDACC certification in January 2009. In February 2008, a suntracker (UT-Suntracker #1) was installed above the PEARL-GBS at PEARL Ridge Lab. Blocked by the railings on the roof, the lowest elevation viewing angle that UT-Suntracker #1 can achieve is only 6°, which is not ideal for MAX-DOAS. In October 2014, a new suntracker housing was constructed and placed on the north-west corner of Ridge Lab roof to enable low-elevation-viewing measurements (the lowest elevation viewing angle was -1°). The UT-Suntracker #2 was refurbished and installed in the new housing. The PEARL-GBS has been using this tracker since 2015. In September 2016, the PEARL-GBS participated in the CINDI-2 campaign at Cabauw, the Netherlands. In general, I was responsible for GBSs operation and data production from 2011 to 2015. M.Sc. student Kristof Bognar participated in the 2016 Eureka and CINDI-2 campaigns and is taking over this UV-Visible project.

Table 1: Measurement history of the UT-GBS and PEARL-GBS instruments.

Campaign	**Location**	**UT-GBS**	**PEARL-GBS**
MANTRA	Vanscoy, Saskatchewan (52°N, 107°W)	19-26 Aug 1998[a, b, c] 18-26 Aug 2000[d] 20 Aug - 3 Sep 2002[d] 3 Aug - 15 Sep 2004[e, f, g]	N/A
Stratospheric Indicators of Climate Change (spring 2001, 2003), Canadian Arctic/OSIRIS Validation Campaigns (spring 2004-present), and CANDAC/PAHA (year-round 2006-present)	Eureka, Nunavut (80°N, 86°W)	22 Mar - 11 Apr 1999[h, i, j]	
		22 Feb - 23 Mar 2000[d, j]	
		28 Feb - 23 Mar 2001[d]	
		18 Mar - 22 Apr 2003[d, j, k]	
		25 Feb - 14 Apr 2004 [e. j, k, l, m]	
		21 Feb - 30 Mar 2005 [e, j, k, m]	
		20 Feb - 31 Mar 2006[e, j, k, m]	13 Aug - 17 Oct 2006[e, j, n]
		21 Feb - 11 May 2007[e, j, k, n]	14 Feb -17 Oct 2007[e, j, k, n]
		26 Feb - 17 Oct 2008[j, k]	14 Feb - 17 Oct 2008[j, k, o]
		18 Feb - 31 Mar 2009[j, k]	14 Feb - 17 Oct 2009[j, k]
		23 Feb - 17 Oct 2010[j, k]	8 Mar - 17 Oct 2011j[j, k]
		14 Feb - 17 Oct 2011[j, k, p]	16 Mar - 15 Apr 2011[j, k, p, q]
		18 Feb - 29 Sept 2012	29 Feb - 17 Oct 2012
		27 Feb - 17 Oct 2013	26 Feb - 17 Oct 2013
		28 Feb - 17 Oct 2014	18 Feb - 17 Oct 2014
		12 Feb - 17 Oct 2015	16 Feb - 17 Oct 2015
		10 Feb - 26 Oct 2016	5 Mar - 10 May 2016
Stratospheric Indicators of Climate Change	Resolute Bay, Nunavut (75°N, 95°W)	15 Mar - 15 Apr 2002	N/A
Toronto Atmospheric Observatory	Toronto, Ontario (44°N, 79°W)	19 Dec - 31 Dec, 2001 1 Jan - 11 Feb, 2002 12 Dec - 31 Dec, 2002 1 Jan - 3 Feb, 2003 29 Jul - 28 Aug, 2003 7 Jan - 3 Feb 2004 2 May - 14 Dec 2005 18 Apr - 31 Dec 2006[e] 27 Jun - 25 Dec 2007 8 Jan - 14 Jan 2008 10 Dec 2013 – 10 Jan 2014	16 Dec 2016 - 13 Jan 2017
CINDI/NDACC Certification	Cabauw, Netherlands (52°N, 56°E)	13 Jun - 17 Jul 2009[r, s, t]	
CINDI-2	Cabauw, Netherlands (52°N, 56°E)	N/A	31 Aug - 29 Sept 2016[u]

a (Bassford et al., 2001)
b (Bassford et al., 2005)
c (Melo et al., 2005)
d (Farahani, 2006)
e (Fraser, 2008)
f (Fraser et al., 2007a)
g (Fraser et al., 2007b)
h (Bassford et al., 2000)
i (Melo et al., 2004)
j (Adams et al., 2012a)
k (Adams et al., 2012b)
l (Kerzenmacher et al., 2005)
m (Fraser et al., 2008)
n (Fraser et al., 2009)
o (Adams et al., 2010)
p (Adams et al., 2013)
q (Zhao et al., 2016a)
r (Roscoe et al., 2010)
s (Piters et al., 2012)
t (Pinardi et al., 2013)
u (Hendrick et al., 2016)

2.1.2 The University of Toronto Ground-Based Spectrometer

The UT-GBS and PEARL-GBS are both Triax-180 grating spectrometers, built by Jobin-Yvon/Horiba. The Triax-180 is a crossed Czerny-Turner triple grating imaging spectrometer, meaning that light is directed by a collimating mirror to a grating and is then focused by a focusing mirror onto a charge-coupled device (CCD). This scheme is advantageous for DOAS applications because the wavelength range can be selected by rotating the grating and stray light is minimised by reducing the reflection of unwanted diffraction orders (Platt and Stutz, 2008). A schematic of the Triax-180 spectrometer is shown in Figure 2.1. The schematic plots are updated from Adams (2012) with these changes: (1) the f-number matcher (and a mechanical entrance slit) on UT-GBS was removed in February 2012, (2) a new wedged CCD mount was added to the PEARL-GBS in March 2013, and (3) both instruments now use a spot-to-slit fibre (SSF) bundle since 2010 and 2011 for PEARL- and UT-GBS respectively (they were liquid light guides (LLG) in Adams (2012)).

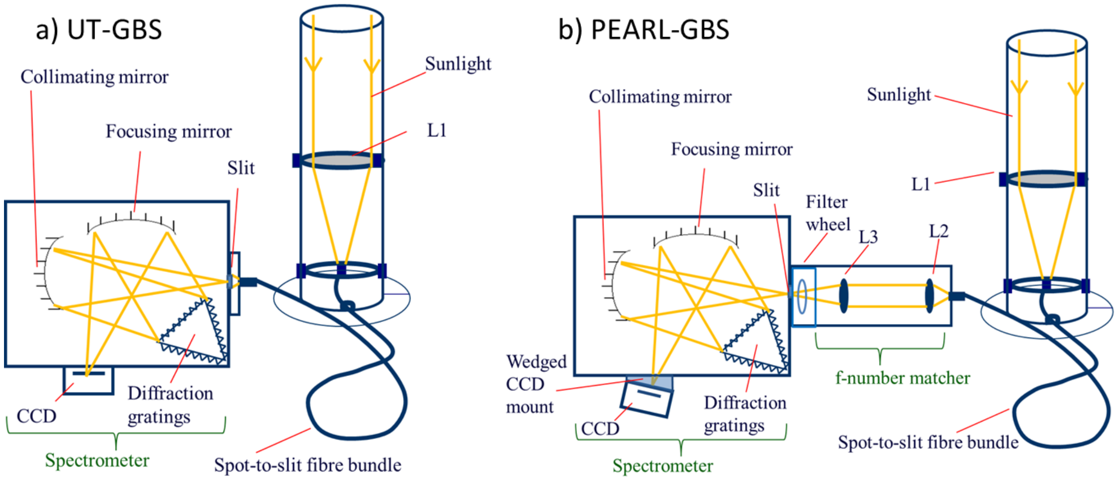

Figure 2.1: Schematics of (a) the UT-GBS and (b) the PEARL-GBS. Figure updated from Adams (2012).

Focused light enters the slit of the instrument and passes through a mechanical shutter. The light is then collimated by the collimating mirror, dispersed by the diffraction grating, and focused by the focusing mirror onto the detector. The optics of the instrument provide point-to-point imaging, generate a flat-field input, and are aspherical to correct for astigmatism. The spectrometer has a focal length of 0.190 m (f/3.9[1]) and a 12×30 mm focal plane.

Technical details of the gratings are summarised in previous Ph.D. theses (Farahani, 2006; Fraser, 2008; Adams, 2012), including groove density, wavelength coverage, grating type (ruled or holographic), and grating efficiencies. No changes have been made to the gratings. In general, the equation for a diffraction grating is

$$sin\alpha + sin\beta = kn\lambda \tag{2.1}$$

where α is the incidence angle, β is the diffraction angle, k is the diffraction order, n is the groove density of the diffraction grating, and λ is the wavelength of light (Kitchin, 2013). By differentiating the above equation (assuming the only variable is the diffraction angle), the spectral resolution of the grating can be written as:

$$\Delta\lambda = \frac{cos\beta\Delta\beta}{kn} \ . \tag{2.2}$$

Higher spectral resolution (smaller $\Delta\lambda$) is obtained at higher groove density, higher order of diffraction, and the diffraction angle closer to 90°. The Triax-180 spectrometer has three gratings with different groove densities. The gratings are attached to a motorized turret, thus the spectral resolution and wavelength range can be selected for different measurements. Typically, the 600 groove per mm (gr/mm) grating is used for ozone, NO_2, and O_4 measurements, while a high-density grating (1800 gr/mm for UT-GBS and 1200 gr/mm for PEARL-GBS) are used for BrO, OClO, and HCHO measurements.

As shown in Figure 2.1, the spectrometer uses a CCD detector to record spectra. The UT-GBS has used three CCD detectors since 1998, which are described by Fraser (2008). Since the 2004 MANTRA campaign, it has used a back-illuminated detector with 2048×512 pixels, each of which has the physical size 13.5×13.5 µm. The 2048 horizontal pixels (X-pixels) correspond to different measurement wavelengths, while 512 vertical pixels (Y-pixels) correspond to the height

---

[1] f-number is the ratio of the lens's focal length to the diameter of the entrance pupil. The number is noted as f/N, where N is the f-number.

of the light incident on the slit. The detector is coated with a UV-enhanced coating, yielding a high quantum efficiency of 50-70% between 300-600 nm. The detector has a Peltier thermo-electric cooling system and operates at a constant temperature of 201 K, provided the ambient temperature is less than 35 °C. Above this temperature, which is outside the suggested operating range of the instrument, the CCD temperature can increase. The low CCD temperature is necessary to minimise the CCD dark current, which is mainly due to thermally generated electrons in the CCD itself. The dark current (DC) increases with CCD temperature and exposure time as:

$$\mathrm{DC} = Ate^{-B/T} \quad . \tag{2.3}$$

Here, A and B are constants of the detector, t is exposure time, and T is CCD temperature (Mackay, 1986).

The UT-GBS had a f-number matcher and a mechanical entrance slit from 1998 to 2011 (Farahani, 2006; Fraser, 2008; Adams, 2012). These units have been removed and were replaced by an AFO-XY fibre mount and a fixed slit in February 2012. In addition, due to these changes, the L1 lens has also been changed (the f-number changed from f/2.5 to f/4) to match the spectrometer f-number. Thus the theoretical field-of-view (FOV) of the input optics has been changed from 2° to 0.2°. There are a couple of reasons for these modifications to the optics. Adams (2012) reported that the input optics of the instruments, particularly the UT-GBS, cause optical aberrations. The removal of the f-number matcher and direct coupling of a fibre bundle to the entrance slit of the instrument reduces these aberrations. In addition, the mechanical slit performance was deteriorating (reported by Adams (2012)); it would jam causing intermittently decreased resolution and unstable instrumental operation. Thirdly, the main purpose of using a f-number matcher in the system was to "increase" the f-number of L1 (original f/2.5) to match the f-number of the Triax-180 spectrometer (f/3.9) (thus to avoid loss of the light signal[2]). However, in March 2011, the 1-m LLG (with a core diameter of 3 mm and f/0.85) was replaced by a 1-m

---

[2] Large f-number corresponds to a small numerical aperture (NA), which is a dimensionless number that characterizes the range of angles over which the system can accept light. For example, the old L1 has NA≈0.2 (f/2.5) and the spectrometer has NA≈0.128 (f/3.9), thus without f-number matcher, the light though old L1 cannot be fully accepted by the spectrometer. However, after the removal of f-number matcher, it is necessary to replace the old lens with the new L1 (NA≈0.125).

SSF (see Figure 2.2, the spot of 0.65 mm diameter at the entrance, the slit end of 3.3×0.1 mm at the exit, and f/2.27). The transmittance and coupling efficiency of the SSF are much higher than those of the LLG, thus with the SSF, the light signal received by the CCD is sufficient to compensate the larger f-number of L1 (as the FOV of the new L1 lens is smaller, less light is collected by L1). In general, the SSF improves the coupling of the signal to the spectrometer and the resolution (Adams, 2012). Thus the f-number matcher no longer provides any advantages.

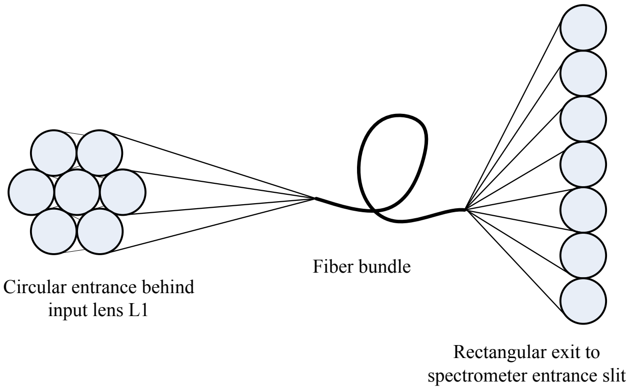

Figure 2.2: Schematic of a spot-to-slit optical fibre bundle. The cross-section changes from a circle at the entrance to a column at the exit to match the shape of the entrance slit of the spectrometer.

The next upgrade for UT-GBS was in February 2013, when a new 10-m slit-to-spot fibre bundle was used to further improve the depolarization. Due to scattering effects in the atmosphere, the polarization of sunlight varies with SZA. Since the GBS gratings are sensitive to polarization (Adams, 2012), light must be depolarised to avoid errors in DOAS retrievals. A long fibre coiled into several loops can scramble the polarization state of the transmitted sunlight, thus effectively removing the polarization sensitivity of a DOAS instrument (Platt and Stutz, 2008). The latest upgrade for UT-GBS was in March 2015, when it was moved to the PEARL-GBS hatch and coupled to UT-Suntracker #1 and GBS cooling unit #2.

There are two cooling units (each unit composed of an insulated aluminum box, air conditioner, and temperature monitor) that were constructed for GBS for mid-latitude summer time deployment. The insulated aluminium box for the first unit (GBS cooling unit #1) was constructed in 1998 by Quantum Scientific and the second box (GBS cooling unit #2) was constructed in 2002 by Cases Unlimited Inc. The GBS cooling unit #1 was used in the MANTRA 1998 and 2000 campaigns, and the CINDI-2 campaign. The GBS cooling unit #2 was used in the MANTRA 2002 and 2004 campaigns (Farahani 2006), and CINDI campaign (Adams 2012). These boxes are insulated by 1.27 cm black foam insulation, and the temperature is controlled by an air conditioner having both cooling and heating capacities.

A summary of UT-GBS configurations for springtime measurements at Eureka is shown in

Table 2 (modified and updated based on Adams (2012)). In general, since 2015, the UT-GBS works as a ZS/MAX-DOAS instrument in the visible (using the 600 gr/mm grating centred at 450 nm), targeting stratospheric O_3, NO_2, and OClO, and tropospheric NO_2 and O_4.

2.1.3 The PEARL Ground-Based Spectrometer

The PEARL-GBS was a near identical instrument to the UT-GBS when it was assembled in 2006, the major difference at that time being the addition of a filter wheel (Fraser, 2008; Adams, 2012). However, as shown in Figure 2.1, the configurations of these two instruments are quite different now. First, the PEARL-GBS has a filter wheel which allows it to perform direct-sun measurements. Second, the PEARL-GBS still has a f-number matcher in its input optics. Third, the PEARL-GBS uses a wedged CCD mount, while UT-GBS uses a flat mount.

The PEARL-GBS has a motorised filter wheel, which holds six filters. Before February 2015, the filter wheel contained an empty slot, a long-wave (>575 nm) filter (Andover 590FG05), and 25%, 1%, 0.1%, and 0.01% neutral density filters (Edmund Optics). These filters were used in direct-sun measurements from 2008 to 2011. However, it was found that the spectra taken with these reflective filters were of poor quality (Adams, 2012) introduced by Fabry-Perot etalon structures, which arise from interference patterns when light encounters two reflecting surfaces (Lipson et al., 2010). These structures can be caused by reflective neutral density filters and the surface of CCD detectors (Stutz and Platt, 1993). Thus a new set of absorption filters was installed in October 2014. These filters are made of fused silica substrates with metallic coatings optimised for the UV spectrum. They are the same filters (BMV Optical) as used in the Brewer spectrometers, and have transmittances of 25%, 1%, 0.1%, and 0.01%. The transmittance curves are shown in Figure 2.3.

Table 2: Summary of UT-GBS springtime measurements at Eureka.

Year	Grating (gr/mm)	Viewing	Spectral quality	Fibre/light guide	Ambient temperature control
1999	400	Zenith-sky	Good (mechanic slit (MS) 0.1 mm)	Liquide light guide (LLG)	N/A
2000	600 and 1800	Zenith-sky	Good (MS 0.1 mm)	LLG	N/A
2001	600	Zenith-sky	Poor - slit jammed open (resolution ~ 4-5 nm, MS > 0.2 mm list)[a,b]	LLG	N/A
2003	400 and 600	Zenith-sky	Fair - error in acquisition software (reduced signal, MS 0.1 mm)	LLG	N/A
2004	400	Zenith-sky	Fair - error in acquisition software (reduced signal, MS 0.1 mm list)	LLG	N/A
2005	600	Zenith-sky	Good (MS 0.1 mm)	LLG	N/A
2006	600	Zenith-sky	Good (MS 0.1 mm)	LLG	N/A
2007	600	Zenith-sky	Good (MS 0.1 mm)	LLG	N/A
2008	600 and 1800	Zenith-sky	Good (MS 0.1 mm)	LLG	N/A
2009	600 and 1800	Zenith-sky	Good (MS 0.1 mm)	LLG	N/A
2010	600 and 1800	Zenith-sky	Fair - slit jammed open (slightly reduced signal/resolution, MS 0.1 mm)	LLG	N/A
2011	600	Zenith-sky	Good, with improved resolution (MS 0.1 mm)	1 m slit-to-spot fibre (SSF)	N/A
2012	600	Zenith-sky	Good, F# matcher and mechanical slit removed (fixed slit (FS) 0.1 mm)	1 m SSF	N/A
2013	600	Zenith-sky	Good (FS 0.1 mm)	10 m SSF (depolarization improved)	N/A
2014	600	Zenith-sky	Good (FS 0.1 mm)	10 m SSF	N/A
2015	600	Zenith-sky and MAX-DOAS	Good (FS 0.1 mm)	10 m SSF	GBS cooling unit #2
2016	600	Zenith-sky and MAX-DOAS	Good (FS 0.1 mm)	10 m SSF	GBS cooling unit #2

a (Farahani 2006)

b (Adams 2012)

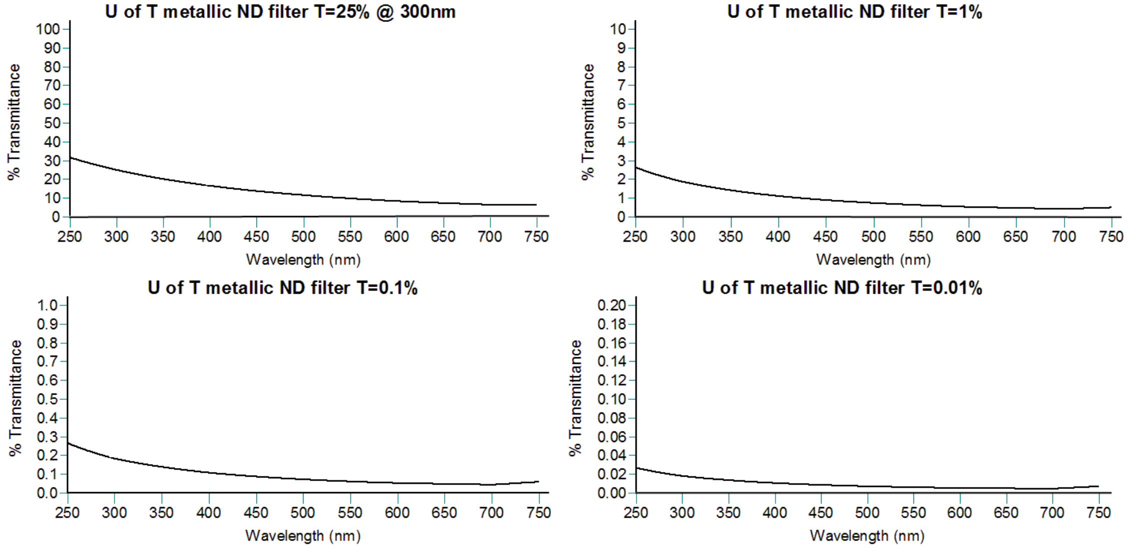

Figure 2.3: Transmittance of the metallic nurture density filters (provided by BMV Optical).

Another improvement in the system is a new wedged CCD mount. The Triax-180 spectrometer was not designed for DOAS applications. As shown in Figure 2.4, there is a 10° angle between the detector normal axis and the main optical axis. This angle does not affect the spectral resolution at the centre of the CCD chip but will cause uneven distribution of the resolution along the horizontal pixels of the CCD. Tremendous efforts were made by Adams (2012) to reduce aberrations. A detailed laboratory assessment of aberrations for PEARL-GBS was done in spring 2011 at Eureka (Adams, 2012). In general, it was observed while focusing the spectrometer that, by moving the CCD closer to the focusing mirror, the mercury lines to the left side of the CCD came into focus. As the CCD is moved further from the focusing mirror, the mercury lines on the right side of the CCD came into focus. This suggested that the CCD or the focusing mirror should be tilted slightly so that all X-pixels of the CCD are in focus at once. In February 2013, by implementing a wedged CCD mount (Jobin-Yvon/Horiba), this problem was solved. Figure 2.5 shows the mercury (blue/purple), neon (brown/green), and xenon (gray/cyan) pen lamp spectra in 2011 (flat mount) and 2013 (wedged mount) measured by the PEARL-GBS. The new wedged CCD mount improved the resolution and line shape on the edge of the CCD. For example, in 2011 (flat mount), the CCD had a resolution of 0.6-0.7 nm at the centre (with 600 gr/mm grating) but had a resolution of 1.5 nm on the right wing and 1.07 on the left wing. In 2013, the wedged mount gave a uniform resolution of 1 nm across the whole CCD chip.

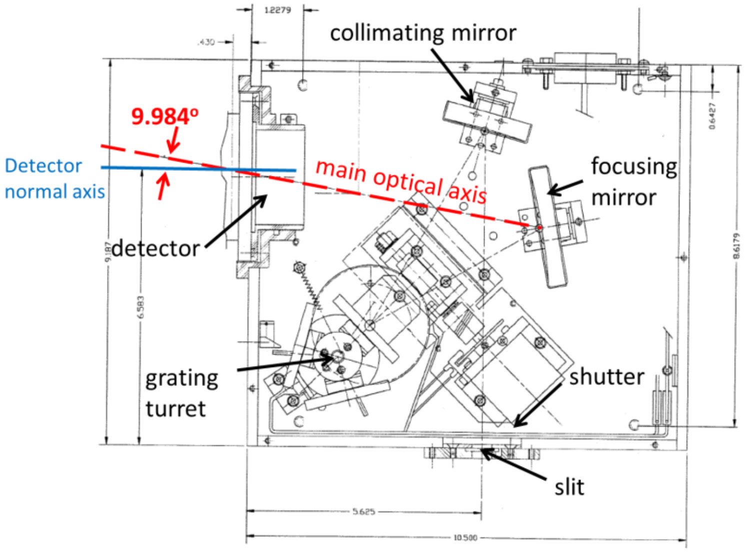

Figure 2.4: Triax-180 spectrometer internal optics (top view). Red dashed line indicates the main optical axis of the system from the focusing mirror to the detector. Blue line indicates the detector normal axis (perpendicular to the CCD chip). Figure adpted from Jobin-Yvon/Horiba Triax-180 drawing.

In October 2014, UT-Suntracker #2 was mounted in a new housing on the Ridge Lab roof (north-west corner), giving PEARL-GBS an unobstructed view of the valley. Thus MAX-DOAS lower elevation viewing angle measurements have been made since then (including -1°, 0°, and 5° in 2015, and expanded to more angles during the spring 2016 and CINDI-2 campaigns). These new low-elevation-angle measurements, which are more sensitive to the boundary layer, can improve the degrees of freedom for signal (DOFS) in the retrieved tropospheric trace gas profiles (Zhao et al., 2016a). The PEARL-GBS (spectrometer parts) was moved from the UV-visible lab to the IR lab (in a crawl space below the floor to improve thermal performance by reducing overheating) in October 2014, and a 30-metre long spot-to-slit fibre was used to connect the spectrometer to the input optics (inside the new housing on the roof).

A summary of PEARL-GBS configurations for springtime measurements at Eureka is shown in Table 3 (modified and updated based on Adams (2012)). In general, since 2010, the PEARL-GBS works as a ZS/MAX-DOAS instrument in the visible band (using the 1200 gr/mm grating centred at 350 nm), targeting stratospheric NO_2 and BrO, and tropospheric NO_2, BrO, and O_4.

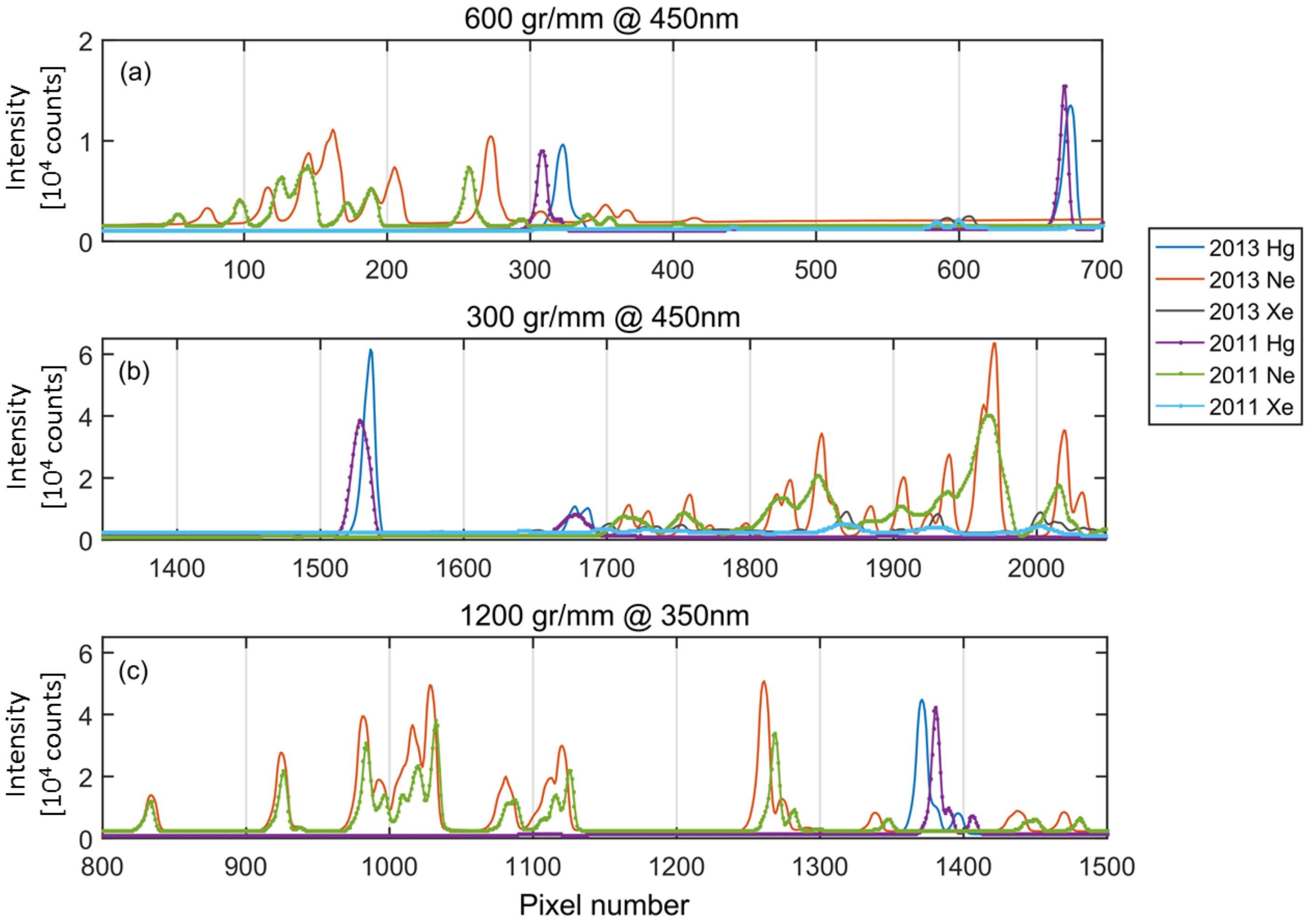

Figure 2.5: The mercury, neon, and xenon lines measured by the PEARL-GBS: (a) 600 gr/mm grating centered at 450 nm, (b) 300 gr/mm grating centered at 450 nm, and (c) 1200 gr/mm centered at 350 nm in 2011 (with flat CCD mount) and 2013 (with wedged CCD mount) at Eureka.

Table 3: Summary of PEARL-GBS springtime measurements at Eureka.

Year	Grating (gr/mm)	Viewing	Spectral quality	Fibre/light guide	Ambient temperature control
2007	600 and 1200	Zenith-sky	Good (0.05 mm slit)	Liquid light guide (LLG)	N/A
2008	600 and 1200	Zenith-sky and direct-sun	Good (0.05 mm slit)	LLG	N/A
2009	600 and 1200	Zenith-sky and direct-sun	Good (0.05 mm slit)	LLG	N/A
2010	600 and 1200	Zenith-sky, direct-sun, and MAX-DOAS	Good with improved resolution (0.05 mm slit)	1 m spot-to-slit fibre (SSF)	N/A
2011	1200	Zenith-sky, direct-sun, and MAX-DOAS	Good (0.1 mm slit)	1 m SSF	N/A
2012	1200	Zenith-sky and MAX-DOAS*	Good (0.1 mm slit)	1 m SSF	N/A
2013	1200	Zenith-sky and MAX-DOAS*	Good (0.1 mm slit)	6 m SSF	GBS cooling unit #2
2014	1200	Zenith-sky and MAX-DOAS*	Good (0.1 mm slit)	6 m SSF	GBS cooling unit #2
2015	1200	Zenith-sky and MAX-DOAS*	Good (0.1 mm slit)	30 m SSF	Crawl space (IR lab)
2016	1200	Zenith-sky and MAX-DOAS*	Good (0.1 mm slit)	30 m SSF	Crawl space (IR lab)

* Note: No direct-sun measurements were made from 2012 to 2016 due to unreliable filter wheel.

2.1.4 Instrument Resolution

The instrument resolution and sampling for both GBSs are shown in Table 4 and Table 5 (modified and updated based on Adams, (2012)). The resolution and sampling of the GBSs change slightly from year-to-year mainly due to refocusing of the CCD at the beginning of each campaign. In addition, the use of different CCDs (e.g., UT-GBS used three CCDs with different pixel sizes, Fraser, 2008; Adams, 2012), and changes made to the entrance slit (e.g., PEARL-GBS used 0.05 mm slit until 2010, Fraser, 2008; Adams, 2012), and the optical input fiber (Adams, 2012) can also affect the instrument resolution.

Table 4: UT-GBS sampling and resolution from 1998 to 2016.

	Sampling (pixel/FWHM)			Resolution (nm)		
Grating (gr/mm)	400	600	1800	400	600	1800
Original CCD: 1998-Eu2004[a]	7-20	6-20	7-16	0.8-5.4	0.5-2.3	0.2-0.8
Loaner CCD: MANTRA 2004[a]	3-19	3-18	3-12	“	“	“
New CCD: 2005-2009[b]	5-14	5.5-16	7-12	“	“	“
New CCD + input optics: 2010[c]	7-13	7.5-13	7.5-10.5	1.1-2.1	0.9-1.3	0.2-0.3
New CCD + SSF + f/2.2 input lens + f-number matcher: 2011[c]	7-13	7.5-13	7.5-10.5	0.9-1.4	0.6-2.0	0.2-0.3
New CCD + SSF + f/4 input lens + AFO-XY fiber mount: 2012-2016	7-13	7.5-13	7.5-10.5	0.5-1.5	0.4-1.8	0.1-0.3

a Values combined from Farahani (2006) and Fraser (2008).
b Values from Fraser (2008).
c Values from Adams (2012).

Table 5: PEARL-GBS sampling and resolution from 2006 to 2016.

	Sampling (pixel/FWHM)			Resolution (nm)		
Grating (gr/mm)	300	600	1200	300	600	1200
Original setup: 2006-2009[a]	5-14	4.5-16	7-12	1.0-3.0	0.5-2.5	0.2-1.8
New SSF : 2010[b]	4-6	3.5-5	4-4.5	0.9-1.3	0.4-0.6	0.17-0.19
New SSF + slit: 2011-2012	7-15	7-15	7-12	1.4-3.0	0.7-1.5	0.3-0.5
New SSF + slit + wedged CCD mount: 2013-2016	7-15	7-15	7-12	1.9-2.5	0.9-1.2	0.4-0.5

a Values combined from Farahani (2006) and Fraser (2008).
b Values from Adams (2012).

2.1.5 Active Solar Tracking System

The UT-Suntracker was developed at the University of Toronto for UV-visible and infrared spectrometers (Adams, 2012), with subsequent improvements (for example, active tracking) made at Dalhousie University (Franklin, 2015). UT-Suntracker #1 was assembled and tested in Toronto from 2006-2007. In February 2008, it was installed permanently above the PEARL-GBS at Eureka so that the instrument could take zenith-sky, direct-sun (with passive tracking), and MAX-DOAS measurements. In summer of 2009, UT-Suntracker #2 was installed above the UT-GBS (mounted on top of the GBS cooling unit #2) during the CINDI campaign to allow for

MAX-DOAS measurements. In October 2014, UT-Suntracker #2 was installed in a new housing on the Ridge Lab roof for the PEARL-GBS, and UT-GBS was coupled to Suntracker #1. In September 2016, another UT-Suntracker (borrowed from Dr. Kaley Walker) was installed above the PEARL-GBS (mounted on top of the GBS cooling unit #1) during the CINDI-2 campaign to allow for ZS/DS/MAX-DOAS measurements. The design, software (Trax2.4), and testing of the UT-Suntracker is described in Adams (2012). This section will briefly describe the upgrades that have been made since 2012.

The active tracking packages (camera, Trax6.3 software, and upgraded GBS LabVIEW control software) were implemented to PEARL-GBS (coupled with UT-Suntracker #2) in March 2015. There are two important features in the upgrade: active tracking and Transmission Control Protocol (TCP) communication. To achieve active tracking, the majority of the solar beam is focused on the collecting optics (L1) of the spectrometer while a portion of the beam is directed to a network video camera by pick-off mirrors. A neutral density filter (shade 11 welding glass) is placed in front of the camera lens to aid intensity level adjustments. The camera (NetcamXL, StarDot Technologies, 2048×1536 pixels, http://www.stardot-tech.com/) is equipped with a 48-mm zoom and optical doubler providing a 0.0019°/pixel image of the solar disk (Franklin, 2015). The camera continuously takes images of the solar disk that are used to update the active altitude and azimuth corrections of the UT-Suntracker. The correction values are calculated by locating the center position of the solar disk (an ellipse is fitted to the edge points of the solar disk image using least squares fitting). The position of the camera serves as the control point for the active tracking system. While any minor shifts in the optics before the camera will be corrected, any changes downstream will not, and therefore it is necessary that the camera is positioned at an appropriate location close to the input of the measuring device.

Both Trax2.4 and the Trax6.3 were written in the open-source programming language of Python. The Trax software is run on the suntracker laptop in a Linux system and is responsible for the direct control of the stage motors and camera. With active tracking, Trax has a better than ±0.01° tracking accuracy (Franklin, 2015). For the GBS system (spectrometer and suntracker), LabVIEW data acquisition software (run on the spectrometer laptop) sends out tracking/pointing commands to Trax2.4 via user datagram protocol (UDP). Next, Trax2.4 controls the UT-Suntracker motors using the Universal Serial Port Python Library (Adams, 2012). However, the broadcasting of the tracking commands by UDP was found to be inefficient and unstable (UDP has no error-checking and works as a one-way stream). Thus in Trax6.3, the communication between suntracker and spectrometer laptops uses a TCP link. The TCP link checks the completeness of the transported data packages and avoids any loss of tracker control commands. This improvement in the communication is critical for the GBSs, because they alternate between multi-elevation angle scanning modes (MAX-DOAS) and direct sun tracking, so the LabVIEW code needs a stable and interactive communicate with Trax code.

Although the hardware and software for active tracking have been implemented since spring 2015, the direct-sun active tracking was not used in 2015 due to the failure of the filter wheel. The first successful active tracking was made during the CINDI-2 campaign in the Netherlands in 2016 (see more details in Section 2.4).

2.2 Methodology

2.2.1 Zenith-Sky Differential Optical Absorption Spectroscopy

The first application of the principal of differential absorption, making use of the difference between the absorptions at two different wavelengths, can be traced back to 1920s when Dobson started TCO measurements (Dobson, 1968a). The modern DOAS method has been used for trace gas measurements in the laboratory and the field since the 1970s (Noxon, 1975; Perner and Platt, 1979; Platt et al., 1979). After four decades, DOAS is now one of the most commonly used spectroscopic techniques to measure trace gases in the open atmosphere from ground-based instruments (Solomon et al., 1987; Van Roozendael et al., 1998; Leser et al., 2003; Roscoe et al., 2010) and satellite instruments (Bovensmann et al., 1999; Burrows et al., 1999; de Vries et al., 2005; Veefkind et al., 2012).

DOAS instruments are categorized as active and passive DOAS, according to their light sources. In general, an active DOAS instrument has an artificial light source and a well-defined light path, while a passive DOAS instrument uses natural light sources, such as the sun and moon (Platt and Stutz, 2008) and relies on using geometric or radiative transfer calculations of the light path. Passive DOAS instruments can be further subdivided into direct and scattered light DOAS. In the current work, zenith-sky scattered sunlight DOAS (ZS-DOAS), multi-axis scattered sunlight DOAS (MAX-DOAS), and direct-sun DOAS (DS-DOAS) are used.

The ZS-DOAS is one of the earliest modern DOAS applications, in use since the 1980s (Mount et al., 1987; Solomon et al., 1987). While DS-DOAS measurements are more accurate (the uncertainties from estimation of the light path are smaller as mentioned above), ZS-DOAS measurements are necessary for generating long-term ozone time series throughout the year at all latitudes, and have greater stratospheric sensitivity than DS- and MAX-DOAS. ZS-DOAS is less sensitive to cloud cover, making it suitable for the validation of satellite algorithms for cloudy scenes (Van Roozendael et al., 1998; Fioletov et al., 2011; Hendrick et al., 2011). The GBSs were initially designed for ZS-DOAS measurements, thus the DOAS technique will be introduced by briefly following the descriptions of ZS-DOAS methodology from Farahani (2006), Fraser (2008), and Adams (2012).

The DOAS method uses the Beer-Lambert Law (Perrin, 1948) as a fundamental description of the attenuation of electromagnetic radiation by matter as:

$$I(\lambda) = I_0(\lambda) exp(-\sigma(\lambda) \cdot cL) \ . \tag{2.4}$$

Here, $I_0(\lambda)$ is the initial radiation intensity from a light source, while $I(\lambda)$ is the intensity of the beam after passing through a layer of absorbing gas, which has a thickness of L and uniform concentration of c. $\sigma(\lambda)$, the absorption cross-section of the absorber at wavelength λ, is a characteristic property of the gas. In atmospheric remote sensing, the light that reaches the detector typically travels through multiple trace gases and undergoes extinctions that are due to absorption, elastic and inelastic scattering, turbulence, and the transmissivity of the instrument. In general, the Beer-Lambert Law can be further expanded as:

$$I(\lambda) = I_0(\lambda) \exp\left[\left(-\sum \sigma_j(\lambda) \cdot c_j + \varepsilon_R(\lambda) + \varepsilon_M(\lambda)\right) L\right] \cdot A(\lambda). \tag{2.5}$$

Here, $\sigma_j(\lambda)$ is the absorption cross-section of absorber j, and c_j is its concentration. $\varepsilon_R(\lambda)$ and $\varepsilon_M(\lambda)$ are the Rayleigh and Mie extinction coefficients, and $A(\lambda)$ is the instrumental function. In atmospheric remote sensing, $I_0(\lambda)$ and $A(\lambda)$ are two parameters that cannot be easily retrieved. In general, when using the sun as the light source, the measurement of $I_0(\lambda)$ requires direct measurement of sunlight without any absorption from the atmosphere. This could be achieved by satellite instruments but not for ground-based instruments. Furthermore, absolute calibration must be performed to determine $A(\lambda)$. However, both of these issues can be solved when using the differential method.

For ZS-DOAS, a midday high-sun spectrum is used as the reference and a twilight spectrum as the measurement. This gives the following two equations:

$$I(\lambda) = I_0(\lambda)\exp\left(-\sum \sigma_j(\lambda)\cdot u_j + OD_{\varepsilon_R}(\lambda) + OD_{\varepsilon_M}(\lambda)\right)\cdot A(\lambda) \tag{2.6}$$

and

$$I'(\lambda) = I_0(\lambda)\exp\left(-\sum \sigma_j(\lambda)\cdot u_j' + OD_{\varepsilon_R}'(\lambda) + OD_{\varepsilon_M}'(\lambda)\right)\cdot A(\lambda)\ . \tag{2.7}$$

Here the prime symbol is used to denote twilight measurement. The equations are also simplified by using u_j to denote the slant column density (SCD, $u = c \cdot L$) of species j, and $OD_{\varepsilon_R}(\lambda)$ and $OD_{\varepsilon_M}(\lambda)$ denote optical density ($OD = \varepsilon \cdot L$) of Rayleigh and Mie scattering. Taking the natural log of the ratio of Eq. 2.7 and 2.6, gives

$$\Delta OD(\lambda) = \ln\left(\frac{I'(\lambda)}{I(\lambda)}\right) = -\sum \sigma_j(\lambda)\cdot \Delta u_j + \Delta OD_{\varepsilon_R}(\lambda) + \Delta OD_{\varepsilon_M}(\lambda)\ , \tag{2.8}$$

where $\Delta OD(\lambda)$ is the differential optical density of two measurements, $\Delta u_j = u_j' - u_j$ is the differential slant column density (dSCD) of species j, and $\Delta OD_{\varepsilon_R}$ and $\Delta OD_{\varepsilon_M}$ are differential optical density of the Rayleigh and Mie scattering.

The $\sigma_j(\lambda)$ can be further separated into a slowly varying part ($\sigma_{j_0(\lambda)}$) and a quickly varying part ($\Delta\sigma_j(\lambda)$, also known as the differential absorption cross-section). In addition, although the Rayleigh and Mie scattering vary throughout the day depending on position of the sun, cloud conditions, aerosol conditions, etc., these scattering effects only vary slowly with wavelength. Eq. 2.8 can be further expanded into two parts (rapidly and slowly varying terms) and the slowly varying term can be removed by performing a low-order polynomial fit and subtracting it from $\Delta OD(\lambda)$, as shown in Eq. 2.9.

$$\Delta OD(\lambda) = -\sum \Delta\sigma_j(\lambda) \cdot \Delta u_j - \sum \sigma_{j_0(\lambda)} \cdot \Delta u_j + \Delta OD_{\varepsilon_R}(\lambda) + \Delta OD_{\varepsilon_M}(\lambda)$$

$$= -\sum \Delta\sigma_j(\lambda) \cdot \Delta u_j + polynomial. \quad (2.9)$$

The differential absorption cross-sections are obtained from laboratory measurements. Thus the dSCDs of species can be retrieved from Eq. 2.9 using non-linear least squares fitting as implemented, for example, in the QDOAS (Fayt, 2012; Danckaert et al., 2015) and DOASIS (Kraus, 2006) DOAS fitting software.

Eq. 2.9 only considers the Rayleigh and Mie scattering, which are both elastic scattering processes. However in the UV-visible band, correction for another inelastic scattering process, rotational Raman scattering (RRS), is also required, especially for weak absorbers like BrO, HCHO, and OClO (Fish and Jones, 1995; Platt and Stutz, 2008). Unlike elastic scattering, which does not change wavelength of the incident light, inelastic scattering can cause an intensity loss at the incident wavelength and a gain at the neighbouring wavelengths. Thus, the RRS caused by molecules in the atmosphere (primarily N_2 and O_2) leads to the so-called "filling-in" of Fraunhofer lines. This effect, now known as the "Ring effect" (Grainger and Ring, 1962), was first observed in 1962 where the Fraunhofer lines in scattered daylight spectrum are were not as deep as those in the direct lunar spectrum. In DOAS applications, the Ring effect is usually taken into account by including a "Ring absorber" in the DOAS fit (Solomon et al., 1987). For example, in QDOAS, a Ring cross-section $\sigma_{Ring}(\lambda)$ is calculated according to a method proposed by Chance and Spurr (1997) (which needs high-resolution solar spectrum and instrument slit function), then it is applied in Eq. 2.9 and fitted as an additional absorber (Danckaert et al., 2015). The fit coefficient of the Ring spectrum in DOAS analysis is proportional to the so-called Raman scattering probability (RSP) (Wagner et al., 2009; Wagner et al., 2014; Ortega et al., 2016), which represents the strength of the RRS. Wagner et al. (2014) reported that inelastic scattering due to RRS on atmospheric molecules accounts for about 2-4% of all molecular scattering events.

After successful spectrum fitting in QDOAS, the dSCD of the trace gas of interest is retrieved; however, the dSCD is only a measure of the difference between the twilight and midday slant columns. The vertical column density (VCD) is a better measure of the amount of trace gas in the atmosphere. The relation between dSCD and VCD is defined by

$$\mathrm{dSCD(SZA)} = \mathrm{VCD(SZA)} \times \mathrm{AMF(SZA)} - \mathrm{RCD} \tag{2.10}$$

where AMF denotes the airmass factor ($\mathrm{AMF} = \mathrm{SCD}/\mathrm{VCD}$), and RCD denotes the reference column density, which is the amount of the absorber in the reference spectrum. A two-step approach is used to calculate the VCD. First, for each twilight period, a Langley plot of dSCD vs. AMF over a range of SZAs is plotted. The RCD is retrieved from the y-intercept of the Langley plot. Next, since dSCD(SZA), AMF(SZA), and RCD are known, VCD(SZA) can be derived using Eq. 2.10. In the normal data processing used in this work, the VCDs for each twilight period are averaged to obtain a final data product.

In fact, the AMF is a function of wavelength, SZA, cloud and aerosol conditions, trace gas profiles, and temperature and pressure profiles. Thus for each dSCD(SZA) measurements, an AMF(SZA) must be calculated. This normally done by using a radiative transfer model (RTM). However, as reported by Van Roozendael et al. (1998), differences in the RTM simulations (such as pressure and temperature profiles, ozone profile shape) can have a significant impact on the resulting AMF values (for example, up to 5-10% for ozone). Thus the NDACC UVVIS-WG has published a climatology of ozone and NO_2 AMF look-up tables (Van Roozendael and Hendrick, 2009, 2012) to homogenize and consolidate the time-series of total ozone and NO_2 measurements produced by NDACC zenith-sky UV-VIS spectrometers. Thus, as a member of the NDACC UVVIS-WG, NDACC look-up tables (LUTs) are used to calculate the ozone and NO_2 AMFs for VCD calculations.

2.2.2 Multi-Axis DOAS

ZS-DOAS has been particularly useful for the measurements of stratospheric trace gases since the 1970s (Noxon, 1975; Solomon et al., 1987). The next development in scattered light DOAS was the employment of off-axis geometry measurement (Sanders et al., 1993). Unlike ZS-DOAS, which measures at only 90° viewing elevation angle, MAX-DOAS measures over a range of viewing elevation angles (typically 3-10 different angles, from 0° to 90°). The motivation for using smaller elevation angles is twofold. For stratospheric measurements, lower elevation viewing angles can improve the detection limits by increasing the light intensity reaching the detector. The stronger motivation is that sunlight arriving at the instrument from a low elevation viewing angle has typically taken a long path through the troposphere and hence has greater sensitivity for tropospheric trace gases (Platt and Stutz, 2008).

As discussed in Section 2.2.1, because scattered light DOAS does not have a clearly defined light path, considerable effort must be invested in converting the observed trace gas absorption strength (for example, SCD or dSCD) into a quantity that is useful for the interpretation of observations (for example, VCD and/or profile). Figure 2.6 illustrates the single scattering scheme for the MAX-DOAS viewing geometry.

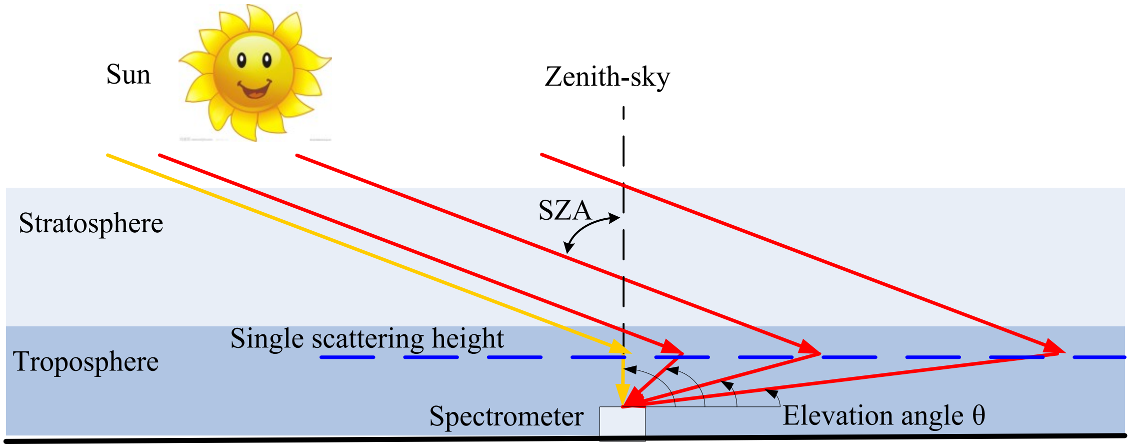

Figure 2.6: Single scattering scheme for MAX-DOAS measurements: the stratospheric paths at low elevations (red arrows) and zenith (golden arrow) are almost identical at low solar zenith angles. Hence if a spectrum at lower elevation is divided by a zenith sky spectrum, the result of the subsequent spectral analysis is only sensitive to the tropospheric absorber amount.

In particular for ground-based instruments, this technique is highly sensitive to trace gas abundances in the lowest 1-2 km of the atmosphere, which is the typical upper range of the marine boundary layer height (Leser et al., 2003), and the ideal range for pollution studies. Following Hönninger et al. (2004b), the MAX-DOAS geometric approximation of the SCD for single scattering is

$$\mathrm{SCD} \approx \left[a \cdot \frac{1}{\sin\theta} + (1-a) \cdot \frac{1}{\cos(\mathrm{SZA})}\right] \cdot \mathrm{VCD}\ , \tag{2.11}$$

where a is the fraction of the total vertical trace gas column that resides below the scattering altitude, θ is the elevation viewing angle, and SZA is solar zenith angle (Hönninger et al., 2004b). An absorber below the single scattering altitude (e.g., in the boundary layer, denoted as the blue dashed line in Figure 2.6) enhances the AMF by a factor of approximately 1/sin(α), demonstrating the strong effect of elevation angle on the tropospheric light path. For elevation angles close to the horizontal, the light path through a low-altitude trace gas layer is increased compared to the light path for higher viewing angles. Conversely, when the trace gas layer is above the scattering altitude (e.g., in the stratosphere), the AMF strongly depends on the SZA, approximated by 1/cos(SZA) (Hönninger and Platt, 2002; Hönninger et al., 2004b). Thus, under the assumption of single scattering in the free troposphere, the AMF of the boundary layer is approximated by 1/sin(θ) and the contribution from the rest of the atmosphere is approximately 1/cos(SZA).

Although this geometric approximation illustrates the dependence of the SCD and the total AMF on the SZA, the elevation angle, and some information about the vertical distribution of trace gas, it is highly simplified. In the case of low elevations, which are often used to increase the tropospheric path length, multiple scattering events, curvature of the Earth, and refraction become more significant (Platt and Stutz, 2008). In addition, the presence of aerosols in the troposphere makes Mie scattering an important process that must be included in the AMF calculation. A detailed RTM is required to simulate these complex scattering processes in the atmosphere. More specifically, because of the enhanced scattering and complex light paths in the troposphere, a single scattering RTM that is suitable for ZS-DOAS is insufficient for MAX-DOAS (Hönninger et al., 2004b; Schofield et al., 2004a). Instead, a sophisticated multiple scattering RTM and the optimal estimation method are necessary to retrieve the tropospheric trace gas profile from MAX-DOAS observations (Rodgers, 2000; Rozanov et al., 2005; Frieß et al., 2011).

The Optimal Estimation Method (OEM, Rodgers, 2000) can be used for both stratospheric and tropospheric trace gas profile retrievals. In the profile retrievals, a RTM is used as the forward model, $F(\boldsymbol{x}, \boldsymbol{b})$, to convert the number density profiles, $\boldsymbol{x}$, into measurement dSCDs, $\boldsymbol{y}$, as

$$\boldsymbol{y} = F(\boldsymbol{x}, \boldsymbol{b}) + \boldsymbol{\varepsilon}\,, \tag{2.12}$$

where **ε** denotes the error in the measurements. The vector ***b*** represents additional forward model parameters (e.g., atmospheric pressure and temperature profiles from radiosondes) which are not retrieved. For optically thin trace gases (optical depth << 1, for example BrO), the forward model is assumed to be linear (Schofield et al., 2004a). Thus, the linear function can be expressed as

$$\boldsymbol{y} = \frac{\partial F(\boldsymbol{x},\boldsymbol{b})}{\partial \boldsymbol{x}} \cdot \boldsymbol{x} + \varepsilon = \boldsymbol{K} \cdot \boldsymbol{x} + \varepsilon \tag{2.13}$$

where ***K*** is the weighting function matrix and describes the sensitivity of the measured dSCDs to changes in the number density profiles.

The OEM model uses maximum a posteriori (MAP) method to solve for ***x***, which is determined by minimising a cost function (Frieß et al., 2011):

$$\chi^2 = [\boldsymbol{y} - F(\boldsymbol{x},\boldsymbol{b})]^T \boldsymbol{S}_\varepsilon^{-1} [\boldsymbol{y} - F(\boldsymbol{x},\boldsymbol{b})] + (\boldsymbol{x} - \boldsymbol{x}_a)^T \boldsymbol{S}_a^{-1} (\boldsymbol{x} - \boldsymbol{x}_a) \ , \tag{2.14}$$

where $\boldsymbol{S}_\varepsilon$ and $\boldsymbol{S}_\mathrm{a}$ are covariance matrices describing the uncertainties in the measurement and the *a priori* profile respectively (assume that there is no error in the forward model). This cost function evaluates the agreement between the measured and calculated dSCDs, taking into account the error from both measurements and *a priori*. For linear problems, the solution for ***x*** can be written as (Rodgers, 2000):

$$\hat{\boldsymbol{x}} = \boldsymbol{x}_a + (\mathbf{K}^T \mathbf{S}_\varepsilon^{-1} \mathbf{K} + \mathbf{S}_a^{-1})^{-1} \mathbf{K}^T \mathbf{S}_\varepsilon^{-1} (\boldsymbol{y} - \mathbf{K}\boldsymbol{x}_a) \ . \tag{2.15}$$

For slightly non-linear problems, Newtonian iteration is a straightforward numerical method for finding the zero of the gradient of the cost function given as:

$$\boldsymbol{x}_{i+1} = \boldsymbol{x}_a + \mathbf{S}_a \mathbf{K}_i^T (\mathbf{K}_i \mathbf{S}_a \mathbf{K}_i^T + \mathbf{S}_\varepsilon)^{-1} [\boldsymbol{y} - \boldsymbol{F}(\boldsymbol{x}_i) + \boldsymbol{K}_i(\boldsymbol{x}_i - \boldsymbol{x}_a)] \ . \tag{2.16}$$

The averaging kernel matrix, **A,** is calculated from the error covariance matrices and the weighting function as:

$$\mathbf{A} = (\mathbf{K}^T \boldsymbol{S}_\varepsilon^{-1} \mathbf{K} + \boldsymbol{S}_a^{-1})^{-1} \mathbf{K}^T \boldsymbol{S}_\varepsilon^{-1} \mathbf{K} \, . \tag{2.17}$$

A describes the sensitivity of the retrieved number density profiles ($\hat{\boldsymbol{x}}$) to the true state of the atmosphere ($\boldsymbol{x}$).

The practical application of the theoretical inversion concepts to MAX-DOAS measurements is shown by the flowchart in Figure 2.7. The flowchart describes the sequence of steps in the University of Heidelberg remote sensing group's profile retrieval code (HeiPro) (Yilmaz, 2012). First, aerosol extinction profiles are retrieved from the measured oxygen dimer (O_4) dSCDs and relative intensities (optional) in the lowermost 4 km of the atmosphere. Here O_4 dSCDs and relative intensities serve as the measurement vector $\boldsymbol{y}$, and the corresponding errors quantify the measurement covariance matrix $\boldsymbol{S}_\varepsilon$. Second, these retrieved aerosol extinction profiles serve as a forward model parameter for the retrieval of trace gas vertical profiles. In MAX-DOAS profile retrieval, the radiative transfer model SCIATRAN2 (Rozanov et al., 2005) works as the forward model $F(\boldsymbol{x}, \boldsymbol{b})$, and the HeiPro OEM (Frieß et al., 2011) uses the MAP method to solve for the profiles $\boldsymbol{x}$. The SCIATRAN2 RTM and HeiPro OEM are used in Sections 2.4.3 and 3.1.2 for the tropospheric aerosol, NO_2, and BrO profile retrievals. In the subsequent chapters, this RTM-OEM combined software package will be just referred as HeiPro. In addition, another OEM and a single scattering RTM (Schofield et al., 2004a) were used in Chapter 3 to retrieve stratospheric BrO from zenith-sky observations. The detailed description of the stratospheric BrO profile retrieval can also be found in Adams (2012) and Schofield et al. (2004a). More technical details about the OEMs and RTMs used in the bromine explosion study are provided in Chapter 3.

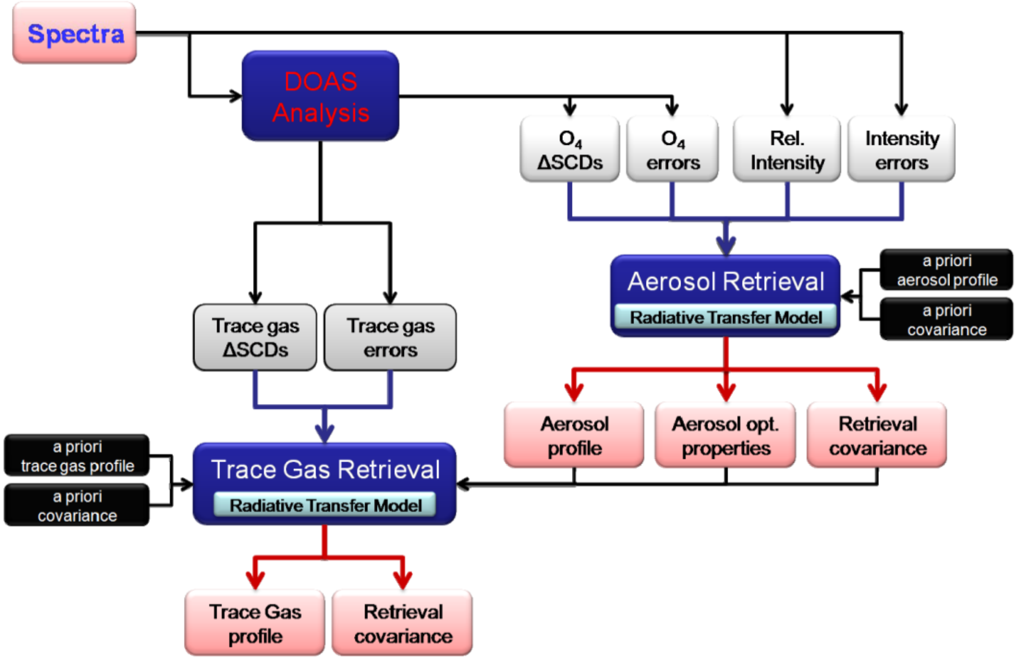

Figure 2.7: Flowchart of the aerosol and trace gas profile retrieval procedure in HeiPro using MAX-DOAS measurements (adapted from Yilmaz, 2012).

2.2.3 Direct-Sun/Moon DOAS

Compared to scattered light ZS-DOAS and MAX-DOAS, DS-DOAS has a few advantages. First, it allows a relatively simple calculation of the optical path. For example, it uses simple geometric estimation of $\mathrm{AMF} = 1/\cos(\mathrm{SZA})$, which is a good approximation up to an SZA of ≈ 75° (Platt and Stutz, 2008). Above 75°, this geometric estimation will not be accurate due to the Earth's curvature and atmospheric refraction. Secondly, the DS signal is much stronger than scattered sunlight; typically filters with optical density in the range of 3-6 are needed to attenuate the DS signal. Thirdly, since the contribution of scattered light in the DS signal is very low, the DS spectra are nearly free of the "Ring effect" (see Section 2.2.1) (Grainger and Ring, 1962; Vountas et al., 1998; Platt and Stutz, 2008; Ortega et al., 2016). Ortega et al. (2016) estimated $\mathrm{RSP}_{\mathrm{ZS}} = 2.34 \pm 0.22$ %, whereas $\mathrm{RSP}_{\mathrm{DS}}$ (0.40 ± 0.20 %) is an order of magnitude smaller than $\mathrm{RSP}_{\mathrm{ZS}}$ (for SZA = 28°, $\mathrm{AOD}_{430} = 0.11$). Lastly, moonlight or starlight could be used instead of sunlight to enable nighttime measurements.

Nighttime measurements are particularly important in the polar region. For example, Eureka has about four months of polar night during which no scattered light DOAS measurements can be obtained. However, compared to sunlight, the intensity of moonlight is about five orders of magnitude lower. Normally, direct moon measurements can only be performed when the lunar phase is larger than 0.5. This requirement is not only because of the size of the visible area but also because the brightness will rapidly diminish when the phase is less than 0.5 (Wagner et al., 2000; Platt and Stutz, 2008).

Compared to ZS-DOAS, DS-DOAS measurements are more sensitive to tropospheric trace gases, as the average path taken by sunlight through the troposphere is up to twenty times larger at sunset than at noon (Schofield, 2003). Schofield et al. (2006) applied their retrieval algorithm to combine ZS-DOAS and DS-DOAS observations to retrieve trace gas stratospheric and tropospheric profiles simultaneously.

DS-DOAS also has limitations; for example, measurements are only possible when direct sunlight (or moonlight) is not blocked by clouds. Also, automatic tracking of the sun or moon requires a tracking system. A high-precision solar tracker system has been developed at the University of Toronto and Dalhousie University for this purpose (Adams, 2012; Franklin, 2015). Based on knowledge of the time and location of the tracker (longitude, latitude, and height), passive tracking can be achieved (Rhodes, 2010; Adams, 2012). This is simpler than active tracking, but its accuracy highly depends on the calibration of the tracker (requiring good mechanical sight and accurate levelling of the tracker, see Adams, 2012). On the other hand, active tracking can be achieved by using image fitting of the sun (or moon) (Franklin, 2015) or intensity fitting (Cede, 2012). The image fitting method is briefly described in Section 2.1.4, as this is the method used by PEARL-GBS's tracker. The intensity fitting used by the Pandora spectrometer is based on astronomical calculation (passive tracking) and intensity (signal) of a series of spectra. For example, every 15 min, the Pandora points its telescope to the calculated solar position, then it scans the sky in the zenith direction ('up-down') and in the azimuth direction ('left-right') and looks for the position of maximum signal. This position serves as the "apparent" solar position (Cede, 2012).

2.3 Canadian Arctic ACE/OSIRIS Validation Campaigns (2011-2015)

The Canadian Arctic ACE/OSIRIS Validation Campaigns are sponsored by the Canadian Space Agency to validate the Atmospheric Chemistry Experiment (ACE) instruments on board the Canadian satellite SCISAT-1 and the Optical Spectrograph and InfraRed Imaging System (OSIRIS) on the Odin satellite. Besides the GBSs, SAOZ is another NDACC-certified ZS-DOAS instrument that has performed springtime measurements at Eureka since 2005. GBS and SAOZ ozone and NO_2 total columns data have been compared during several mid-latitude and Arctic campaigns (Fraser et al., 2007a; Fraser et al., 2008; Fraser et al., 2009; Roscoe et al., 2010; Adams et al., 2012b). Figure 2.8a shows ozone and NO_2 total columns measured by the GBSs and SAOZ in Eureka. In 2000, 2005, 2007, and 2011, the polar vortex was overhead, and low ozone and NO_2 columns were observed. However, 2011 is notably different, with a maximum percent ozone loss of 47% or 250 Dobson Units (DU, 1 DU = 2.69×10^{16} molec cm^{-2}) derived from UT-GBS data on 5 April 2011 (Adams et al., 2012a). These measurements agree with photochemical model runs, which indicate that prolonged denitrification by sedimentation of polar stratospheric clouds delayed chlorine deactivation, leading to the record ozone loss (Adams et al., 2012a). Unusual conditions were also observed in late spring 2011, when a frozen-in anticyclone in the middle stratosphere above Eureka resulted in anomalous chemistry, enhancing the NO_2 VMR in this region and causing unusually large ozone loss in April/May compared with previous years (Adams et al., 2013). Over the next few decades, while stratospheric chlorine and bromine loading remain high, similar ozone depletion events are expected to occur whenever dynamic variability results in an isolated polar vortex with a persistently cold stratosphere (WMO, 2014).

The Eureka GBS zenith-sky ozone and NO_2 columns were submitted to NDACC archive in NASA Ames format in 2013. The NDACC UV-VIS WG implemented a new archiving format (Hierarchical Data Format, HDF) in 2015. GBS data in HDF format will be updated and submitted to the NDACC archive in early 2017.

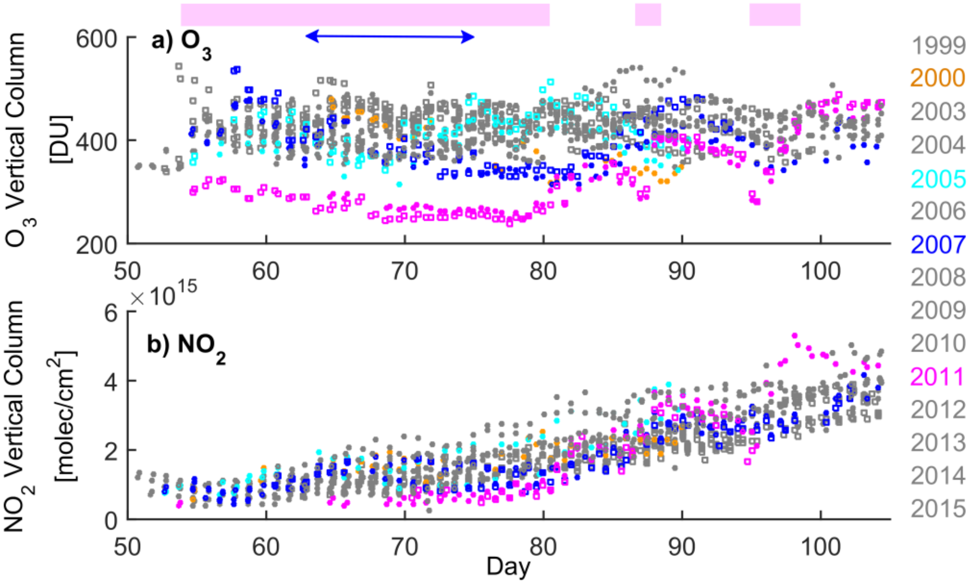

Figure 2.8: Time series of zenith-sky DOAS measurements of ozone and NO_2 for 1999-2015 versus day of the year (figure adapted and updated based on Adams et al. (2012a)). The year 2000 is shown in orange, 2005 in cyan, 2007 in blue, 2011 in magenta, and all other years are shown in grey. (a) Ozone total columns measured by the UT-GBS (closed circles) and SAOZ (open squares). The magenta bar at the top indicates periods when the polar vortex was above Eureka in 2011 and the blue line indicates when temperatures were below the threshold for the formation of polar stratospheric clouds in 2011. (b) NO_2 partial columns (17 km to top of atmosphere) measured by UT-GBS (closed circles) and PEARL-GBS (open squares).

2.4 CINDI-2 Campaign (2016)

The Second Cabauw Intercomparison of Nitrogen Dioxide Measuring Instruments (CINDI-2, http://www.tropomi.eu/science/cindi-2) campaign was held at the Royal Netherlands Meteorological Institute (KNMI) Cabauw Experimental Site for Atmospheric Research (CESAR; 51.971°N, 4.927° E; 0.7m below sea level) site in the Netherlands in September 2016, and the PEARL-GBS participated. The CESAR is located in an extended and flat polder landscape in close proximity (<40 km) to the four largest cities in the Netherlands. The CINDI-2 campaign is a follow-up of the 2009 CINDI campaign (Piters et al., 2012) held at the same site, and in which the UT-GBS participated (Roscoe et al., 2010). The goals of CINDI-2 were to prepare for the Sentinel 5 Precursor/Tropospheric Monitoring Instrument (TROPOMI) satellite validation and to initialize the suite of instruments that will be used to create the European Fiducial Reference Measurements for Ground-Based DOAS Air-Quality Observations (FRM4DIAS) network of MAX-DOAS instruments. The PEARL-GBS was one of 36 passive

DOAS instruments participating in this initiative (see Figure 2.9b). In addition to MAX-DOAS instruments, imaging DOAS, long-path DOAS (LP-DOAS), and cavity-enhanced DOAS (CE-DOAS) instruments were also deployed. In addition, many complementary instruments took part in the campaign, including ozone and NO_2 sondes, in-situ ozone and NO_2 monitors, sun photometers, an all-sky imager, a Raman Lidar, ceilometer, and an NO_2 Lidar (Hendrick et al., 2016).

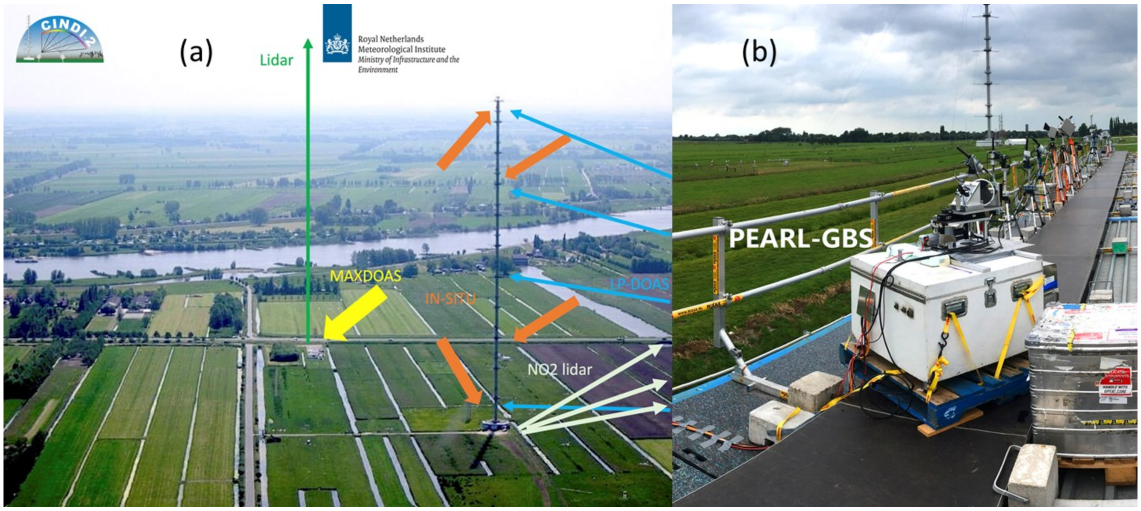

Figure 2.9: (a) General placement of instruments at the Cabauw site during CINDI-2 (figure adapted from Hendrick et al. (2016)), (b) MAX-DOAS instruments performing measurements during CINDI-2. PEARL-GBS is inside the white box (GBS cooling unit #1) in the middle of the panel (b), with its tracking system mounted on top of the box.

2.4.1 CINDI-2 PEARL-GBS Configuration and Data Products

The GBS cooling unit #1 used in MANTRA campaign was refurbished and a new air conditioner unit (ISC Sales Inc., 2000 BTU cooling power) was installed for CINDI-2 (see Figure 2.9b). A UT-Suntracker was mounted on the box. The active tracking was successfully tested in Toronto and performed well during the campaign. However, it was found that the natural density filters were not strong enough for direct-sun acquisition (our strongest filter was OD = 4), thus without a stronger filter (with OD = 5 to 6), most of the DS spectra were saturated.

Due to the high signal level in the daytime, a diffuser was placed on top of the collecting optics and the 1% transmission metallic filter was used for the entire campaign (for both ZS- and

MAX-DOAS) to attenuate the signal[3]. To maintain consistency of the instrument function, this optical setup was also used for twilight zenith-sky measurements, although it reduced the SNR and may affect the quality of the twilight data. In addition, similar to the 2009 CINDI campaign, a Plexiglass cube was used to cover the UT-Suntracker during the night. The cube prevents the heavy dew in the morning but may affect the morning zenith-sky measurements; so it was removed before the start of the daytime 2D MAX-DOAS sequence (see Section2.4.2) daily. A small 90° FOV web camera was mounted on the UT-Suntracker to capture images of sky conditions. The camera was set to capture one image for each azimuthal measurement during the daytime.

Table 6: Data products included in the CINDI-2 semi-blind intercomparison (adapted from Hendrick et al. (2016)). PEARL-GBS measured NO_2 (VIS range), O_4 (VIS range), and O_3 (Chappuis bands).

Data product	Typical wavelengths
NO_2 (VIS range)	425 – 490 nm
NO_2 (UV range)	338 – 370 nm
O_4 (VIS range)	425 – 490 nm
O_4 (UV range)	338 – 370 nm
HCHO	336.5 – 359 nm
O_3 (Chappuis bands)	450 – 520 nm
O_3 (Huggins bands)	320 – 340 nm
Relative intensity	340, 380, 440, 500 nm
Colour Index	To be defined

The CINDI-2 organisation group proposed targeting species as shown in Table 6. PEARL-GBS used the 600 gr/mm grating centred at 450 nm, with a 0.1 mm entrance slit. This configuration provides NO_2 (visible), O_4 (visible), and O_3 (Chappuis bands) data products following the recommended retrieval settings (see Table 7 for NO_2 and O_4 in the visible).

2.4.2 CINDI-2 2-D MAX-DOAS and Combination Scan

The PEARL-GBS started acquiring 1-D MAX-DOAS (fixed azimuth viewing angle, multiple elevation viewing angles) measurements at Eureka in 2010. For CINDI-2, the organisation group

---

[3] For DS measurements, based on light signal level, the LabVIEW code selects a filter with sufficient OD (typically the strongest two filters). For ZS- and MAX-DOAS, only the 1% filter was used.

proposed a detailed combination scanning sequence (Hendrick et al., 2016) which included 2D MAX-DOAS (multiple azimuth and elevation viewing angles), direct sun (DS), zenith-sky (ZS), horizontal scan (HS), and almucantar scan (AS). Unlike traditional MAX-DOAS measurements that use a single azimuth viewing angle, 2D MAX-DOAS, which was introduced to study spatial inhomogeneity in the airmasses, uses multiple azimuths (Wagner et al., 2011; Piters et al., 2012; Sinreich et al., 2013; Wang et al., 2014; Ortega et al., 2015; Hendrick et al., 2016). For example, with 2D MAX-DOAS, Wang et al. (2014) reported measurements of 2D surface mixing ratios of NO_2, SO_2, and HCHO, and Ortega et al. (2015) retrieved NO_2 near the surface in 3D.

Table 7: DOAS settings for NO_2 and O_4 in VIS range (adapted from Hendrick et al. (2016)).

Wavelength range	425-490 nm	
Fraunhofer reference spectra	Noon zenith-sky spectra averaged between 11:30:00 and 11:40:00 UT	
Polynomial degree	Order 5 (6 coefficients)	
Intensity off-set	Constant	
Cross-sections	NO_2 (298 K)	Vandaele et al. (1998) with I_0 correction (SCD of 10^{17} molecules/cm^2) File: no2_298K_vanDaele.xs
	NO_2 (220 K)	Pre-orthogonalized Vandaele et al. (1998) with I_0 correction (SCD of 10^{17} molecules/cm^2) File: no2a_220p298K_vanDaele_425-490nm.xs
	O_3 (223 K)	Serdyuchenko et al. (2014) with I_0 correction (SCD of 10^{20} molecules/cm^2) File: o3_223K_SDY_air.xs
	O_4 (293 K)	Thalman and Volkamer (2013) File: o4_thalman_volkamer_293K_inAir.xs
	H_2O	HITEMP (Rothman et al., 2010) File: H2O_HITEMP_2010_390-700_296K_1013mbar_air.xs
	Ring	RING_QDOAS_SAO2010 File: Ring_QDOAScalc_HighResSAO2010_Norm.xs

The data acquisition protocol distinguished between twilight (morning and evening) and daytime conditions. According to the solar position on the site, the daytime period was set between 6:00 and 16:45 UTC, while the twilight period was set to 4:00 to 6:00 UTC and 16:45 to 18:45 UTC. The daytime PEARL-GBS measurement sequence is shown in Table 2.6 and Table 9. In general, the protocol requires that a full azimuthal scan be acquired by 2D MAX-DOAS instruments in one hour at the following azimuth angles: 355°, 45°, 135°, 195°, 245°, and 287° (see Figure 2.10). All other optional measurements (such as direct-sun, almucantar, and horizon scan) were also included in the PEARL-GBS scanning sequence. The protocol required that each 2D MAX-DOAS measurement be finished within a one-minute block. To achieve required timing, the PEARL-GBS total exposure time was set to 45 seconds, and the typical overhead time (from tracker movement, CCD preparation, and communication delay) for each measurement was 10 ± 5 seconds.

Table 8: PEARL-GBS daytime measurement sequence during CINDI-2.

TIME (UTC)	**2D-MAXDOAS**	
	Azimuth(°) 0°: north; 90°: east 180°: south; 270°: west	Elevation (°)
hh:00:00	287	1
	287	2
	287	3
	287	4
	287	5
hh:05:00	287	6
	287	8
	287	15
	287	30
	287	90
hh:10:00	Two direct-sun acquisitions (DS)	
hh:15:00	355	1
	355	3
	355	5
	355	15
	355	90*
hh:20:00	45	1
	45	3
	45	5
	45	15
	45	90
hh:25:00	Eleven almucantar scans (AS)	
hh:30:00	95	1
	95	3
	95	5
	95	15
	95	90*
hh:35:00	135	1
	135	3
	135	5
	135	15
	135	90
hh:40:00	Two direct-sun acquisition	
hh:45:00	195	1
	195	3
	195	5
	195	15
	195	90*
hh:50:00	245	1
	245	3
	245	5
	245	15
	245	90
hh:55:00	Elven almucantar scans	

Notes:

This table shows the sequence for PEARL-GBS measurements at the following UTC times (hh in the Table): 06, 07, 08, 09, 10, 12, 13, 14, 15, 16h. The contents in blue colour were customized for PEARL-GBS as follows.

DS: The protocol requires one DS measurement for the 5 min block at hh:10:00. For PEARL-GBS, two DS measurements in this 5 min were performed. The 1st DS acquisition time was set to 10 s as a test run (to determine the solar intensity, in order to select the neutral density filter for the 2nd DS measurement), and the 2nd DS measurement acquisition time was set to 45 s.

AS: The protocol proposed 15 measurements, each with a 10s integration time + 5s overhead at the realtime solar elevation for the following relative azimuth angles (RAA): -15, -10, -6, -5, 5, 6, 10, 15, 30, 50, 70, 90, 120, 150, and 180°. RAA values are given with respect the current position of the sun and not its position at the start of the Almucantar sequence. The sign convention for the relative azimuth angle is + for the side that is clockwise with respect to the instrument-sun direction and – for the other side. To conform to the acquisition schedule, RAAs of 30,70,120 and 150° were dropped from the almucantar sequence. So PEARL-GBS AS measurements inlcude only elven RRAs as -15, -10, -6, -5, 5, 6, 10, 15, 50, 90, and 180°. In addition, due to acquisition code issues (in Trax6.3), measurements with Solar Azimuth Angle + RAA > 355 were not possible in AS modes.

*: These 90° zenith-sky measurements are not included in the protocol (only one zenith-sky measurement is required for each 15 min sequence). PEARL-GBS uses this “free” 1 min window to perform an extra zenith-sky measurement with the tracker mirror at the specified azimuth angle.

Table 9: PEARL-GBS daytime measurement sequence (noon) during CINDI-2.

TIME (UTC)	**2D-MAXDOAS**	
	Azimuth(°) 0°: north; 90°: east 180°: south; 270°: west	Elevation (°)
hh:00:00	287	1
	287	2
	287	3
	287	4
	287	5
hh:05:00	287	6
	287	8
	287	15
	287	30
	287	90
hh:10:00	Two direct-sun acquisitions	
hh:15:00	287	1
	287	2
	287	3
	287	4
	287	5
hh:20:00	287	6
	287	8
	287	15
	287	30
	287	90
hh:25:00	Eleven almucantar scans	
hh:30:00	287	90
	287	90
	287	90
	287	90
	287	90
hh:35:00	287	90
	287	90
	287	90
	287	90
	287	90
hh:40:00	287	90
	287	Horizon scan (HS)
	287	
	287	
	287	
hh:45:00	287	1
	287	2
	287	3
	287	4
	287	5
hh:50:00	287	6
	287	8
	287	15
	287	30
	287	90
hh:55:00	Two direct-sun acquisitions	

Notes: This table is the sequence for PEARL-GBS measurements between 11:00:00 and 11:59:00 UTC. The contents in blue are customized for PEARL-GBS. HS: between -5° and +5° relative to the horizon with a step of 0.2° between -2 and +2° and a step of 1° outside this range. 5s integration time + 5s overhead per elevation.

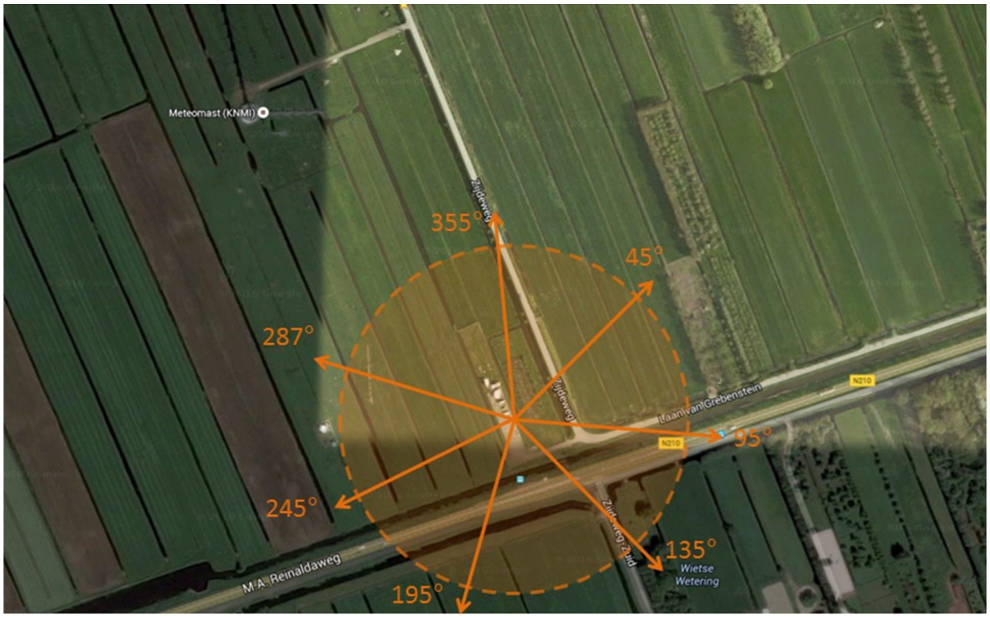

Figure 2.10: Azimuthal directions for the 2D-MAXDOAS measurements during CINDI-2 (north is 0°) (figure adapted from Hendrick et al. (2016)).

2.4.3 AOD and NO_2 Profile Retrievals

The trace gas profiling task team for the CINDI-2 campaign is focused on the intercomparison of NO_2, O_4, and other trace gas (for example, HCHO) vertical profiles retrieved by different research groups. There are sixteen groups using more than ten different OEMs. PEARL-GBS participated the O_4 and NO_2 profile retrieval intercomparison using the HeiPro as the OEM (see more details about HeiPro in Sections 2.2.2 and 3.1.2). Four "golden" days (mostly clear) from 12 to 15 September 2016 were selected for the initial comparison. To reduce possible sources of discrepancy, the profiling task team implemented some fixed retrieval settings, such as ozone profile (from climatology data), altitude grid, wavelength used in the RTM, aerosol parameters (e.g., scattering albedo), trace gas cross sections, *a priori* profiles of O_4 and NO_2, elevation and azimuth angles. Detailed settings used in PEARL-GBS O_4 and NO_2 comparison tests are summarised in Table 10.

Table 10: PEARL-GBS O_4 and NO_2 profile retrieval settings (adapted from the CINDI-2 profiling task team preparatory document).

Parameter	**Values for O_4 and NO_2 preliminary comparison tests**
Atmosphere definition	Pressure, temperature, total air density, and O_3 vertical profiles averaged from ozonesonde measurements in De Bilt (09/2013-2015). Surface albedo should be fixed to 0.06.
Retrieval altitude grid	0-4 km, step 200 m. The surface height and instrument altitude are fixed to 0m.
Wavelength	477 nm for aerosols; 460nm for NO_2.
Aerosol settings	The single scattering albedo is fixed to 0.92 and the asymmetry factor to 0.68 for 477 nm. These are mean values for 14/09/2016 (day 258) derived from AERONET measurements at 440nm in Cabauw.
Measured O_4 and NO_2 DSCDs	PEARL-GBS retrieved O_4 and NO_2 DSCDs. Zenith spectrum of the scan as reference. Only the measured DSCDs corresponding to the 287° azimuth direction are used.
Cross-sections	CINDI-2 cross section data sets used.
O_4 scaling	Aerosol retrievals are done without scaling.
Elevation angles	1, 2, 3, 4, 5, 6, 8, 15, 30, and 90°.
A priori profiles	Exponentially-decreasing profiles derived using the following AOD/VCD and scaling height (SH) values: *AOD: 0.18 for 477 nm *NO_2 VCD: 9e15 molec/cm^2 *1 km scaling height.
A priori covariance matrices	Variance of 50% of the *a priori* profile for the diagonal terms and extra-diagonal terms are added as Gaussian functions with a correlation length of 200 m.
Aerosol extinction profiles to be used in the NO_2 retrievals	PEARL-GBS retrieved extinction profiles.

The retrieved extinction profiles are shown in Figure 2.11. Aloft layers of retrieved aerosol extinction are seen in Figure 2.11a and 2.11b in the afternoon measurements. The optical depth time series and PEARL-GBS monitoring camera images are shown in Figure 2.12 and Figure 2.13 respectively. In general, the retrieved extinction profile successfully captured some of the features in the lower 0-2 km of the atmosphere. Six time steps (13:00 UTC profiles for each day, 10:00 UTC profile on 12 September, and 7:00 UTC profile on 15 September) were selected to illustrate the performance of the profile retrieval. For example, 10:00 UTC 12 September has the lowest optical depth (Figure 2.12) and low extinction profile (Figure 2.11a), which agree with the camera image shown in Figure 2.13a. The elevated extinction values on 13:00 UTC 12 September (Figure 2.11a) from 0.3 to 1 km matched with the low-level clouds in the horizon (Figure 2.13b). And the breaking clouds as shown in Figure 2.13e (7:06 UTC 15 September) are consistent with the retrieved high optical depth (see the green dot on Figure 2.12) for that time. The averaging kernels for the extinction retrievals are shown in Figure 2.14. The DOFS in the extinction retrievals is in the range of 1.8-2.6 (see the text in Figure 2.14), with the breaking clouds scene (Figure 2.14e) has the lowest value. However, the retrieval that has the lowest AOD (see Figure 2.12 and Figure 2.12) does not have the highest DOFS (Figure 2.14a). In general, the aerosol extinction profiles retrieved by PEARL-GBS have very limited information above 2 km altitude. Further comparison with other instruments will be performed in future.

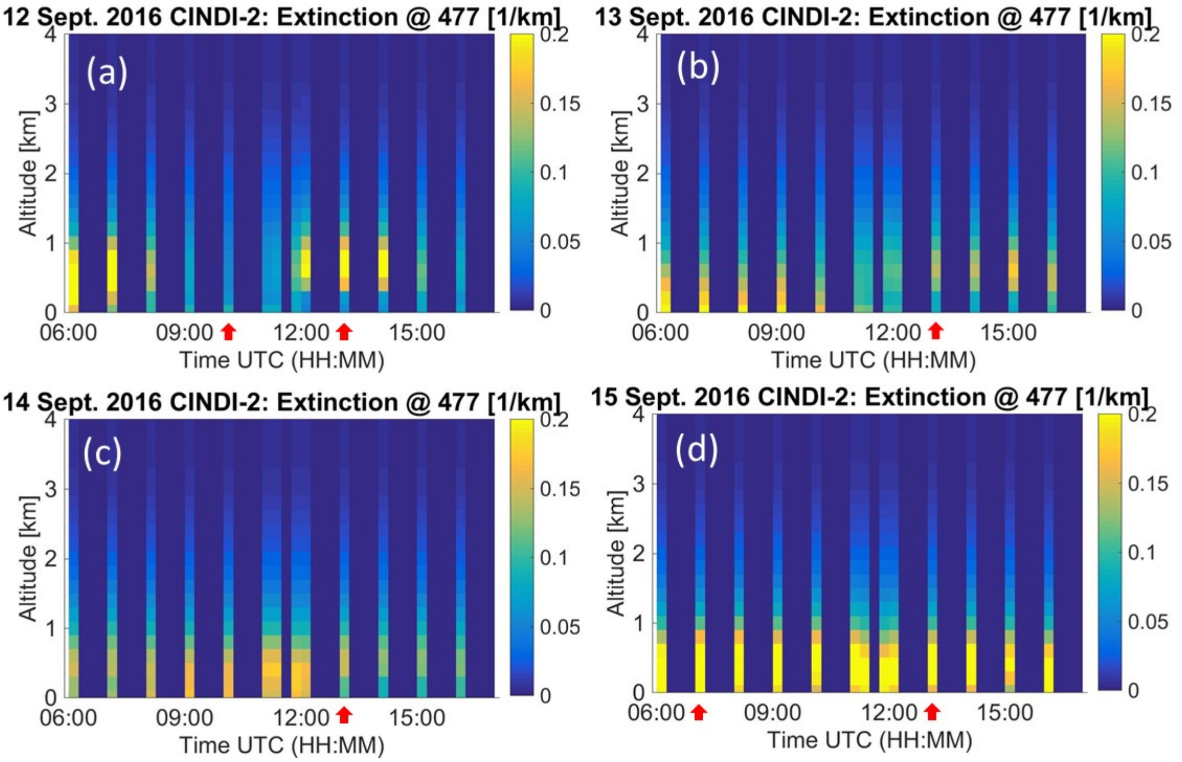

Figure 2.11: PEARL-GBS MAX-DOAS 0-4 km extinction profiles retrieved on four “golden days” during CINDI-2. The PEARL-GBS made 2D MAX-DOAS measurements throughout the day, but the preliminary results only show the measurements with azimuth viewing angle = 287°. The dark blue areas represent of measurements at different azimuths which have not been retrieved yet. The red arrows corresponding to the selected six time steps (13:00 UTC profiles for each day, 10:00 UTC profile on 12 September, and 7:00 UTC profile on 15 September).

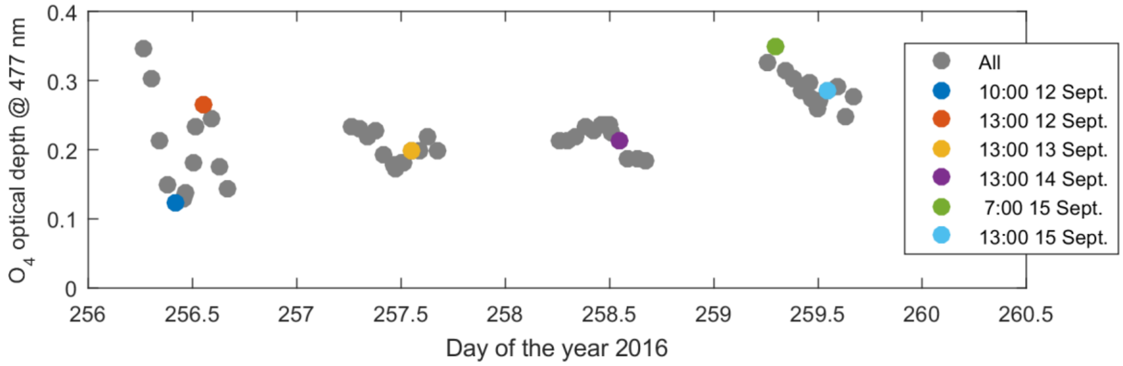

Figure 2.12: PEARL-GBS O_4 retrieved optical depth time series during CINDI-2.

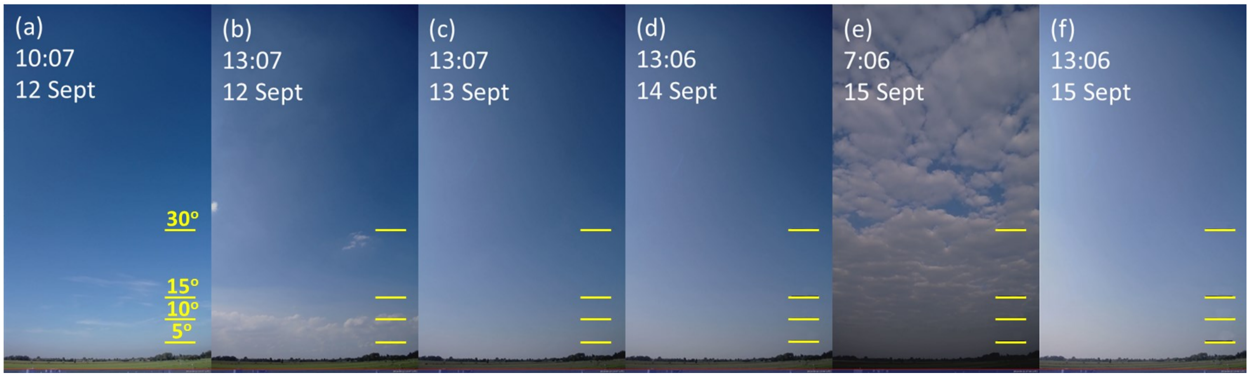

Figure 2.13: PEARL-GBS monitoring camera images during CINDI-2. The camera viewing direction was the same as the PEARL-GBS scanning direction (287° from true North). The estimated viewing elevation angles are noted on the images.

The retrieved aerosol extinction profiles (see Figure 2.11) are used in the NO_2 profile retrievals. Figure 2.15 shows an example of HeiPro modelled NO_2 dSCDs and PEARL-GBS measured values. Figure 2.16 shows the retrieved 0-4 km NO_2 VMR profiles. The DOFS in the NO_2 retrievals is in the range of 2.5-3.0 (see the text in Figure 2.17). Figure 2.18 shows the preliminary NO_2 profile comparison of the RIVM mobile Lidar (Volten et al., 2009) with PEARL-GBS. The retrieved NO_2 concentration profiles from the two instruments show similarities in the three areas indicated in Figure 2.18. In area α, both Lidar and GBS observed an aloft NO_2 layer above ground but below 500 m (note that the GBS NO_2 retrieval has a 200 m altitude grid, which is coarser than the Lidar). In area β, both instruments observed a clean airmass (NO_2 concentration < 10 μg m^{-3}) from 0.5 to 2 km. In area γ, both instruments observed increased vertical mixing of NO_2 from the surface to 1.5 km.

Figure 2.19 shows the NO_2 VCD time series from PEARL-GBS and Ozone Monitoring Instrument (OMI, see more information about OMI in Section 5.1.3). The OMI data used here are version OMNO2d, which is the level-3 daily global gridded (0.25×0.25°) NO_2 product for sky conditions where the cloud fraction is less than 30% (http://disc.sci.gsfc.nasa.gov/uui/datasets/OMNO2d_003/summary). The OMNO2d data that come from the grid point over the CESAR site compared well with PEARL-GBS NO_2 VCD data. Due to the satellite temporal sampling, OMI does not capture the daily variability in the NO_2 VCD, particularly the large values in the morning and afternoon of 15 September.

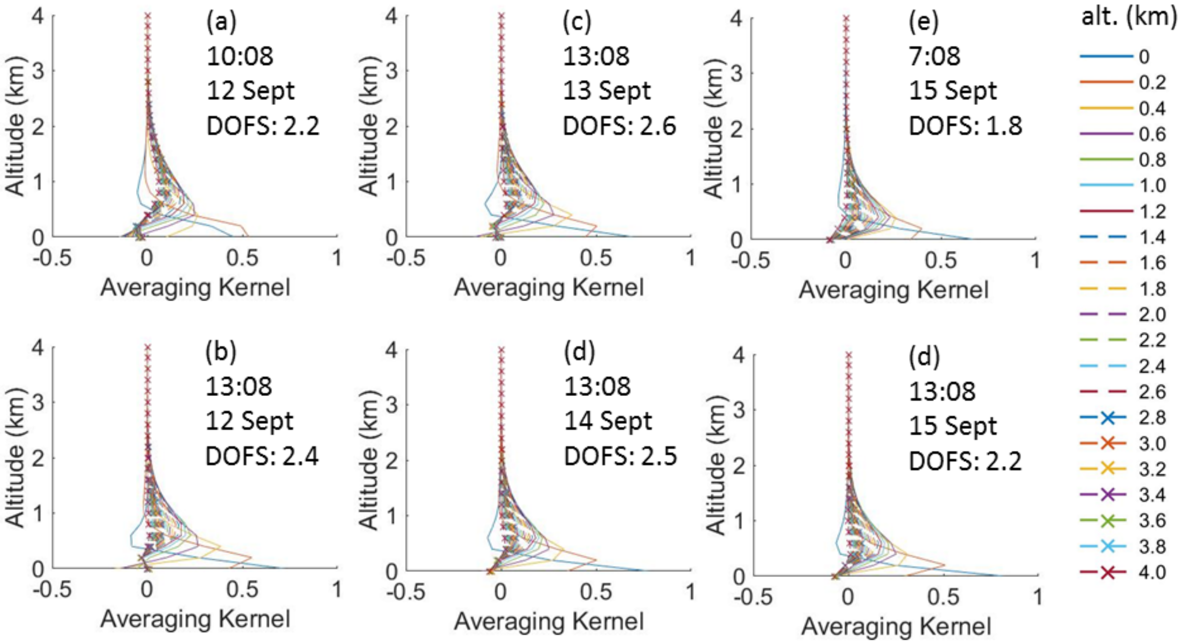

Figure 2.14: PEARL-GBS MAX-DOAS 0-4 km averaging kernels for CINDI-2 aerosol extinction retrievals.

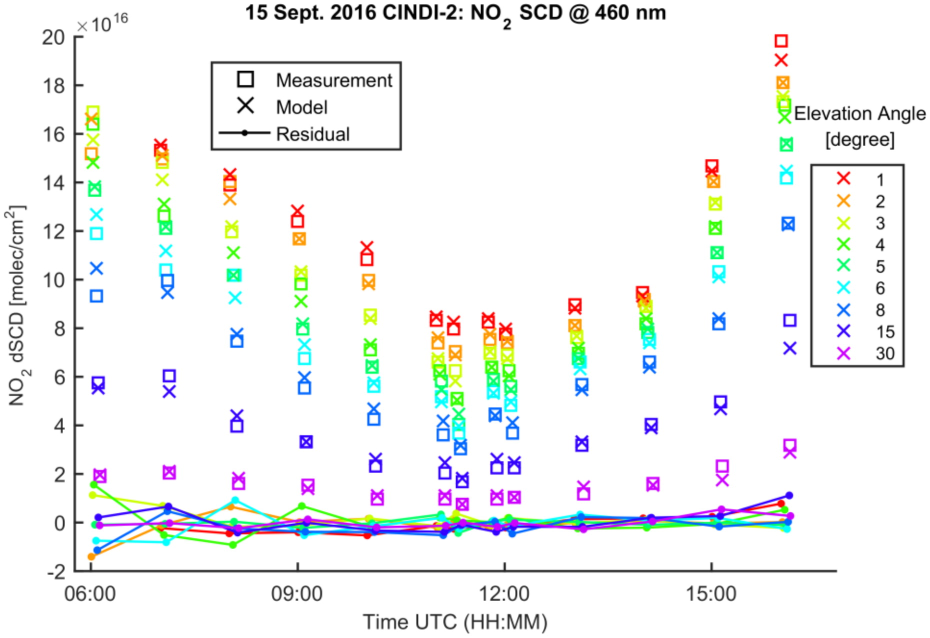

Figure 2.15: PEARL-GBS MAX-DOAS NO$_2$ dSCDs fitting results for 15 September 2016. The squares indicate PEARL-GBS measured NO$_2$ dSCDs, the x signs indicate HeiPro modelled NO$_2$ dSCDs, and the dot lines indicate dSCDs residual (measurement − model). The measurement and modelled values are colour coded by the MAX-DOAS elevation viewing angles.

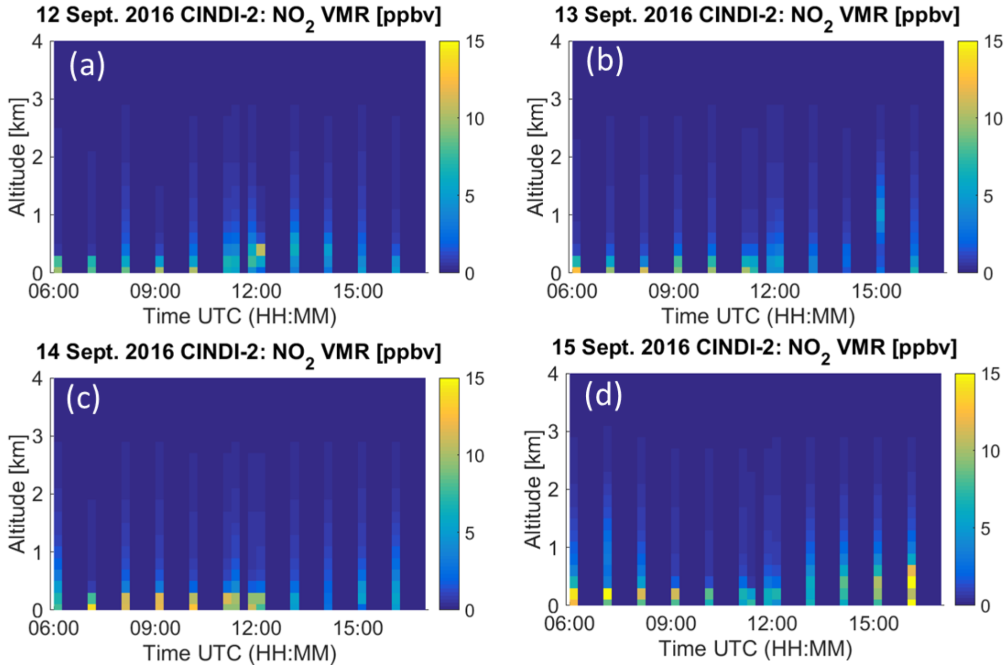

Figure 2.16: PEARL-GBS MAX-DOAS 0-4 km NO$_2$ volume mixing ratio profiles retrieved on four “golden days” during CINDI-2. The PEARL-GBS made 2D MAX-DOAS measurements throughout the day, but the preliminary results only show the measurements with azimuth viewing angle = 287°. The dark blue areas represent of measurements at different azimuths which have not been retrieved yet.

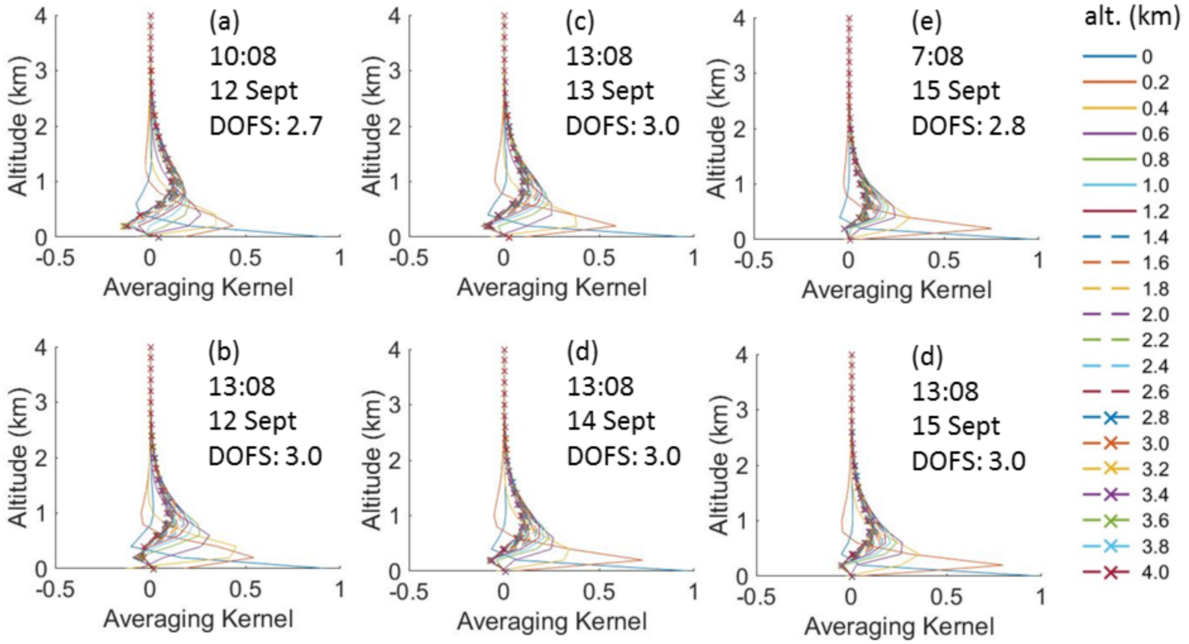

Figure 2.17: PEARL-GBS MAX-DOAS 0-4 km averaging kernels for CINDI-2 NO_2 retrievals.

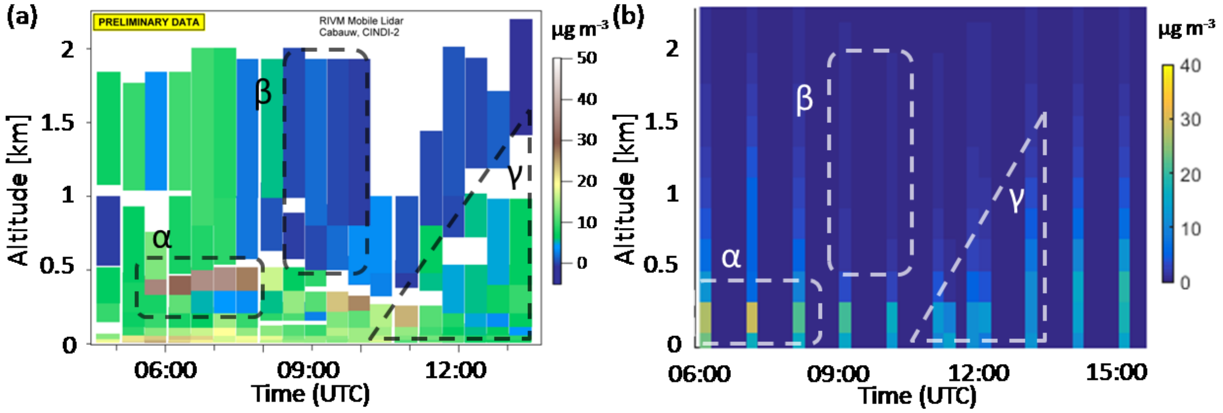

Figure 2.18: Preliminary comparison of CINDI-2 NO_2 0-2 km density profiles on 15 September measured by (a) RIVM NO_2 Lidar (data credit: Stijn Berkhout from RIVM), and (b) PEARL-GBS. The retrieved NO_2 concentration profiles from the two instruments show similarities in the three areas (α, β, and γ) as indicated on the figures: α) aloft NO_2 layer, β) clean airmass, and γ) increased vertical mixing.

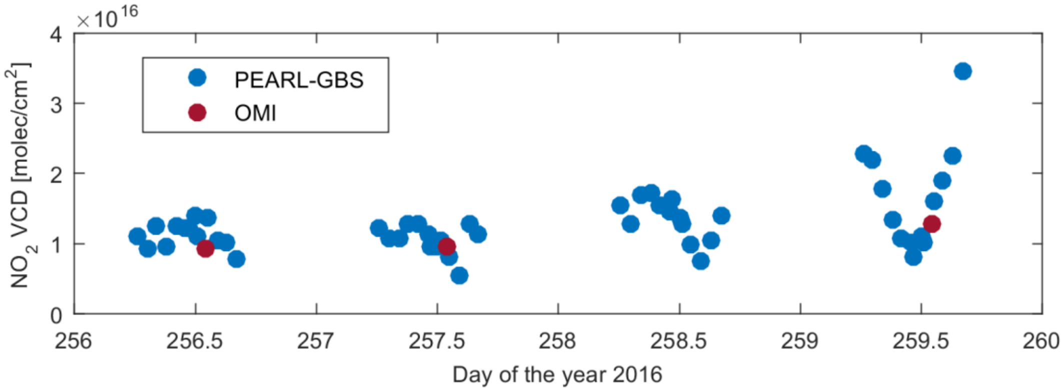

Figure 2.19: NO_2 VCD time series during CINDI-2. Blue dots represent PEARL-GBS MAX-DOAS, and red dots represent OMI (OMNO2d).

2.5 Summary

This chapter described the GBS instruments, the data analysis methodology used to retrieve columns and profiles, and the measurement campaigns with a focus on CINDI-2. The GBS Eureka dataset now covers 17 spring periods and ten full years (without measurements in polar night). The Eureka GBS zenith-sky ozone and NO_2 columns were submitted to NDACC archive in NASA Ames format in 2013. GBS data in new HDF format will be updated and submitted to the NDACC archive in early 2017.

Several improvements to both hardware and software were made between 2011 and 2016. For example, UT-GBS's f-number matcher and mechanical slit have been replaced by a direct fibre-mount and fixed slit; PEARL-GBS's flat CCD mount, which is the cause of uneven distribution of the resolution along the horizontal pixels of the CCD, has been replaced by a wedged one. Most importantly, both GBSs have been upgraded to MAX-DOAS instruments with capabilities to retrieve tropospheric trace gas profiles.

PEARL-GBS participated in the CINDI-2 campaign in September 2016, during which it performed combination measurements (including 2D MAX-DOAS, direct-sun, zenith-sky, almucantar scan, and horizon scan). Successful active tracking was also performed during the campaign. PEARL-GBS O_4 and NO_2 dSCDs were found to agree well with other instruments and the resulting retrieved aerosol and NO_2 profiles (in compliance with CINDI-2 organisation group profile retrieval protocol) are consistent with other instruments. Detailed instrument intercomparisons are currently underway.

Chapter 3

3 A Transported Bromine Explosion Event in 2011

A bromine explosion event associated with both blowing snow and a stable shallow boundary layer above Eureka, Canada in April 2011 is examined in this chapter. From 3 to 5 April 2011, 0-4 km BrO partial columns measured in the Canadian High Arctic at the PEARL Ridge Lab (Fogal et al., 2013) using ground-based MAX-DOAS were enhanced by a factor of three compared to previous days. It was found that the BEE was initiated during blowing snow conditions over the Beaufort Sea and transported to Eureka. In addition to low visibility conditions observed over Eureka for the first two days after the bromine plume arrived, local recycling of BrO over Eureka was also observed in calm and clear weather conditions on the third day of the event. To determine the source of this bromine explosion event and the driving meteorological conditions, an investigation of ground-based, satellite, and modelled BrO and ozone datasets is presented. A nudged version of the UM-UKCA chemistry-climate model is used to generate BrO and O_3 fields for comparison with the MAX-DOAS measurements.

BrO is one of the dominant species indicative of radical bromine chemistry and has been measured by various satellite and ground-based instruments. One method for measuring tropospheric BrO is MAX-DOAS, which has detection limits of 1-2 pptv, varying with visibility (Hönninger et al., 2004a; Platt and Stutz, 2008). For comparison, the BrO detection limits for in-situ chemical ionization mass spectroscopy (Neuman et al., 2010; Liao et al., 2012; Peterson et al., 2015) and long-path DOAS (Frieß et al., 2011; Liao et al., 2011) are 0.3-3 and 0.7-2 pptv respectively. Ground-based instruments can provide good temporal coverage and some vertical profile resolution (Frieß et al., 2011; Peterson et al., 2015), while nadir-viewing satellite instruments can be used to study bromine explosion events on the global scale (e.g., Richter et al. (1998). However, nadir-viewing UV-visible spectrometers have limited vertical resolution, making it difficult to separate BrO signals from the boundary layer, the free troposphere, and the stratosphere. Salawitch et al. (2010) showed that some of the locations of satellite BrO "hotspots" during Arctic spring could be associated with observations of elevated total column ozone and low tropopause height, suggesting a stratospheric origin for these regions of enhanced "tropospheric" bromine. Choi et al. (2012) also showed that the tropopause height is important and that properly accounting for the stratospheric signal is essential for accurate determination of satellite-derived tropospheric BrO, but for most clear-sky conditions, satellite measurements were in reasonable agreement with aircraft in-situ observations in the troposphere. Theys et al. (2011) and Koo et al. (2012) demonstrated that tropospheric BrO columns reflect the near-surface ozone depletion pattern. The partitioning of satellite-based BrO vertical column densities (VCDs) between the troposphere and stratosphere can be undertaken using the methods of Theys et al. (2011) and Sihler et al. (2012).

3.1 Methodology and Datasets

In this work, the following four local instruments at Eureka were used: a passive DOAS instrument (Adams et al., 2012a), radiosondes, ozonesondes, and a cloud radar. The DOAS instrument site, the PEARL Ridge Lab, is located on Ellesmere Island, Nunavut, Canada (86.4°W, 80.1°N), 610 m above sea-level, located near many fjords within the Canadian Arctic archipelago. During the 2011 Canadian Arctic ACE/OSIRIS Validation Campaign (Adams et al., 2012b), DOAS BrO and O_4 measurements were made by PEARL-GBS from 10 March to 5 April 2011. To investigate the BrO recycling, aerosol profiles were retrieved from O_4 measurements following the methods of Wagner et al. (2004) and Frieß et al. (2011).Other local instruments were located near the Eureka Weather Station (10 m above sea-level, 15 km away from the Ridge Lab).

Figure 3.1 shows a map of the field site, indicating the location of the MAX-DOAS instrument in relation to the Eureka Weather Station, as well as the viewing azimuth of the MAX-DOAS measurements (35° from true north in 2011). Typically, two radiosonde launches were made daily from the Eureka Weather Station during the campaign, recording vertical profiles of temperature, relative humidity, wind speed and direction. Ozonesondes were launched daily from 5-12 March 2011, and weekly from 17 March to 6 April, providing ozone profiles. The ozonesonde data have been corrected for non-standard solution volume and concentration, and normalised to a total ozone measurement (where available), with residual ozone interpolated from the 2011 Microwave Limb Sounder (MLS) climatology (McPeters and Labow, 2012). The uncertainty estimate is based on an analysis of known sources of electrochemical concentration cell (ECC) ozonesonde uncertainty, including pump rate, cell temperature, and radiosonde pressure errors, as well as background current correction and the corrections noted above (Tarasick et al., 2016). The uncertainty estimate is individual for each ozone profile, and agrees well on average with error profiles derived from field intercomparisons and laboratory studies (Kerr et al., 1994; Smit et al., 2007). The Millimetre Cloud Radar (MMCR, Shupe et al. (2010)) was working 24 hours/day during the campaign, providing equivalent radar reflectivity, Doppler velocity, spectral width, and Doppler spectra, from which information about cloud height, thickness, internal structure and vertical motion can be determined.

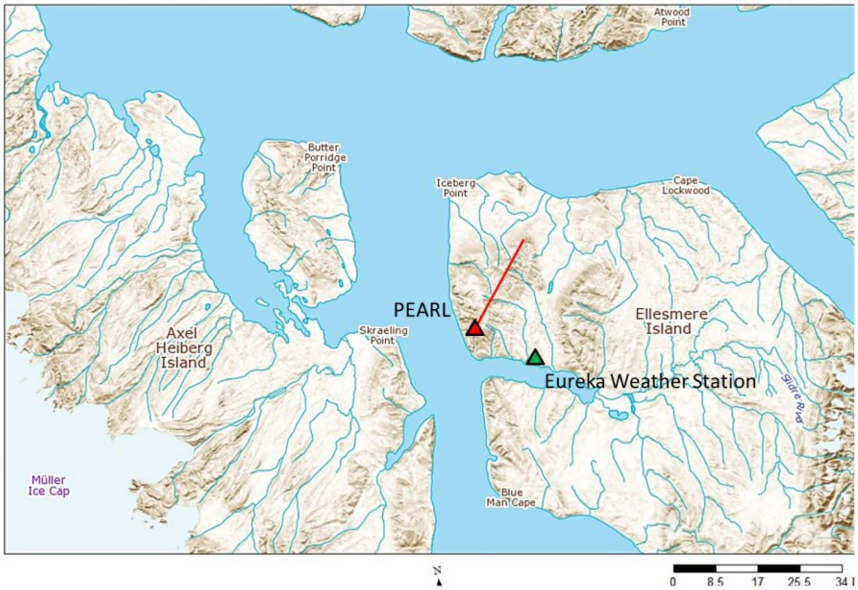

Figure 3.1: Locations of Eureka Weather Station and PEARL Ridge Lab (map data: Natural Resources Canada, http://atlas.gc.ca, 79.5° to 80.7° N, 83.4° to 90.7° W). The red line (representing 20 km in length) represents the viewing azimuth direction of MAX-DOAS measurements, which is 35° from true north.

3.1.1 Spectrum Processing

In 2011, PEARL-GBS used the 1200 gr/mm grating which provided coverage from 320 to 400 nm with a full-width at half-maximum resolution of ~0.45 nm. The PEARL-GBS was installed under UT-Suntracker #1 inside a UV-transparent acrylic dome. In order to measure tropospheric BrO, MAX-DOAS spectra were recorded from 320-400 nm at elevations of 6°, 8°, 10°, 15°, 30°, and 90° (with the minimum viewing elevation angle restricted by railings on the roof). The time required for a full MAX-DOAS measurement sequence of six viewing elevation angles was about 15 min. The azimuth angle of the suntracker was selected as 35° clockwise from the north when performing the MAX-DOAS sequence.

Table 11: Settings used for 2011 MAX-DOAS and ZS-DOAS spectral analysis.

	BrO		**O_4**
	MAX-DOAS	ZS-DOAS	MAX-DOAS
BrO cross section	bro_223K_Fleischmann (Fleischmann et al., 2004)	bro_223K_Fleischmann (Fleischmann et al., 2004)	bro_223K_Fleischmann (Fleischmann et al., 2004)
O_4 cross section	Hermans (Hermans et al., 2003)	Hermans (Hermans et al., 2003)	Hermans (Hermans et al., 2003)
O_3 cross section	O3_223_BOGUMIL (Bogumil et al., 2003)	O3_223_BOGUMIL (Bogumil et al., 2003)	O3_223_BOGUMIL (Bogumil et al., 2003)
O_3 cross section	O3_243_BOGUMIL (Bogumil et al., 2003)	N/A	O3_243_BOGUMIL (Bogumil et al., 2003)
NO_2 cross section	NO2_220_VANDAELE (Vandaele et al., 1998)	NO2_220_VANDAELE (Vandaele et al., 1998)	NO2_220_VANDAELE (Vandaele et al., 1998)
OClO cross section	OClO_Wahner_204K (Wahner et al., 1987)	OClO_Wahner_204K (Wahner et al., 1987)	OClO_Wahner_204K (Wahner et al., 1987)
Ring spectrum	Ring (Chance and Spurr, 1997)	Ring (Chance and Spurr, 1997)	Ring (Chance and Spurr, 1997)
Wavelength	337 - 361.9 nm	345 - 359 nm	335 - 367 nm
Polynomial	4th order	3rd order	4th order
Shift and stretch	1st order	1st order	1st order
Offset	1st order	1st order	1st order

The observed spectra were analysed with the DOAS method (Platt and Stutz, 2008) implemented using QDOAS software (Danckaert et al., 2015). ZS-DOAS and MAX-DOAS spectra have been analysed with the settings shown in Table 11. The ZS-DOAS spectra were analysed using daily noon reference spectra, and MAX-DOAS spectra were analysed using the 90° elevation angle measurement within a scan sequence as the reference. Since ZS-DOAS and MAX-DOAS sample different regions of the atmosphere and hence different temperatures, the 223 K ozone cross section was used for the analysis of spectra from ZS-DOAS, while two ozone cross sections at 223 K and 243 K were used in the MAX-DOAS analysis to limit the systematic error due to the temperature dependence of the cross sections. This approach was only applied for ozone as it is a strong absorber present in both the stratosphere and troposphere. Two BrO fitting windows were selected: 337-361.9 nm following Hay (2010) (a wide fitting window containing four absorption lines) for MAX-DOAS spectra and 345-359 nm following Hendrick et al. (2007) (a smaller fitting window containing two absorption lines) for zenith-sky spectra. The smaller wavelength region was used for the zenith-sky retrievals to avoid two strong absorption features between 337 nm and 341.5 nm from stratospheric ozone (Aliwell et al., 2002; Adams, 2012). The selection of the BrO fitting windows were based on sensitivity tests (see Appendix A), in which we evaluated six different BrO fitting windows that have been used in retrievals for satellite, airborne, and ground-based DOAS instruments (Theys et al., 2009; Hay, 2010; Prados-Roman et al., 2011; Theys et al., 2011; Adams, 2012). Note that the MAX-DOAS O_4 fitting window was 335-367 nm (containing two O_4 absorption features).

The output of QDOAS is differential slant column density (dSCD), which is the difference between the trace gas columns along the effective light paths of the analysed spectrum and the reference spectrum. The MAX-DOAS dSCDs of BrO and O_4 measured at Eureka from 1-5 April 2011 are shown in Figure 3.2, along with root mean square (RMS) fitting residuals. In Figure 3.2, from 4-5 April, the MAX-DOAS BrO dSCDs at different elevation viewing angles are well separated, characteristic of enhanced BrO in the lower atmosphere. The well-separated O_4 dSCDs show that 5 April was a clear day, and so MAX-DOAS data should be of high quality on that day.

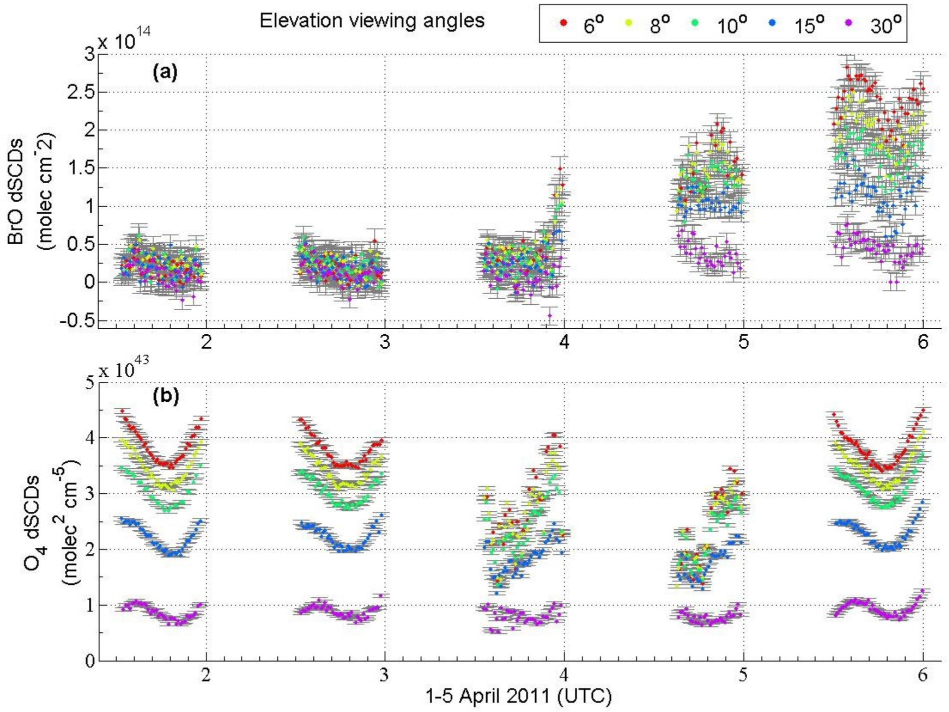

Figure 3.2: MAX-DOAS dSCDs at different elevation viewing angles (indicated in the legend) measured at Eureka from 1-5 April 2011. (a) BrO dSCDs with error bars; (b) O_4 dSCDs with error bars. Note: These dSCDs are relative to the 90° zenith spectrum for each MAX-DOAS scan sequence.

3.1.2 DOAS Profile Retrievals

The OEM (Rodgers, 2000) was used for both stratospheric and tropospheric BrO profile retrievals. As described in Section 2.1.3, the PEARL-GBS provided both ZS-DOAS and MAX-DOAS data, enabling the retrieval of both stratospheric and tropospheric BrO. The MAX-DOAS data (from which tropospheric aerosol extinction profiles, tropospheric BrO profiles, and BrO partial column densities are retrieved) are sensitive to the boundary layer, and thus are more suitable for studying bromine explosion events. However, because the descent of stratospheric BrO has been suggested as a possible source for a false bromine explosion signal (Salawitch et al., 2010), the ZS-DOAS data, which are sensitive to the stratosphere, were used to retrieve BrO stratospheric profiles and total vertical column densities (VCDs). The basic profile retrieval methodology is described in Section 2.2.2. Since the method for retrieving stratospheric BrO applied in this work has been described in detail by Schofield et al. (2004b), and the method used for tropospheric BrO and aerosol retrievals has been described in Frieß et al. (2011), both methods are described only briefly here.

For the stratospheric retrievals, the method of Schofield et al. (2006) was followed. In this work, a single scattering RTM was used as the forward model (Schofield, 2003). The forward model is a spherical shell radiative transfer model, which includes refraction, Rayleigh scattering, Mie scattering, and molecular absorption. The forward model parameters of ozone, temperature and pressure were provided by ozonesonde measurements. The tropopause heights were derived by considering the available ozonesonde data. The diurnal variation of the vertical distribution of BrO adds complication to the retrieval, and this has been addressed by Schofield et al. (2006) and Hendrick et al. (2007) by incorporating a photochemical model in the forward modelling of the inversion problem. Therefore in the stratospheric retrievals, a chemical-climate model (UM-UKCA, details presented in Section 3.4) was used to define the *a priori* set of profiles.

For the tropospheric retrievals, a two-step approach for the retrieval of tropospheric aerosol and trace gas profiles from MAX-DOAS spectra (Frieß et al., 2011) was followed. First, aerosol extinction profiles were retrieved from the measured O_4 dSCDs in the lowermost 4 km of the atmosphere on a 250-m vertical grid. In the second step, these aerosol extinction profiles served as a forward model parameter for the retrieval of BrO vertical profiles. The radiative transfer model SCIATRAN2 (Rozanov et al., 2005) and the HeiPro (Frieß et al., 2011) OEM (see Section 2.4.3) were used in this work for the tropospheric aerosol and BrO profile retrievals. As for the aerosol extinction profile retrievals, a vertical grid of 250-m resolution for the lowermost 4 km of the atmosphere was used for the BrO profile retrievals. Use of a finer grid of 50 m or 100 m did not have a significant impact on the results.

The *a priori* BrO profile for MAX-DOAS profile retrievals was chosen as exponentially decreasing with altitude (with a scale height of 500 m or 1000 m depending on the condition of atmospheric stability: 500 m when a strong surface inversion was seen in the radiosonde data, 1000 m for a weak inversion layer), and the surface VMR was set to 5 pptv for 4-5 April and 1 pptv for 1-3 April. Like Peterson et al. (2015), the retrieved BrO profiles were found to be sensitive to the choice of scale height in the *a priori* profile, due to the limited degrees of freedom for signal (DOFS) in the MAX-DOAS retrieval. The diagonal elements of the *a priori* covariance matrix, $\mathbf{S}_\mathrm{a}$, were set to twice the values of the *a priori* VMR. The off-diagonal elements of the *a priori* covariance matrix were chosen to decrease exponentially with the distance between the layers (with a correlation length of 500 m) to improve the smoothness of the retrieved BrO profiles (Frieß et al., 2011). Except for the different vertical grid resolution and *a priori* profiles, other aspects of the MAX-DOAS profile retrievals in this work are identical to those of Frieß et al. (2011).

3.1.3 Chemistry-Climate Model

UM-UKCA is a global chemistry-climate model; its dynamical core is version 7.3 running in the HadGEM3-A configuration (Morgenstern et al., 2009). The UMUKCA-CheST version contains a comprehensive stratospheric chemistry scheme as well as a detailed tropospheric chemistry scheme, including isoprene chemistry. Tropospheric bromine chemistry was introduced based on the work in pTOMCAT (Yang et al., 2005; Yang et al., 2010). The bromine source includes on inorganic sea salt source from both the open ocean and the sea ice zone (from blowing snow (Yang et al., 2008)), and halocarbons from long-lived (e.g., CH_3Br) and very short-lived substances (VSLSs, e.g., $CHBr_3$ and CH_2Br_2) based on Warwick et al. (2006). The total amount of inorganic Br_y (from both halocarbons and sea salt) in the stratosphere is about 20 pptv (Braesicke et al., 2013). A number of heterogeneous reactions on atmospheric particles (including sulphate aerosols and polar stratospheric clouds) have been included in the model to account for inter-halogen (chlorine and bromine) reactivation as in the recent study by Braesicke et al. (2013) and Yang et al. (2014). In the polar boundary layer, heterogeneous reactivation of inactive bromine on sulphate aerosols has been considered with sulphate field being monthly climatology data from the CLASSIC aerosol scheme (Johnson et al., 2010). There are no other reactivations within the snowpack or on aloft snow particles included in this study. The model's horizontal resolution was 3.75° in longitude and 2.5° in latitude on an Arakawa-C grid. A hybrid sigma-geometric height coordinate was used to resolve the vertical range from the surface to ~84 km on 60 levels. Since the scheme of blowing-snow SSA production and bromine release applied in this work has been described in detail by Yang et al. (2008; 2010), the main features of the blowing snow scheme is described only briefly here.

3.1.3.1 Blowing-Snow Sea-Salt Aerosol Production

The snow on first-year sea ice contains bromine salts. The blowing-snow bromine source included in the model arises when wind lifts the bromine-containing snow into the atmosphere (Yang et al., 2008). If the air is not saturated, water may sublime from the salty snow particles, which reduces their size and eventually leads to the formation of SSA. The amount of SSA produced in blowing snow is calculated based on the sublimation flux and the particle size distribution (Yang et al., 2008). Following Déry and Yau (1999; 2001), the blowing-snow sublimation flux is calculated by

$$Q_s = \frac{kA' Q_s' q_b}{q_{b0}} \quad . \tag{3.1}$$

Here, Q_s is the total sublimation flux, Q'_s is a normalized column-integrated sublimation rate (mm day^{-1}), k is a constant to converts Q_s into units of kg m^{-2} s^{-1}. A' is a factor to describe the efficient of wind lifting, which depends on the age of snow (Li and Pomeroy, 1997; Box et al., 2004). q_b (kg kg^{-1}) is the blowing snow mass mixing ratio under ambient conditions, and q_{b0} is the value under the threshold wind speed (6.975 m s^{-1}, Déry and Yau, 2001). The Q'_s is calculated by a fitting of wind speed and another parameter (which depends on the RH, heat conductivity, and vapour diffusion for sublimation; see Eq. 14 in Déry and Yau, 2001). In general, Q_s depends on a variety of factors including the surface wind speed and temperature, the RH of the air, and the age of the snow.

The total sea salt production rate can be calculated by

$$Q_{seasalt} = \frac{Q_s}{1000} \iint_0^{\infty} f(d_i) \varsigma \psi(\varsigma) d(d_i) d\varsigma \ . \tag{3.2}$$

Here, d_i is the snow particle diameter, $f(d_i)$ is the size distribution function of the suspended particles in blowing snow events (Budd, 1966; Schmidt, 1982), ς is the snow salinity in units of practical salinity units (psu), and $\psi(\varsigma)$ is the salinity frequency distribution function (Sander et al., 2003; Yang et al., 2008).

3.1.3.2 Bromine Release from Sea Salt Aerosol

In this blowing-snow induced ODE simulation, the bromine release flux (Q_{Br}, which is in unit of kg m^{-2} s^{-1}) is calculated by

$$Q_{Br} = \frac{R_a}{1000} \sum_i \mathrm{DF}(d_{dry}) f(d_i) Q_s \varsigma \qquad . \tag{3.3}$$

Here, R_a is the mass ratio of Br to NaCl in sea salt, d_{dry} the corresponding dry sea salt diameter (Yang et al., 2008), DF(d_{dry}) is a nonlinear size-dependent bromine depletion function, which derived from the observation dataset (Sander et al., 2003). For example, DF reaches its maximum value of about 0.4 at d_{dry} = 1.3 µm, and drops to about 0.1 at d_{dry} = 10 µm (Yang et al., 2008). Following Yang et al. (2008; 2010), in this work, only SSA with d_{dry} less than 10 µm is treated as bromine source.

In general, a large sublimation flux is expected with low RH and high wind speed condition, and in consequence this leads to high SSA production and bromine release flux in the model (Yang et al., 2008).

3.1.4 Complementary Datasets

In addition to the instruments at Eureka (PEARL-GBS, ozonesondes, radiosondes, and MMCR), several other datasets were employed in this study: the GOME-2 satellite tropospheric BrO columns (Begoin et al., 2010; Blechschmidt et al., 2016), the Hybrid Single-Particle Lagrangian

Integrated Trajectory (HYSPLIT) model (Draxler and Hess, 1998; Draxler et al., 2014), the European Centre for Medium-Range Weather Forecasts (ECMWF) interim meteorological data (ERA-Interim data) (wind speed, boundary layer height, and large-scale snow-fall) (Dee et al., 2011), the National Snow and Ice Data Center (NSIDC) data (sea-ice age and snow depth over sea-ice) (Kurtz et al., 2012), and the UM-UKCA chemistry-climate model (Morgenstern et al., 2009; Yang et al., 2014).

The GOME-2 data used in this paper are described in detail by Blechschmidt et al. (2016). In short, tropospheric BrO partial columns (VCD_{tropo}) were obtained based on Begoin et al. (2010) for deriving total slant column densities of BrO using the DOAS method (336-347 nm fitting window (Afe et al., 2004)) and on Theys et al. (2011) for stratospheric correction. Stratospheric vertical column densities of BrO were estimated using the Theys et al. (2011) climatology of stratospheric BrO from the BASCOE (Errera et al., 2008; Viscardy et al., 2010) chemical transport model and NCEP/NCAR Reanalysis 1 (Kalnay et al., 1996) thermal tropopause heights. A sensitivity study showed that the GOME-2 VCD_{trop} used in this study has a moderate sensitivity to the stratospheric BrO column assumed during the BrO event. A variation in the VCD_{strat} of 15-30% leads to a change in VCD_{trop} of about 0.5 to 1×10^{13} molec cm^{-2}, respectively. The BrO VCD_{trop} doesn't vary much with time, as the stratospheric column only varies between about 2.9 to 3.4×10^{13} molec cm^{-2} over the time period studied. Note that dynamical tropopause heights derived from Weather Research and Forecasting (WRF) (Skamarock et al., 2008) simulations are used in Blechschmidt et al. (2016) instead of NCEP tropopause heights. Comparison of the GOME-2 data used in the present study and the one by Blechschmidt et al. (2016) for the time period up to 2 April 2011 showed a minor effect of the different tropopause data on the data analysis. The influence of clouds on the GOME-2 BrO retrievals for the time period 31 March to 2 April 2011 and implications on studying the bromine explosion event using the GOME-2 data are discussed in detail in Blechschmidt et al. (2016).

To explore the history of the bromine-enriched airmass and the source region of the bromine explosion event, the GOME-2 data along with HYSPLIT back-trajectories were examined. Since bromine explosion events are known to occur in windy conditions over first-year sea ice regions (Abbatt et al., 2012), the ERA-Interim data and sea-ice information over the Beaufort Sea were investigated, including snow depth data from the Advanced Microwave Scanning Radiometer-

Earth Observing System (AMSR-E) aboard the Aqua satellite (Comiso et al., 2003), and Arctic sea-ice age data from the NSIDC.

3.2 Results and Discussion

3.2.1 BrO and Aerosol Vertical Profiles

For the stratospheric BrO profile retrievals, Figure 3.3a shows the ZS-DOAS measured and fitted BrO dSCDs on 4 April 2011 PM. The retrieved BrO profiles at various SZAs (which differ due to the strong diurnal variation of BrO) on 4 April PM are shown in Figure 3.3b along with the *a priori* profiles from the UM-UKCA chemistry-climate model hourly runs. The averaging kernels for this retrieval are a function of both altitude and time (SZA), which means each element of the state vector has a two-dimensional averaging kernel (Schofield et al., 2004b). The profile (at 74° SZA) has DOFS of 1.75. The averaging kernels (not shown) indicate that the retrieved profile is more sensitive to the stratosphere, and the tropospheric part of the retrieved profile is mostly determined by the *a priori* information. The shape and magnitude of the stratospheric BrO profiles before and during the bromine explosion event provides some insight into whether the descent of stratospheric BrO was the source of tropospheric BrO enhancement as discussed in Section 3.2.3.

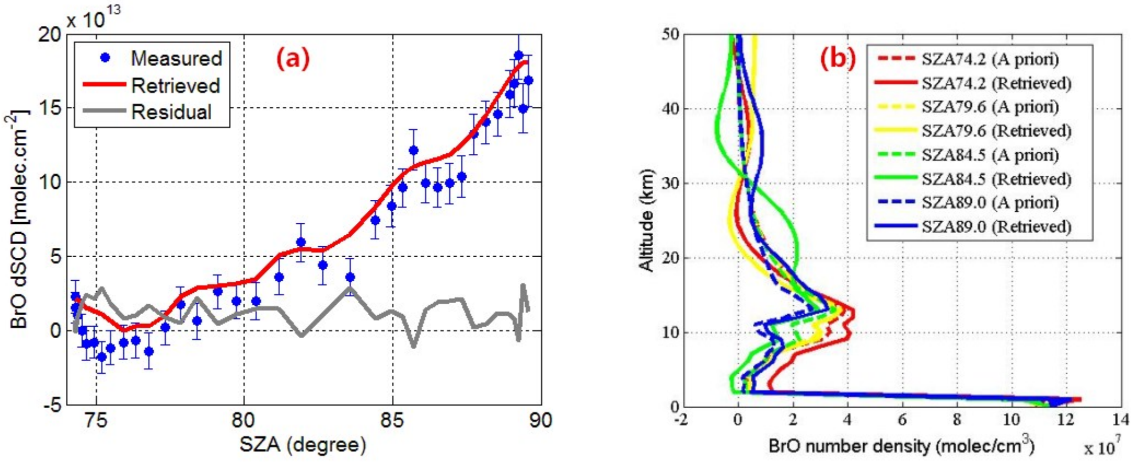

Figure 3.3: (a) ZS-DOAS measured and fitted BrO dSCDs and corresponding residuals at Eureka on 4 April 2011 PM; (b) BrO profiles retrieved from ZS-DOAS data at various SZAs on 4 April 2011 PM. Solid lines indicate retrieved profiles, and dashed lines indicate *a priori* profiles (generated from the UM-UKCA chemistry-climate model). Note: These dSCDs are relative to local solar noon on 4 April.

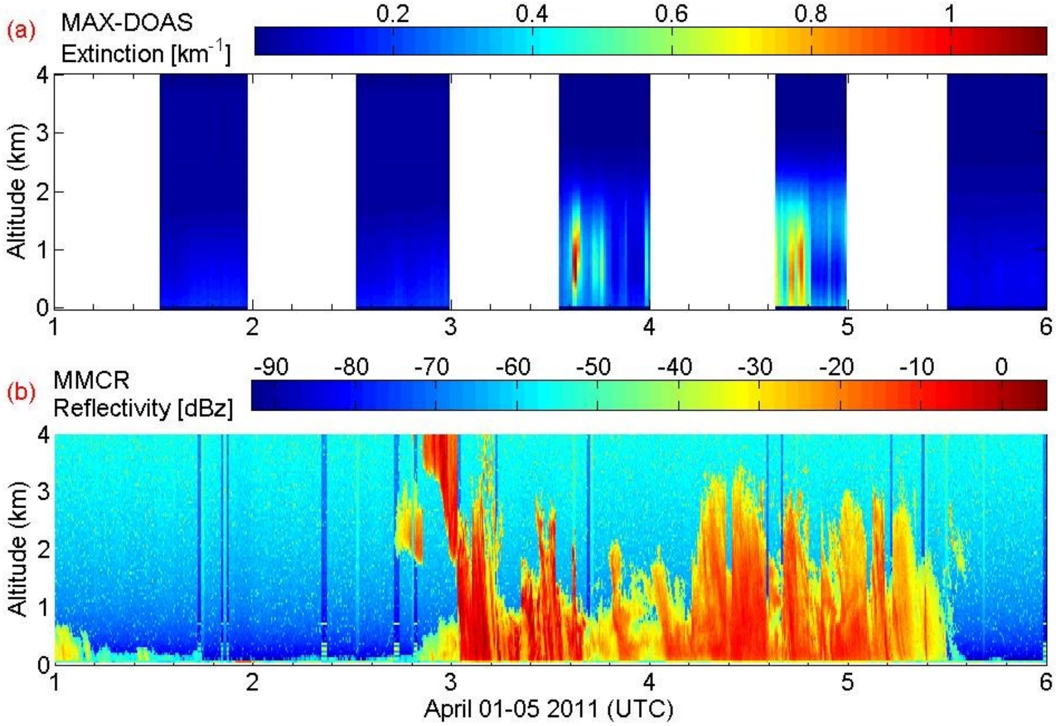

Figure 3.4: (a) MAX-DOAS aerosol extinction profiles and (b) MMCR reflectivity from 1-5 April 2011. Note that the MAX-DOAS only works during sunlit conditions (SZA < 86°), while the MMCR works continuously.

As mentioned in Section 3.1.1, the tropospheric aerosol and BrO profiles were retrieved using MAX-DOAS data. First, the aerosol extinction profiles with MMCR reflectivity data and local meteorological records were compared at the Eureka Weather Station. Figure 3.4 shows the direct comparison of MAX-DOAS aerosol extinction profiles with MMCR reflectivity profiles for the lowermost 4 km of the atmosphere. The MMCR data are more sensitive to cloud rather than fine aerosol particles, however, high values of extinction and reflectivity were consistently observed by the two instruments from 3-4 April 2011, indicating low visibility conditions (light falling snow is found in MMCR Doppler velocity data, not shown). In this blowing-snow-initialized event, cloud cover was observed from the surface to ~3 km altitude by the MMCR. The meteorological record at the Eureka Weather Station (10 m above sea-level, 15 km away from the PEARL Ridge Lab) showed a combination of drifting snow, falling snow, and ice crystal conditions on 3-4 April. Meanwhile, the visibility was down to 1.5-4 km, consistent with the MAX-DOAS aerosol extinction near surface being as high as 1.1 km^{-1}, corresponding to a visibility of about 3.5 km. Figure 3.4 shows that low aerosol extinction and low reflectivity were observed on 1 and 5 April, indicating clear-sky conditions on those days. The visibility record at the Eureka Weather Station was 15 km on 5 April, consistent with the MAX-DOAS aerosol extinction measurements (~0.2 km^{-1}). The clear-sky conditions on 5 April are ideal for the MAX-DOAS BrO profile retrievals (Frieß et al., 2011).

Averaging kernels for MAX-DOAS aerosol extinction and BrO profile retrievals on 4 and 5 April PM are shown in Figure 3.5. The averaging kernels for the aerosol retrieval indicate higher sensitivity to upper layers during clear-sky conditions (5 April) than during low visibility conditions (4 April), consistent with the results in Frieß et al. (2011). Since the averaging kernels for the BrO retrieval show little sensitivity above 2 km especially under low visibility conditions, the retrieved mixing ratio above 2-3 km was constrained tightly to the *a priori*. The DOFS represent the number of independent pieces of information that can be retrieved from the MAX-DOAS measurements. Due to the absence of near-horizon measurements in the MAX-DOAS scanning sequence (6°, 8°, 10°, 15°, and 30°), the DOFS for BrO profile retrievals increased from 1.1 during low-visibility conditions on 4 April only to 1.5 in clear-sky conditions on 5 April. The DOFS in low-visibility conditions is similar to that reported by Frieß et al. (2011) (1.0), which indicate the retrieved MAX-DOAS profiles in the low-visibility conditions are effectively just a scaling of the *a priori* profile. The clear-sky DOFS in this work is lower than that reported by Frieß et al. (2011) and Peterson et al. (2015) (2.1 and 2.0 respectively), who both used scanning sequences of 1°, 2°, 5°, 10°, and 20°. To illustrate the different sensitivity for 1° and 6° elevation angle measurements, box-AMFs (Wagner et al., 2007) were modelled for 1°, 6°, and 90° elevations for Arctic springtime condition (see Appendix B). The retrieved MAX-DOAS BrO profiles are shown and discussed in detail in Section 3.2.4, along with the modelled BrO profiles.

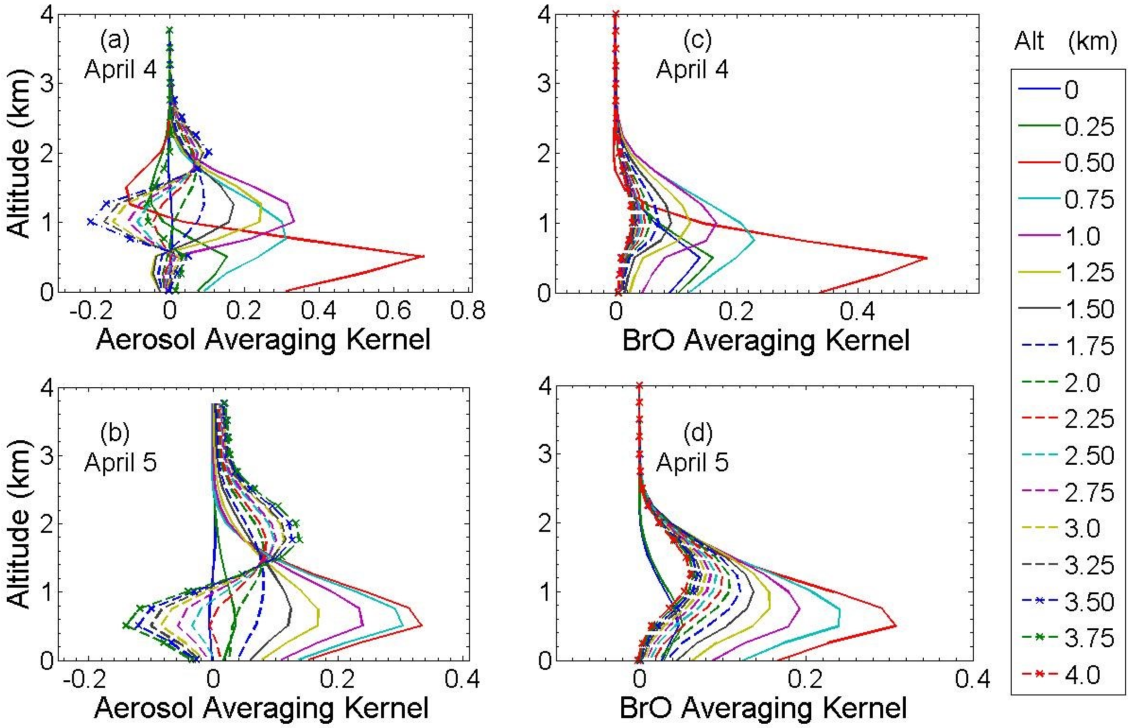

Figure 3.5: MAX-DOAS 0-4 km averaging kernels for 4 and 5 April 2011 PM. (a) and (b) for aerosol extinction retrievals; (c) and (d) for BrO retrievals.

3.2.2 Comparison with GOME-2

To assess the ground-based BrO measurements, a comparison of retrieved DOAS BrO columns with GOME-2 BrO tropospheric vertical column density (VCD_{tropo}) was performed. The ground-based VCD_{tropo} (not shown here) was generated by the integration of BrO profiles using the 0-4 km altitude profiles from MAX-DOAS and 4-8 km from ZS-DOAS. The two DOAS measurements generally sample different airmasses, with the combined tropospheric product having a horizontal sampling distance of less than 20 km, which is more local than GOME-2. Thus only the satellite pixels over Eureka (approximately within a distance of 45 km from Eureka) were used in the comparison.

During the bromine explosion event, the 4-8 km partial columns only contribute 1-4% of the ground-based BrO VCD_{tropo} (note that due to the limited vertical sensitivity at these altitudes, this contribution consists of *a priori* information). Therefore, in Figure 3.6, the GOME-2 BrO

VCD$_{tropo}$ products are directly compared with the MAX-DOAS 0-4 km partial columns. Figure 3.6a shows the GOME-2 BrO VCD$_{tropo}$ (approximately 0-8 km partial column, with the tropopause heights used in the satellite retrieval adapted from NCEP/NCAR Reanalysis 1 data) and the MAX-DOAS 0-4 km partial columns on 4-5 April 2011 agreed within error bars during the days with enhanced BrO. Figure 3.6b shows GOME-2 versus MAX-DOAS BrO VCD$_{trop}$ with 100 min coincident criterion for five days of measurements. The weighted linear regression accounting for MAX-DOAS and GOME-2 measurement errors indicates that GOME-2 measurements are highly correlated (R = 0.79) with the MAX-DOAS measurements with a slope of 1.02 and offset of 7.0×10^{12} molec cm^{-2}. Changing the coincident time to 20 min provides comparable results with R = 0.74, but with fewer coincident measurements (14 vs. 9).

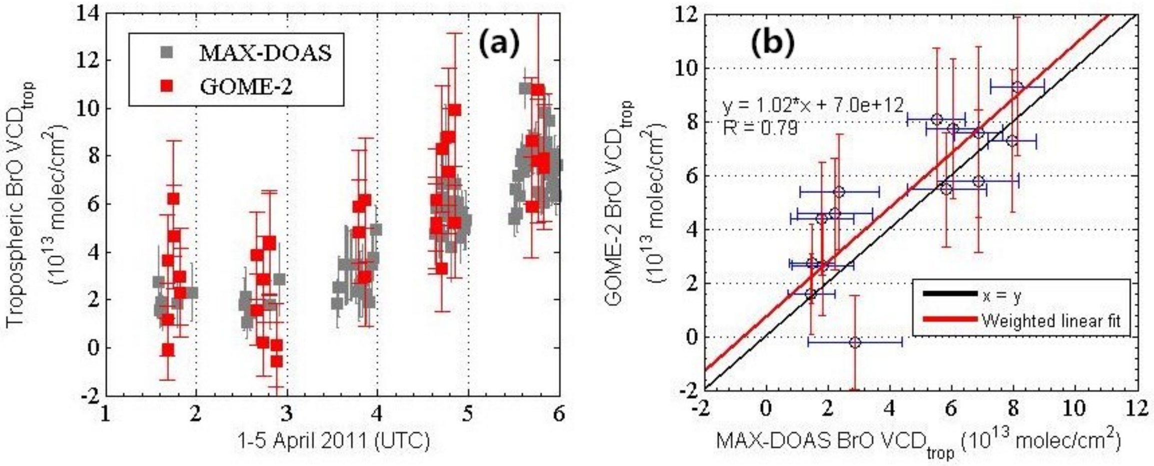

Figure 3.6: (a) Time series of BrO tropospheric partial column densities (VCD$_{trop}$) from PEARL-GBS MAX-DOAS (0-4 km altitude) and GOME-2 (approximately 0-8 km altitude, full troposphere) within 45 km of Eureka. (b) GOME-2 versus MAX-DOAS tropospheric BrO partial column densities. MAX-DOAS error bars are total retrieval error, based on Frieß et al. (2011). GOME-2 error bars are systematic error, estimated based on Theys et al. (2011).

The retrieval errors for the ground-based and satellite DOAS BrO measurements on a clear day (5 April 2011) are smaller than those under low visibility conditions (4 April 2011); the ground-based MAX-DOAS BrO partial column density mean retrieval error on 5 April 2011 was 11.1%, while the error on 4 April 2011 was 21.6%. In general, the MAX-DOAS retrieval errors (statistical dSCD error, *a priori* error, and retrieved VCD error) are consistent with those of Frieß et al. (2011).

3.2.3 History of the 2011 Bromine Explosion Event

The air-mass history related to the local BrO enhancement at Eureka can be examined based on the analysis of back-trajectories and model results. In Figure 3.7, HYSPLIT six-day back-trajectories ending at Eureka at 00:00 UTC on 4 April 2011 are shown at six different altitudes (100 m, 600 m, 1 km, 2 km, 3 km, and 4 km). The back-trajectories confirmed that the high BrO airmass observed at Eureka on 4 April was over the Beaufort Sea on 31 March 2011. In addition, the trajectories showed a strong uplift of the lower tropospheric air to the middle troposphere inside the cyclone from 31 March to 1 April, consistent with the vertical transport of boundary layer bromine up to the free troposphere by frontal lifting described in Blechschmidt et al. (2016) (more evidences of the cyclone is provided in Section 4.3.1).

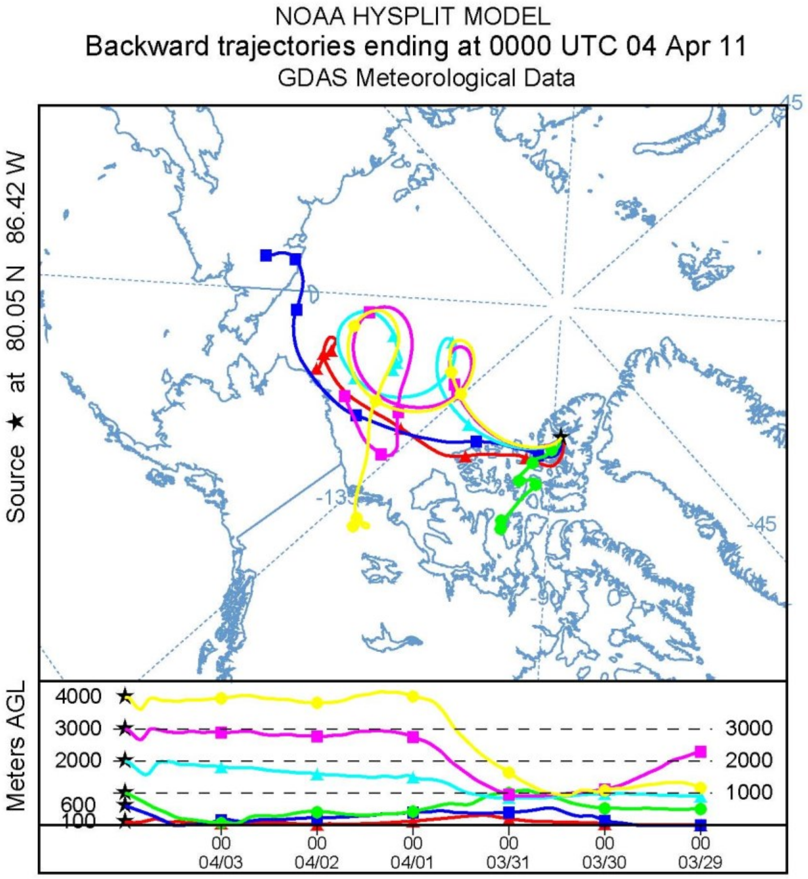

Figure 3.7: HYSPLIT six-day back-trajectories for Eureka (80.05°N, 86.42°W), ending at 00:00 UTC on 4 April 2011.

Blechschmidt et al. (2016) investigated the meteorological conditions during this bromine explosion event over the Beaufort Sea observed by GOME-2 and concluded that the bromine plume was most likely confined to the lowest 3 km of the atmosphere from 31 March to 2 April. Maps of GOME-2 tropospheric BrO from 28 March to 5 April 2011 (see Figure 3.8) suggest that a bromine-enriched cyclone was generated on 31 March (the cyclone itself arrived at the Beaufort Sea on 30 March), and then moved eastward and passed over Eureka during the next four to five days. While the maximum BrO VCD_{trop} decreased from ~1.5×10^{14} molec cm^{-2} (31 March) to ~7×10^{13} molec cm^{-2} (4 April) when the plume arrived at Eureka, it still exceeded the background BrO VCD_{trop} (1-2×10^{13} molec cm^{-2}).

Figure 3.9a shows that the bromine explosion event source region over the Beaufort Sea was covered by first-year sea ice during the third week of March, while Figure 3.9b shows that the same region was also covered by deep snow (~ 25-35 cm) from 31 March to 4 April. The 10-metre wind gust and boundary-layer height from ERA-Interim data are used to investigate the meteorological conditions in the bromine explosion source region. The ERA-Interim data show that on 1 April, the wind speed in the cyclone increased to 24 m s^{-1} (Figure 3.10a), and the boundary layer height increased to 800 m (Figure 3.10b). This is strong enough to lift salty snow particles into the air (Jones et al., 2009) and accelerates multiphase chemical reactions (R1-R4) on them to release bromine (Yang et al., 2008; Yang et al., 2010). This is discussed in detail in Section 3.4. The size of airborne snow grains could change by sedimentation and sublimation processes during the transport, and these processes could produce small aerosol particles, which can be lifted to higher altitudes and transported over larger distances (Pomeroy et al., 1997). Choi et al. (2012) show a similar comma-shaped bromine plume (maximum BrO VCD_{trop} ~8×10^{13} molec cm^{-2}) with wind speed (~9 m/s) on 19 April 2008 over the Chukchi Sea with an increased boundary layer height to 500 m and a weak surface temperature inversion. The strength of the low-pressure system in the present study is stronger than the one reported by Choi et al. (2012), which makes the deep vertical mixing and long-range transport more likely. When the bromine plume arrived over Eureka on 3-4 April, high aerosol extinction values were also observed by MAX-DOAS (see Figure 3.4). Thus the sea salt aerosol could play an important role in this event, contributing to the persistence of the bromine plume for ~six days (from 31 March to 5 April), while it was transported eastward for ~1,800 km.

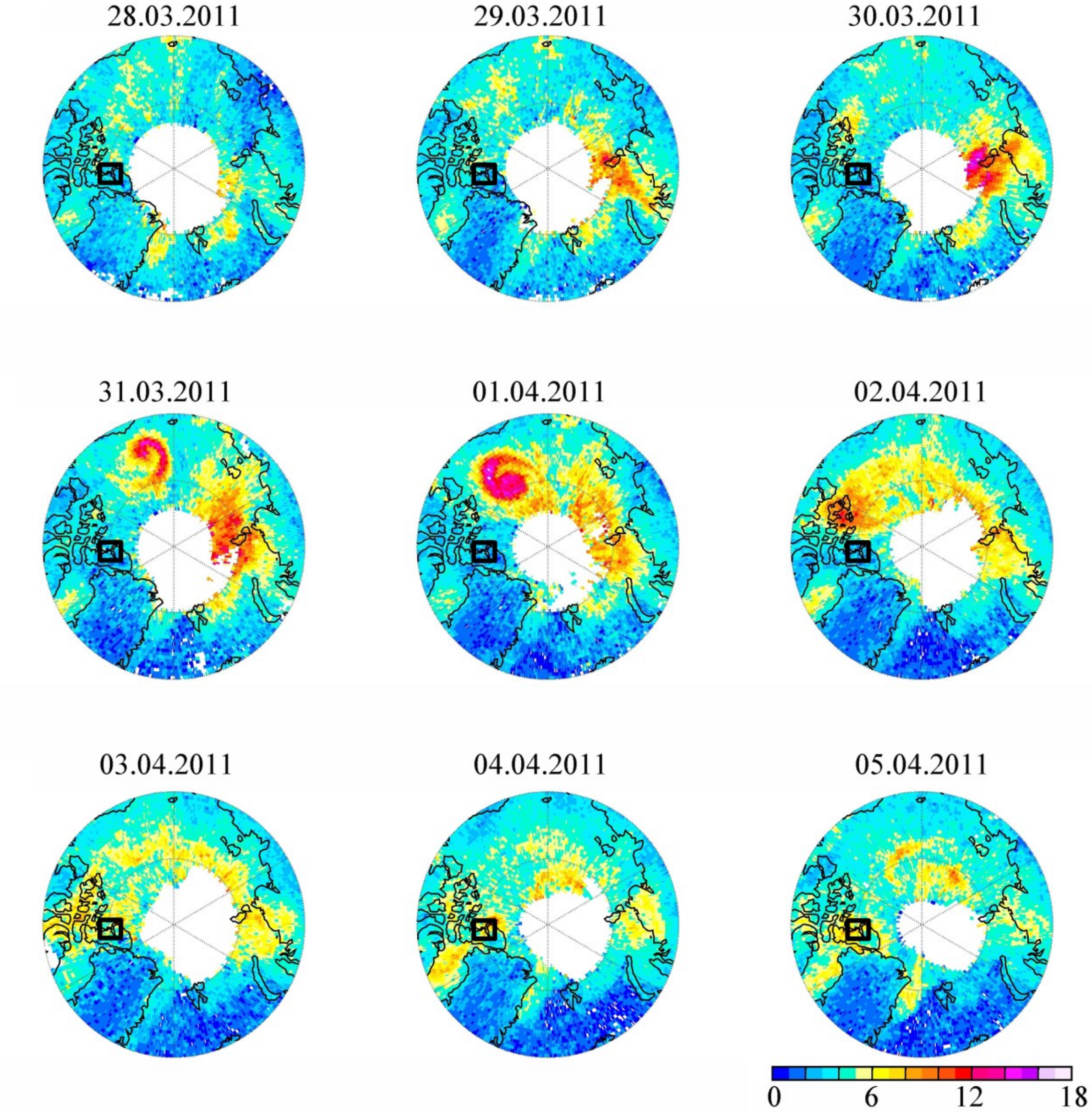

Figure 3.8: GOME-2 BrO VCD_{trop} ($\times 10^{13}$ molec cm^{-2}) north of 70°N from 28 March to 5 April 2011. The location of Eureka is indicated by the black square on each panel.

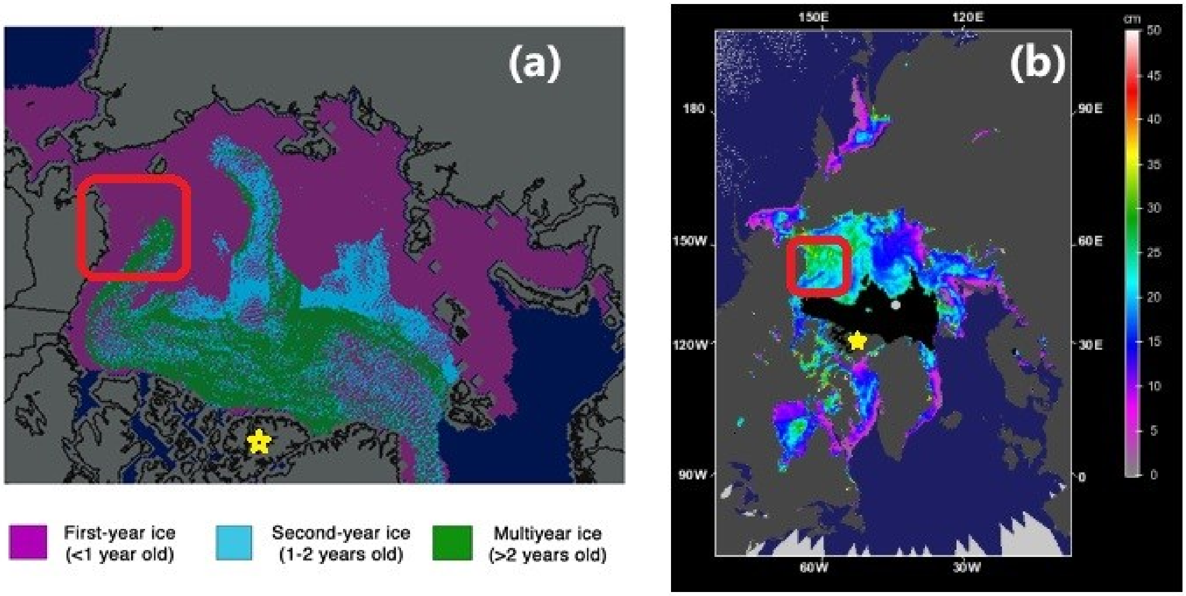

Figure 3.9: Sea-ice and snow information. Eureka is indicated by the yellow star in both figures and the Beaufort Sea is indicated by the red box. (a) Arctic sea-ice age during the third week of March 2011. Figure adapted from NSIDC (Image courtesy of J. Maslanik and C. Fowler, and the NSIDC, University of Colorado, Boulder). (b) AMSR-E on Aqua snow depth over ice data, averaged from 31 March to 4 April 2011. Note that the Beaufort Sea was covered by ~30 cm snow during this period. Figure adapted from NASA Distributed Active Archive Center at NSIDC (http://nsidc.org/data/amsre/data_summaries/index.html).

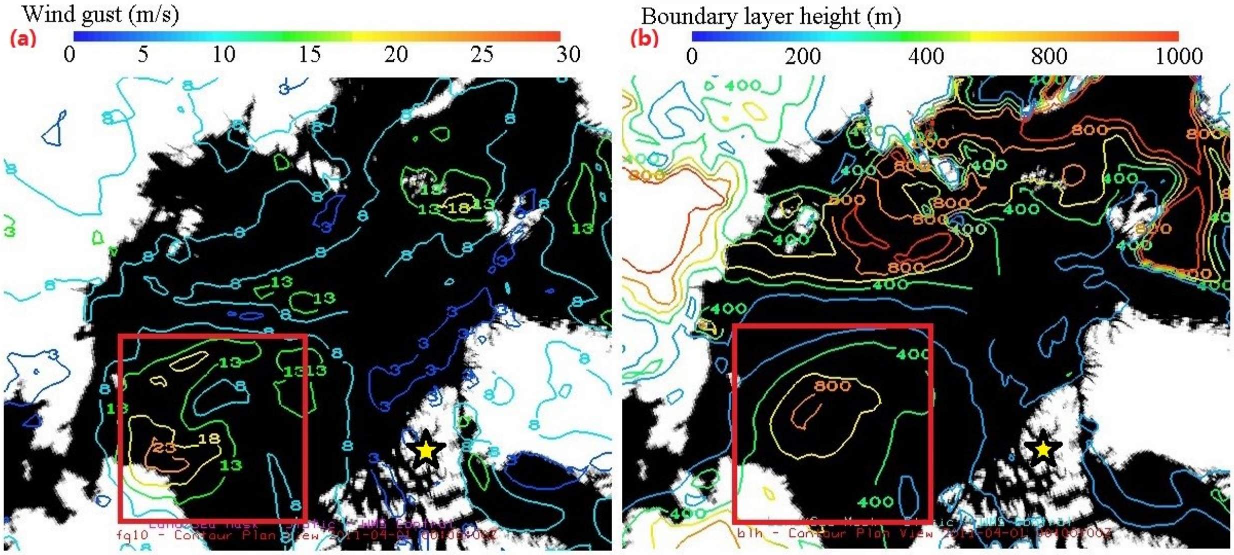

Figure 3.10: ERA-Interim data over the Beaufort Sea (indicated by the red box) for 00:00 UTC on 1 April 2011. (a) wind gust; (b) Boundary layer height. Eureka is indicated by the yellow star in both figures.

ERA-Interim data and radiosondes indicated that the tropopause height at Eureka decreased from ~8.5 km to ~7 km with the arrival of this low-pressure system. Low-pressure systems are known to contribute to the transport of BrO plumes over large distances (Begoin et al., 2010). Investigation of the cloud information (not shown here) from the Moderate Resolution Imaging Spectroradiometer (MODIS) were made. The cloud images show that the front arrived late on 3 April at Eureka, which is consistent with the MAX-DOAS and satellite BrO retrievals shown in Figure 3.6. MODIS images further indicate that the front either passed or dispersed during the following two days, while the measured tropospheric BrO levels were still high over Eureka.

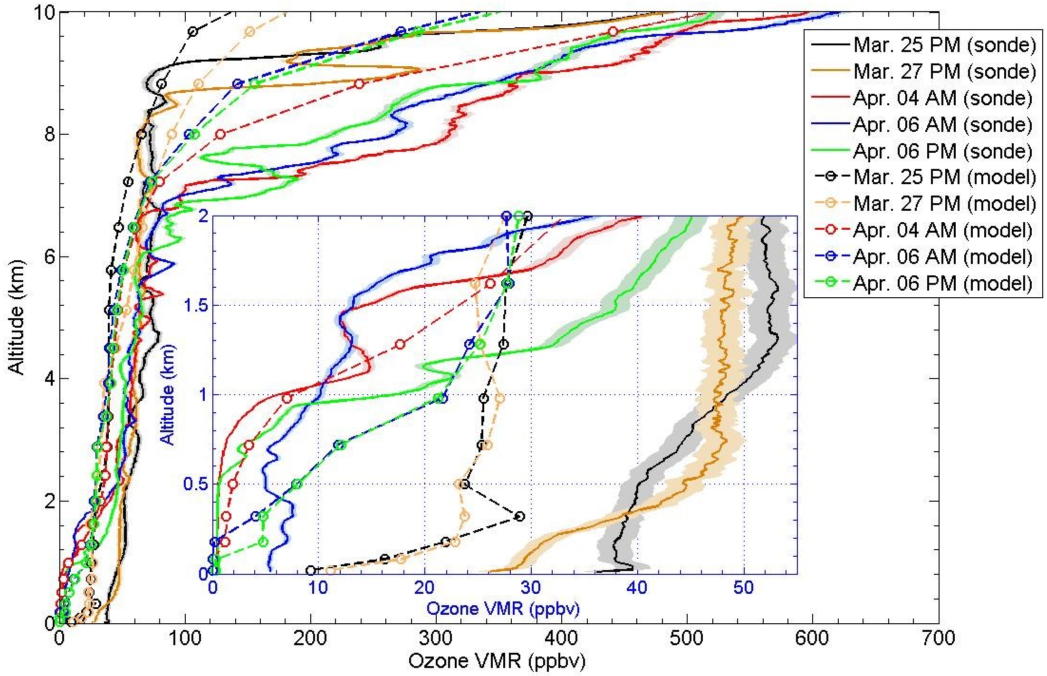

Figure 3.11: Tropospheric ozone profiles above Eureka (the inset panel shows 0-2 km). Solid lines (as indicated in the legend) show ozonesonde measurements on 25 March (23:15 UTC), 27 March (23:15 UTC), 4 April (6:52 UTC), and 6 April (3:42 and 20:00 UTC) 2011, the shaded regions represent the 1-sigma uncertainty envelope. The dashed lines with circles show the UM-UKCA modelled ozone profiles for 25 March (23:00 UTC), 27 March (23:00 UTC), 4 April (7:00 UTC), and 6 April (4:00 and 20:00 UTC) 2011.

During the days when the bromine plume was passing over Eureka, no evidence for the intrusion of stratospheric BrO into the free troposphere was found. As described in Section 3.2.2, the 4-8 km BrO partial column only contributed ~1-4% of the BrO VCD_{trop} during this time (comprised of *a priori* information). Ozonesonde profiles in Figure 3.11 show that stratospheric ozone

(ozone VMR > 100 ppbv) descended from ~8 km to ~7 km on 4 and 6 April, consistent with a small decrease in the tropopause height. The relative humidity profiles measured by radiosondes from 1-6 April also indicated no stratospheric intrusions (characterized by very low relative humidity) into the troposphere (Figure 3.12). Figure 3.12a and b shows that the temperature profiles were strongly inverted in the lowest ~500 m both before and after the bromine explosion event, but that the inversion weakened from 3-4 April when the wind speed increased (7 m s^{-1}). The high wind conditions favoured the destruction of the surface inversion layer over Eureka from 3-4 April, thus the boundary layer was not stable, consistent with the potential temperature profiles in Figure 3.12c and d. This reduction of atmospheric stability over Eureka is the result of the cyclone and its much higher wind speed (24 m s^{-1} over the Beaufort Sea), and was involved in the vertical distribution of the BrO plume from the surface to ~2 km altitude (details are discussed in Section 3.2.4.2). The role of wind speed and near-surface temperature in BrO vertical mixing is also reported by Peterson et al. (2015).

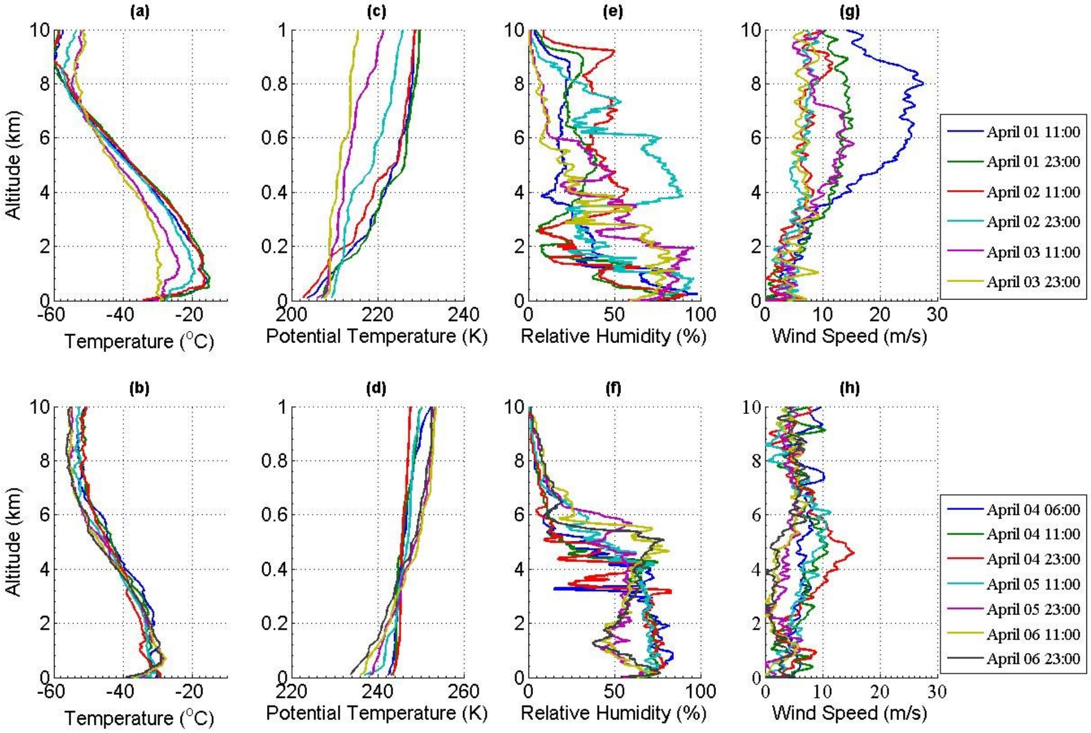

Figure 3.12: Eureka radiosonde data from 1 to 6 April 2011, with launch times (UTC) indicated in the legends. Upper panels: 1-3 April, lower panels: 4-6 April. (a) and (b) temperature; (c) and (d) potential temperature; (e) and (f) relative humidity; (g) and (h) wind speed. Note: Panel (c) and (d) shows altitude range from 0-1 km.

In summary, this bromine explosion event observed at Eureka during relatively low wind speeds was initiated by strong winds in a cyclone over the Beaufort Sea, and the transported bromine plume was subsequently coupled to local production/recycling over Eureka under stable shallow boundary layer conditions (this is further discussed in Section 3.2.4).

3.2.4 Comparison with a Chemistry-Climate Model

In this work, the nudged version of the UM-UKCA model was used, which was driven by ERA-Interim data. Figure 3.13 shows the modelled tropospheric BrO column over the Arctic region from 30 March to 6 April 2011. The model captured the bromine plume, which was generated over the Beaufort Sea on 30 March and also its propagation towards Eureka in the following days, although the maximum modelled BrO VCD_{trop} (~9×10^{13} molec cm^{-2}) over the Beaufort Sea was not as large as that observed by GOME-2 (~1.5×10^{14} molec cm^{-2}). In particular, the measured and modelled vertical profiles of BrO over Eureka have been compared for the first time, and despite the differences in timing and absolute concentrations, the general features of this bromine explosion are captured by the model, especially the height of both the BrO layer and the ozone-depleted layer.

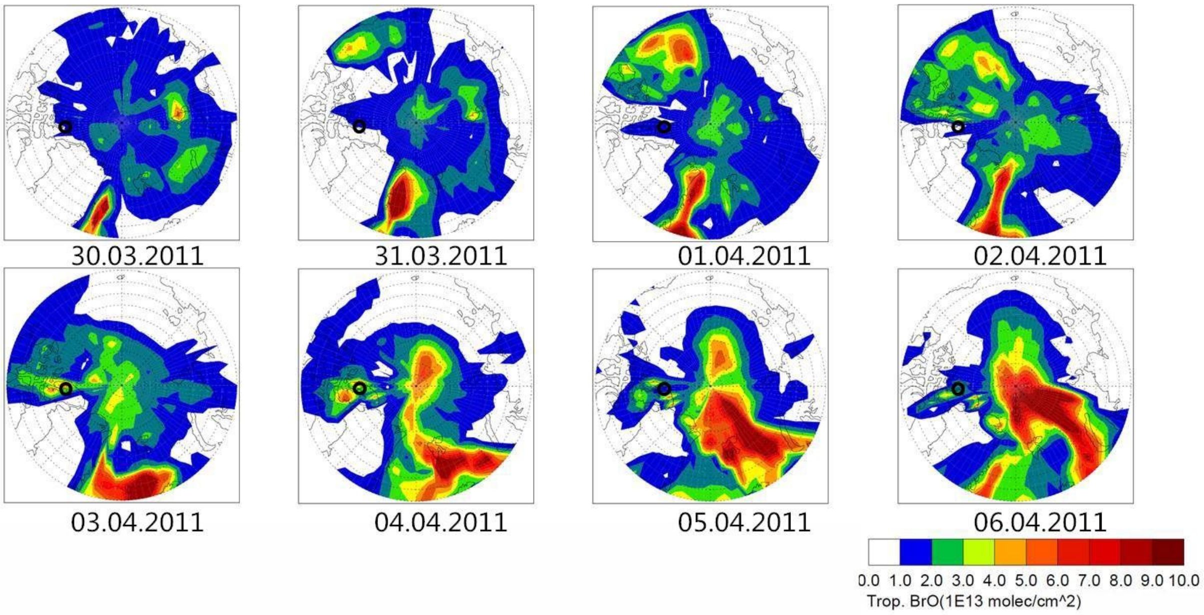

Figure 3.13: UM-UKCA modelled tropospheric BrO (daily maximum value) for north of 60°N from 30 March to 6 April 2011. The location of Eureka is indicated by the black circle on the panels.

3.2.4.1 Ozone Vertical Profile Comparison

To evaluate the model, the modelled ozone profiles with ozonesonde measurements were compared first. One strong surface ozone depletion event was found in both the observations and the model on 4-6 April 2011. Figure 3.11 shows the ozone profiles over Eureka from ozonesonde measurements and the UM-UKCA model.

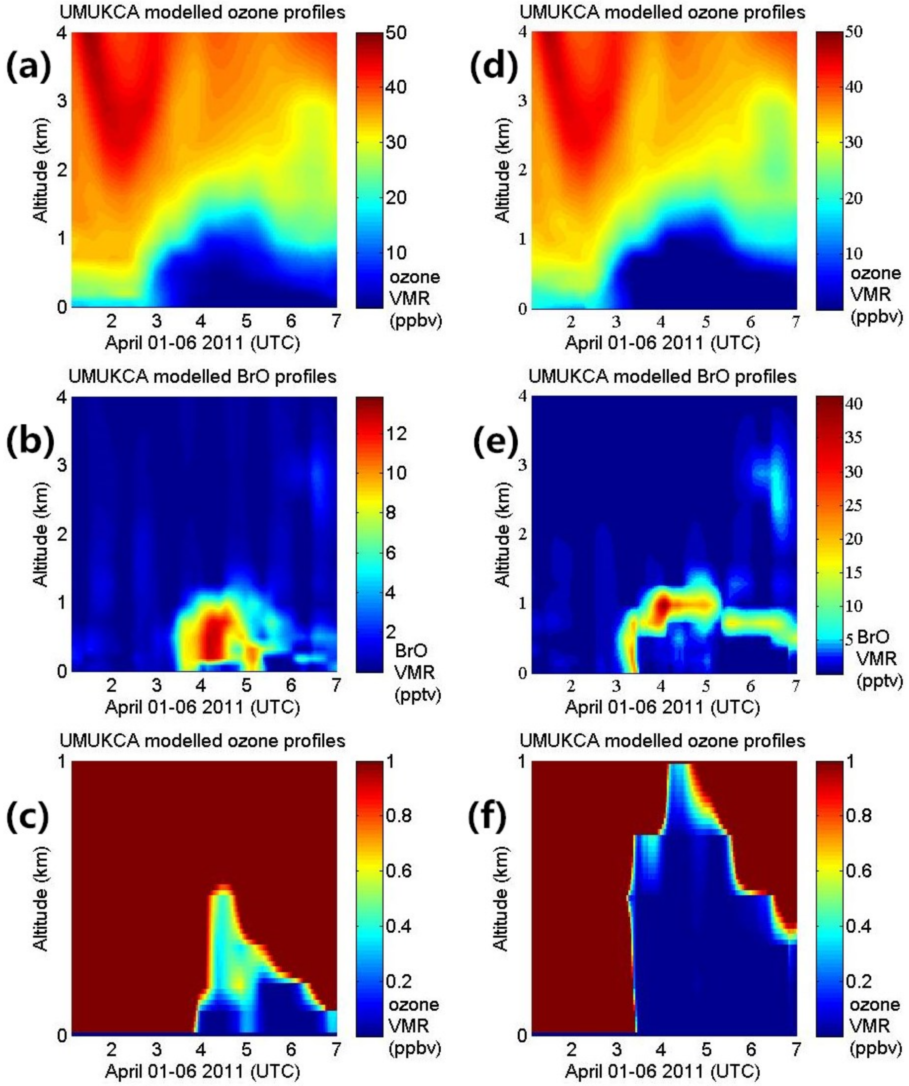

Figure 3.14: UM-UKCA modelled O_3 and BrO profiles for 1 to 6 April 2011 (UTC) over Eureka. The left column (panels a, b, and c) shows runs with a low bromine release flux, the right column (panels d, e, and f) shows runs with a high bromine release flux. (a) and (d) 0-4 km ozone profiles; (b) and (e) 0-4 km BrO profiles; (c) and (f) 0-1 km ozone profiles with 1 ppbv mask. Note: To show the detailed structure of the modelled bromine plume and ozone vertical structures, the colour scale for panel (e) is different from panel (b), and the altitude range for panels (c) and (f) is 0-1 km.

The model underestimates the boundary layer ozone over Eureka on 25 and 27 March before the ozone depletion event occurred. However, on 4 April, measured ozone was depleted to 0.5-1.3 ppbv from 10-720 m altitude at 6:52 AM UTC, and the modelled surface ozone VMR at 7:00 AM UTC also dropped to ~1 ppbv for the lowermost 400 m. The UM-UKCA model captured the whole bromine explosion event in this period with one-hour time resolution, revealing that the surface ozone depletion (Figure 3.14a) was associated with the surface bromine surge (Figure 3.14b). In the modelled ozone profiles shown in Figure 3.14a, the surface ozone depletion over Eureka starts during 3 April, and lasts for the next three days, which is consistent with the low surface ozone measured by ozonesondes on 4 and 6 April (see Figure 3.11).

3.2.4.2 BrO Vertical Profile Comparison

The tropospheric BrO profiles retrieved by applying the OEM to the MAX-DOAS data as described in Section 3.1.2 reveal that a bromine plume was over Eureka from late on 3 April to 5 April (see Figure 3.15a). The UM-UKCA model BrO is compared on the same colour scale in Figure 3.15b. The modelled BrO also shows an increase from 3 to 5 April with similar temporal and spatial structure to that of the measured plume. Figure 3.16 shows scatter plots of UM-UKCA model BrO partial columns (0-4 km) versus MAX-DOAS measurements. The MAX-DOAS data are hourly averages for the same time bins as the model. The model shows the best agreement with measurements on 4 April, with fitted slope = 0.84 and R = 0.75 (see Figure 3.16c). However, the modelled bromine explosion event started a half day earlier than seen in the observations (see Figure 3.15b). On 5 April, the modelled BrO decreased faster than the measurements; when the latter still showed ~20 pptv BrO VMR in the boundary layer, the model value dropped to ~5 pptv (see Figure 3.16d). However in general, the bromine explosion event initialized by blowing snow over the Beaufort Sea was captured by the UM-UKCA model.

Although UV-visible DOAS measurements are sensitive to the visibility and Frieß et al. (2011) reported that MAX-DOAS measurements could overestimate BrO concentration during low visibility events (surface aerosol extinction > 0.5 km^{-1}), this case study shows BrO enhancements under both clear (surface aerosol extinction ~ 0.1 km^{-1}) and low visibility (surface aerosol extinction ~0.6 km^{-1}) conditions (see Figure 3.4). Moreover, the comparison between the ground-based and GOME-2 satellite BrO VCD$_{trop}$ shows good consistency during those five days, giving confidence in the magnitude of the measured BrO. Taking all of these factors into consideration, the model clearly underestimated the BrO concentration.

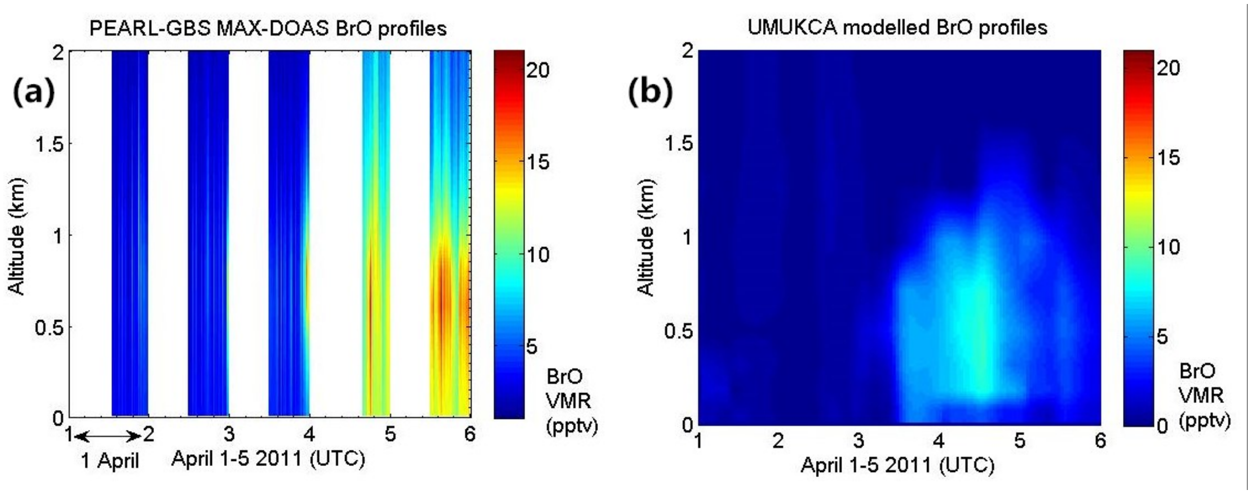

Figure 3.15: (a) MAX-DOAS tropospheric BrO profiles measured at Eureka; (b) UM-UKCA modelled tropospheric BrO profiles over Eureka on the same colour scale as (a). Note: the modelled BrO in Figure 3.15b is the same as in Figure 3.14b. Figure 3.15 highlights the lowest 2 km, and uses a different colour scale for comparison with the MAX-DOAS measurements.

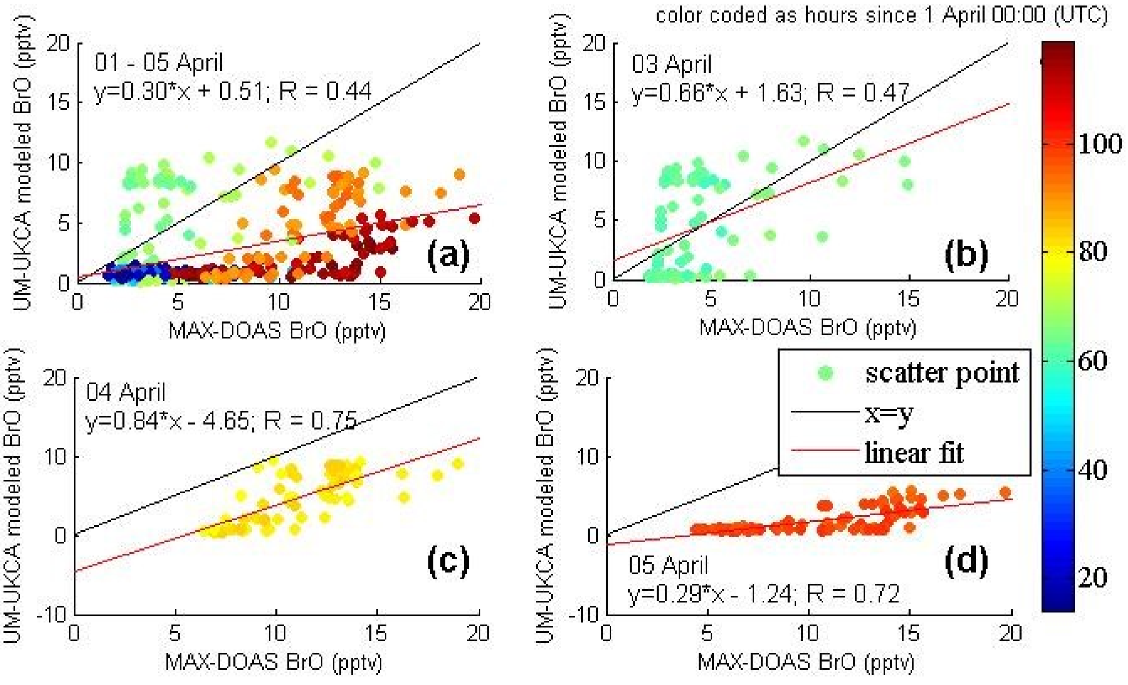

Figure 3.16: UM-UKCA modelled BrO partial columns (0-4 km) versus MAX-DOAS measurements at Eureka. All scatter points are colour coded by time, in hours since 1 April 00:00. Data are shown for: (a) 1 to 5 April (the complete data set), (b) 3 April, (c) 4 April, and (d) 5 April.

To investigate the difference between the model and measurements, a sensitivity experiment with two different calculations for bromine release fluxes in the UM-UKCA model was implemented (see Figure 3.14). The bromine release fluxes were calculated by a complex function of the sea-salt bromine depletion factor, wind speed at 10 m, air temperature, relative humidity, snow age, and snow salinity (Yang et al., 2008). In the high bromine release flux run, a larger sea-salt bromine depletion factor was selected, following Breider et al. (2010); and in the low bromine release flux run, a smaller sea-salt bromine depletion factor was selected, following Yang et al. (2008). These two factors were derived from the same field observations dataset compiled by Sander et al. (2003), and the difference was caused by the limited total number of samples in the dataset (the higher factor is the median value of the factors in the samples; the smaller factor is the mean value). The difference in the sea-salt depletion factors thus resulted in a difference in bromine release fluxes from sea salt by a factor of 2-3 in the source region (Yang et al., 2010).

In Figure 3.14, the modelled ozone and BrO profiles from 1-6 April 2011 are compared. As seen in the first row of the figure (Figure 3.14a and d), the ozone profiles look similar for these two model runs using low and high bromine fluxes. Unexpectedly, the model results using the high bromine flux run did not produce 2-3 times larger surface BrO VMR values compared to the low bromine flux run (see Figure 3.14b and e), but instead revealed an "uplift" of the very high value BrO plume (~30 pptv) in the upper boundary layer; and a reduction in BrO (< 5 pptv) below that height (~600 m) (see Figure 3.14e). In the high flux run, more bromine was initially introduced into the system, resulting in lower ozone concentrations, while the stable boundary layer limited the dynamical entrainment of ozone-rich air from aloft into the boundary layer. Thus BrO production through reaction R3 was lowest during these near-zero ozone concentrations in the boundary layer and caused the decreased surface BrO VMR (compared to the low bromine flux run), similar to another case observed in Barrow by Helmig et al. (2012). To show this more clearly, Figure 3.14c and Figure 3.14f show ozone profiles with a 1 ppbv mask applied.

The sensitivity experiment reveals that the surface ozone depletion is more severe in the high bromine release flux run than in the low flux run, while the surface BrO is a result of a complex combination of local photochemistry (related to the ozone as well as BrO production and loss) and boundary layer dynamics (for example, wind pumping over the snowpack, venting and mixing of chemical compounds through the boundary layer, and varying boundary layer height). The sensitivity experiment and ozonesonde data reveal that this bromine explosion event was accompanied by very low concentrations of ozone, which complicates the relationship between total reactive halogen production (BrO_x = Br + BrO) and BrO. For this reason, in the absence of more frequent ozonesonde measurements and/or more intensive modelling (high temepral and spatial resolution), it is difficult to achieve quantitative agreement between the BrO peak mixing ratio observed by MAX-DOAS and that modelled. The fastest loss of BrO is by photolysis, which varies diurnally, and when ozone is relatively high, the fastest loss of Br is via reaction R3. The break-even point where half of BrO_x is present as BrO is a few ppbv of ozone, and is also dependent on the photolysis rate J_{BrO}. Thus, at 1 ppbv O_3 or less, most of the reactive halogens are not BrO and the amount of BrO is highly sensitive to the actual O_3 level, which is only observed twice per day in this study. BrO is also sensitive to J_{BrO}, and the data in Figure 3.15 show morning and afternoon peaks of BrO with a near-noon dip on 4 and 5 April. That could be due to increased J_{BrO} near noon partitioning BrO_x away from BrO. In general, when ozone mixing ratios are high (a few pbbv), BrO is a robust indicator of halogen activation and is less dependent on the amount of ozone present. However, for the case observed here, with very little ozone, infrequent measurements, and varying solar illumination, it is difficult for the model to capture the measured BrO. The meteorology also plays an important role in the vertical distributions of BrO and ozone in the Arctic (Stutz et al., 2011; Peterson et al., 2015), creating an additional challenge for accurate modelling of BrO.

The differences between the model and measurements may also be due to several other factors. First, the horizontal sampling length of MAX-DOAS is dependent on wavelength and aerosol optical thickness, but its spatial coverage can be estimated based on simple geometric considerations. In this case study, the bromine layer extended to approximately 2 km and the lowest viewing elevation angle was 6°, and thus the MAX-DOAS effective spatial sampling was within 20 km (as discussed in Section 3.2). However, the model grid box near Eureka was about 72 km × 278 km (3.75° longitude × 2.5° latitude). So the model output was an average of the BrO VMR over a much larger area than either the ground-based or satellite (GOME- 2 footprint size was about 40 km × 80 km) measurements. Second, the UM-UKCA model's primary BrO source was mainly driven by wind speed, however, Figure 3.12 shows that 5 April was a calm day. In Figure 3.12, the Eureka radiosonde data reveal a breakdown of the surface temperature inversion from 3-4 April and also show a recovery of the surface temperature inversion and calm wind conditions from 5-6 April. The ERA-Interim data show that the daytime boundary layer heights at Eureka dropped from 450 m to 200 m throughout 4-6 April (not shown here). Thus during these calm conditions on 5-6 April, a stable shallow boundary layer (~200 m during daytime) formed. The combination of the transported bromine and favourable meteorological conditions near Eureka triggered local activation or recycling of bromine. This is supported by the prolonged lifetime of the bromine explosion in the observations (surface ozone depletion lasted to the end of 6 April, as observed by ozonesondes) compared to the model prediction on 5-6 April. Also, when the bromine plume entered the Canadian archipelago, the wind speeds decreased, which could cause increased sedimentation of saline aerosol on tundra snowpack, potentially enhancing the bromine regeneration scheme proposed by Pratt et al. (2013) and Toyota et al. (2014). However, none of these regeneration or recycling mechanisms are currently included in the chemical model. The modelled BrO has a clear diurnal cycle from 1 to 3 April. However this diurnal variation disappeared from 4 to 5 April due to the arrival of the bromine plume. The high nighttime BrO VMR on 4 and 5 April was the result of transport.

In general, the model was able to simulate this bromine explosion event initiated by blowing snow and subsequently subjected to long-range transport. The differences between the model and measurements indicate that this event was not a simple case of transportation of a bromine plume, but was a combination of transportation and two different local recycling mechanisms for bromine. The first recycling mechanism involves airborne saline aerosol on low visibility days (which explains the high BrO VMR measurements relative to the modeled BrO on 3-4 April), and the second one involves shallow stable boundary layer conditions over surface snow or sea-ice on calm clear days (which explains the prolonged lifetime of the bromine explosion event in the observations compared to the model on 5 April). This work supports the idea of Jones et al. (2009) that two sets of environmental conditions favour ODEs: high wind/blowing snow and low wind/stable boundary layer. Furthermore, this work demonstrates that both blowing snow and stable boundary layer mechanisms should be included in halogen-related chemistry-climate models.

3.2.5 Bromine and Ozone along the Trajectories

Additional backward trajectories (Figure 3.17) were simulated with an ending time of 12:00 UTC on 4 April (12 hours later than those shown in Figure 3.7, which were used to simulate the arrival of the bromine plume).

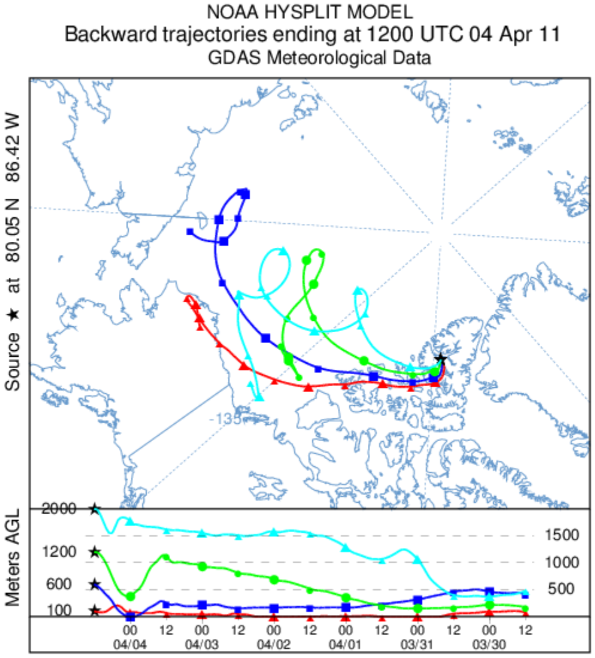

Figure 3.17: HYSPLIT six-day back-trajectories for Eureka (80.05°N, 86.42°W), ending at 12:00 UTC on 4 April 2011.

The UM-UKCA model shows the highest BrO VMR near 12:00 UTC. The modelled BrO and ozone VMR values from the high bromine release flux run were extracted and plotted on top of the trajectories as shown in Figure 3.18. High BrO VMR (>12 pptv) along the 100 and 600 m trajectories can be seen in Figure 3.18 (a, c). However, the BrO VMR decreased to less than 2 pptv before the plume arrived at Eureka. The ozone VMR along the 100 and 600 m trajectories is consistently low (in the 1-2 ppbv range) from the Beaufort Sea to Eureka. The ozone VMR along the 2000 m trajectory is around 30 ppbv (close the normal background value) indicating that the bromine plume was transported below this altitude. Figure 3.19 shows the time series of modelled BrO and ozone VMRs along the trajectories, along with the local sunlight conditions as represented by the local SZA (in cloud-free condition, SZA is negatively correlated with sunlight intensity). For example, the decreased BrO VMR at point A in Figure 3.19a is due to extreme low-ozone condition (< 1 ppbv); the decreased BrO VMR at point B is due to both extreme low-ozone and lack of sunlight (SZA > 90°). The high BrO VMR at point C is coincident with sunrise and sufficient ozone (although depleted, but > 1 ppbv). The strong anti-correlation of ozone and BrO VMRs is seen at point D.

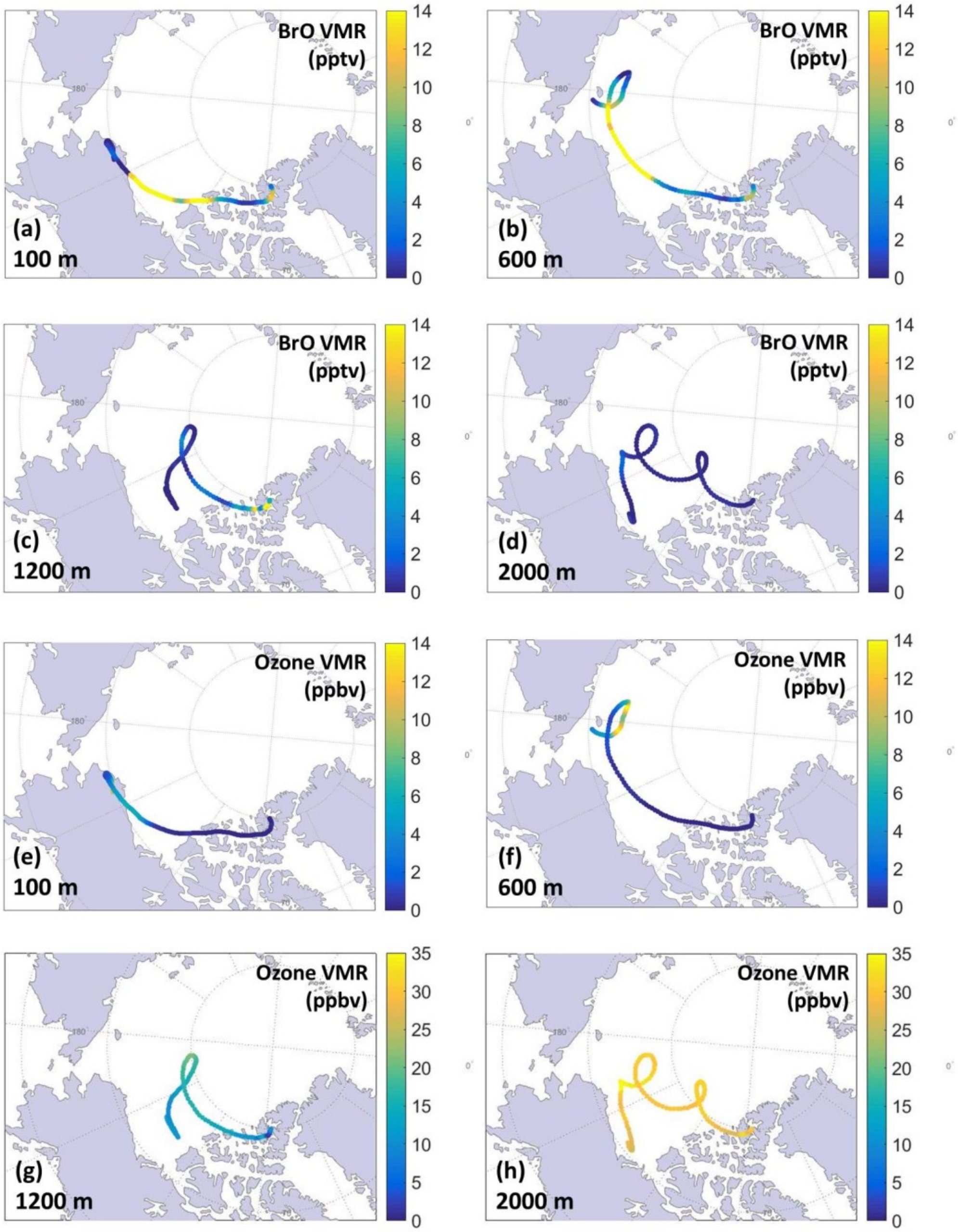

Figure 3.18: UM-UKCA modelled BrO (panel a-d) and ozone (panel e-h) VMR along the HYSPLIT trajectories shown in Figure 3.17. These BrO and ozone values are from the model run with high bromine release flux.

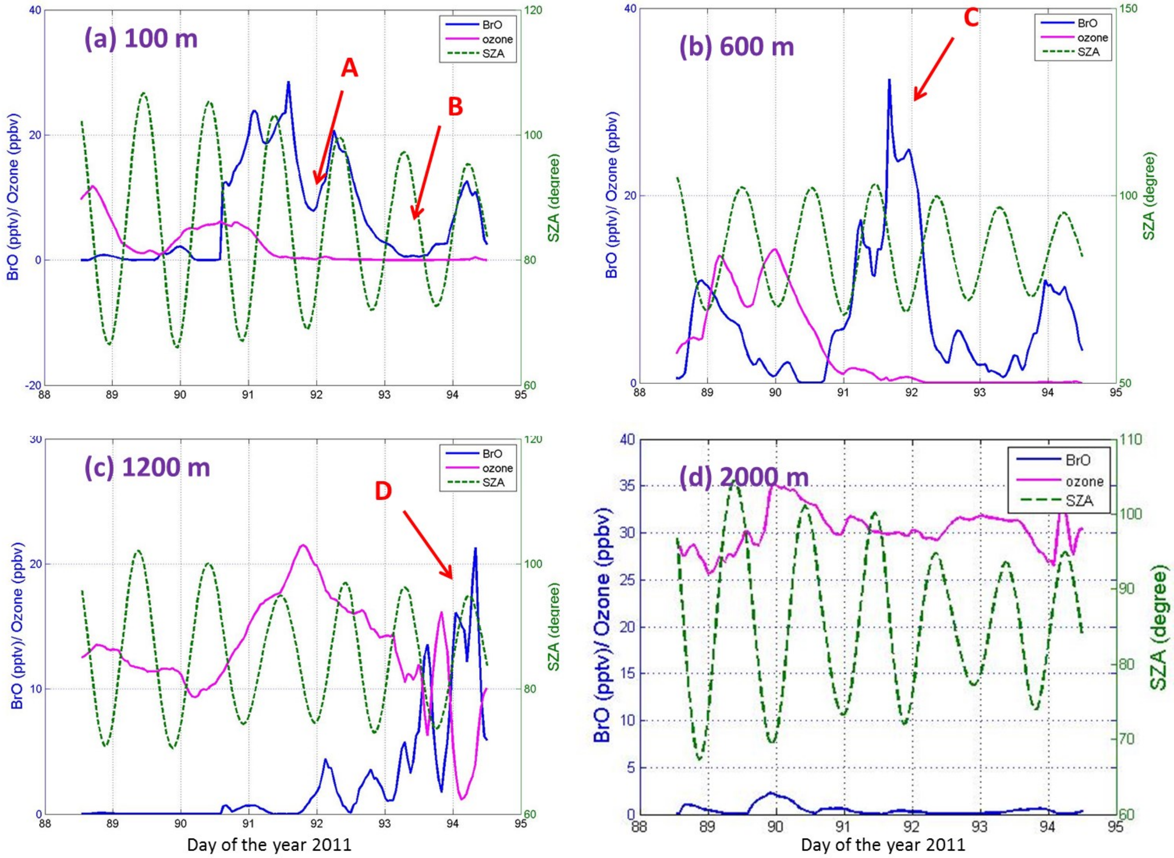

Figure 3.19: UM-UKCA modelled BrO and ozone VMR (left y-axis, BrO in pptv or ozone in ppbv) and solar zenith angle (SZA, right y-axis) along the HYSPLIT trajectories shown in Figure 3.17 at (a) 100 m, (b) 600 m, (c) 1200 m, and (d) 2000 m. These BrO and ozone values are from the model run with high bromine release flux.

A similar back-trajectory analysis was made for the low bromine release flux run as shown in Figure 3.20 and Figure 3.21.The general pattern of Figure 3.20 is similar to Figure 3.18, however the time series (Figure 3.21) reveals the differences between these two runs. For example, the BrO VMR at point A on Figure 3.21a is larger than the counterpart point on Figure 3.19a. This result is likely due to the non-depleted ozone in the low bromine release flux run. Another difference in the low bromine release flux run is seen for the point B on Figure 3.21b, which has the highest BrO VMR (near 50 pptv), while the counterpart point on Figure 3.19b has less than 35 pptv. In general, these simulations confirm that the tropospheric BrO concentration is a result of a complex combination of local photochemistry related to ozone concentrations as well as sunlight conditions.

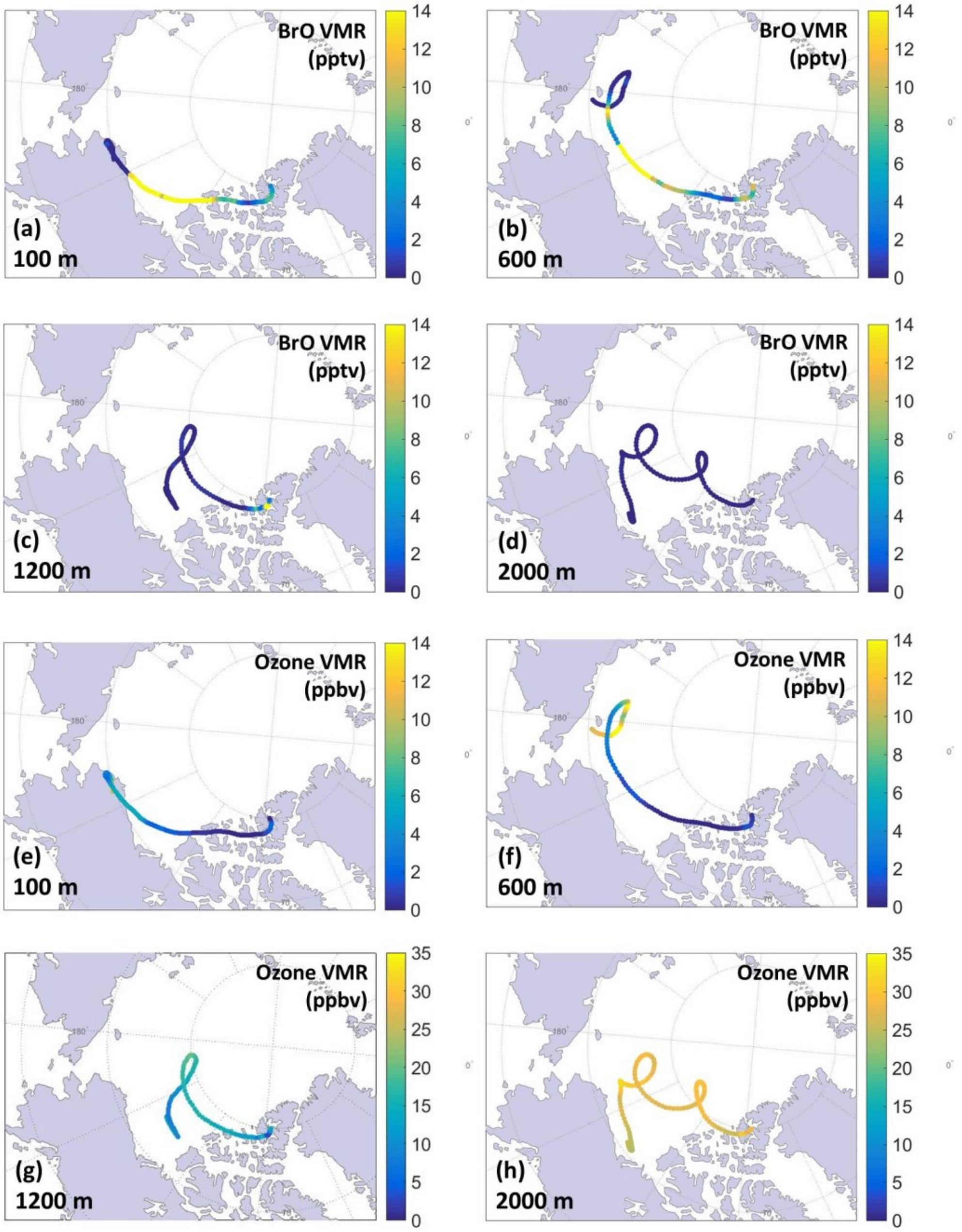

Figure 3.20: UM-UKCA modelled BrO (panel a-d) and ozone (panel e-h) VMR along the HYSPLIT trajectories shown in Figure 3.17. These BrO and ozone values are from the model run with low bromine release flux.

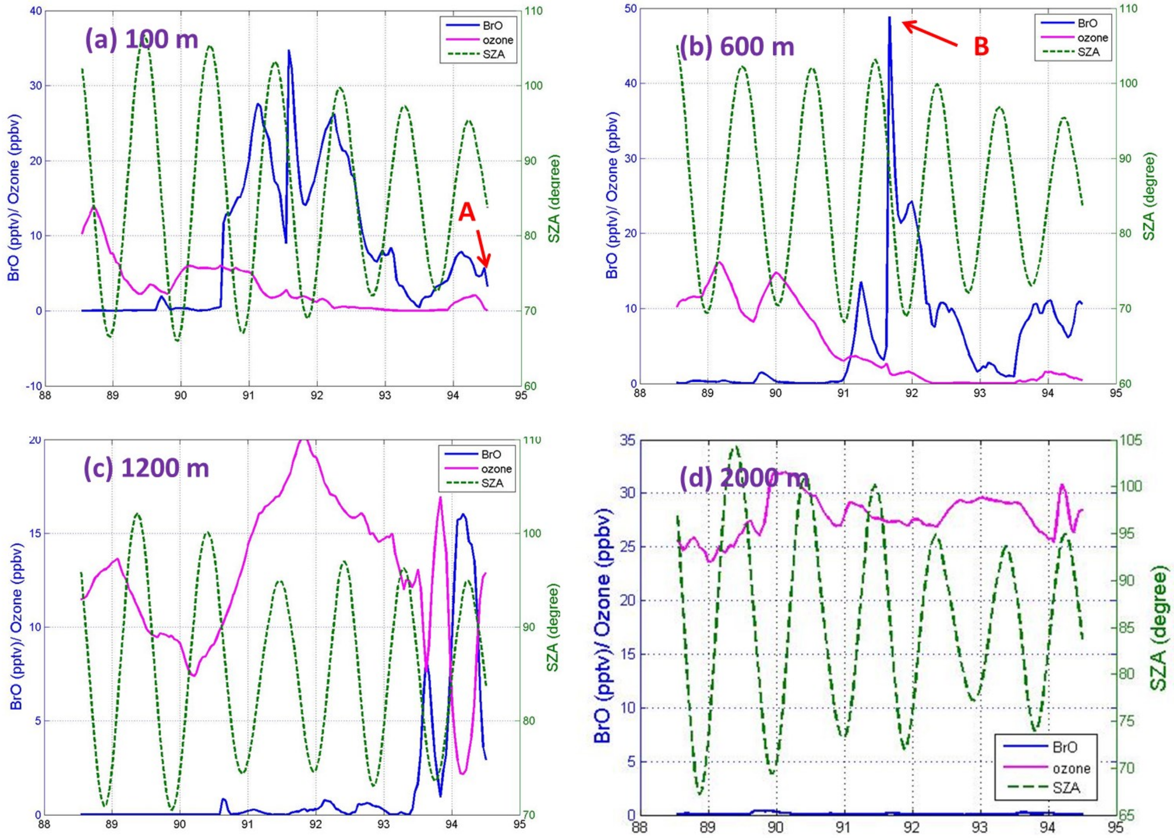

Figure 3.21: UM-UKCA modelled BrO and ozone VMR (left y-axis, BrO in pptv or ozone in ppbv) and solar zenith angle (SZA, right y-axis) along the HYSPLIT trajectories show in Figure 3.17 at (a) 100 m, (b) 600 m, (c) 1200 m, and (d) 2000 m. These BrO and ozone values are from model run with low bromine release flux.

3.3 Summary

This chapter presented a bromine explosion event observed from 3 to 5 April 2011 at Eureka by ground-based and satellite instruments. This event involved transportation of a bromine plume ~1800 km from the Beaufort Sea over three days with evidence of "unusual" (not a stable shallow boundary layer) meteorological conditions at the bromine source. During the initial formation of the bromine explosion, a strong cyclone developed over the Beaufort Sea, and the boundary layer height increased to three times its background level. Tropospheric and stratospheric BrO profiles and partial column densities at Eureka were retrieved from ground-based MAX-DOAS and ZS-DOAS data. The DOAS BrO profiles, ozonesonde data, and radiosonde data reveal no evidence of a stratospheric intrusion over Eureka during the event. MAX-DOAS aerosol extinction profiles and MMCR reflectivity data indicate that this bromine explosion event was observed at Eureka during both blowing snow and clear weather conditions. The MAX-DOAS tropospheric partial columns show good consistency with GOME-2 satellite data.

The UM-UKCA chemistry-climate model successfully reproduced some of the main features (such as the vertical structure of the bromine plume) of this bromine explosion event after including a bromine source from blowing snow related to sea-salt production. The modelled ozone profiles on 4 and 6 April 2011 are consistent with ozonesonde data. Comparison between the model and measurements indicates that surface BrO is not only controlled by photochemistry, but also by local dynamics, which also influence ozone through vertical mixing, indicating the difficulties in simulating BrO concentrations. Further study of local meteorological conditions reveals that the boundary layer stability could have a significant effect on the surface BrO; a stable boundary layer may increase the likelihood of trapping a transported bromine plume and triggering local bromine release from the snowpack within the boundary layer, thus prolonging the duration of bromine explosion events, a process which is not currently included in chemical-climate models. This combination of observations and modelling confirms that both high wind/blowing snow and low wind/stable boundary layer are favourable environmental conditions for bromine explosion events, and in some cases, the combination of these two conditions will affect the lifetime of a bromine explosion event.

Chapter 4

4 Cyclone-Induced Surface Ozone and HDO Depletion

Following the work in Chapter 3, by using multiple ground-based and satellite datasets, two similar cyclone-induced induced surface ozone depletion events in Eureka were identified on March 2007 and April 2011. These two events were coincident with observations of HDO depletion, indicating that condensation and sublimation occurred during the transportation of the ozone-depleted airmass. Lidar and radar measured ice cloud (vapour and ice crystals) and aerosol when the ozone- and HDO-depleted airmass arrived over Eureka. For the 2007 event, an ice cloud layer was coincident with an aloft ozone depletion layer at 870 m height. The following shallow surface ODE after the ice precipitation is likely due to the deposition of bromine-enriched particles onto the local snow pack. A global chemistry climate model and a global chemistry transport model were used to simulate the surface ozone depletion events. By implementing the latest surface snow salinity data that was collected in the Weddell Sea, the performance of the models improved. MERRA-2 global reanalysis model data and the FLEXPART particle dispersion model were used to study the link between the ozone and HDO depletion.

4.1 Datasets

In this study, ground-based, satellite, and model datasets were combined to produce a comprehensive picture of two ODEs. Ground-based UV-visible and infrared measurements were used to provide ozone column and δD respectively above Eureka. Ozone profiles measured by ozonesondes were used to identify surface ODEs. Lidar and radar data were used to identify the ice cloud and sea-salt particles. Satellite images from the MODIS were used to identify the location of the cyclone.

4.1.1 Ozone Measurements

Brewer spectrophotometers measure TCO using direct sunlight at four UV wavelengths (Kerr et al., 1981; Fioletov et al., 2005). The Brewer instrument is the WMO/GAW standard for total column ozone measurement (Kerr et al., 1981; 1988). Four Brewers have been deployed at the

Eureka Weather Station (EWS) by ECCC. Brewer no. 69 is an MKV single spectrophotometer (Adams et al., 2012b) located on the roof of the EWS main building. It was installed in 2004 and has recorded the longest Brewer dataset at Eureka. The current work uses TCO data from Brewer no. 69 analysed using the standard Brewer network operational algorithm (Kerr, 2002), with small changes to the analysis parameters due to the high latitude of the site. Normally, high-quality Brewer TCO data need an ozone AMF less than 3 (Fioletov et al., 2000; Zhao et al., 2016b). However, to cope with the low sun condition in the high-latitude spring, following Adams et al. (2012b), the ozone AMF threshold was increased to 5, which is acceptable under low ozone conditions and allows for more days with good data in the early spring. The uncertainty in Brewer TCO measurements is typically less than 1% (Fioletov et al., 2005), and for high-quality data (eg., AMF < 3) it is less than 0.6% (Zhao et al., 2016b).

The EWS has records of ECC ozonesonde measurements since 1992 (Tarasick et al., 2016). Ozonesondes are launched from the EWS weekly year-round and daily during the intensive phase of the Canadian Arctic ACE/OSIRIS Validation Campaigns (2004-2016) (Kerzenmacher et al., 2005; Adams et al., 2012b). The well-calibrated ECC ozonesondes have 3-5% precision for total column and ~5-6% uncertainty for the 0-4 km ozone profile (Tarasick et al., 2016). The Brewer and ozonesonde datasets from 2006 to 2014 were used in this study.

4.1.2 Water Vapour and HDO Measurements

The CANDAC Bruker IFS 125HR is a FTIR that is part of NDACC. The Bruker 125HR was deployed at the PEARL Ridge Lab in 2006 (Batchelor et al., 2009). The Bruker 125HR provides measurements of multiple trace gases and water vapour (including H_2O and isotopologues $H_2^{16}O$, $H_2^{18}O$, and $HD^{16}O$) (Barthlott et al., 2017; Weaver et al., 2017). The tropospheric H_2O and HDO used in the current study were generated as part of the MUSICA (MUlti-platform remote Sensing of Isotopologues for investigating the Cycle of Atmospheric water) project (Schneider et al., 2016) and were used to calculate the δD values (see Section 1.2 Eq. 1.1). Schneider et al. (2016) reported the accuracy of the MUSICA δD product to be about 10‰.

To further interpret the paired H_2O-HDO observations, a method developed by Noone (2012) was adapted, which uses the change in δD relative to change in water vapour mixing ratio to provide information about condensation, precipitation, and mixing process in the atmosphere. In general, the method is based on Rayleigh isotope fractioning model (Rayleigh and Ramsay, 1894; Jouzel and Merlivat, 1984)

$$\frac{d\delta}{1+\delta} = (\alpha - 1)\frac{dq}{q} \ , \tag{2}$$

where α is the equilibrium isotopic fractionation coefficient, which depends on the temperature of the air parcel (Merlivat and Nief, 1967), and q is the water vapour mixing ratio of the airmass. The Rayleigh model can be applied to both liquid and solid phase formation. The basic assumption of the Rayleigh model is that the condensed phase is formed at isotopic equilibrium with the surrounding vapour and is immediately removed from the airmass after its formation. This is because droplets can be isotopically modified when evaporation occurs (Ehhalt et al., 1963; Stewart, 1975; Jouzel and Merlivat, 1984; Rozanski et al., 1992; Noone, 2012). The Rayleigh model also assumes that during the formation of ice crystals, there is neither isotopic exchange with the surrounding vapour nor isotopic modification of the ice crystals during their subsequent fallout to the ground (Jouzel and Merlivat, 1984). The additional kinetic fractionation effect (Jouzel and Merlivat, 1984; Noone et al., 2013) of ice clouds formed in supersaturation conditions is not applicable for the present study (see Section 4.3).

MUSICA water vapour isotopologue remote sensing data have two data types (Barthlott et al., 2017). The type-1 data is best suited for tropospheric water vapour distribution studies that disregard isotopologues (e.g., comparison with radiosonde data, analyses of water vapour variability and trends, etc.). The type-2 data is designed for analysing moisture pathways by means of H_2O-δD pair distributions. Thus the Bruker 125HR/MUSICA water vapour isotopologue type-2 data from 2006 to 2014 were used in the present study. Similar to the Brewer TCO dataset, the SZA filter of the water vapour isotopologue dataset has also been relaxed to expand the temporal coverage of dataset for these High Arctic conditions.

4.1.3 Cloud and Aerosol Measurements

MODIS on board the NASA Terra-1 satellite measures visible and thermal electromagnetic radiation. In this work, false colour images constructed using bands 2, 3, and 31 are used to identify cyclonic polar low systems (http://modis.gsfc.nasa.gov). The Arctic High Spectral Resolution Lidar (AHSRL) and MMCR measurements were used to provide cloud and aerosol information. The AHSRL and MMCR were located at the Zero Altitude PEARL Auxilary Laboratory (0PAL), which is located at the northwest corner of the EWS site. The AHSRL was developed at the University of Wisconsin and deployed at Eureka from August 2005 to 2010. It has a frequency-doubled diode-pumped Nd:YAG laser at 532 nm (Bourdages et al., 2009), and measures the particle backscatter cross-section (β_{lidar}) and circular depolarization ratio, which can be used to differentiate between spherical liquid droplets and crystalline particles. The MMCR (Shupe et al., 2010) has been deployed at Eureka since 2005. MMCR measures Doppler velocity, Doppler spectra, spectral width, and equivalent radar reflectivity for clouds, from which the particle backscatter cross-section (β_{radar}) can be determined (Bourdages et al., 2009). Bourdages et al. (2009) proposed a method to categorise atmospheric particles and their mixtures by combining information from the lidar and radar measurements. They calculated a colour ratio defined as the ratio between the radar and lidar backscatter cross-sections

$$R_{colour} = \frac{\beta_{radar}}{\beta_{lidar}} \quad . \tag{3}$$

The colour ratio is an average property for particles in a measurement volume, and is a good proxy for particle size (Bourdages et al., 2009). The MMCR measures reflectivity from 90 m to 20 km in altitude, and is sensitive to volume backscatter cross-sections greater than 10^{-14} m^{-1} sr^{-1}. Following Bourdages et al. (2009), an interpretation in terms of particle size is possible for the colour ratio in the range of 10^{-9} to 10^{-3}, which corresponds to a particle size of about 10 to 150 μm. This cloud ratio method cannot provide particle size information for fine and medium aerosol particles (radius less than 10 μm), but aerosol layers can be distinguished by β_{lidar} smaller than 2×10^{-5} m^{-1} sr^{-1}. In the present work, this colour ratio method was adapted to distinguish between aerosols, ice clouds, and ice crystals.

4.2 Models

4.2.1 MERRA-2

The second Modern-Era Retrospective analysis for Research and Applications (MERRA-2) is a NASA atmospheric reanalysis that begins in 1980. It replaces the original MERRA reanalysis (Rienecker et al., 2011) using an upgraded version of the Goddard Earth Observing System Model, Version 5 (GEOS-5) data assimilation system (Bosilovich et al., 2015; Fujiwara et al., 2017). MERRA-2 has a horizontal resolution of 0.625° in longitude and 0.5° in latitude. In the present work, vertical profiles of MERRA-2 ozone, temperature, pressure, and scaled potential vorticity (sPV, potential vorticity scaled in "vorticity units" to give a similar range of values at each level) (Dunkerton and Delisi, 1986; Manney et al., 1994; Adams et al., 2013) over Eureka were used. The profile data are on 72 model layers with 3-hour temporal resolution.

4.2.2 pTOMCAT

The Cambridge Parallelised-Tropospheric Offline Model of Chemistry and Transport (pTOMCAT) is a global 3-D chemistry transport model (CTM) (O'Connor et al., 2005; Yang et al., 2005). The forcing files for pTOMCAT are 6-hourly ERA-Interim data from ECMWF. Monthly sea-ice coverage and sea surface temperatures are taken from the Hadley Centre Sea Ice and Sea Surface Temperature (HadISST) dataset (Rayner et al., 2003). The model's horizontal resolution is 2.8° × 2.8° (longitude × latitude) with 31 vertical layers from the surface to about 10 hPa at the top layer.

A detailed process-based SSA scheme has been implemented in the model (Levine et al., 2014) based on the work of Reader and McFarlane (2003). Since the Levine et al. (2014) work, some updates have been introduced to the model, including improved precipitation, dry deposition velocities on snow for inorganic bromine species, and reduced snow salinity applied to the blowing snow (Legrand et al., 2016). Both open-ocean sourced and sea-ice sourced SSA (OO-SSA and SI-SSA) are tagged in order to track their history. Both OO-SSA and SI-SSA are in 21 size bins covering the range of 0.1-10 μm in dry radius (Rhodes et al., 2017). To study the transport of the SSA in the present work, SI-SSA with dry radius at 0.25, 1, and 5 μm were used in the comparison with another particle dispersion model.

The tropospheric bromine chemistry scheme in pTOMCAT is based on the work of Yang et al. (2005; 2010). The bromine source includes inorganic sea-salt from both the open ocean and the sea-ice zone (from blowing snow, Yang et al., 2008), and halocarbons from long-lived (e.g. CH_3Br) and very short-lived substances (VSLSs, e.g. $CHBr_3$ and CH_2Br_2) based on Warwick et al. (2006). Heterogeneous reactions that reactivate inactive inorganic bromine species (such as HBr) to active Br radicals, on both atmospheric background particles (offline data taken from (Heintzenberg et al., 2000)) and on the SSA produced from sea spray and blowing snow (online calculated) have been included in this model integration. In general, the calculation of the bromine flux depends on the rate at which snow particles are lifted from the surface and subsequent sublimation (which depends on wind speed, temperature, relative humidity, and the age of snow) and the rate of bromine release from the suspended SSA (based on observed bromine depletion factors, snow salinity, etc.) (Yang et al., 2010). More details about the calculation of bromine release flux from blowing snow can be found in Zhao et al. (Zhao et al., 2016a). The current work uses the transported SI-SSA information from pTOMCAT to make a direct comparison with ground-based measurements.

4.2.3 UM-UKCA

The United Kingdom Chemistry and Aerosols (UKCA) model is a global chemistry-climate model (CCM); its dynamical core is the Met Office Unified Model (UM) version 7.3 running in the HadGEM3-A configuration (Morgenstern et al., 2009). Details about the UM-UKCA have been described in Section 3.1.3. The UM-UKCA-CheST version contains a comprehensive stratospheric chemistry scheme as well as a detailed tropospheric chemistry scheme, including isoprene chemistry (this UM-UKCA-CheST version model will be referred as UKCA to simply). The model's horizontal resolution is 3.75° × 2.5° with 60 vertical layers from the surface to about 84 km. A nudged UKCA version (forcing by ERA-Interim, the same meteorological fields as pTOMCAT) is used in this study. Tropospheric bromine chemistry was introduced to UKCA based on the work in pTOMCAT (Yang et al., 2005; Yang et al., 2010). In general, UKCA and pTOMCAT share the same SSA production flux from the same particle size bins (and thus have same bromine release flux). However, unlike pTOMCAT, UKCA does not trace the SSA transport after the emission, therefore no online SSA is taken into account in the heterogeneous rate calculation (only a monthly climatology aerosol dataset from the CLASSIC aerosol scheme was used (Johnson et al., 2010)). In terms of dynamics, the UM model is much different to the atmosphere-only pTOMCAT in many aspects, for example, from boundary layer vertical mixing scheme to the cloud parameterisation, see more details in Russo et al. (2011) and Ruti et al. (2011).

The UKCA model successfully simulated the 2011 blowing-snow-induced ODE for previous study as shown in Section 3.2.4.2 (Zhao et al., 2016a). The difference between the model simulations in Chapter 3 and those in Chapter 4 is mainly snow salinity, as this parameter has recently been updated in the latter based on samples collected in the Weddell Sea (Legrand et al., 2016). The new surface snow salinity (top 10 cm snow layer, about 0.3 practical salinity unit) in the present work is only one tenth of the value that was used in Zhao et al. (2016a), which was the column mean salinity (Sander et al., 2003; Yang et al., 2008).

4.2.4 FLEXPART

The Lagrangian FLEXible PARTicle dispersion model (FLEXPART) was first released in 1998 for calculating the long-range and mesoscale dispersion of air pollutants from point sources. It has been used to examine source regions for aircraft, satellite, ground-based station, and ship-based studies e.g., (Stohl et al., 2005; Begoin et al., 2010; Gilman et al., 2010; Blechschmidt et al., 2016; Lutsch et al., 2016). In the present work, FLEXPART is run backwards in time for a group of passive SSA tracers that are transported by winds from 0.5° × 0.5° resolution NCEP Climate Forecast System Version 2 (CFSv2) 6-hourly products (http://rda.ucar.edu/datasets/ds094.0/). To compare with pTOMCAT modelled SSA, three different-sized SSA tracers (0.25, 1, and 5 μm) were used in the simulation, and released them at Eureka on two different grids. One grid was 0.4° × 0.4° (longitude × latitude, ~20 km × 20 km) and had Eureka at the centre of the grid, and the other grid 2.8° × 2.8° (~56 km × 310 km) was selected to match one of the pTOMCAT grids that includes Eureka.

4.3 Results

4.3.1 Surface Ozone Depletion

In the atmosphere, most ozone (~90%) is in the stratosphere. Thus the TCO is a function of tropopause height, with a low tropopause generally increasing the TCO. In contrast, H_2O and HDO are most abundant in the troposphere, thus δD is also a function of tropopause height, with a low tropopause generally decreasing the δD. TCO, tropopause height, and δD can be combined in a 3-D scatter plot that contains dynamical and chemical information. Figure 4.1a shows the 3-D scatter plot generated by merging nine years of Brewer TCO, MERRA-2 tropopause height, and Bruker 125HR δD. The data points are colour coded by precipitable water vapour (PWV) amount (measured by the Bruker 125HR). The 3-D scatter plot reveals the general linear relation between each pair of the three variables as discussed in above. The low δD outliers marked on Figure 4.1a are on 5 and 6 April 2011 (when δD values are -503‰ and -505‰ respectively), suggesting unusual meteorological condition.

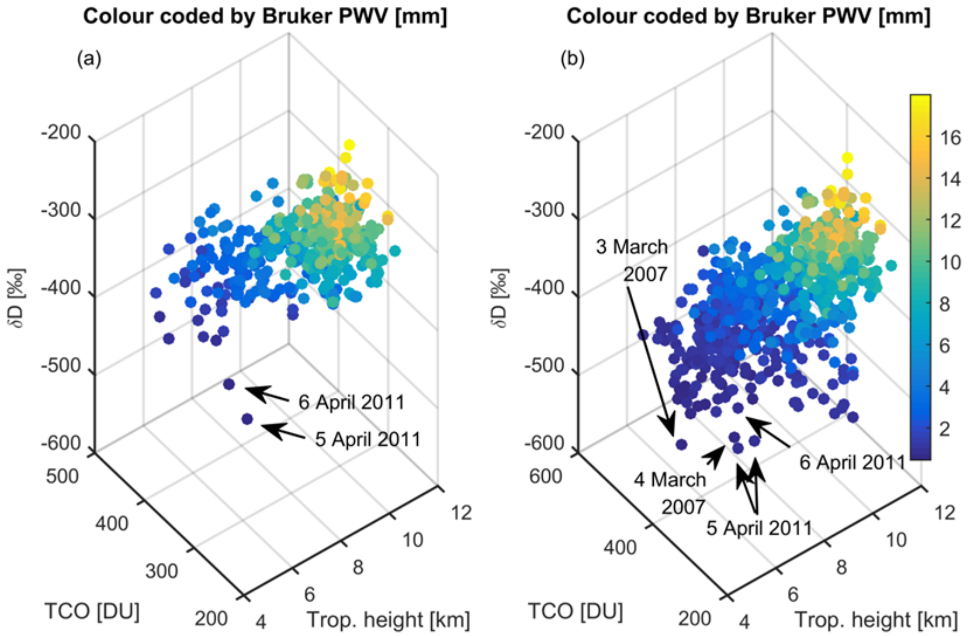

Figure 4.1: 3-D scatter plots of total ozone column, tropopause height, δD total column, and total precipitable water (Eureka, 2006-2014). TCO data in (a) are from Brewer no. 69 measurements. TCO data in (b) are from MERRA-2 model output. Tropopause heights are WMO temperature gradient tropopause values calculated from MERRA-2. The δD and PWV are from the Bruker 125HR measurements.

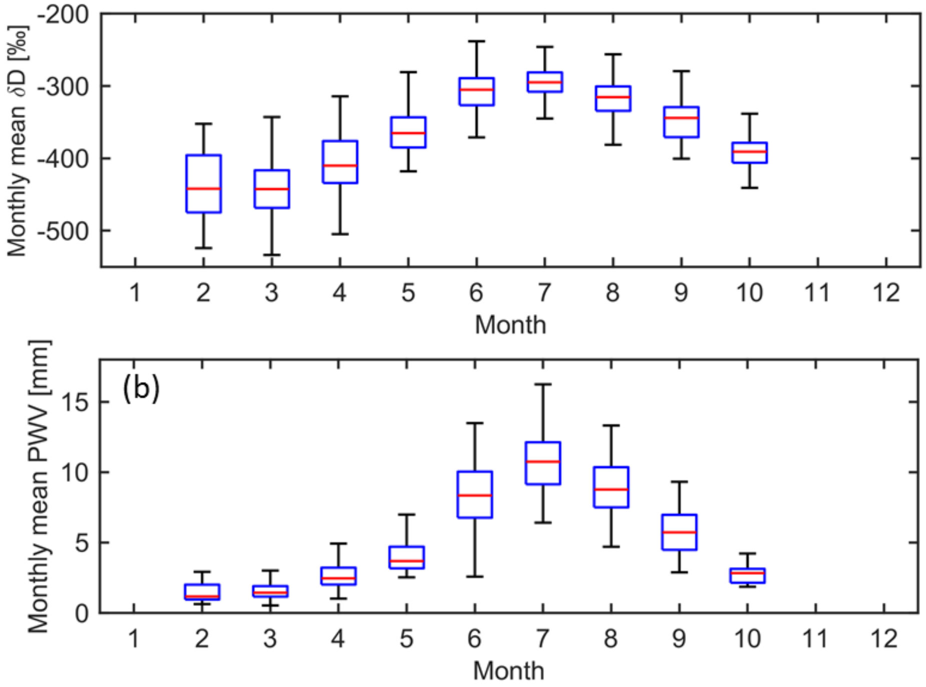

Figure 4.2: Whisker plot of Bruker 125HR monthly (a) δD and (b) PWV. On each box, the central red line is the median, the edges of the blue box are the 25th and 75th percentiles, and the black whiskers extend to the most extreme data points not considered outliers. The outliers are defined as greater than $q_3 + 1.5\,(q_3 - q_1)$ or less than $q_1 - 1.5\,(q_3 - q_1)$, where q_1 and q_3 are the 25th and 75th percentiles of the sample data, respectively (Tukey, 1977).

The size of the combined dataset is limited by the Brewer TCO measurements, which only start in late March. To expand the dataset, the MERRA-2 TCO was used instead of Brewer TCO. The MERRA-2 TCO for Eureka has a high correlation (R = 0.99) and a low positive bias (1.6%) compared to Brewer TCO (not shown here). The resulting increase in the number of coincident data points seen in Figure 4.1b reveals a similar event for 3 and 4 March 2007(-529 and -551‰ for δD values respectively). Figure 4.2 shows the whisker plot (Tukey, 1977) of Bruker 125HR monthly δD and PWV measurements. The median (mean) δD values for March and April at Eureka are -443 (-442) ‰ and -410 (-408) ‰ respectively. The δD value describes the relative deviation of HDO content from the standard mean ocean water. Thus the HDO value on 4 March 2007 is 55.1% less than the standard; the δD value is 24.7% less than the March mean. Similarly, the δD value on 5 April 2011 is 23.8% less than the monthly mean of April. The coincidence of these two events (2007 and 2011) on the 3-D plot (Figure 4.1b) indicates they may share similar dynamical and chemical causes. Figure 4.2b shows that the median (mean) PWV is 1.4 (1.7) mm in March and 2.5 (2.6) mm in April. The daily mean PWV value was only 0.5 mm on 4 March

2007 and was 1.0 mm on 5 April 2011, which indicates relatively dry conditions for these two events.

Figure 4.3(a and b) shows Eureka ozonesonde records from February to March 2007 and March to May 2011. The 0-3 km ozone profiles on 3 and 4 March 2007 and 4 and 6 April 2011 are indicated in the figure. Surface ozone depletion during these two events can be seen, although the 2007 event is weaker than the 2011 event. Figure 4.3 (c and d) shows 0-8 km RH values measured by radiosondes. The reduced RH and PWV during these two events can facilitate SSA production though the blowing-snow mechanism proposed by Yang et al., (2008).

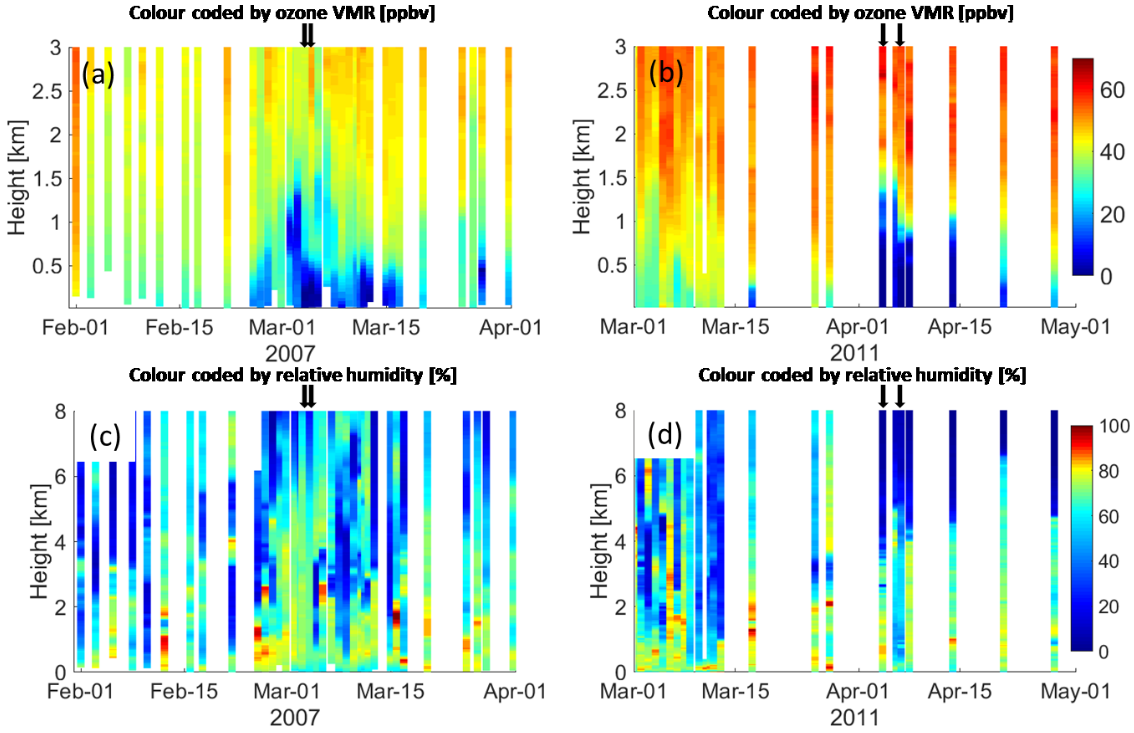

Figure 4.3: 0-3 km ozone and 0-8 km relative humidity profiles above Eureka from ozonesondes and radiosondes: (a) and (c) from 1 February to 1 April 2007; (b) and (d) from 1 March to 1 May 2011. The measurements on 3 and 4 March 2007 and 4 and 6 April 2011 are indicated by the arrows.

4.3.1.1 Chemical Model Results

Figure 4.4 shows the ozone and BrO volume mixing ratio profiles over Eureka for the 2007 event from ozonesondes and model simulations. A shallow surface ozone depletion layer (see the UKCA result in Figure 4.4b, minimum value ~5 ppbv) can be found similar to the ozonesonde measurements (see Figure 4.4a, minimum value ~1 ppbv) from 3 to 5 March. The ozonesondes measured 40-50 ppbv background ozone for 2-4 km, but both the pTOMCAT and UKCA modelled about 10 ppbv less at these altitudes. The BrO concentrations from both models are less than 5 pptv. One interesting feature in Figure 4.4 is that the ozone depletion was also found from 1 to 2 March. The ozone depletion layer on 1 and 2 March is aloft above the surface, with a maximum depletion at ~800-900 m (see Figure 4.5). However, this aloft layer is not captured by either model.

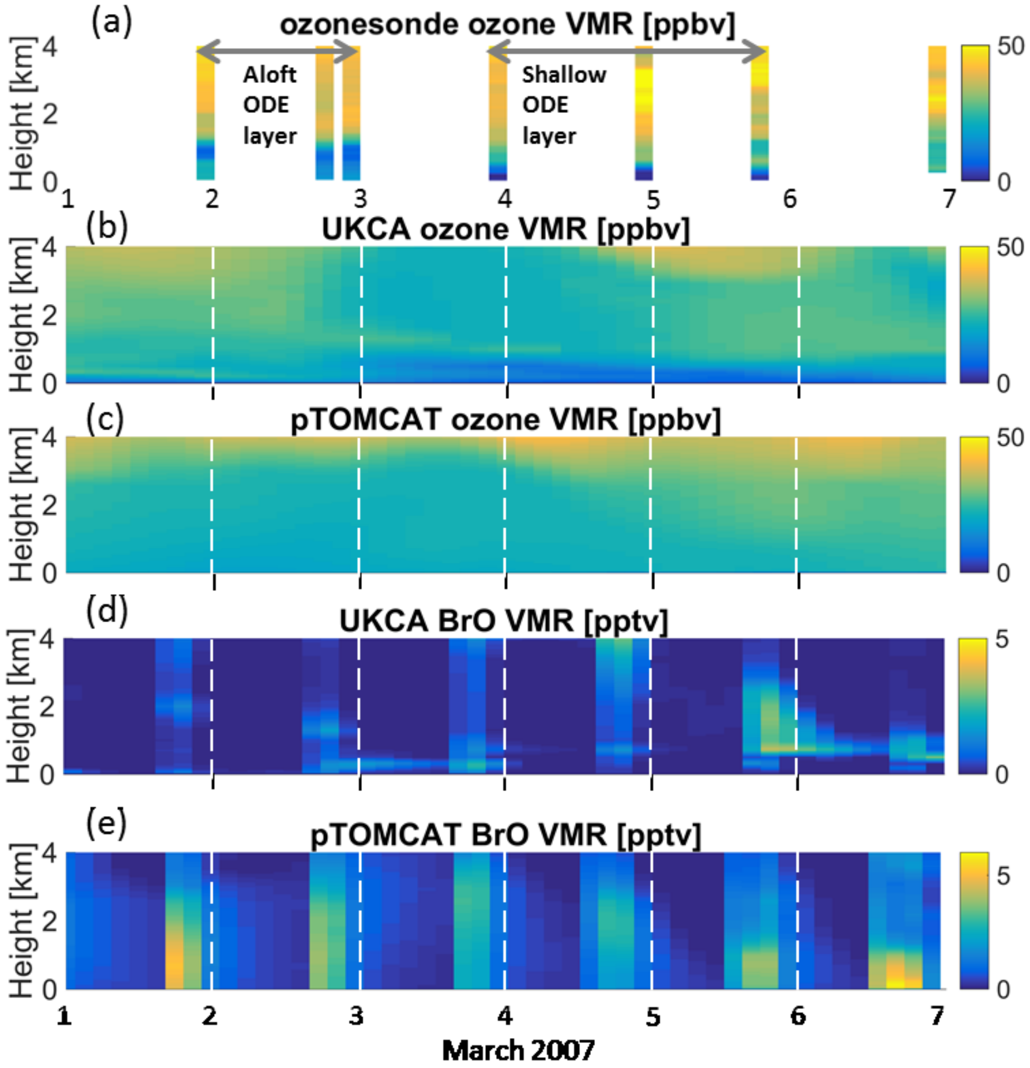

Figure 4.4: Ozone and BrO volume mixing ratio profiles from 0 to 4 km over Eureka from 1 to 7 March 2007 (UTC): (a) ozonesonde measurements, (b) UKCA modelled ozone profile, (c) pTOMCAT modelled ozone profile, (d) UKCA modelled BrO profile, (e) pTOMCAT modelled BrO profile. Grey horizontal double-headed arrows on (a) indicate the periods when ozonesondes measured the aloft ozone depletion layer and the shallow depletion layer.

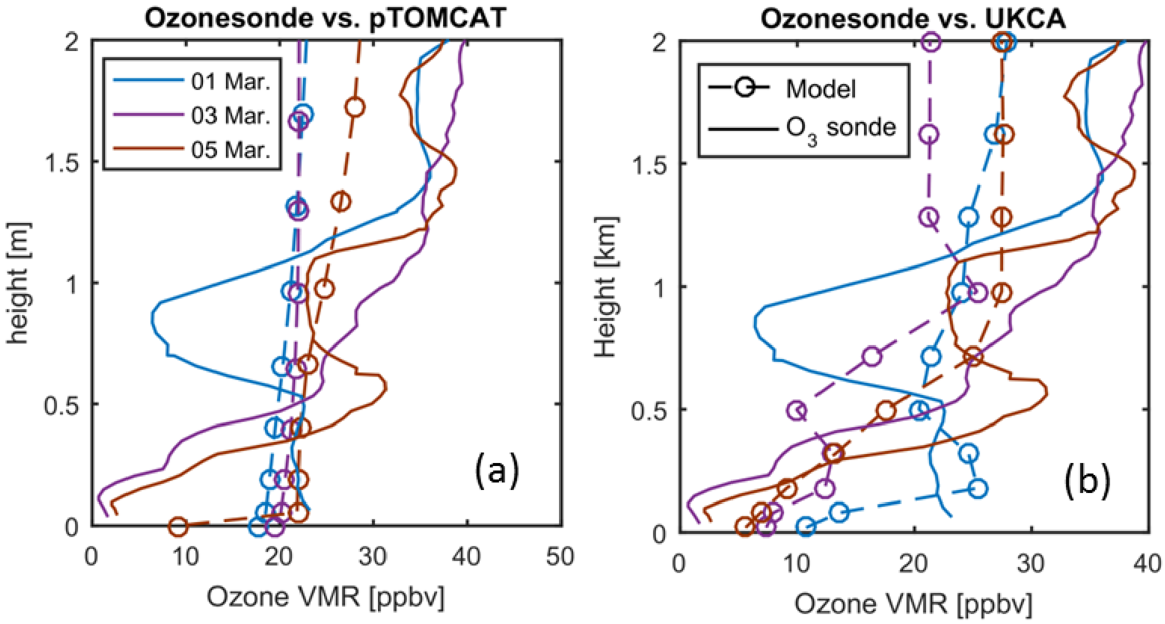

Figure 4.5: Observed and modelled ozone profiles from 0-2 km on March 1, 3, and5: ozonesonde vs. (a) pTOMCAT, (b) UKCA. Modelled profiles are shown by dashed lines with marker o, and measured profiles are shown by solid lines.

Figure 4.6 shows the ozone and BrO volume mixing ratio profiles over Eureka for the 2011 event. The highlight of the re-run of the UKCA model for 2011 is the increased BrO volume mixing ratio. In the previous study in Chapter 3 (Zhao et al., 2016a), UKCA only modelled about half of the maximum BrO VMR compared to ground-based measurements. The previous sensitivity study found that even doubling the bromine release flux from the source region in the model did not increase the BrO VMR over Eureka, due to very low ozone VMR (< 1ppbv) in this case (Zhao et al., 2016a). However, interestingly, in this re-run, the decreased snow salinity in the model input (which decreases the bromine release flux from the source region) surprisingly increased the modelled BrO VMR (to ~23 pptv) over Eureka, which is comparable to the ground-based MAX-DOAS measurements of ~21 pptv (the UKCA previously modelled ~13 pptv see Section 3.2.4.2 for more details). The reduced bromine flux from the source region

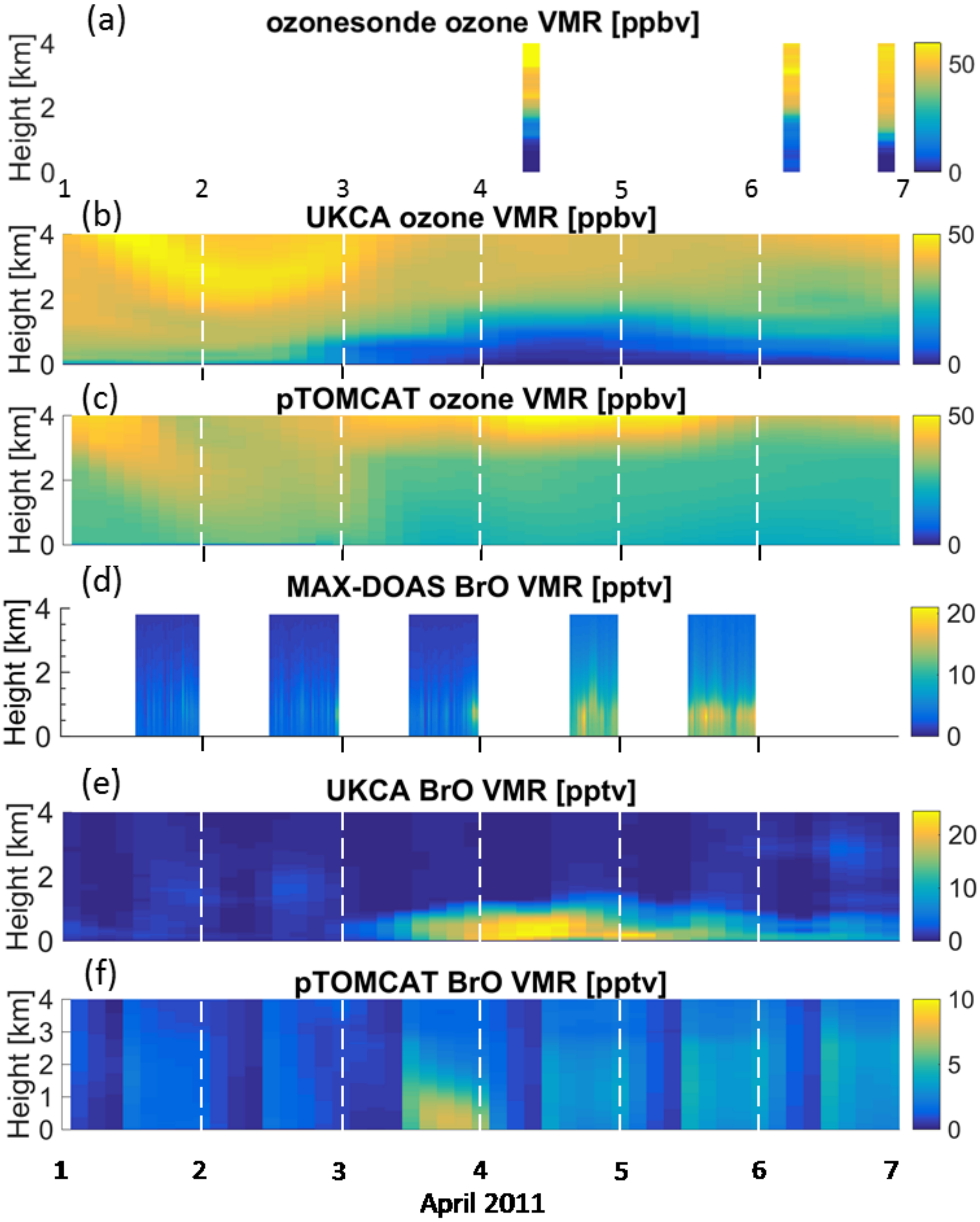

Figure 4.6: Ozone and BrO volume mixing ratio profiles from 0 to 4 km over Eureka from 1 to 7 April 2011 (UTC): (a) ozonesonde measurements, (b) UKCA modelled ozone profile, (c) pTOMCAT modelled ozone profile, (d) MAX-DOAS retrieved BrO profile, (e) UKCA modelled BrO profile, (f) pTOMCAT modelled BrO profile.

reduced the depletion of ozone along the trajectory, which in turn preserved the high concentration of bromine. In general, this result supports the hypothesis of Zhao et al. (2016a) that during a strong surface ODE (ozone VMR < 1 ppbv), the bromine concentration and partitioning can be significantly controlled by the ozone concentration. pTOMCAT also captured the 2011 event, but the results are not as good as those of the UKCA model. This could due to the difference in the models' dynamics in the boundary layer (Hoyle et al., 2011; Ruti et al., 2011), model resolution, and the background aerosol scheme (Yang et al., 2005; Yang et al., 2010; Zhao et al., 2016a)

Comparing the measured and modelled ozone profiles for the two events (see Figure 4.4 and Figure 4.6), the surface ozone depletion on March 2007 is weaker than the April 2011 event. The weaker ODE in 2007 is likely due to insufficient sunlight. The first sunrise at Eureka is on 21 February. On 4 March, the daylight length is only 7.5 hours and the maximum solar elevation angle is only 3.7°, but on 4 April the daylight length is 17.5 hours and maximum solar elevation angle is 16°. Note that the insufficient sunlight will make reaction R2 the rate limiting step in the bromine reaction cycle (Section 1.2, R1 to R4). In addition, the strength of the two cyclonic polar low systems was different (discussed in Section 4.3.1.2).

4.3.1.2 Airmass History

To examine the history of the ozone-depleted airmass and aerosol transportation, FLEXPART (Stohl et al., 2011) is used in the present study. Figure 4.7 shows some of the FLEXPART SSA-TRACER total column sensitivities, which, when multiplied with emission flux, provide the simulated concentration at the receptor (Stohl et al., 2013). As knowledge of the SSA type is limited, simulations are kept as simple as possible. The SSA-TRACER had a scavenging scheme (both wet and dry deposition) applied (Seibert and Frank, 2004; Stohl et al., 2005; Stohl et al., 2011), but had no assumption on its lifetime. Each release had 20,000 tracer particles. The release times were set to be coincident with the Bruker 125HR δD measurements, and the duration of each release was one hour. Each backwards run lasted for 6 days, and the release heights were set to 0 to 500 m and 1500 to 2000 m respectively. The particle release location areas were set to use the coarse grid from pTOMCAT (which includes Eureka) and a much finer grid (only 2% of pTOMCAT grid size, not shown here) as described in Sect. 4.2.4. The aerosol tracers released in all backwards simulations show sensitivity to the Beaufort Sea region, and the plumes reveal the structure of the cyclones (see Figure 4.7).

MODIS false colour images (Figure 4.8) show cloud tops of two polar cyclones, which were formed over the Beaufort Sea during both periods of interest. The ERA-Interim data (see Figure 4.9) show that the wind speed in the cyclone increased to 20 and 24 m s^{-1} for the 2007 and 2011 cases respectively; and the boundary layer heights increased to 710 and 800 m for those two events, respectively. Thus the cyclone in 2007 was weaker than the one in 2011. In general, these observations and model simulations confirm that the ozone-depleted airmass and aerosols that were observed at Eureka during these two events were generated in high wind conditions in the Beaufort Sea region and then transported by the polar cyclones.

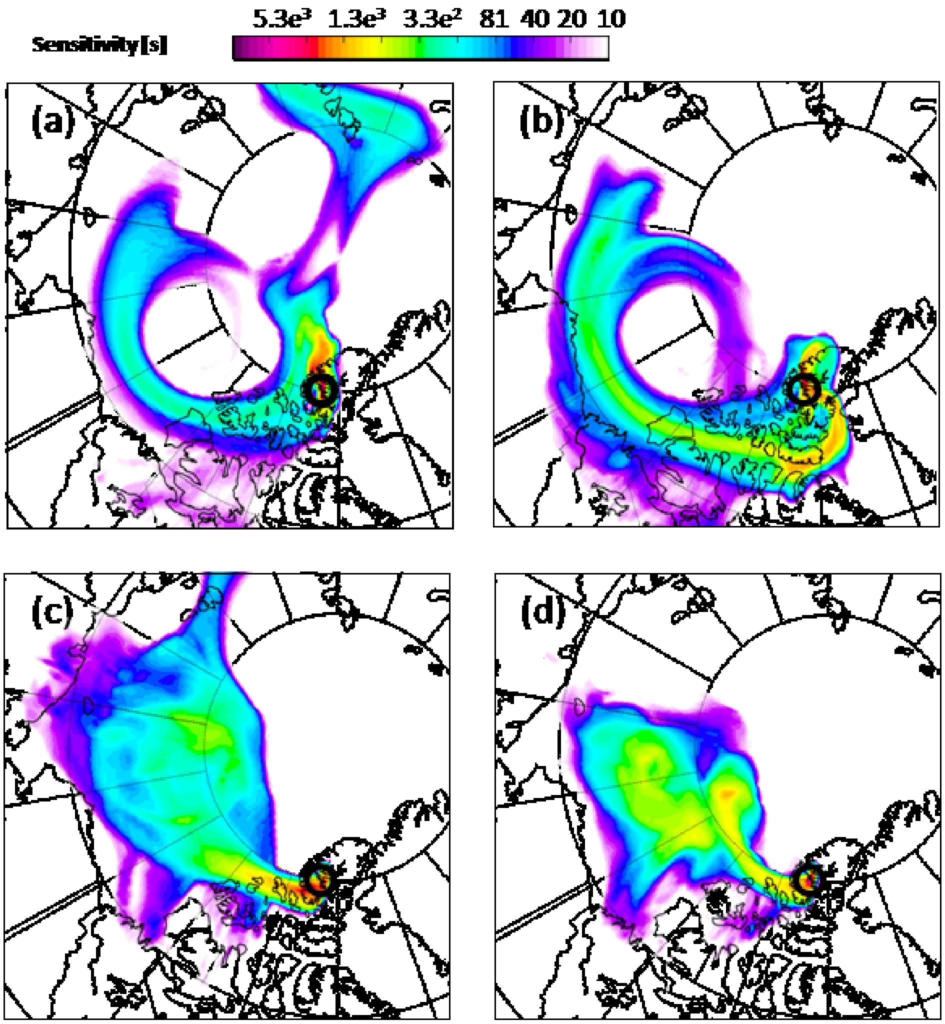

Figure 4.7: FLEXPART SSA-TRACER 6-day backward run showing total column sensitivity for release times and heights as follows: (a) 17:00-18:00 UTC, 3 March 2007, 0-0.5 km, (b) 17:00-18:00 UTC, 3 March 2007, 1.5-2.0 km, (c) 14:00-15:00 UTC, 3 April 2011, 0-0.5 km, and (d) 14:00-15:00 UTC, 3 April 2011, 1.5-2.0 km.

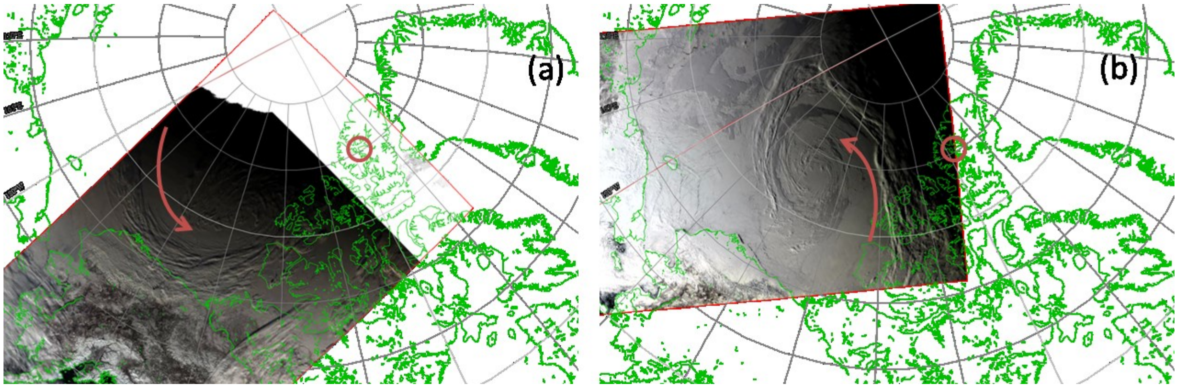

Figure 4.8: MODIS images show the cyclones (indicated with arrows) over the Beaufort Sea for the 2007 and 2011 events: (a) 27 February 2007, (b) 1 April 2011. Eureka is indicated by the red circle on both panels.

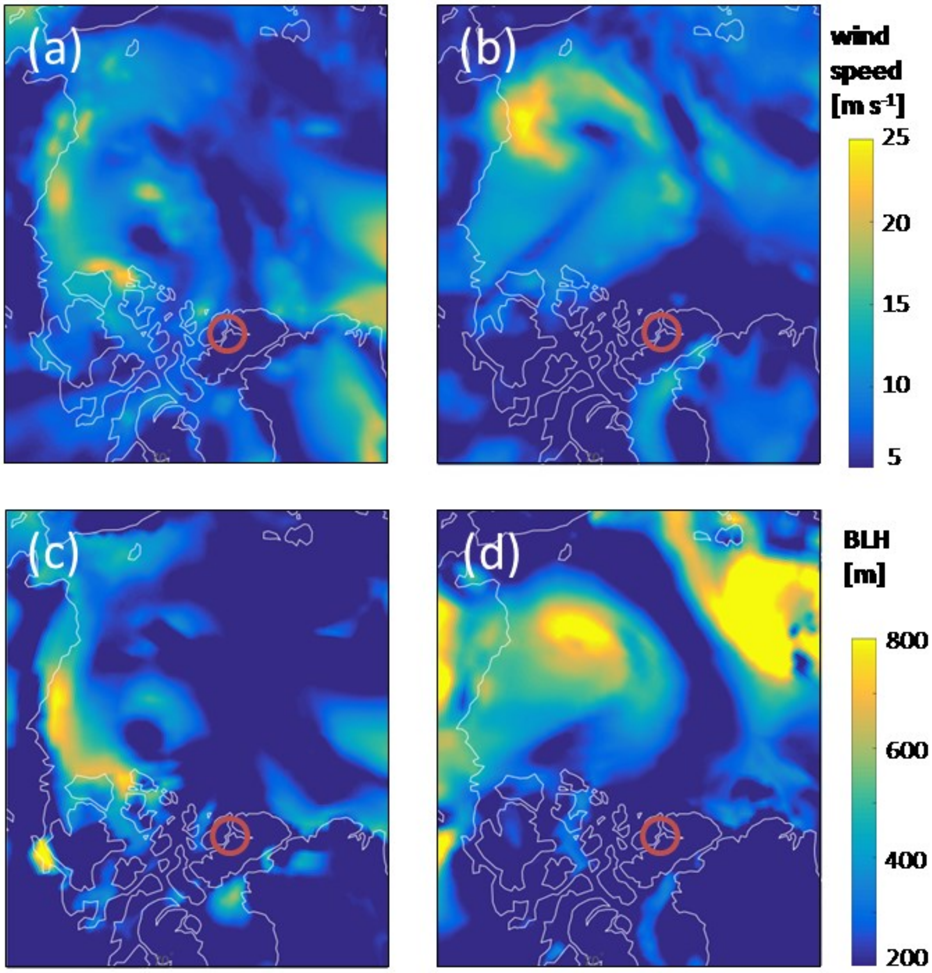

Figure 4.9: ERA-Interim 10-metre wind gust and boundary layer heights (BLH): (a) wind gust on 28 February 2007 00:00 UTC, (b) wind gust on 1 April 2011 00:00 UTC, (c) boundary layer height at the same time as (a), and (d) boundary layer height at the same time as (b). Eureka is indicated by the red circle on each panel. These two dates were selected for when the cyclones were fully developed.

4.3.2 Cloud and Aerosol

Among many different proposed bromine sources (Abbatt et al., 2012), this work focused on the SSA. In the Arctic spring, the SSA concentration depends on meteorological, sea-ice, and snow conditions (Nilsson et al., 2001; Rannik, 2001; Lewis and Schwartz, 2004; Yang et al., 2008; May et al., 2016). Wind speed, RH, sea surface and air temperature gradient, water/ice/snow salinity, and removal processes (wet and dry deposition) will all affect the SSA formation and concentration. For the present work, the meteorological conditions for the 2007 and 2011 events support the work of Yang et al. (2008), which reported that SSA production rate from snow can be significant in high wind conditions.

4.3.2.1 Lidar and Radar Observations

The lifetime of SSA in the atmospheric boundary layer can range from minutes to days, depending on its size and meteorological conditions. Fine SSA (diameter < 2.5 μm) has slower deposition rates compared to medium-sized SSA (diameter from 2.5 to 10 μm). Following the work of Yang et al. (2008), large SSA (diameter > 10 μm) was not included in pTOMCAT and UKCA due to their short lifetime (faster dry deposition rate) in the atmosphere. In the Arctic spring, the low temperature makes the SSA contributed from the open ocean less important. Thus although pTOMCAT includes both OO-SSA and SI-SSA, only the latter is considered in this study. For these two events, both ground-based observations and model data revealed high aerosol concentration during the ODEs. For the 2011 case, the aerosol extinction measurements from PEARL-GBS and the cloud measurements from the MMCR were presented in Chapter 3. In the present work, the pTOMCAT SI-SSA data during the 2007 event with aerosol and cloud measurements from the AHSRL and MMCR were compared (note that the MAX-DOAS measurements started in 2010, and the AHSRL measurements ended in 2010).

Figure 4.10 shows the comparison of lidar/radar profile data with the pTOMCAT SI-SSA VMR profile. Figure 4.10a shows the measurement time for the ozonesondes (dashed lines) and Bruker 125HR (green lines/boxes). Figure 4.10b and c show the linear depolarization and backscatter cross-sections measured by the lidar. The backscatter cross-sections measured by the lidar (β_{lidar}) and radar (β_{radar}) were used to calculate the colour ratio (see Figure 4.10d).

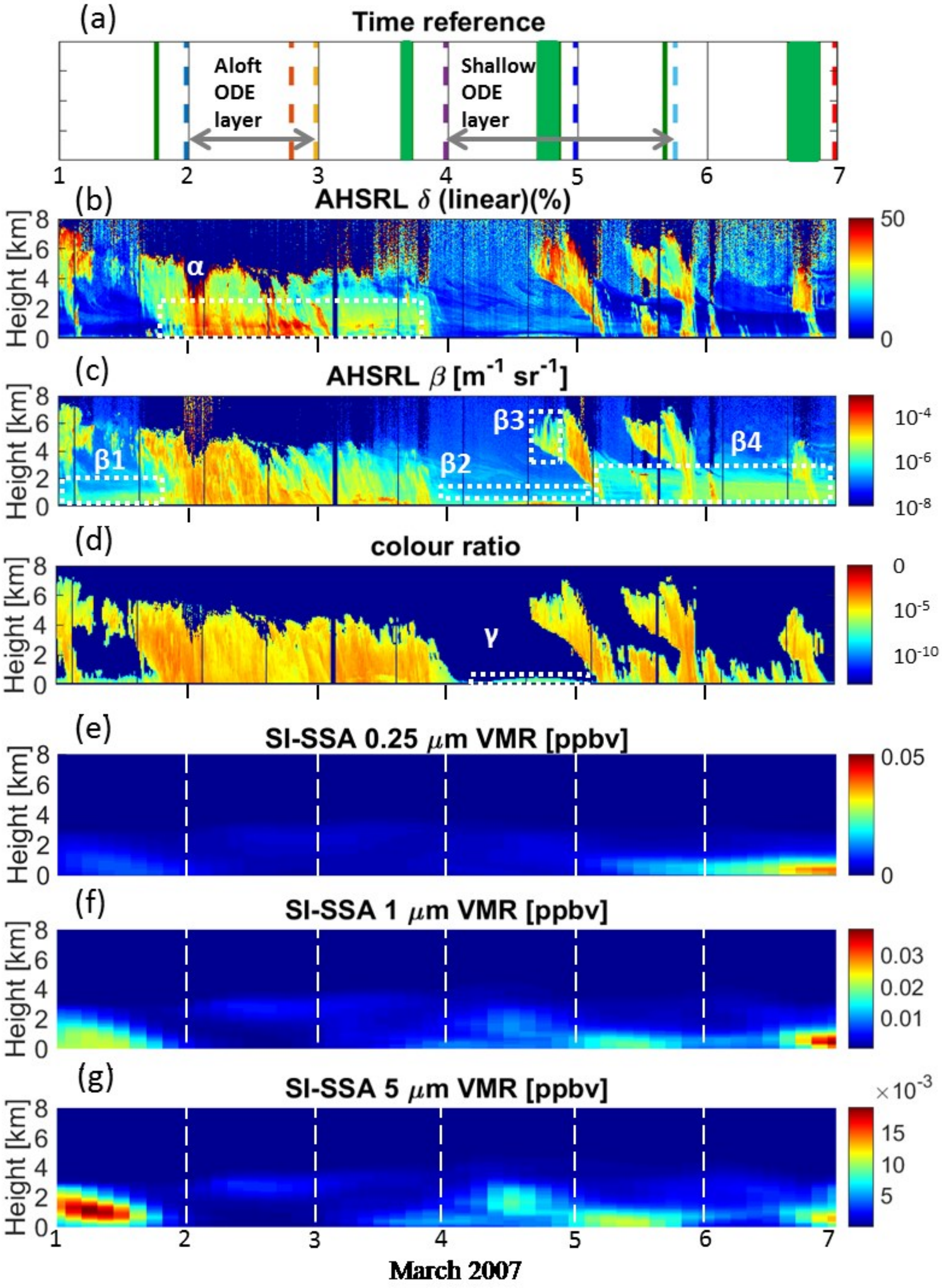

Figure 4.10: Comparison of lidar (AHSRL) aerosol measurements with pTOMCAT modelled sea-ice sea-salt aerosol (SI-SSA), 0-4 km over Eureka from 1 to 7 March 2007: (a) time reference for coincident measurements from ozonesondes (indicated by colour dashed lines) and Bruker 125HR (indicated by solid green lines/boxes), (b) lidar linear depolarization, (c) lidar backscatter cross-section, (d) colour ratio, (e) pTOMCAT 0.25 μm SI-SSA volume mixing ratio, (f) pTOMCAT 1.0 μm SI-SSA VMR, (g) pTOMCAT 5.0 μm SI-SSA VMR. Grey horizontal double-headed arrows on (a) indicate the periods when ozonesondes measured the aloft and the shallow ozone depletion layer. White boxes on (b), (c), and (d) indicate detection of ice cloud (α), aerosol (β1, β2, and β4), ice cloud (β3), and ice crystal (γ).

The cyclonic airmass arrived at Eureka on 18:00 UTC 1 March. AHSRL linear depolarization data indicates that there was an aloft layer of particles (Figure 4.10b, area α) that showed high depolarization from 30 to 50% at 700 to 1000 m. The colour ratio (Figure 4.10d) for this layer was in the range of 10^{-5} to 10^{-3}, indicating that it was ice cloud (vapour and ice crystals) with ice precipitation (see Figure 10 in Bourdages et al. (2009) for the classification chart). And that the effective radius of the particles was in the range of 50-150 μm. This layer of ice cloud was coincident with the aloft ODE layer (for example, the ozonesonde at 23:28 on 1 March has the greatest ozone depletion (to 7 ppbv) at 870 m), as shown in Figure 4.11. Bourdages et al. (2009) described the lidar and radar measurements from 4-5 March 2007 in detail. An ice crystal layer (high depolarization, low colour ratio) is seen from the surface to 300 m from 14:00 to 24:00 UTC on 4 March (Figure 4.10d, area γ). A thin aerosol layer (low depolarization, low colour ratio, 300-500 m) for that period is also seen (Figure 4.10c, area β2). Ice clouds were identified in the middle troposphere from 16:00 on 4 March to 8:00 on 5 March UTC (Figure 4.10c, area β3). These shallow layers of ice crystal (area γ) and aerosol (area β2) were coincident with the shallow ODE layer (for example, the ozonesonde at 23:16 on 4 March shows ozone depletion to 1 ppbv from the surface to 200 m, with the ozone mixing ratio increasing to 32 ppbv at 650 m) as shown in Figure 4.11. Another two aerosol-enhanced events were also observed as indicated in Figure 4.10c (areas β1 and β4). In addition, small water clouds were observed at 2.2 to 2.5 km between 10:00 and 14:00 UTC on 5 March and at 2.4 km at about 1:00 UTC on 6 March. A very thin water cloud was observed at about 1.8 km between 8:00 to 14:00 UTC on 6 March.

The lidar/radar observations of the ice clouds, ice crystal, and boundary layer aerosol from the cyclonic airmass explained why strong HDO depletion was observed coincidently with the arrival of the front. Interestingly, the ice cloud was at the same height as the aloft ODE layer. The lidar/radar observation also reveals deposition (falling snow and ice crystals) processes at Eureka; the ice precipitate has high depolarization and vertically aligned fall streaks. The prolonged surface ODE on 4 and 5 March could be due to the deposition of bromine-enriched particles onto the local snow pack.

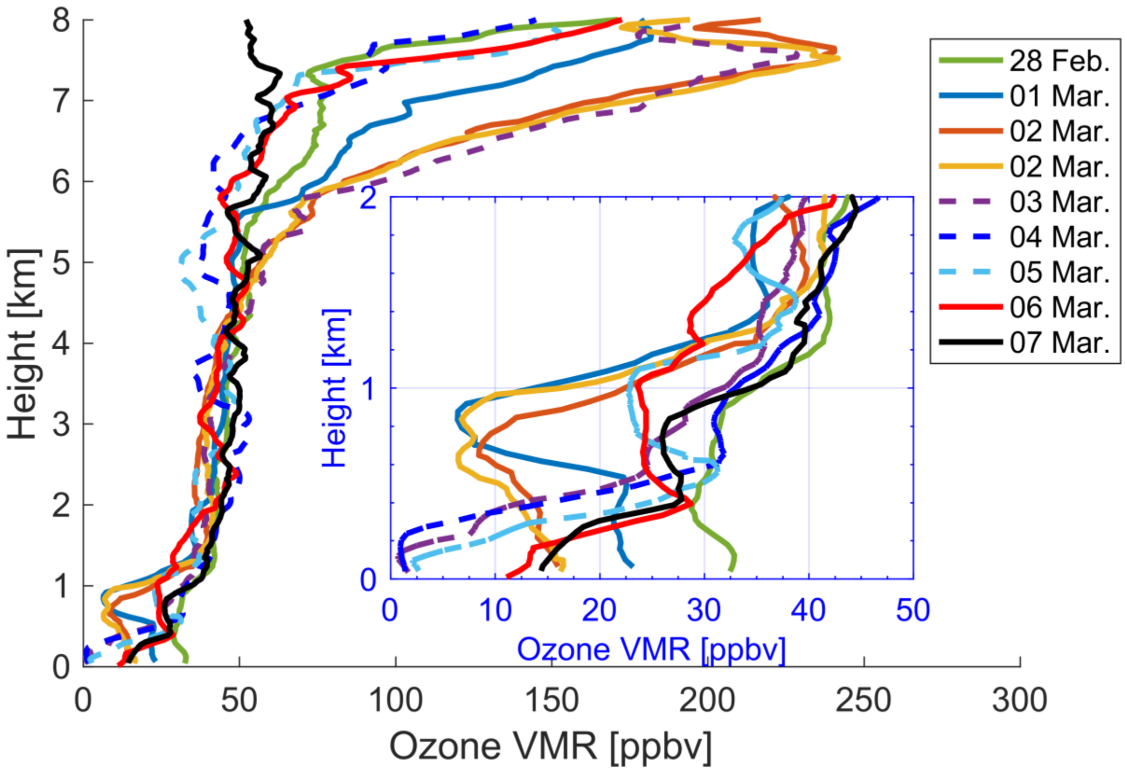

Figure 4.11: Ozonesonde ozone profiles (from ozonesondes) above Eureka (the inset panel shows 0-2 km) from 28 February to 7 March 2007.

4.3.2.2 Model Results

The modelled SI-SSA from pTOMCAT in three bins (0.25, 1, and 5 μm) captured some features of the transported aerosols during this period (Figure 4.10e to g). For example, the three aerosol events seen in Figure 4.10c (areas β1, β2, and β4) can also be found in the modelled SI-SSA. Modelled 5 μm SI-SSA is most abundant in area β1, whereas 1 μm and 0.25 μm SI-SSA are most abundant in area β4. Furthermore, back-trajectory results show that the fine aerosol on 6 March was transported from the north, whereas the medium-size SSA on 1 March came from the south (not shown here). A weak shallow aerosol layer on 4 March (area β2) was also captured by pTOMCAT, and it was transported from the west (as from the cyclonic airmass).

As discussed in Sect. 3.1, the modelled and observed ozone depletion for the 2007 event is weaker than that for 2011 event. In addition, pTOMCAT modelled ozone depletion results were less prominent compared to UKCA modelled results (see Figure 4.5). One possible explanation is that pTOMCAT did not fully capture the production of SSA during the blowing snow. Figure

4.7 and Figure 4.9 show that the high-wind areas for the 2011 event were over sea ice, however, the high-wind areas for the 2007 event were close to land. Due to the coarse model grid and time step in both pTOMCAT and UKCA, the models underestimated the production of SSA in that close-to-land cyclone case. Thus the underestimated SSA may reduce the strength of the ODEs.

As discussed in Section 4.3.2.1, none of the chemical models used in the present study reproduced the aloft ozone depletion layer. pTOMCAT results show that there was almost no SI-SSA during that period (see Figure 4.10,e-g area α). Thus the production and deposition mechanisms of SI-SSA in the models still need further investigation. For example, the SI-SSA deposition rates (wet and/or dry) might be too high in this case. In general, this comparison of lidar/radar measurements and modelled SI-SSA provides supports to the blowing-snow SSA production mechanism, and suggests that further improvements in SI-SSA modelling are important to improve blowing-snow ODE simulations.

4.3.3 HDO Depletion

4.3.3.1 δD-PWV Observations

Figure 4.12 shows the evolution of δD as a function of PWV during the two cyclone events. The grey dots are nine-year δD-PWV Bruker 125HR measurements. The red and blue dots are daily mean δD-PWV for the dates indicated. The green dots in (a)/(b) represents March/April mean δD-PWV values over all nine years, and the black curve represents Rayleigh fractioning (using the monthly mean data point as the origin, with a fraction coefficients of 1.209). Other Rayleigh curves with different phase equilibrium ice-vapour fraction factors ($\alpha_{e\text{-ice-vapour}}$) are indicated by coloured dashed lines. Figure 4.12a using the δD-PWV daily mean on 1 March 2007 as the origin and Figure 4.12b using the δD-PWV daily mean on 2 April 2011 as the origin. The dashed green ($\alpha_{e\text{-ice-vapour}} = 1.198$) and blue ($\alpha_{e\text{-ice-vapour}} = 1.228$) Rayleigh curves correspond to the condensation process at temperatures of -30 and -40 °C respectively (Merlivat and Nief, 1967). The error bars on the red and blue dots are standard deviations of the δD-PWV values used to calculate the daily means.

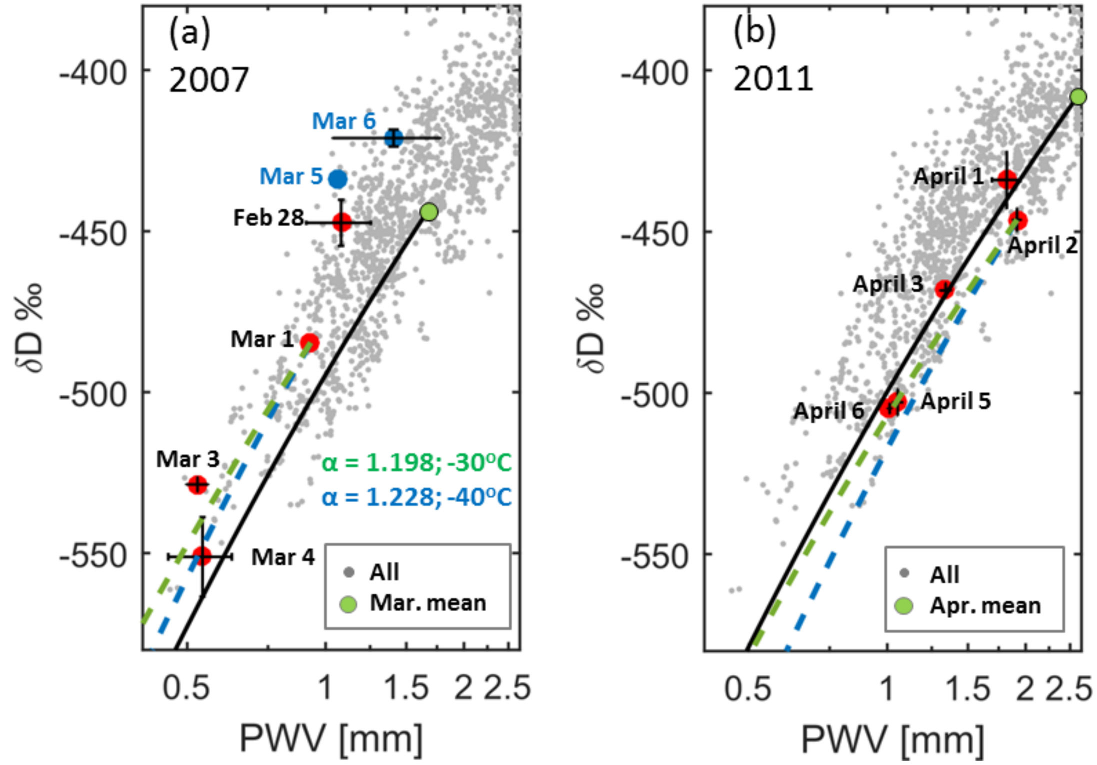

Figure 4.12: Evolution of δD as a function of PWV (log scale). Grey dots are nine-year (2006-2014) Bruker 125HR δD-PWV measurements. (a) The 2007 event, with daily mean δD-PWV values from 28 February to 7 March 2007 indicated by red (a depletion process, with both δD and PWV decreasing with time) and blue (a remoistening process, with both δD and PWV increasing with time) points. (b) The 2011 event, with daily mean δD-PWV values from 1 to 6 April 2011 indicated by red points. The green point in panel (a)/(b) represents the March/April mean value over all nine years, and the black curve represents the Rayleigh fractionation process using the monthly mean as the original airmass with fraction coefficient of 1.209. Other Rayleigh curves with different fraction coefficients are indicated by coloured dashed lines, with (a) using the δD-PWV daily mean value on 1 March 2007 as the origin, and (b) using the δD-PWV daily mean value on 2 April 2011 as the origin. The error bars are standard deviations of the δD-PWV values used to calculate the daily mean.

Figure 4.12a shows an HDO depletion process from 28 February to 4 March 2007 (red dots), followed by a moistening process from 5 to 6 March (blue bots). The HDO depletion from 2 to 4 March 2007 corresponds to the condensation process in the cyclonic airmass, which was captured by the Rayleigh fractioning model (see the green and blue Rayleigh curves). Tropospheric RH measured by radiosondes is below 75% from 2 to 4 March 2007, and temperatures in the 0-4 km cloud layers were -35 to -45 °C during the period. Thus kinetic fractionation due to supersaturation in ice clouds is not applicable for this case. The deviation of the δD-PWV pair from Rayleigh curves on 3 March 2007 is possibly due to sublimation of

HDO-enriched blowing snow. The water vapour sublimation flux from blowing snow is 0.5 mm/day, with conditions of 10 m/s wind speed, -20 °C ambient temperature, and 80% RH. With conditions of 20 m/s wind speed, -20 °C ambient temperature, and 75% RH, the water vapour sublimation flux from blowing snow can increase to 2.6 mm/day. These amounts of water vapour sublimation flux from δD-enriched blowing snow are strong enough to affect the atmospheric δD value (since the PWV on 4 March 2007 is only 0.5 mm) through mixing. The temporal mixing line method (Keeling, 1958; Miller and Tans, 2003; Noone et al., 2013) can be used to estimate the δD and/or sublimation flux of blowing snow. However, isotopologue measurements for precipitation at the source region (for example, near the Beaufort Sea) are necessary to validate the results and to make meaningful comparison of measured with modelled sublimation flux. In general, more detailed water isotopologue modelling and observations are necessary to further evaluate the blowing-snow HDO evolution.

Figure 4.12a also shows a remoistening process that started on 5 March (see blue dots), which was due to the cyclonic airmass start to mixing with a different airmass transported from the north. This mixing process is also coincident with the termination of the ODE. As shown in Figure 4.11, the shallow surface ODE became weaker on 5 March than on 3 and 4 March, and terminated on 6 to 7 March, as the surface ozone VMR increased from 11 to 15 ppbv.

Figure 4.12b shows an HDO depletion process from 1 to 6 April 2011. The depletion process from 2 to 5 April is also deviated from the Rayleigh process (green and blue dashed lines) on 3 April (the measured 0-4 km cloud temperature is -30 to -35 °C). Tropospheric RH measured by radiosondes is below 80% from 3 to 5 April 2011. Surface clouds containing ice crystals were observed for the 2011 case (Zhao et al., 2016a), and other meteorological conditions were also similar to the 2007 case. Thus, as with the 2007 event, the sublimation of HDO-enriched blowing snow is likely the cause of this deviation; the measured fractionation result on 3 April 2011 appears to be weaker (less HDO loss) than the modelled green and blue Rayleigh fractionation lines (note that the black line is the monthly mean). In general, the δD-PWV values provide useful information regarding the history of the cyclonic airmass. HDO depletion during the 2007 and 2011 events was found to deviate from (weaker than) pure Rayleigh fractionation, suggesting that sublimation likely contributed to the δD evolution.

4.3.3.2 Influence of the Polar Vortex

The previous sections described surface ODEs coincident with the observation of depleted HDO and increased SSA. Derived Meteorological Products (DMPs), similar to those described by Manney et al. (2007), were calculated for above Eureka and along the lines-of-sight of the Bruker instrument (Lindenmaier et al., 2012) using MERRA-2 analysis. Figure 4.13 shows the MERRA-2 temperature profiles over Eureka with the boundaries of the polar vortex indicated (defined by sPV value of 1.6×10^{-4} (Manney et al., 2007). Both the 2007 and 2011 events show strong cooling (210-220 K) in the stratosphere from 15-25 km, which is caused by the presence of the stratospheric polar vortex overhead (Manney et al., 2008; Adams et al., 2013). In both cases, the stratospheric vortex and the tropospheric cyclonic low-pressure system were present at the same time. MERRA-2 captured the surface pressure and temperature changes in the polar lows, as seen from the decreased surface temperature in Figure 4.13a for 3-4 March 2007 and in Figure 4.13b for 5-6 April 2011. MERRA-2 PV data (not shown here) indicate the edge of the elongated vortex was over Eureka for both years. The cold stratospheric airmass inside the vortex is more HDO depleted than the warm airmass outside. Since the extremely low δD values measured during these two events are coincident with the presence of the stratospheric vortex, the δD sensitivity in the stratosphere was examined.

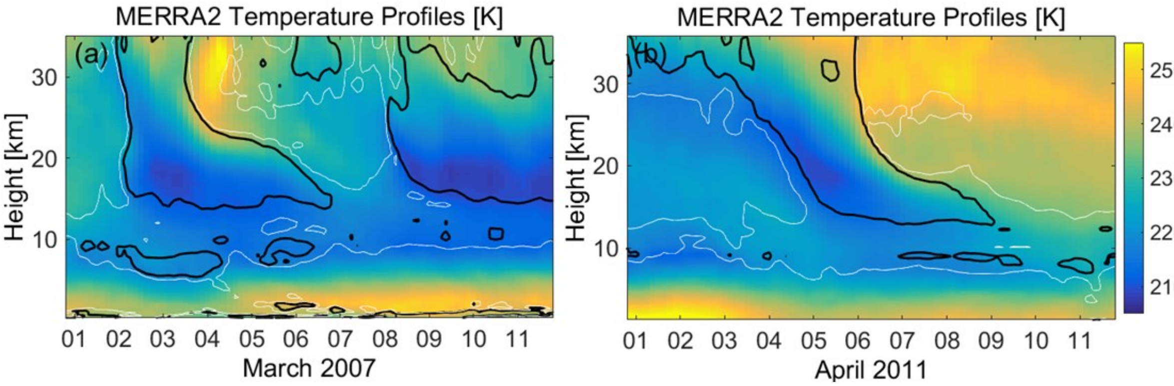

Figure 4.13: Vertical temperature profiles over Eureka from MERRA-2. The black contour indicates inner boundaries of the polar vortex determined by sPV = 1.6×10^{-4} s^{-1}, and the white contour indicates the outer boundaries (sPV = 1.4×10^{-4} s^{-1}).

The Bruker 125HR water vapour measurements have limited sensitivity in the stratosphere and therefor the δD data should have limited sensitivity to the presence of the polar vortex. The δD sensitivity to the airmass being inside and outside the stratospheric vortex was investigated.

Following Manney et al. (2007) and Adams et al. (2012a), sPV values along the lines-of-sight of the Bruker instrument were interpolated to the 490-K potential temperature level (lower stratosphere, ~19 km). The inner vortex edge is identified at sPV$_{490K}$ values of 1.6×10^{-4}. With the sPV$_{490K}$ values, the Bruker 125HR measurements can be categorised into two regimes, inside and outside the polar vortex.

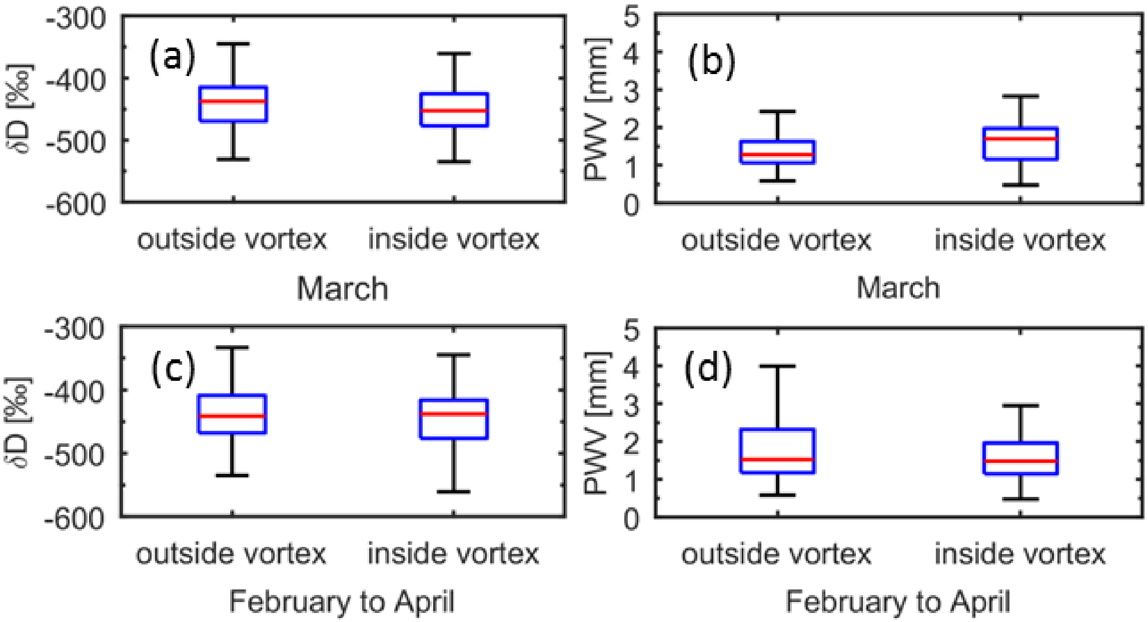

Figure 4.14: Bruker 125HR δD and PWV whisker plots for nine years measurements (2006-2014) outside and inside vortex. (a) and (b) show March δD and PWV measurements respectively, and (c) and (d) show springtime measurements (from February to April). In each box, the central red line is the median, the edges of the blue box are the 25th and 75th percentiles, and the black whiskers extend to the most extreme data points not considered outliers.

Figure 4.14 shows the whisker plots of Bruker δD and PWV data. Figure 4.14a and b show the δD and PWV data in March of all nine years. The median δD outside the vortex in March is -438^{+23}_{-31}‰ (75th to 25th percentile), while the value inside the vortex is -453^{+28}_{-24}‰. Thus statistically, there is no significant difference of δD between these two regimes. In Figure 4.14c and d, the period is expanded to February to April (by which time the stratospheric vortex has broken up), and these panels also confirmed that the Bruker δD and PWV data are not sensitive to the presence of the polar vortex. Moreover, no evidence was found in the ozonesonde ozone and radiosonde RH measurements to indicate the existence of a stratospheric intrusion, which could cause low HDO. Thus to summarize, this sensitivity test and the observations indicate that the extremely low δD measured during the two events studied here were caused by tropospheric HDO depletion.

4.3.4 Summary

Data from six instruments and four models were used to investigate Arctic ODEs. By using the TCO, tropopause height, and δD data, two similar cyclonic events were identified from the nine-year dataset that show both depleted surface ozone and HDO at Eureka in March 2007 and April 2011. The FLEXPART particle dispersion model was used to simulate airmass transport. The aerosol tracers released in all backwards simulations show sensitivity to the Beaufort Sea region, and the plumes reveal the structure of the cyclones. The ERA-Interim data show that the wind speed in the cyclone increased to 20 and 24 m s^{-1} for the 2007 and 2011 cases, respectively, and the boundary layer heights increased to 710 and 800 m, respectively.

In general, the ground-based observations show good agreement with modelled ozone and BrO data. One key result is that the modelled BrO and ozone in the near surface layer are quite sensitive to snow salinity. Newly incorporated surface salinity data reduced the bromine release flux from the source region, but increased the modelled BrO concentration above Eureka, bringing them into agreement with the previous measurements for the 2011 event (Zhao et al., 2016a). This is likely due to the reduced bromine flux from the source region reducing the depletion of ozone along the trajectory, which in turn preserved the high BrO concentrations. This result supports the conclusion of that study that during a strong surface ODE (ozone VMR < 1 ppbv), BrO concentrations can be significantly controlled by ozone concentrations.

Modelled blowing-snow SSA was compared with lidar/radar measurements showing that pTOMCAT SI-SSA data captured some features of the increased aerosol in the 2007 and 2011 events. For the 2007 event, the lidar and radar observed ice cloud (vapour and ice crystals) from 700 to 1000 m height (from the end of 1 March to 3 March), which is coincident with an aloft ozone depletion layer having the greatest ozone depletion (to 7 ppbv) at 870 m. However, pTOMCAT and UKCA both failed to reproduce this feature in their modelled ozone profiles. pTOMCAT results show that there was almost no modelled SI-SSA during that period. Thus the production and especially the deposition mechanisms of SI-SSA in the models still need further investigation. The 2007 lidar/radar observations also reveal deposition (falling snow and ice crystals) from this ice cloud at Eureka. Thus the following shallow surface ODE (0 to 200 m) on 4 and 5 March was likely due to the deposition of bromine-enriched particles onto the local snow pack. The detailed vertical structure of ice clouds, ice crystal, and aerosol layers obtained for the 2007 event could be used in future bromine modelling comparisons.

HDO depletion observed during these two blowing-snow ODEs is found to be weaker than pure Rayleigh fractionation. The evolution of δD-PWV was used to distinguish cyclone-originating airmasses from non-cyclone-originating airmasses, indicating that the termination of the shallow surface ODE is due to mixing with a different airmass. Although the edge of the stratospheric polar vortex was found over Eureka during both periods, no evidence was found that the low δD value was caused by the polar vortex or a stratospheric intrusion. This work thus provides evidence of a blowing-snow sublimation process, which is a key step in producing bromine-enriched SSA. In general, this work improved our understanding of ODE processes by combining a variety of measurements with atmospheric models, and it facilitated both improved modelling of the atmosphere and the interpretation of the measurements.

Chapter 5

5 Pandora and Brewer Total Ozone Measurements

Routine TCO measurements started in the 1920s with the Dobson instrument (Dobson, 1968b). During the International Geophysical Year, 1957, the worldwide Dobson ozone-monitoring network was formed. Stratospheric ozone has been an important scientific topic since the 1970s and became a matter of intense interest with the discovery and subsequent studies of the Antarctic ozone hole (Farman et al., 1985; Solomon et al., 1986; Stolarski et al., 1986) and depletion on the global scale (Stolarski et al., 1991; Ramaswamy et al., 1992). To improve their accuracy and to automate the TCO measurements, the Brewer spectrophotometer was developed in the early 1980s (Kerr et al., 1981; 1988). In 1988, the Brewer was designated (in addition to the Dobson) as the WMO/GAW standard for total column ozone measurement. By 2014, there were more than 220 Brewer instruments installed around the world, with most in operation today. To maintain the measurement stability and characterize each individual Brewer, field instruments need to be regularly calibrated against the travelling standard reference instrument. The travelling standard itself is calibrated against the set of three Brewer instruments (serial numbers 8, 14, and 15) operated by ECCC, located in Toronto, and known as the Brewer reference Triad (BrT) (Fioletov et al., 2005). Due to the well-known stray light issue in the UV region (Bais et al., 1996; Fioletov et al., 2000), the MkIII Brewer (double Brewer) was introduced in 1992. The double Brewer has two spectrometers in series, significantly improving UV response and measuring global UV spectral irradiance, O_3, SO_2 and aerosol optical depth. The double Brewer instruments also have a set of three instruments (serial numbers 145, 187, and 191) co-located with BrT to form the Brewer reference Triad-Double (BrT-D). Individual Brewer instruments of the BrT and BrT-D are independently calibrated at Mauna Loa, Hawaii every 2-6 years (Fioletov et al., 2005).

The Pandora system was developed at NASA's Goddard Space Flight Center and first deployed in the field in 2006. Pandora instruments are based on a commercial spectrometer with stability and stray light characteristics that make them suitable candidates for both direct-sun and zenith-sky measurements of total column ozone and other trace gases (Herman et al., 2009; Tzortziou et al., 2012). Pandora instruments have been tested and deployed in multiple scientific measurement campaigns around the world. These include the CINDI campaign in the Netherlands in 2009 (Roscoe et al., 2010) and four NASA DISCOVER-AQ campaigns since 2011 (Tzortziou et al., 2012). The Pandora instruments have been used for validation of satellite ozone (Tzortziou et al., 2012) and NO_2 (Herman et al., 2009; Tzortziou et al., 2012) measurements. By 2015, several long-term Pandora sites had been established in the United States and worldwide (including Austria, Canada, Canary Islands, Finland, and New Zealand). In 2013, two Pandora instruments (serial numbers 103 and 104) were deployed at Toronto co-located with BrT and BrT-D on the roof of the ECCC Downsview building (43.782° N, 79.47° W).

The instrument random uncertainties of BrT were analysed by Kerr et al. (1998) and Fioletov et al. (2005) using similar methods. These methods both require knowledge of the extra-terrestrial calibration (ETC) values, the ozone absorption coefficients, and the Rayleigh scattering coefficients for each instrument. Fioletov et al. (2005) reported that the random uncertainties of individual observations from the BrT are within ±1% in about 90% of all measurements. This work takes a different approach, using a statistical variable estimation method to determine the random uncertainties for BrT, BrT-D, and the two Pandora instruments together. The variable estimation method follows the work of Fioletov et al. (2006) to estimate the random uncertainties with the assumption that there is no multiplicative bias between Pandoras and Brewers. Details of the method are provided in Section 5.2.1. Since the instrument random uncertainties for BrT were last reported 10 years ago using data to 2004 (Fioletov et al., 2005), this work provides a new assessment of the performance of both the BrT and BrT-D in recent years, along with a comparison between coincident Brewer and Pandora measurements.

It is well known that the Dobson and Brewer ozone retrievals exhibit dependence on stratospheric temperature (Kerr et al., 1988; Scarnato et al., 2009; Redondas et al., 2014). This is because the retrievals use different wavelengths and ozone cross sections measured at fixed temperatures. Brewer instruments have a very low temperature dependence (typically < 0.1 $\% \ K^{-1}$) (Kerr et al., 1988; Van Roozendael et al., 1998; Kerr, 2002; Scarnato et al., 2009; Herman et al., 2015). For example, Kerr et al. (1988) reported a 0.07 $\% \ K^{-1}$ temperature dependence for Brewer #8 (one of the BrT) and Kerr (2002) reported a 0.094 $\% \ K^{-1}$ temperature dependence for Brewer #14 (one of the BrT). In addition, Scarnato et al. (2009) reported that

Brewer instruments (#40, #72, and #156) exhibited less temperature dependence than Dobson instruments (#83 and #101). Redondas et al. (2014) reported a 0.133 % K^{-1} temperature dependence for Dobson #83.

The Pandora ozone retrievals are more sensitive to stratospheric temperatures. In Herman et al. (2015), the temperature dependence for Pandora #34 (0.333 % K^{-1}) was determined by applying retrievals at a series of different ozone temperatures from 215 to 240 K for the ozone cross sections, and then obtaining a linear fit to the percent change. As the small Brewer temperature dependence is known, coincident measurements from the BrT and BrT-D were used to determine the temperature dependence factors for Pandora #103 and #104, and then the correction to remove the difference between Pandora and Brewer instruments was applied.

5.1 Instruments and Datasets

5.1.1 Pandora

The Pandora spectrometer system uses a temperature-stabilized (1°C) symmetric Czerny-Turner system with a 50 micron entrance slit, and 1200 lines/mm grating. Unlike the Brewer instruments, which only measure intensities at selected wavelengths, the Pandora instruments, with a 2048×64 back-thinned Hamamatsu CCD detector, record spectra from 280 to 530 nm at 0.6 nm resolution (Herman et al., 2015). The spectra are analyzed using the DOAS technique (Noxon, 1975; Solomon et al., 1987; Platt, 1994; Platt and Stutz, 2008), in which absorption cross sections for multiple atmospheric absorbers (including ozone, NO_2, SO_2, HCHO, and BrO) are fitted to the spectra (Tzortziou et al., 2012). The Daumont, Brion, and Malicet (DBM) (Daumont et al., 1992; Brion et al., 1993; Brion et al., 1998) ozone cross section at an effective temperature of 225 K is used in the Pandora retrievals (Herman et al., 2015). Additional information on Pandora calibrations and operation can be found in Herman et al. (2015).

Two commercial Pandoras (#103 and #104) were used in this study with no modifications to operational and data processing algorithms (available from SciGlob http://www.sciglob.com/). Pandoras #103 and #104 were deployed in Toronto in September 2013, and in this work, all available Pandora data from these instruments are used. Pandora #104 was moved to the Canadian oil sands region in August 2014. Following the work of Tzortziou et al. (2012), the

Pandora ozone dataset is filtered to remove data from which the normalized root-mean square (RMS) of weighted spectral fitting residuals is greater than 0.05 and the Pandora calculated standard uncertainty (Tzortziou et al., 2012) in TCO is greater than 2 DU.

5.1.2 Brewer

The Brewer instruments use a holographic grating in combination with a slit mask to select six channels in the UV (303.2, 306.3, 310.1, 313.5, 316.8, and 320 nm) to be detected by a photomultiplier. The first and second wavelengths are used for internal calibration and measuring SO_2 respectively. The four longer wavelengths are used for the ozone retrieval. The total column of ozone is calculated by analysing the relative intensities at these different wavelengths using the Bass and Paur (1985) ozone cross sections at a fixed effective temperature of 228.3° K (Kerr, 2002).

Table 12: Coincident measurement periods and number of data points for comparisons between Pandora and Brewer instruments.

		Pandora#103	Pandora#104
Brewer#8	Coincident period	18 Oct 2013 to 14 May 2015	20 Jan 2014 to 08 Aug 2014
	Coincident data points	5008	2671
Brewer#14	Coincident period	25 Nov 2013 to 24 Dec 2015	16 Feb 2014 to 08 Aug 2014
	Coincident data points	7797	1701
Brewer#15	Coincident period	31 Nov 2013 to 31 Jul 2014	20 Jan 2014 to 08 Aug 2014
	Coincident data points	2297	1376
Brewer#145	Coincident period	15 Jan 2015 to 24 Dec 2015	N/A
	Coincident data points	1474	N/A
Brewer#187	Coincident period	18 Oct 2013 to 23 Apr 2014	20 Jan 2014 to 23 Apr 2014
	Coincident data points	608	397
Brewer#191	Coincident period	20 Nov 2013 to 24 Dec 2015	21 Jan 2014 to 08 Aug 2014
	Coincident data points	5359	1490

Most of the instruments in the BrT (#8, #14, and #15) and BrT-D (#145, #187, and #191) have been in operation since Pandora instruments were deployed. However, there are a few measurement gaps for some of the Brewers. For example, Brewers #14 and #15 were recalibrated at Mauna Loa, Hawaii in October 2013, and Brewer #145 was in Spain in March 2014. Some periods were excluded due to instrument malfunction and repairs. The coincident measurement periods for the instruments are shown in Table 12. The TCO data from Brewer and

Pandora instruments are both time binned (3 min) for the comparison. Following the work of Tzortziou et al. (2012), the Brewer dataset is filtered to remove data with calculated standard uncertainty in TCO greater than 2 DU. In addition, the Brewer dataset is filtered for clouds by removing data for which the logarithm of the signal at 320 nm is less than the mean value minus two standard deviations (4% of data was removed with this filter).

5.1.3 OMI

OMI is a nadir-viewing near-UV/Vis spectrometer aboard NASA's Earth Observing System (EOS) Aura satellite (launched in July 2004). The OMI instrument measures the solar radiation backscattered by the Earth's atmosphere and surface between 270-500 nm with a spectral resolution of about 0.5 nm (Levelt et al., 2006). The OMI TCO data are retrieved using both the Total Ozone Mapping Spectrometer (TOMS) technique (developed by NASA (Bhartia and Wellemeyer, 2002) and based on a retrieval using four wavelengths at 313, 318, 331, and 360 nm) and the DOAS technique (developed by KNMI (Veefkind et al., 2006; Kroon et al., 2008) and based on the spectrum measured in the wavelength range 331.1-336.6 nm). The OMI TCO validation done by Balis et al. (2007) shows a globally averaged agreement of better than 1% for OMI-TOMS data and better than 2% for OMI-DOAS data in comparison with Brewer and Dobson measurements.

The OMI TCO products used in the present study are the Level-3 Aura/OMI daily global TCO gridded product (OMTO3e) retrieved by the enhanced TOMS Version 8 algorithm (Balis et al., 2007). The OMTO3e data (Bhartia, 2012) are generated by the NASA OMI science team by selecting the best pixel (shortest path length) data from the good quality Level-2 TCO orbital swath data (for example, L2 observations with SZA < 70°; details can be found in (Bhartia, 2012) that fall in the 0.25×0.25° global grids. The OMTO3e data that from the grid point over the ground-based site are used in this work to validate the correction method for Pandora TCO data.

5.1.4 ECMWF Interim Data

In this work, the ozone-weighted effective temperature was used to assess the temperature sensitivity of Pandora ozone retrievals. Temperature and ozone profiles were extracted from the ERA-Interim data for 2013-2015 (Dee et al., 2011) with 0.5°×0.5° spatial resolution on 37 standard pressure levels, available from http://apps.ecmwf.int/datasets/. The ozone-weighted effective temperature (T_{eff}) is calculated based on daily ozone and temperature profiles (at 18:00 UTC) over Toronto, defined as

$$T_{eff} = \sum_{i=6}^{30} w_{eff,i} \cdot T_i \tag{5.1}$$

$$w_{eff,i} = \frac{n_i}{\sum_{j=6}^{30} n_j} = \frac{MMR_i \cdot p_i / T_i}{\sum_{j=6}^{30} MMR_j \cdot p_j / T_j} \tag{5.2}$$

where w_{eff} is the weighting function, T_i is the temperature, n_i is the ozone number density, MMR_i is the ozone mass mixing ratio, and p_i is the pressure at pressure level i. In this work, profile data on ECMWF standard pressure levels from #6 to #30 (10-800 mbar) were used to decrease the noise from variable surface temperatures.

5.2 Statistical Uncertainty Estimation

Figure 5.1 shows the time series of the total column ozone datasets used in this work. The seasonal cycles of TCO from the ground-based and satellite instruments track each other well, and the high-frequency daily variations from all ground-based instruments are consistent.

By comparing the same quantity retrieved from different remote sensing instruments, the differences between them can be characterized, which are a combination of random uncertainties and systematic bias. Theoretically, information about the random uncertainties can be derived from the measurements themselves (Grubbs, 1948; Toohey and Strong, 2007). The following method for doing this is described in Fioletov et al. (2006), and briefly explained below.

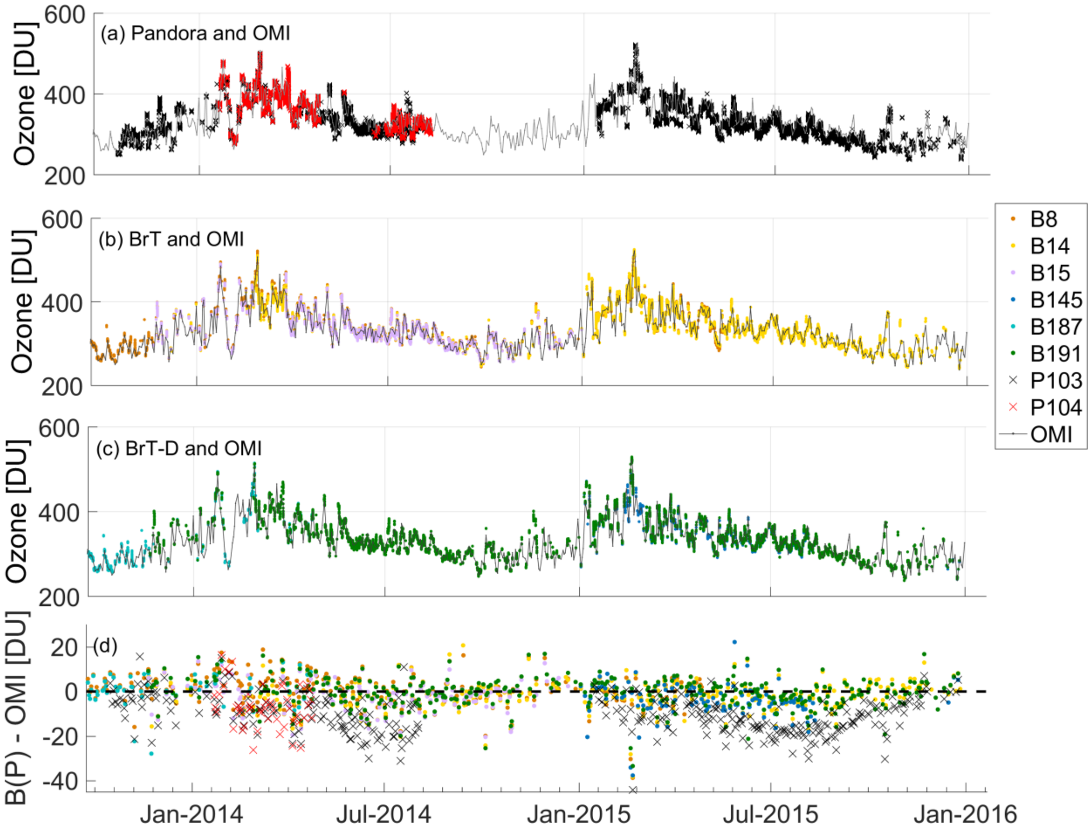

Figure 5.1: Ozone total column data from Pandoras, Brewers, and OMI: (a) Pandora #103 and #104 compared with OMI, (b) Brewer triad (Brewer # 8, #14, and #15) compared with OMI, (c) Brewer triad double (Brewer #145, #187, and #191) compared with OMI, (d) the daily mean difference, Brewer (or Pandora) – OMI.

5.2.1 Methodology

5.2.1.1 Method 1

Define the two types of measured TCO (denoted as M_B and M_P, for Brewer and Pandora, respectively) as simple linear functions of the true TCO value (X) and instrument random uncertainties (δ_B and δ_P), and assume that there is no multiplicative or additive bias between Pandora and Brewer, giving

$$M_B = X + \delta_B$$

$$M_P = X + \delta_P \ . \tag{5.3}$$

If assume that the instrument random uncertainties are independent of the measured TCO, the variance of *M* is the sum of the variances of *X* (around the mean of the dataset) and δ,

$$\sigma_{M_B}^2 = \sigma_X^2 + \sigma_{\delta_B}^2$$

$$\sigma_{M_P}^2 = \sigma_X^2 + \sigma_{\delta_P}^2 \; . \tag{5.4}$$

If the difference between Pandora and Brewer does not depend on *X* (no multiplicative bias), and the random uncertainties of the two instruments are not correlated, then the variance of the difference is equal to the sum of the variance of the random uncertainties,

$$\sigma_{M_B-M_P}^2 = \sigma_{\delta_B}^2 + \sigma_{\delta_P}^2 \; . \tag{5.5}$$

Since the measured TCO and the difference between the Pandora and Brewer datasets are known, the variance of the TCO and instrument random uncertainties can be solved by

$$\sigma_X^2 = \left(\sigma_{M_B}^2 + \sigma_{M_P}^2 - \sigma_{M_B-M_P}^2\right)/2$$

$$\sigma_{\delta_B}^2 = \left(\sigma_{M_B}^2 - \sigma_{M_P}^2 + \sigma_{M_B-M_P}^2\right)/2$$

$$\sigma_{\delta_P}^2 = \left(\sigma_{M_P}^2 - \sigma_{M_B}^2 + \sigma_{M_B-M_P}^2\right)/2 \; . \tag{5.6}$$

Eq. 5.6 can be used to estimate the standard deviation (SD) of instrument random uncertainties (σ_{δ_B} and σ_{δ_P}) and the SD of ozone variability (σ_X). The variances $\sigma_{M_i}^2$ and $\sigma_{M_B-M_P}^2$ are not actually known; with some uncertainty, they can be estimated from the available measurements. It can be shown that the uncertainties in the σ_X^2, $\sigma_{\delta_B}^2$, and $\sigma_{\delta_P}^2$ estimates depend on the sum of all three variances $\sigma_{M_B}^2$, $\sigma_{M_P}^2$, and $\sigma_{M_B-M_P}^2$, and can be high even if the estimated variance itself is low (but one or more of the variances $\sigma_{M_B}^2$, $\sigma_{M_P}^2$, and $\sigma_{M_B-M_P}^2$ are high). The estimates are thus only as accurate as the least accurate of these parameters. The variance estimates can be improved by increasing the number of data points or by reducing variances of *X* by removing some of the daily variability. To remove the variability in *X*, the residual ozone here is defined as the difference between the high-frequency TCO and the low-frequency TCO measured by an instrument,

$$dM_{res} = M_{high-f} - M_{low-f} \quad . \tag{5.7}$$

For example, the Brewer residual ozone could be the Brewer TCO measurements minus the Brewer ozone daily mean for that day, whereas the corresponding Pandora residual ozone would be the Pandora TCO measurements minus the Pandora ozone daily mean. By subtracting the low-frequency signal, most of the ozone variability is removed. In addition, as proposed in Fioletov et al. (2005), to improve the removal of the bias, the following statistical model can be used to calculate the low-frequency signal:

$$M_{low-f} = A_B \cdot I_B + A_P \cdot I_P + B \cdot (t - t_0) + C \cdot (t - t_0)^2 \tag{5.8}$$

where t is the time of the measurement and t_0 is the time of local solar noon. I_B is an indicator function for the Brewer instrument; it is set to 1 if the TCO is measured by the Brewer and to 0 otherwise. I_p is the indicator function for the Pandora. The coefficients A_B, A_P, B, and C are estimated by the least-squares method for each day (for example, the calculated low-frequency signal for Brewer and Pandora will share the same B and C terms, but they have their own offsets A_B and A_P). In the following, the residual ozone calculated by subtracting the daily mean value will be referred as residual type 1, and that obtained by subtracting this 2nd order function as residual type 2. The present work is focused on evaluating the high-quality TCO data. Thus to avoid the stray light effect, in the statistical uncertainty estimation, only Pandora and Brewer data with ozone AMF less than 3 were used (see Section 5.4 for more details about the stray light effect).

5.2.1.2 Method 2

Note that the assumption of no multiplicative and additive bias between the Pandora and Brewer measurements might be not valid, since it is already known that the Pandora and Brewer instruments have different temperature sensitivities (the temperature effect). Thus it is reasonable to modify the linear function Eq. 5.3 to

$$M_B = X + \delta_B$$

$$M_P = \beta \cdot X + \delta_P \tag{5.9}$$

where, a relative multiplicative bias β is introduced to describe the potential bias between Pandora and Brewer measurements. Similar to method 1, the following equations should be obtained if the assumption that the two instruments' measurement uncertainties are uncorrelated is made,

$$\sigma_{M_B}^2 = \sigma_X^2 + \sigma_{\delta_B}^2$$

$$\sigma_{M_P}^2 = \beta^2 \cdot \sigma_X^2 + \sigma_{\delta_P}^2$$

$$\sigma_{M_B M_P} = \beta \cdot \sigma_X^2 \quad . \tag{5.10}$$

Now there are three equations with four unknowns. There are many ways to solve the above equations with various assumptions. Dunn (2009) explored the relative assumptions and solutions in detail in a general context. In this work, one of the simple assumptions that the precision of one measurement is known (equivalent to σ_δ^2) was followed. Generally, this is justified if the precision of the standard measurement is known, e.g., has good calibration, high precision, and etc. better than the other. However, without the knowledge of which instrument is more precise, here Brewer calculated standard uncertainty (the standard error of the TCO from the Brewer dataset) will be used to help estimate Pandora uncertainty, then Pandora calculated standard uncertainty (the standard error of the TCO from the Pandora dataset) will be used to help estimate Brewer uncertainty.

Following Toohey and Strong (2007), the predictions of statistical parameters based on calculated quantities (the calculated standard uncertainty) are denoted by a tilde (~) above the variable, and the estimates (the estimated uncertainty) are denoted by a caret. For example, if the calculated uncertainty from Brewer is used, then the Pandora uncertainty and bias can be estimated by

$$\hat{\sigma}_{\delta_P}^2 = \sigma_{M_P}^2 - \frac{\sigma_{M_B M_P}^2}{\sigma_{M_B}^2 - \tilde{\sigma}_{\delta_B}^2}$$

$$\hat{\beta}_P = \frac{\sigma_{M_B M_P}}{\sigma_{M_B}^2 - \tilde{\sigma}_{\delta_B}^2} \quad . \tag{5.11}$$

Similarly, estimated Brewer uncertainty and bias are

$$\hat{\sigma}_{\delta_B}^2 = \sigma_{M_B}^2 - \frac{\sigma_{M_B M_P}^2}{\sigma_{M_P}^2 - \tilde{\sigma}_{\delta_P}^2}$$

$$\hat{\beta}_B = \frac{\sigma_{M_P}^2 - \tilde{\sigma}_{\delta_P}^2}{\sigma_{M_B M_P}} \quad . \qquad (5.12)$$

5.2.2 Results

In this work, two different types of residual ozone (see Eq. 5.7) were calculated as defined in Section 5.2.1.1, and then they were used to calculate the instrument random uncertainty with the statistical variable estimation method (Eq. 5.6, more details can be found in Fioletov et al. (2006)). For example, Eq. 5.7 and 5.8 were used to calculate two type 2 residuals for both Brewer and Pandora ($dM_{b\text{-}res2}$ and $dM_{p\text{-}res2}$), and then these residuals were used to calculate the difference ($dM_{b\text{-}res2}$ - $dM_{p\text{-}res2}$). Next, their variances values $\sigma^2(dM_{b\text{-}res2})$, $\sigma^2(dM_{p\text{-}res2})$, and $\sigma^2(dM_{b\text{-}res2} - dM_{p\text{-}res2})$ were calculated. Those variance terms are used in Eq. 5.6 to estimate the random uncertainties. The residual types and relevant terminologies are summarised in Table 13.

Table 13: Definition of terminologies used in the uncertainty estimation.

	Definition
Estimated random uncertainty (σ_δ)	Random uncertainty estimated using the statistical variable estimation method described in Section 5.2.1
$M_{\text{high-f}}$	High-frequency TCO measurements, averaged in 3 min bin
$M_{\text{low-f (daily-mean)}}$	Low-frequency TCO, calculated as the daily mean TCO
$M_{\text{low-f (2nd order function)}}$	Low-frequency TCO, calculated using the 2nd order function (Eq. 5.8)
Residual type 1	$M_{\text{high-f}} - M_{\text{low-f (daily-mean)}}$
Residual type 2	$M_{\text{high-f}} - M_{\text{low-f (2nd order function)}}$
Method 1	Estimate both Pandora and Brewer random uncertainty, but without bias between Pandora and Brewer (see Eq. 5.6)
Method 2	Estimate Pandora (Brewer) random uncertainty and bias, but need use Brewer (Pandora) predicated error (see Eqs. 5.11 and 5.12)

Figure 5.2 shows the Brewer estimated random uncertainties obtained using the two types of residual ozone data (Figure 5.2a for residual type 1, Figure 5.2b for type 2). For example, in Figure 5.2a, the estimated random uncertainty with Method 1 for Brewer #8 using Pandora #103 data (residual type 1, derived from M_{P103}) is shown as a black square in the column for Brewer

#8, while its estimated random uncertainty with Method 1using Pandora #104 data (residual type 1, derived from M_{P104}) is shown as a red triangle in the same column. The results with Method 2 are shown as grey and pink symbols. Figure 5.2 demonstrates that type 1 (Figure 5.2a) and type 2 (Figure 5.2b) residual ozone data provide comparable results, and confirm that Brewer instruments have random uncertainties of 1-2 DU.

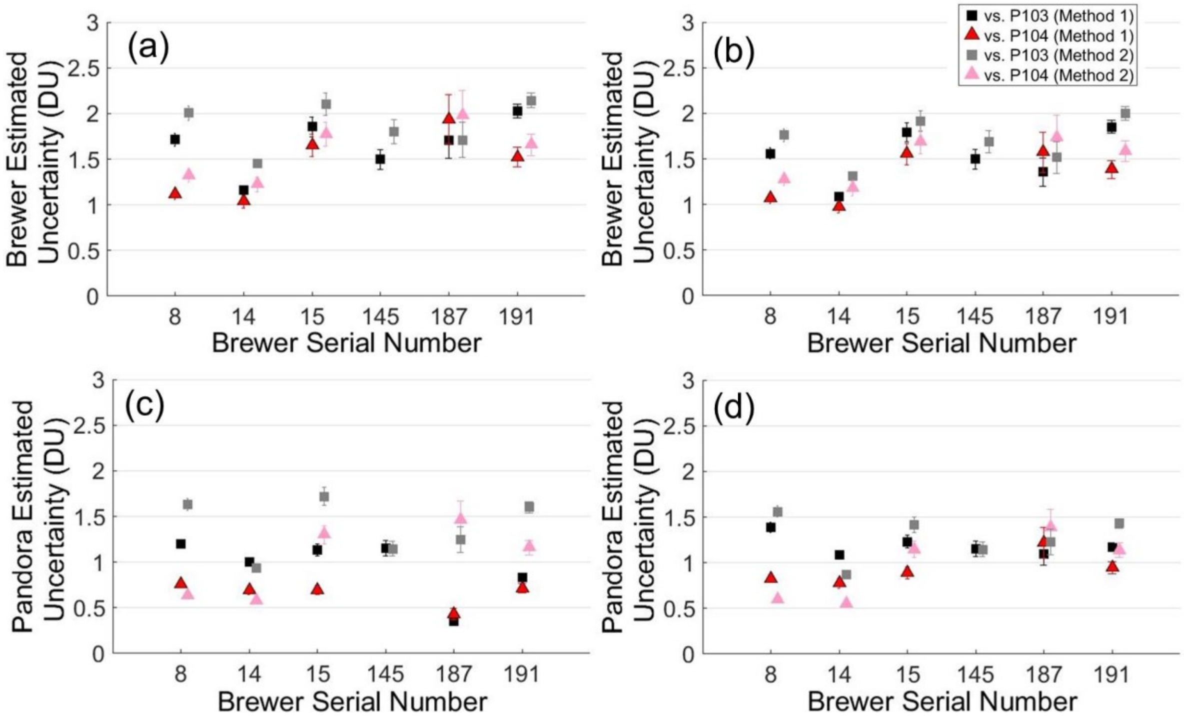

Figure 5.2: Estimated random uncertainties: for the Brewer instruments using (a) residual ozone type 1, and (b) residual ozone type 2; for the Pandora instruments using (c) residual ozone type 1, and (d) residual ozone type 2. The black (grey) squares indicate data from Pandora #103 and the red (pink) triangles indicate data from Pandora #104 with Method 1 (2). The error bars show the 95 % confidence bounds.

Figure 5.2 also shows the Pandora estimated random uncertainties using the two types of residual ozone data (Figure 5.2c for residual type 1, Figure 5.2d for type 2). For example, in Figure 5.2c, the estimated random uncertainty for Pandora #103 using Brewer #8 data is shown as a black square in the column of Brewer #8, while its estimated random uncertainties using other Brewer data are shown by respective Brewer columns. Figure 5.2 demonstrates that the Pandora instruments have estimated random uncertainties less than 1.5 DU. Slight differences in the estimated Pandora random uncertainties were found using different Brewer instruments. This is due to the sample size; when the sample size is large (> 1200 coincident points, see Table 12), the Pandora estimated random uncertainties from different instruments are more consistent. For example, in Figure 5.2c, one of the estimated random uncertainties for Pandora #103 (black square in Brewer #187 column) is below 0.5 DU. This result is undesirable (the value is ~0.5 DU lower than the other values), but not unusual. Dunn (2009) describes this issue in detail and points out that the low (even negative in some cases) variance estimate is due to small sample size. In general, Dunn (2009) concludes that, even with the correct model, the comparisons and estimation of precision are only viable with large sample sizes. Figure 5.3c shows that the low variance was indeed from the smallest sample size (608 coincident points for Pandora #103 vs. Brewer #187 and 397 for Pandora #104 vs. Brewer #187). In addition, when using the data from the same pair of Brewer and Pandora instruments, the estimated random uncertainty for Pandora is consistently lower than that for Brewer by ~0.5 DU. Figure 5.2 also demonstrates that both statistical estimation methods 1 and 2 provide similar estimated random uncertainties for Brewer and Pandora, while method 2 is more sensitive to ozone natural variability.

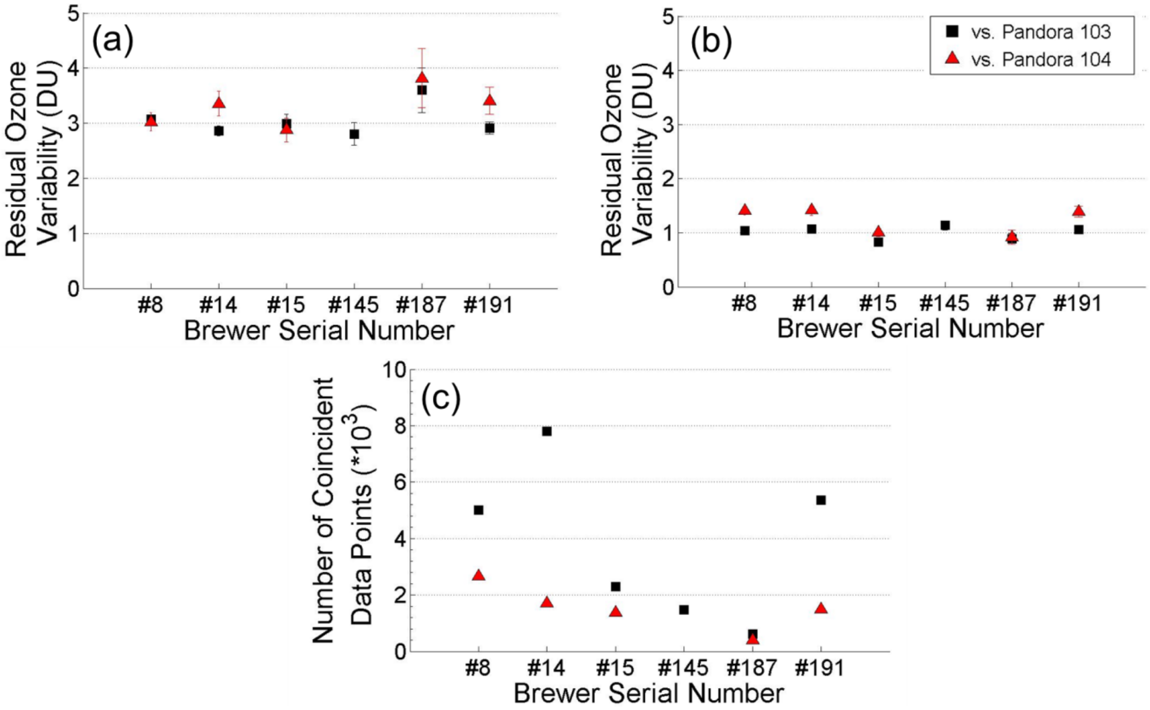

Figure 5.3: Estimated residual ozone variability (σ_X) using (a) residual ozone type 1, and (b) residual ozone type 2. (c) Number of coincident measurements used in the statistical uncertainty estimation. The black squares indicate data from Pandora #103 and the red triangles indicate data from Pandora #104. The error bars show the 95 % confidence bounds.

Fioletov et al. (2006) estimated natural ozone variability (σ_X) using Eq. 5.6. However, because this work is using the residual ozone instead of the TCO in the statistical analysis, the σ_X calculated from the current method is not the estimated natural ozone variability but the estimated residual ozone variability for the measurement period. It can be used to characterize the difference between residual types 1 and 2. Figure 5.3a shows the estimated residual ozone variability using residual type 1 data, while Figure 5.3b shows the variability using residual type 2. Figure 5.3a and 5.3b demonstrate that residual type 1 data has larger variability than type 2 data, indicating that using the daily mean value as the low-frequency signal did not fully remove the natural ozone variability. Ideally, the random uncertainty estimate should only contain random noise caused by the instrument and no natural ozone variation. Scatter plots of Brewer vs. Pandora residual ozone (Figure 5.4) illustrate the same results. Figure 5.4 shows that the correlation coefficients for residual type 1 (R = 0.813 for Brewer #8 vs. Pandora #103, see Figure 5.4a; 0.909 for Brewer #8 vs. Pandora #104, see Figure 5.4b) are higher than the ones for residual type 2 (0.333 for Brewer #8 vs. Pandora #103, see Figure 5.4c; 0.688 for Brewer #8 vs. Pandora #104, see Figure 5.4d). The low correlation coefficients for ozone residual type 2 data indicate that the ozone variability has been largely removed from Pandora and Brewer data. Thus when this work use residual ozone type 2, even with relatively small sample size, the estimated uncertainties for Pandoras are still consistent with those obtained from comparisons with other Brewers having larger sample sizes (see Figure 5.2c and 5.2d, Brewer #187 column).

To summarise, this work tested two different methods for calculating residual ozone, and applied them in the statistical uncertainty estimation. The comparison of two residuals helps us understand the variable estimation method. Although using the daily mean value as a low-frequency signal (as in the residual type 1 calculation) has some shortcomings, it is more straightforward than using the complex 2nd order statistical model (Eq. 5.8). By showing the consistency of results from both type 1 and 2 in Figure 5.2, this work validated the use of the 2nd order statistical model (Eq. 5.8) and proved some of the advantages when using type 2. For example, the residual type 2 could work with a smaller dataset than the residual type 1 (without making the estimated variance unrealistic, too low or even negative). In general, Figure 5.2 demonstrates that the Pandora TCO data has ~0.5 DU smaller estimated random uncertainties compared to the Brewer TCO data. The mean estimated random uncertainties for BrT and BrT-D are in the range of 1-2 DU (~0.6%). The mean estimated random uncertainties for Pandora #103 and #104 are in the range of 0.5-1.5 DU (~0.4%). These results confirm the quality of the TCO data, with all eight instruments meeting the GAW requirement for a precision better than 1% to measure ozone (WMO, 2014).

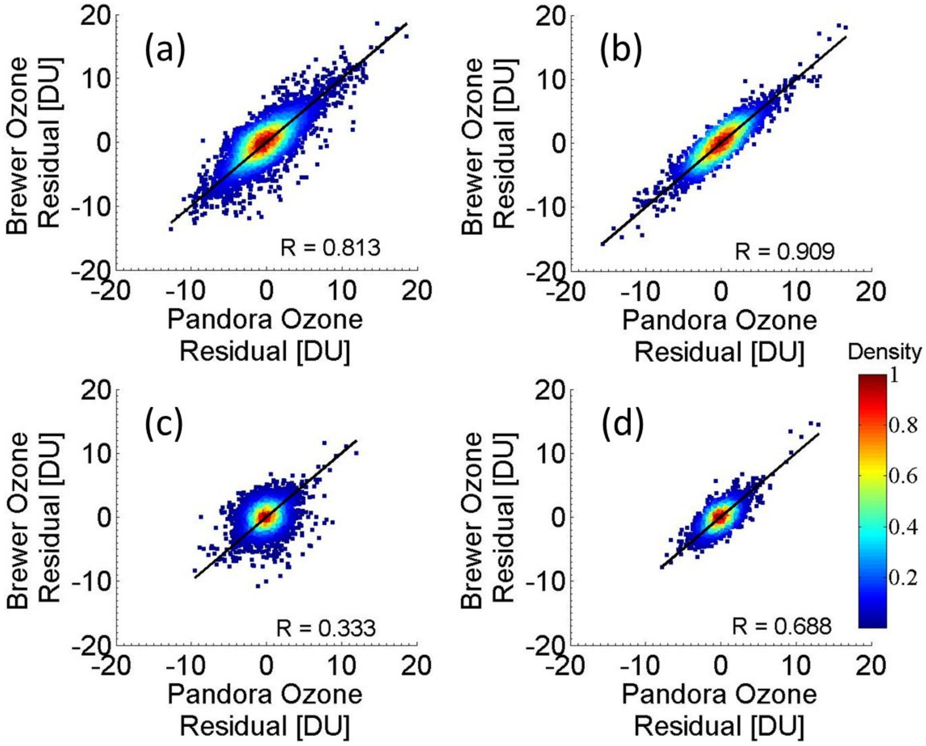

Figure 5.4: Scatter plots for residual ozone type 1 and 2, colour coded by the normalized density of the points. (a) Brewer #8 vs. Pandora #103 (residual type 1), (b) Brewer #8 vs. Pandora #104 (residual type 1), (c) Brewer #8 vs. Pandora #103 (residual type 2), (d) Brewer #8 vs. Pandora #104 (residual type 2). The black line is the 1-to-1 line.

5.3 Temperature Dependence Effect and Correction

5.3.1 Methodology

When comparing Pandora and Brewer TCO data, a clear seasonal structure and a bias in the difference and ratio can be seen. Figure 5.5a shows the time series of Brewer #14 – Pandora #103 TCO difference; the seasonal amplitude is 3-4 DU and the mean bias is 10.81 DU. Figure 5.5b (which uses the corrected data) will be discussed in Section 0. The locally weighted scatterplot smoothing fit (Lowess(x), the dashed line) is based on local least squares fitting applied to a specified *x* fraction of the data (Cleveland and Devlin, 1988). The bias between Pandora and Brewer TCO is mainly due to the fact that both retrievals depend on the choice of ozone absorption cross section (Scarnato et al., 2009; Herman et al., 2015).

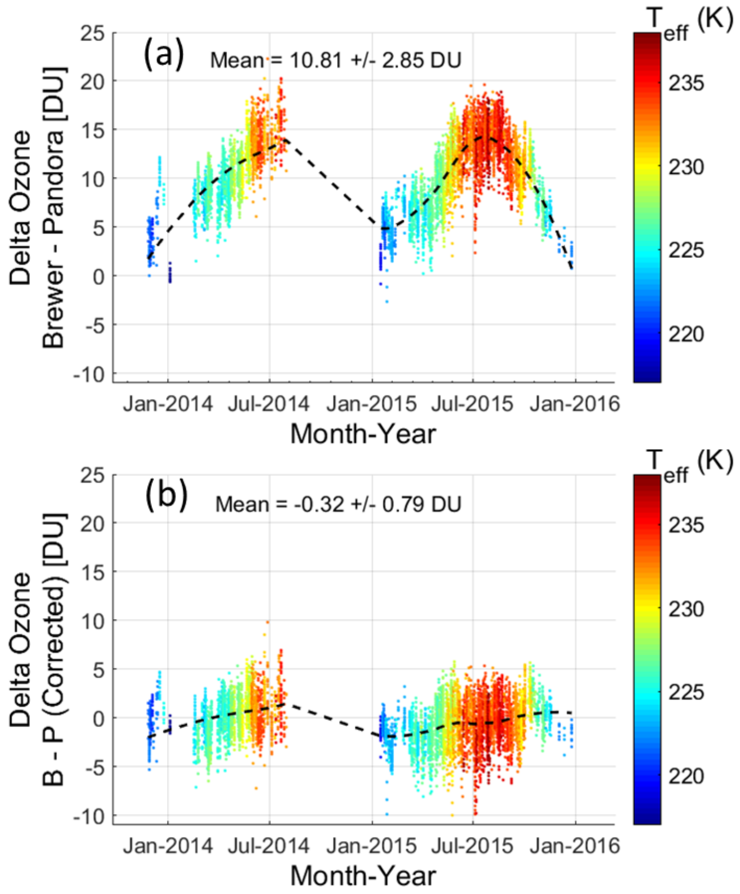

Figure 5.5: Time series of Brewer #14 – Pandora #103 TCO difference colour coded by ozone effective temperature (see Eq. 5.1): (a) before applying the temperature dependence correction, (b) after applying the correction. The dashed lines are Lowess(0.5) fits.

The Brewer TCO in this work was retrieved using the standard Brewer network operational ozone cross section (Bass and Paur, 1985), while the Pandora TCO was retrieved using the standard Pandora network operational ozone cross section (the DBM ozone cross section). Redondas et al. (2014) reported that changing the Brewer operational ozone cross section from Bass and Paur (1985) to Daumont et al. (1992) (DBM) will change the calculated TCO by -3.2%. In addition to the offset caused by the use of different ozone cross sections, the seasonal difference between Pandora and Brewer TCO data is due to their differing temperature dependence, which varies from instrument to instrument because of the differences in ozone retrieval algorithm and instrument design. Moreover, even for the same type of instrument, the temperature sensitivity can be different due to imperfections in the wavelength settings and slit function for each individual instrument. This work will study these differences (offset and temperature effect) by using the standard TCO products from Pandora and Brewer instruments.

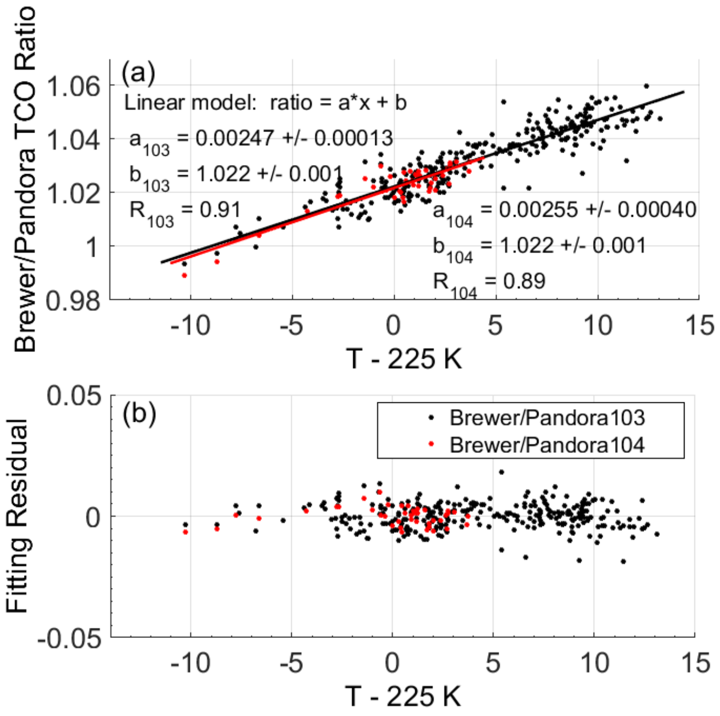

Figure 5.6: Linear regression of Brewer/Pandora TCO ratio as a function of effective temperature minus 225 K. (a) Linear regression results; (b) residual plot of the linear regression.

In this work, ECMWF Interim ozone and temperature profiles were used to calculate daily ozone effective temperature (described in Section 5.1.4). Then the following simple linear regression model was used to find the temperature dependence factor for Pandora instruments,

$$\frac{M_B}{M_P} = a \cdot \left(T_{eff} - 225\right) + b \tag{5.13}$$

where a is the temperature dependence factor for Pandora, b is the (systematic) multiplicative bias between Pandora and Brewer, and 225 refers to effective temperature of 225 K for ozone cross-sections used in the Pandora retrievals. Here, the M_B and M_P are TCO daily means measured by the Brewer and Pandora respectively. To increase the number of coincident data points, the M_B dataset is formed by merging all measurements from the six Brewers (see Table

12). A successfully merged M_B data point has coincident measurements from at least two Brewers, to avoid domination by a single instrument. The coincident time period of the M_B and M_{P103} datasets is from October 2013 to December 2015 with 272 coincident days (points). Figure 5.6 shows the linear regression results for Pandoras #103 and #104. This work found the relative temperature dependence factor for Pandora #103 to be 0.247 ± 0.013 % K^{-1} (from the term *a* in Eq. 5.13), with a 2.2 ± 0.1 % multiplicative bias (from the term *b* in Eq. 5.13). Although Pandora #104 only has measurements from January to April 2014 (53 coincident days), the linear regression still results in a similar temperature dependence factor (0.255 ± 0.040 % K^{-1}) and the same bias as Pandora #103. The correlation coefficients for those two linear regressions are 0.91 and 0.89 respectively.

The Pandora temperature dependence factors were applied to the Pandora TCO to remove its bias and seasonal difference relative to Brewer TCO data. Similar to the correction function used in Herman et al. (2015) for Pandora #34, the following function was used to correct Pandora TCO data:

$$M_{corr} = M_P \cdot \left(a \cdot \left(T_{eff} - 225\right) + b\right) \tag{5.14}$$

where M_{corr} is corrected Pandora TCO, and other terms are as defined for Eq. 5.13. For the Pandora #103 dataset, this becomes

$$M_{corr} = M_{P103} \cdot \left(0.00247 \cdot \left(T_{eff} - 225\right) + 1.022\right) \tag{5.15}$$

where M_{p103} is the TCO data from Pandora #103. The temperature dependence factor (0.247 ± 0.013 % K^{-1}) and the multiplicative bias (1.022) are found in Figure 5.6. The same regression model and method give 0.255 ± 0.040 % K^{-1} temperature dependence factor with a 2% multiplicative bias to Pandora #104, and hence

$$M_{corr} = M_{P104} \cdot \left(0.00255 \cdot \left(T_{eff} - 225\right) + 1.022\right) \tag{5.16}$$

where M_{p104} is the Pandora #104 TCO. For comparison, Herman et al. (2015) derived the correction function for Pandora #34 as

$$M_{corr} = M_{P34} \cdot \left(0.00333 \cdot \left(T_{eff} - 225\right) + 1\right) \tag{5.17}$$

where the 0.00333 (0.333 % K^{-1}) is the temperature dependence factor for Pandora #34. Note that this value was determined by applying retrievals using ozone cross sections from 215 to 240 K, and then obtaining a linear fit to the percent change (Herman et al., 2015). However in this work, the factors for Pandora #103 and #104 were found by statistical analysis (comparison) of the Pandora and Brewer TCO datasets. Thus temperature dependence factor found by this work combines the temperature sensitivity from both Pandora and Brewer instruments, and describes the relative temperature sensitivity between the Pandora and Brewer standard TCO products. This factor is called as a "relative temperature dependence factor" (RTDF), while that from Herman et al. (2015) is an "absolute temperature dependence factor" (ATDF). Although the RTDF is a non-linear combination of ATDF from both Pandora and Brewer (note that the Pandora used an ozone cross section at an effective temperature of 225 K, while the Brewer used that at 223.8 K), a simple linear estimation of the RTDF from reported ATDFs still can be made. In fact, the reported ATDF for Pandora #34 (0.333 % K^{-1}, (Herman et al., 2015)) minus the reported ATDF for Brewer #8 and #14 (0.07 and 0.094 % K^{-1}, (Kerr et al., 1988; Kerr, 2002)) gives relative numbers (0.26 and 0.24 % K^{-1}) that are close to the model-calculated RTDF (~0.25 % K^{-1}). The correction functions from this work (Eqs. 15-16), which have a constant b term of 1.022 given 0.001 uncertainty, indicate a multiplicative bias of ~2% (not caused by the temperature effect) between the Pandora and Brewer instruments due to their different selection of ozone cross sections.

Merging data from all six Brewers could lead to variation of the Brewer temperature dependence, so sensitivity tests were performed on the dataset. Figure 5.3 summarises the tests; the combined Brewer data are merged from all available Brewer data during the data period indicated in the table. Figure 5.7 shows the RTDFs, multiplicative bias, correlation coefficient, and number of data points for the thirteen sensitivity tests. Tests 1 and 2 are the results adapted from Figure 5.6. Due to the small data size, the RTDF for test 2 has larger error bars than test 1. Test 3 shows Pandora #103 RTDF using combined Brewer data for the same time period as Pandora #104. Pandora #103 has a measurement gap from Aug. to Dec. 2014 due to instrument failure (see Figure 5.1), hence, tests 4 and 5 use combined Brewer data for 2013-2014 (~ one year coverage, before the instrument failure of Pandora #103) and 2015 (one year coverage, after Pandora #103 was repaired) separately. Brewer #191 was one of the most reliable Brewer instruments during the comparison period. Thus tests 6-8 use only Brewer #191 data; test 6 uses all available data (2013-2015), test 7 uses only 2013-2014 data (before the instrument failure of Pandora #103), test 8 uses 2015 data (after Pandora #103 was repaired). Tests 9-13 use individual Brewer data (all available data for each individual Brewer). For the thirteen tests, the RTDFs (see Figure 5.7a) are in the range of 0.24-2.9%, and the multiplicative biases (see Figure 5.7b) are in the range of 1.7-2.5%. The correlation coefficients (see Figure 5.7c) for most tests are above 0.8. In general, the RTDFs found for the Pandora instruments are stable when derived from combined Brewer data or reliable individual Brewer data. For this two-year data period, the derived RTDFs from BrT-D instruments are lower (0.241-0.246 % K^{-1}) than the ones from BrT instruments (0.262-0.290 % K^{-1}). However, with the large uncertainties on the estimated RTDFs and the bias, the current work could not conclude whether this is due to the different instrument designs or a sampling issue.

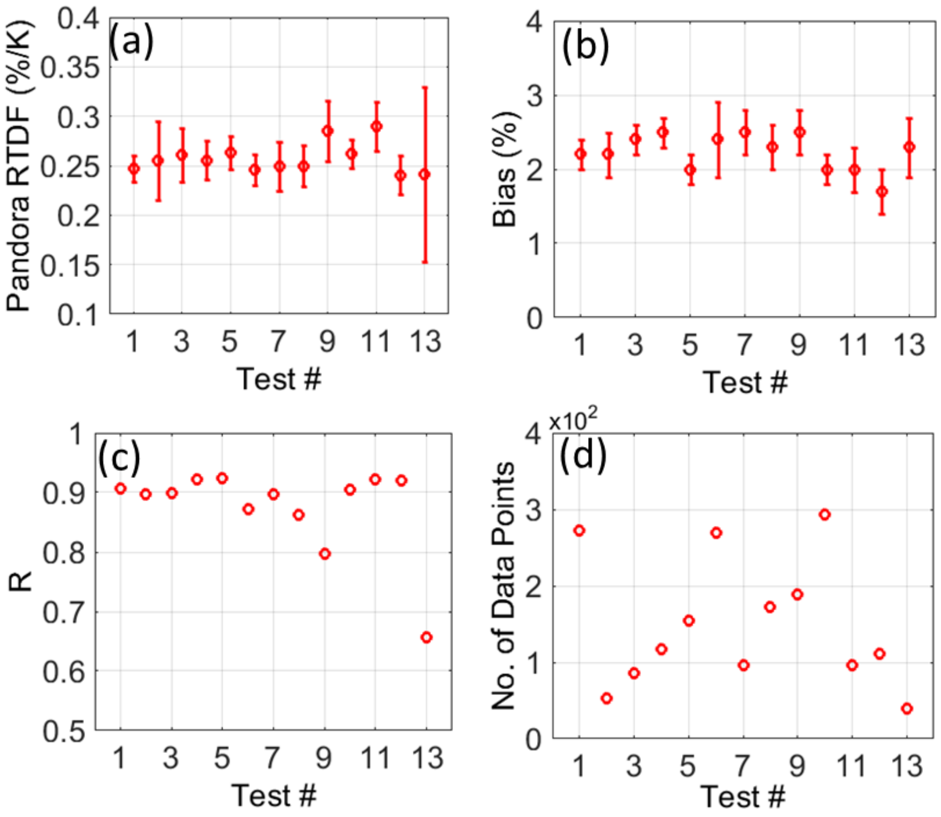

Figure 5.7: Pandora relative temperature dependence factors derived from 13 sensitivity tests (shown in Table 14). (a) RTDFs, (b) multiplicative biases, (c) correlation coefficients (R), and (d) number of data points in sensitivity tests. The error bars show the 95 % confidence bounds.

Table 14: Summary of sensitivity tests for Pandora relative temperature dependence factors.

Test no.	Pandora	Brewer	Data period	RTDF (%/K)
1	#103	Combined Brewer (#8, #14, #15, #145, #187, #191)	Oct. 2013 – Dec. 2015	0.247 ± 0.013
2	#104	Combined Brewer (#8, #14, #15, #187, #191)	Jan. 2014 – Apr. 2014	0.255 ± 0.040
3	#103	Combined Brewer (#8, #14, #15, #187, #191)	Jan. 2014 – Apr. 2014	0.261 ± 0.027
4	#103	Combined Brewer (#8, #14, #15, #187, #191)	Oct. 2013 – Aug. 2014	0.255 ± 0.020
5	#103	Combined Brewer (#8, #14, #145, #191)	Jan. 2015 – Dec. 2015	0.263 ± 0.017
6	#103	Brewer #191	Oct. 2013 – Dec. 2015	0.246 ± 0.016
7	#103	Brewer #191	Oct. 2013 – Aug. 2014	0.249 ± 0.025
8	#103	Brewer #191	Jan. 2015 – Dec. 2015	0.250 ± 0.021
9	#103	Brewer #8	Oct. 2013 – May. 2015	0.285 ± 0.031
10	#103	Brewer #14	Nov. 2013 – Dec. 2015	0.262 ± 0.014
11	#103	Brewer #15	Nov. 2013 – Jul. 2015	0.290 ± 0.025
12	#103	Brewer #145	Jan. 2015 – Dec. 2015	0.241 ± 0.020
13	#103	Brewer #187	Oct. 2013 – Apr. 2014	0.242 ± 0.088

5.3.2 Results

5.3.2.1 Pandora TCO Correction

As an example, Figure 5.5 shows the time series of Brewer #14 – Pandora #103 TCO differences, before and after applying the Pandora correction (Eq. 5.15). A clear seasonal signal is seen due to the variation of T_{eff} before the temperature dependence correction is applied (see Figure 5.5a). Figure 5.8 shows scatter plots of Pandora #103 versus Brewer #14 TCO. In Figure 5.8a, the linear regression (green line, weighted to account for uncertainties from both measurements (York et al., 2004)) between Pandora #103 and Brewer #14 gives a slope of 1.023, an offset of -18.486 DU, and strong correlation (R = 0.9954). Forcing the intercept to zero gives a slope of 0.969, indicating -3.1% mean bias. This is consistent with the work of Redondas et al. (2014), which showed that changing the Brewer ozone cross section from Bass and Paur to DBM changed the Brewer TCO by -3.2%. By colour coding the scatter points, it is obvious that this non-ideal slope and offset are related to T_{eff}. After applying the correction, the seasonal Brewer – Pandora difference disappears as seen in Figure 5.5b, and the linear regression (green line) gives a slope of 1.008, an offset of -2.678 DU, and an improved correlation (R = 0.9982) (see Figure

5.8b). Linear fitting with zero intercept gives a slope of 1.001, indicating that the correction improves the mean bias between Pandora and Brewer TCO from -3.1% to 0.1%.

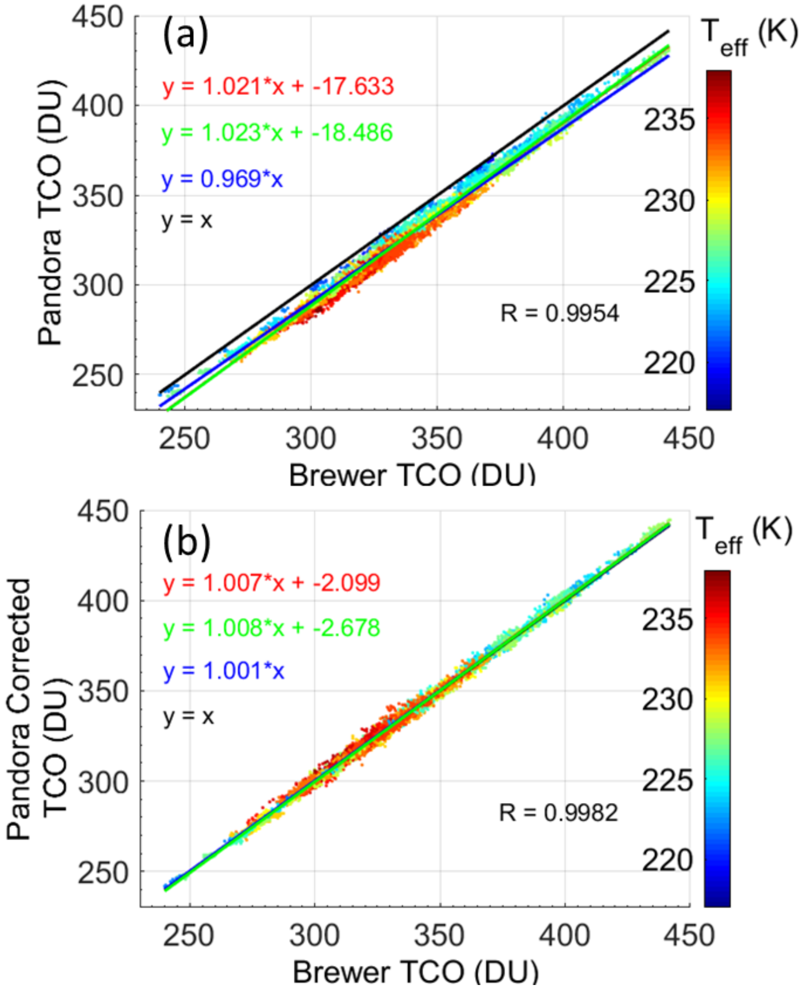

Figure 5.8: Scatter plots of Pandora #103 vs. Brewer #14 TCO, colour coded by ozone effective temperature: (a) before applying the correction, (b) after applying the correction. The red line is a simple linear fit, the green line is the linear fit weighted by the calculated standard uncertainty from Pandora and Brewer TCO data, the blue line is the linear fit with intercept set to zero, and the black line is the 1-to-1 line.

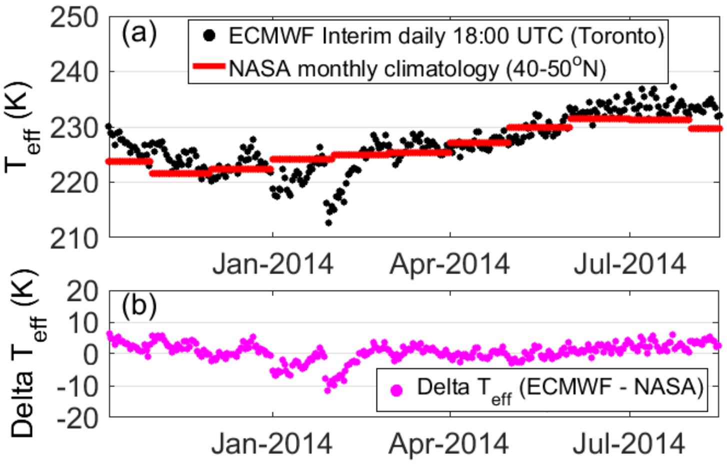

Figure 5.9: Effective ozone temperature: (a) T_{eff} calculated using ERA-Interim data (18:00 UTC over Toronto) and NASA climatology data (monthly mean for 40-50° N), (b) the difference between these two.

To calculate the effective temperature, this work uses daily temperature and ozone profiles from ERA-Interim data at 18:00 UTC for Toronto, but Herman et al. (2015) used monthly averaged temperature and ozone climatology data (interpolating the climatological ozone profile to the observed TCO in order to capture day-to-day variability, see ftp://toms.gsfc.nasa.gov/pub/ML_climatology) for latitudes of 30-40° N and 40-50° N to form an average suitable for Boulder (40° N). To understand the difference due to the selection of T_{eff}, this work adapted the climatology data used in Herman et al. (2015), and used the data from 40-50° N to calculate effective ozone temperature for Toronto (44° N). Figure 5.9 shows the comparison between the ECMWF daily T_{eff} and the NASA monthly climatology T_{eff}. A sudden cooling event happened at Toronto on 29-30 January 2014, for which the difference between the daily and monthly T_{eff} was -10 K. Figure 5.10 shows the time series of TCO difference (combined Brewer − Pandora #103) before and after applying the temperature dependence correction using both the monthly climatology T_{eff} and daily T_{eff}. Because the monthly climatology T_{eff} does not reflect the low temperature during those two days, the correction function (see Eq. 5.15) overcompensated for the temperature effect (the minimum delta ozone value on 29 January changed from -8 DU in Figure 5.10a to -14 DU in Figure 5.10b). The low-temperature event was captured by the daily T_{eff}, thus the compensation from the temperature effect was reasonably small when using ECMWF daily T_{eff} (the minimum value was -7 DU, see Figure 5.10c). In general, the ECMWF daily T_{eff} can better capture some ozone variation events that are associated with rapid temperature changes.

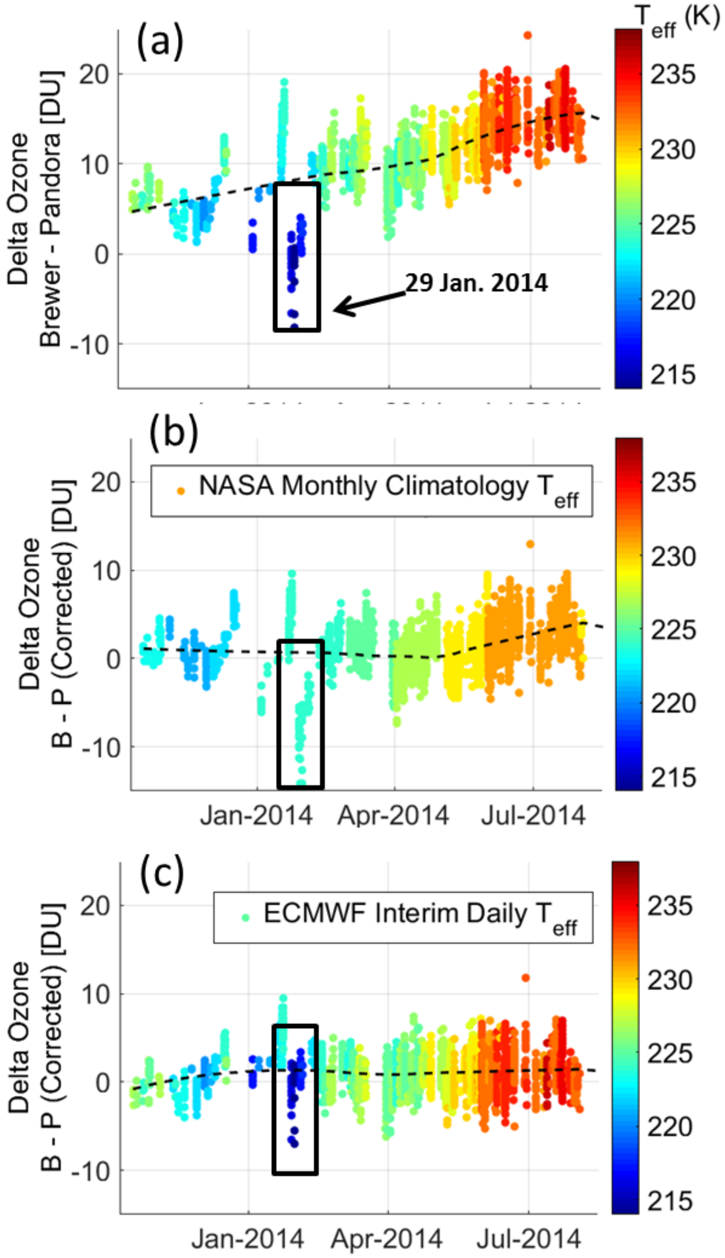

Figure 5.10: Time series of combined Brewer – Pandora #103 TCO difference colour coded by ozone effective temperature: (a) before applying the temperature dependence correction, (b) after applying the correction using NASA monthly climatology T_{eff}, and (c) after applying the correction using ERA-Interim daily T_{eff}. The sudden cooling event on 29-30 January 2014 is marked by black box. The dashed lines are Lowess(0.5) fits.

Figure 5.11 shows time series of the monthly average TCO difference in percentage before and after applying the temperature dependence correction for eight pairs of instruments (six individual Brewers vs. Pandora #103, combined Brewer vs. Pandora #103, and combined Brewer vs. Pandora #104). Figure 5.11a shows that both Pandora #103 and #104 have similar offsets relative to the Brewers before applying the correction to Pandora data. In addition, the seasonal variations are consistent when comparing Pandora #103 to six individual Brewers (see Figure 5.11a). After applying the TCO corrections (Figure 5.11b), the seasonal differences decreased from ±1.02% to ±0.25% for Pandora #103 and from ±0.40% to ±0.25% for Pandora #104, as did the offset which decreased from 2.92% to -0.04% for Pandora #103 and from 2.1% to -0.01% for Pandora #104. The 1σ uncertainty in Figure 5.11b shows that, statistically, the corrected Pandora datasets have no significant seasonal differences or offsets compared to the Brewer datasets.

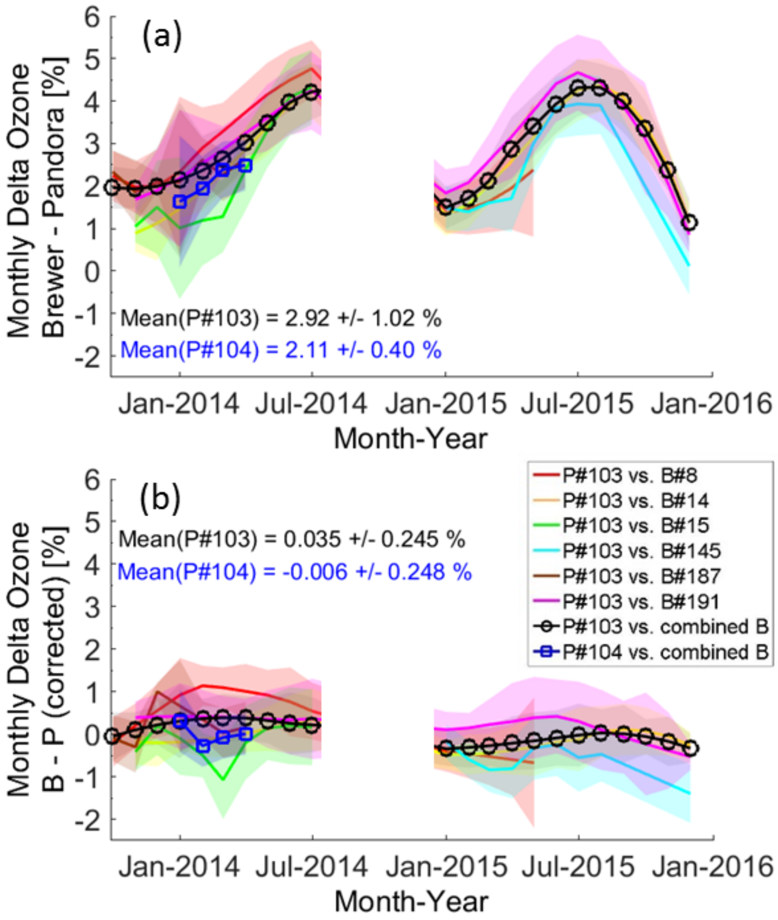

Figure 5.11: Monthly mean time series of the (Brewer – Pandora)/Brewer % TCO difference: (a) before applying the Pandora temperature dependence correction, and (b) after applying the correction. The shaded regions represent 1σ uncertainty.

5.3.2.2 Comparison with Satellite

To further validate the temperature dependence correction for the Pandora data, this work used OMI ozone data (version OMTO3e). Pandora data are averaged within ±10 min of OMI overpass times. In Figure 5.12, scatter plots of OMI vs. Pandora TCO are shown in panels a and b; OMI vs. corrected Pandora TCO (using Eq. 5.15 and 5.16 with the correction functions found from the statistical model) is shown in panels c and d; OMI vs. corrected Pandora TCO (using Eq. 5.17 with the correction function from (Herman et al., 2015)) is shown in panels e and f. All the Pandora TCO corrections shown in Figure 5.12 used the same T_{eff} calculated with the ERA-Interim daily ozone data.

Figure 5.12a and c show that, after applying the TCO correction (Eq. 5.15) to Pandora #103, the slope of the linear regression improved from 0.987 to 0.990, the offset improved from 14.84 to -3.59 DU, the correlation coefficient improved from 0.987 to 0.991, and the mean bias between OMI and Pandora improved from 3.1% to 0.0 %. Similar improvement is seen in the comparison between Pandora #104 and OMI (see Figure 5.12b and d), although the size of the coincident measurement dataset is smaller, with the mean bias improving from 1.5% to -0.6%. In addition, Figure 5.12e and f show that, by using the correction function from (Herman et al., 2015), the comparisons also improve, although 1.9% (1.4%) bias remains for Pandora #103 (#104) (indicated by the slop of linear fit with force the intercept to zero, see the green lines in Figure 5.12). Note that the ATDF in Herman et al. (2015) is only 0.08 % K^{-1} higher than the RTDF.

Figure 5.13a and b show the monthly mean time series of the OMI – Pandora TCO percentage difference, before and after applying the three correction functions. All three correction models reduced the difference between Pandora and OMI. The relative correction model (Eqs. 5.15 and 5.16) reduces the seasonal difference (indicated by the δ of the percentage monthly delta ozone) between Pandora #103 and OMI from ±1.68% to ±1.00%, with the mean bias decreasing from 2.65% to -0.19% (the mean of the percentage monthly delta ozone). Pandora #104 has a similar improvement. The absolute correction model (Eq. 5.17) reduces the seasonal difference between Pandora #103 and OMI to 0.87%, with the mean bias decreased to 1.71%. The reduction in the mean bias between Pandora and OMI is better for the relative correction model. This result (-0.19 ± 1.00 % mean bias) is consistent with Balis et al. (2007) who showed that the global average difference between OMI-TOMS and Brewer instruments is within 0.6%, and that the difference in the 40-50° N band (Toronto is at 44° N) is close to zero (see their Fig. 1).

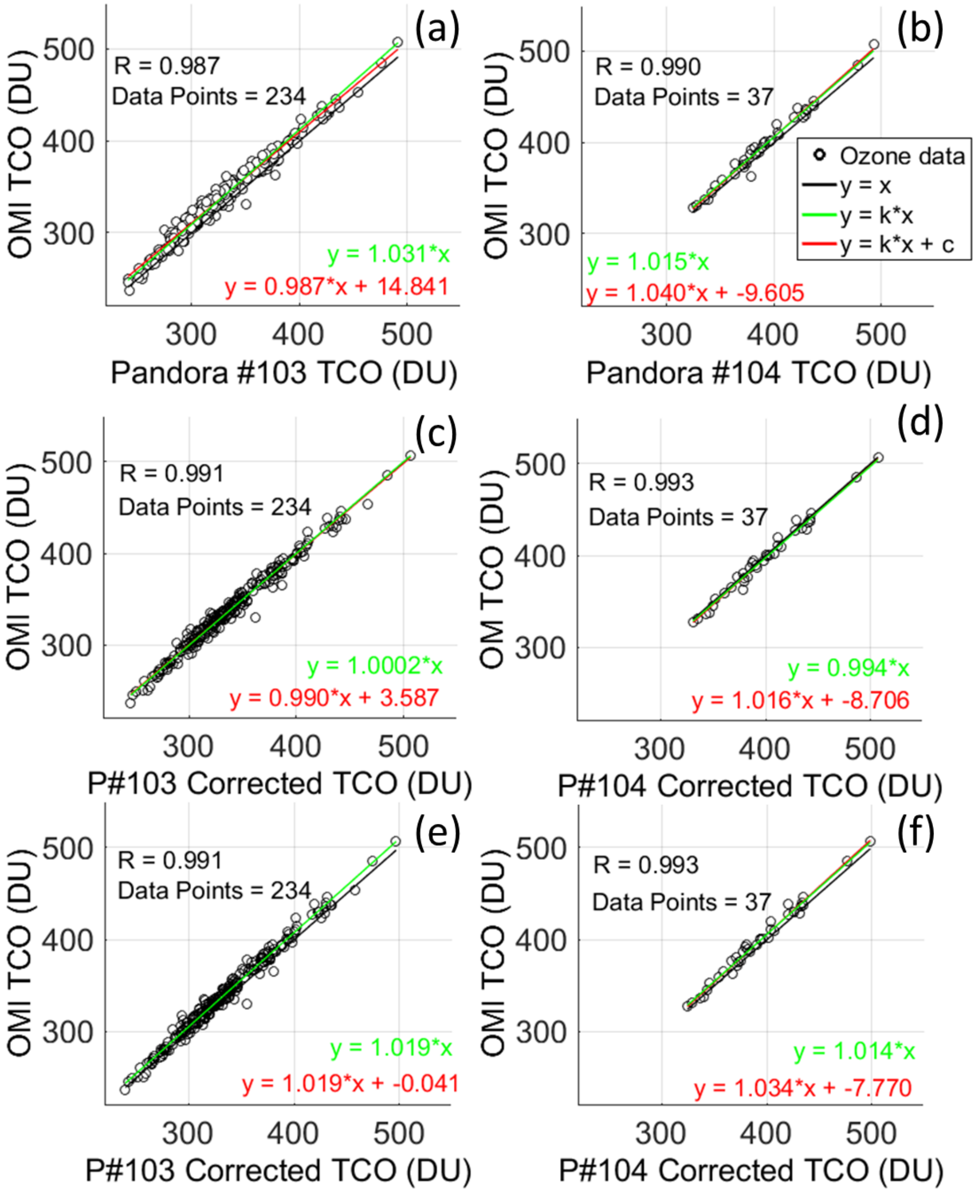

Figure 5.12: Scatter plots of OMI TCO vs. Pandora TCO for (a) Pandora #103 without TCO correction, (b) Pandora #104 without TCO correction, (c) Pandora #103 with correction using Eq. 5.15, (d) Pandora #104 with correction using Eq. 5.16, (e) Pandora #103 with correction using Eq. 5.17, (f) Pandora #104 with correction using Eq. 5.17.

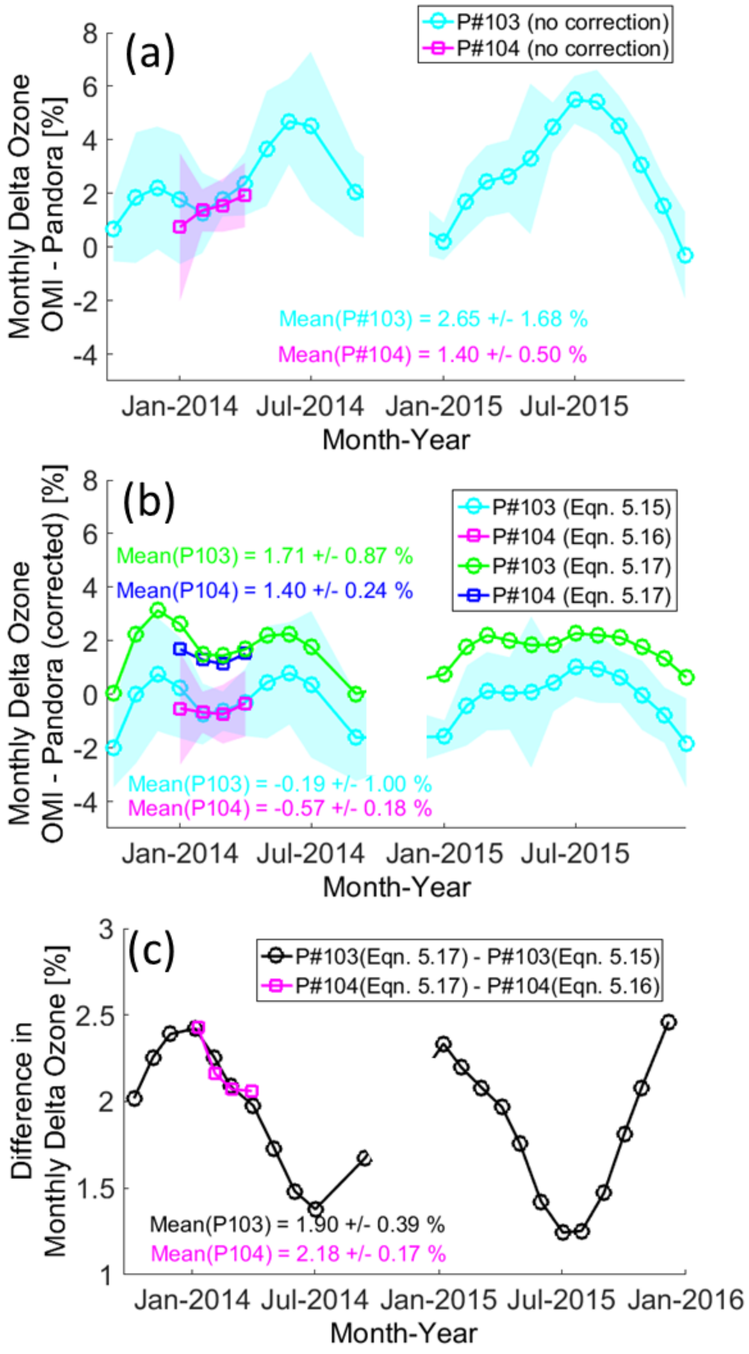

Figure 5.13: Monthly mean time series of the (OMI – Pandora)/OMI % TCO difference: (a) before applying the correction, (b) after applying the correction using Eqs. 5.15 - 5.17, and (c) the difference between the corrections. The shaded regions represent the 1σ uncertainty.

Balis et al. (2007) reported that the time series of globally averaged differences between OMI-TOMS and Brewer instruments shows almost no annual variation, and the OMI-TOMS data theoretically have no temperature dependence (McPeters and Labow, 1996; Bhartia and

Wellemeyer, 2002). By using the relative correction, the corrected Pandora TCO should have similar performance to the Brewer TCO. Figure 5.13c shows the difference between the absolute correction method and the relative correction method. Although both methods removed some of the seasonal signal (reduced from 1.68% to 1.00% for the relative correction, and 0.87% for the absolute correction), Figure 5.13c shows that there is still a weak seasonal signal residual (0.39 %) left between these two methods.

5.4 Stray Light Effect

It is well known that direct-sun UV spectrometers are affected by stray light when the solar zenith angle is too large. In general, when the ozone AMF is larger than 3 (SZA > 70°), the retrieved TCO will show an unrealistic decrease with increasing SZA (thus this effect is also known as the airmass dependence effect). In general, the stray light from longer wavelengths results in overestimation of the UV signal at short wavelengths and makes the measured UV signal in that part of the spectrum less sensitive to TCO. The double Brewer spectrometer was introduced in 1992, which uses two spectrometers in series to reduce the stray light (Bais et al., 1996; Wardle et al., 1996; Fioletov et al., 2000). The BrT-D has the advantage of very low internal stray light fraction (10^{-7}, stray light signal divided by total signal) compared to BrT (10^{-5}) in the 300-330 nm spectral range (Fioletov et al., 2000; Tzortziou et al., 2012). For Pandora instruments, a UV340 filter is used to remove most of the stray light that originates from wavelengths longer than 380 nm (Herman et al., 2015). A typical UV340 filter has a small leakage (5 %) at ~720 nm, which misses the detector and hits the internal baffles. Further stray light correction is done by subtracting the signal of pixels corresponding to 280 to 285 nm (which contain almost zero direct illumination) from the rest of the spectrum. However, a very small (but unknown) amount of this stray light may scatter on to the detector (Herman et al., 2015). Tzortziou et al. (2012) tested the stray light effect for Pandora #34 and Brewer #171 and concluded that the Pandora stray light fraction ($\sim10^{-5}$) was comparable to the single Brewer. Pandora ozone retrievals are accurate up to a slant column between 1400 and 1500 DU or 70 and 80° SZA, depending on the TCO amount (Herman et al., 2015).

To assess the airmass dependence, this work compared Brewer TCO to the corrected Pandora TCO data. Figure 5.14 shows an example of the Brewer/Pandora ratio as a function of ozone

AMF (reported value in Brewer data) before and after applying the TCO correction (Eq. 5.15), with the data points grouped by effective temperature. Before applying the correction (Figure 5.14a), the linear fits show consistently low (-0.1 to 0.5%) relative AMF dependence between Brewer and Pandora (defined as the slope of the linear fit) for each T_{eff} group. However, the linear fit to the whole dataset (all effective temperatures, black line) shows that the relative AMF dependence is -0.007. Figure 5.14b shows that the correction changed the slope of the black line to -0.001; removing the temperature effect for the Pandora dataset thus reduces the relative AMF dependence from -0.7% to -0.1%. To characterize only the airmass dependence, therefore the temperature dependence effect from the Pandora dataset was removed.

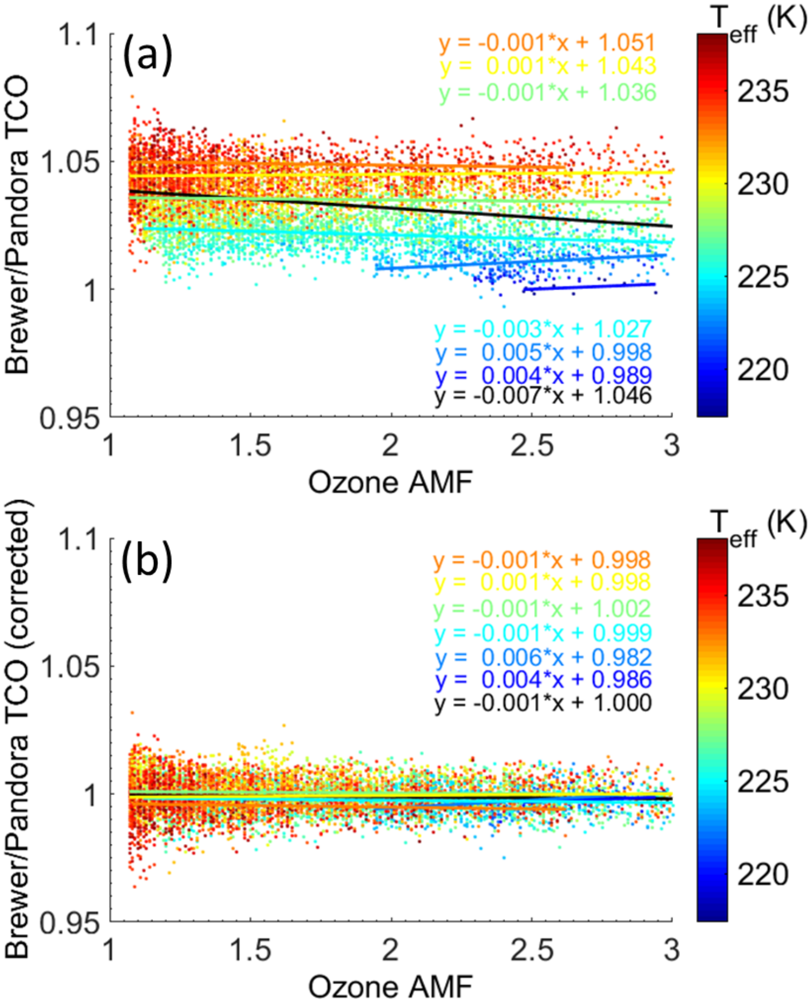

Figure 5.14: Brewer #14/Pandora #103 TCO ratio vs. ozone airmass factor: (a) before and (b) after applying the Pandora temperature dependence correction. The points are grouped by effective temperature (from 215 to 240 K, in 5 K bins), and the linear fits for each group are colour coded. The black line and linear fit is for the whole dataset.

To show how the different instrument designs affect the stray light performance, this work merged the six Brewer datasets into two groups (BrT and BrT-D) to compare with the corrected Pandora data. Figure 5.15 shows the (Brewer − Pandora)/Brewer percentage difference as a function of ozone AMF. In Sections 5.2 and 5.3, the TCO data with ozone AMF > 3 was discarded. The purpose of this filter was to ensure that only the best direct-sun measurements (with low airmass dependence) from both instruments were used. However, to study the instrument performance for large AMFs, and also to characterize the performance of Brewer and Pandora instruments, the AMF threshold was changed from 3 to 6. Figure 5.15 indicates that Pandora, BrT, and BrT-D instruments have similar airmass dependence for ozone AMF < 3 (~71° SZA), consistent with the result reported by Tzortziou et al. (2012). Pandora and BrT-D have similar AMF dependence up to ozone AMF of 5.5-6 (80.6-81.6° SZA), but Pandora and BrT diverge above AMF of 3-4 (71-76° SZA). In general, these results indicate the Pandora and BrT-D instruments have very good stray light control.

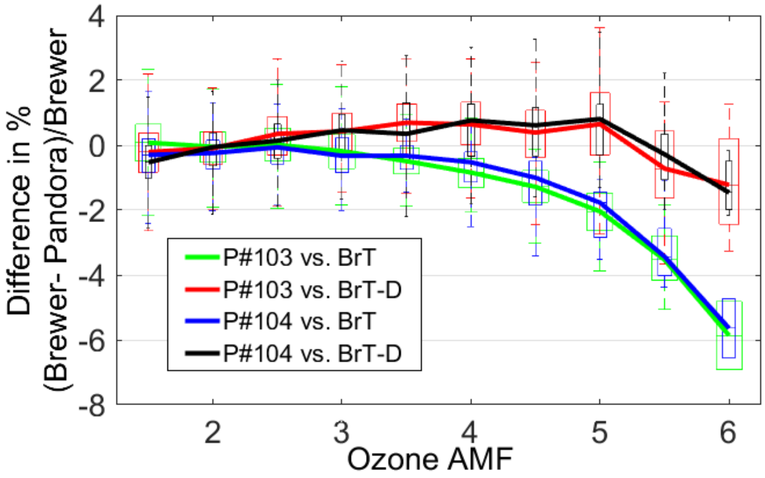

Figure 5.15: Percentage difference between Pandoras (#103 and #104) and Brewers (grouped as BrT and BrT-D) as a function of ozone airmass factor. On each box, the central mark is the median, the edges of the box are the 25th and 75th percentiles, and the whiskers extend to the most extreme data points not considered outliers.

5.5 Summary

The instrument random uncertainty, TCO temperature dependence, and ozone airmass dependence have been determined using two Pandora and six Brewer instruments. In general, Pandora and Brewer instruments both have very low random uncertainty (< 2 DU) in the total column ozone measurements, with that for Pandora being ~0.5 DU lower than Brewer. This indicates that Pandora instruments could provide more precise measurements than the Brewer for the study of small-scale (temporal and magnitude) atmospheric changes. This work confirms the quality of the TCO data, with all eight instruments meeting the GAW requirement for a precision better than 1% (WMO, 2014), however, the Brewer instruments have smaller ozone temperature dependence than the Pandoras.

By using the ERA-Interim and Brewer ozone data in the statistical method, this work successfully corrected the Pandora TCO to decrease its temperature dependence. Relative temperature dependence factors of 0.247 % K^{-1} for Pandora #103 and 0.255 % K^{-1} for Pandora #104 against the Brewer instruments were found. This relative temperature dependence factor is comparable to the absolute temperature dependence factors previously found for Pandora (0.333 % K^{-1}, by applying retrievals with different ozone cross sections, (Herman et al., 2015) and Brewers (0.07-0.094 % K^{-1} (Kerr et al., 1988; Kerr, 2002)). In addition, a 2% multiplicative bias was found between the Pandora and Brewer standard TCO products, which is due to the different ozone cross sections used in the retrievals. After applying the corrections, the annual seasonal difference between Pandora and Brewer instruments decreased from ±1.02 to ±0.25 % and the mean bias decreased from 2.92 to 0.04 %. In addition to using model ozone data (ERA-Interim for this case) to calculate the effective ozone temperature, T_{eff} *could* also be estimated from Brewer or Pandora measurements (Kerr, 2002; Tiefengraber et al., 2016), however, at a cost of decreased TCO measurement precision. An effective ozone temperature algorithm is under development for the Pandora. The future operational Pandora ozone retrieval algorithm will use this derived effective ozone temperature to minimise the temperature dependence of the ozone product (Tiefengraber et al., 2016).

This study confirmed that the Pandora and Brewer TCO data have negligible airmass dependence when the ozone AMF < 3. The Pandora and BrT instruments have similar airmass dependence (relative airmass dependence < ±0.1%) up to 71° SZA (AMF < 3); the Pandora and BrT-D instruments have very good stray light control, and their AMF dependence is comparably low up to 81.6° SZA (within 1% up to AMF = 5.5 and within 1.5% up to AMF = 6).

Chapter 6

6 Conclusions and Future Work

6.1 Summary and Contributions of the Thesis

Ozone is one of the most important atmospheric trace gases, with impacts on human health and links to climate change. Thus monitoring and studying the depletion processes of ozone in both the stratosphere and troposphere are crucial to improving our understanding of the changing environment.

6.1.1 Experimental Contributions

With regard to experimental contributions, this thesis described the instrumentation, data collection, and data processing for the GBSs. These instruments have had many upgrades in both hardware and software since 2011. The UT-GBS input optics have been modified to improve spectral resolution and depolarization (thorough removal of the f-number matcher and mechanical entrance slit in 2012, and replacement of the 1-m fibre with a 10-m fibre in 2013). The instrument was upgraded to a MAX-DOAS system in 2015 by coupling it to UT-Suntracker #1. The PEARL-GBS was equipped with a wedged CCD mount that has improved the uniformity of spectral resolution across the CCD since 2013. New metallic natural density filters have been mounted in the PEARL-GBS filter wheel since 2014 to improve the quality of direct-sun spectra. The new UT-Suntracker #2 was mounted on the north-west corner on PEARL Ridge Lab, which has improved the viewing geometry for PEARL-GBS MAX-DOAS observations since 2015. Also, the GBSs' communication with the UT-Suntrackers was upgraded from UDP to TCP in 2015. The PEARL-GBS participated the CINDI-2 campaign in September 2016, during which many new features (for example, active tracking, 2D MAX-DOAS, horizon scan, and almucantar scan) have been successfully tested and implemented and will be implemented in Eureka when measurements resume in February 2017.

The Eureka GBS zenith-sky dataset has been extended to 17 years (1999-2016, not 2002), and the MAX-DOAS dataset has been extended to seven years (2010-2016). Using the MAX-DOAS spectra, aerosol, BrO, and NO_2 vertical profiles have been retrieved. The Eureka GBS zenith-sky ozone and NO_2 columns were submitted to the NDACC archive in NASA Ames format in 2013. GBS data in HDF format will be updated and submitted to the NDACC archive in early 2017.

6.1.2 Contributions to the Study of Tropospheric Ozone Depletion

Measurements of ozone, NO_2, BrO and other species were obtained using two ground-based UV-visible spectrometers in the Canadian High Arctic. In addition, data from lidar, radar, ozonesondes, radiosondes, FTIR, satellite instruments, and models were presented and used in this thesis. A case study of a transported bromine explosion event in 2011 was presented in Chapter 3. By using observational (Brewer and Bruker FTIR) and modelled (MERRA-2) data, a unique picture of dynamic and chemical links between surface ODE and HDO depletion were presented in Chapter 4. In these two chapters, the following scientific questions were addressed:

- What is the source of the extremely high concentrations of bromine in the polar troposphere? Do we have observations at Eureka that provide evidence that the blowing-snow induced sea-salt aerosol is one of the bromine sources?
- What are the differences between high-wind-condition and low-wind-condition ODEs? What meteorological conditions can enable bromine explosion events at Eureka?

The MAX-DOAS aerosol and BrO profiles were used to examine a bromine explosion event observed on 3 to 5 April 2011 at Eureka. This event involved transportation of a bromine plume ~1800 km from the Beaufort Sea over three days with evidence of “unusual” (not a stable shallow boundary layer) meteorological conditions at the bromine source. During the initial formation of the bromine explosion, a strong cyclone developed over the Beaufort Sea, and the boundary layer height increased to three times its background level. Tropospheric and stratospheric BrO profiles and partial column densities at Eureka were retrieved from ground-based MAX-DOAS and ZS-DOAS data. Further study of local meteorological conditions reveals that the boundary layer stability could have a significant effect on the surface BrO; a stable boundary layer may increase the likelihood of trapping a transported bromine plume and triggering local bromine release from the snowpack within the boundary layer, thus prolonging the duration of bromine explosion events, a process which is not currently included in chemical-climate models. This combination of observations and modelling confirms that both high wind/blowing snow and low wind/stable boundary layer are favourable environmental conditions for bromine explosion events, and in some cases, the combination of these two conditions will affect the lifetime of a bromine explosion event.

- How well do the satellite measurements of tropospheric BrO agree with ground-based measurements at Eureka?

The MAX-DOAS tropospheric partial columns show good consistency with GOME-2 satellite data. The weighted linear regression accounting for MAX-DOAS and GOME-2 measurement errors indicates that GOME-2 measurements are good correlated ($R = 0.79$) with the MAX-DOAS measurements with a slope of 1.02 and offset of 7.0×10^{12} molec cm^{-2}. The difference between MAX-DOAS and GOME-2 is partially due to the fact that the ground-based BrO VCD_{trop} data are only 0-4 km partial columns, whereas the GOME-2 VCD_{trop} data are approximately 0-8 km partial columns. In addition, the MAX-DOAS effective spatial sampling was within 20 km. However, GOME- 2 footprint size was about 40 km × 80 km.

- Do our current ODE modelling results agree with ground-based measurements at Eureka? How well can models simulate BrO, ozone, and sea-salt aerosol (compared to measurements)?
- The lifetime of reactive bromine is only a few hours in the absence of recycling. Do we have evidence of this recycling over aerosol or blowing-snow/ice particles at Eureka (for example, lofted ozone depletion layer coincident with lofted aerosol layer)?

The UKCA chemistry-climate model successfully reproduced some of the main features (such as the vertical structure of the bromine plume) of the 2011 bromine explosion event after including a bromine source from blowing snow related to sea-salt production. Comparison between the model and measurements indicates that surface BrO is not only controlled by photochemistry, but also by local dynamics, which influence ozone through vertical mixing, indicating the difficulties in simulating BrO concentrations.

The latest sea-ice surface salinity data has been applied in the UKCA model in Chapter 4. The new surface salinity data reduced the bromine release flux from the source region, but increased the modelled bromine concentration above Eureka to agree with the previous ground-based observation for the 2011 event (Zhao et al., 2016a). This result supports the conclusion of that study that during a strong surface ODE (ozone VMR < 1 ppbv), BrO concentration can be significantly affected by the near-zero ozone concentration.

Comparison of modelled blowing-snow SSA with lidar/radar measurements was also made. The pTOMCAT SI-SSA data captured some features of the increased aerosol in the 2007 and 2011 event. For the 2007 event, the ground-based lidar and radar instruments observed ice cloud (vapour and ice crystals) from 700 to 1000 m height (from the end of 1 March to 3 March), which is coincident with an aloft ozone depletion layer (strongest ozone depletion to 7 ppbv at 870 m height). However, pTOMCAT and UKCA both failed to reproduce this feature in their modelled ozone profiles. The pTOMCAT model results show that there was almost no SI-SSA during that period. Thus production and especially deposition mechanisms of SI-SSA in the models still need further investigation. The lidar/radar observations also reveal the deposition (falling snow and ice crystals) process from this ice cloud at Eureka. Thus the following shallow surface ODE (0 to 200 m) on 4 and 5 March is likely due to the deposition of bromine-enriched particles onto the local snow pack. This detailed vertical structure of ice clouds, ice crystal, and aerosol layers for the 2007 event could be used in future bromine modelling comparisons.

- Blowing-snow sublimation process is a key step in producing bromine-enriched sea-salt aerosol. Can we use isotopologue measurements at Eureka to provide evidence of this sublimation process?

Bruker 125HR δD data were used in Chapter 4 to expand the ODE study. The 3-D scatter plot of TCO, tropopause height, and δD data revealed two similar cyclone events from the nine-year dataset that show both depleted surface ozone and depleted HDO at Eureka in March 2007 and April 2011. The FLEXPART particle dispersion model was used to simulate airmass transportation, which revealed the cyclonic shaped plumes over the Beaufort Sea region. The observed HDO depletions during these two blowing-snow ODEs are found to deviated (weaker than) from pure Rayleigh fractionation model. This result provides evidence of the blowing-snow sublimation process, which is a key step in producing bromine-enriched SSA. A plot of δD-PWV evolution is used to distinguish airmasses from the cyclone (from west) and another source (from north), which shows the termination of the shallow surface ODE is due to mixing with a different airmass. Although the edge of the stratospheric polar vortex was found over Eureka during those periods, no evidence was found that the low δD value was caused by the polar vortex or a stratospheric intrusion.

6.1.3 Contributions to the Study of Pandora and Brewer Total Column Ozone

Another component of this thesis involved intercomparison of TCO measurements by Pandora and Brewer instruments. The instrument random uncertainty, TCO temperature dependence, and ozone airmass dependence were determined using two Pandora and six Brewer instruments. By using two-year TCO datasets collected in Toronto, the following scientific questions were addressed:

- What is the cause of the difference between Brewer and Pandora TCO measurements?

The major causes include different temperature dependence of the instruments and the different ozone cross sections used in their TCO retrievals. Relative temperature dependence factors of 0.247 % K^{-1} for Pandora #103 and 0.255 % K^{-1} for Pandora #104 against the Brewer instruments were found. This relative temperature dependence factor is comparable to the absolute temperature dependence factors previously found for Pandora (0.333 % K^{-1}, by applying retrievals with different ozone cross sections, Herman et al., 2015) and Brewers (0.07-0.094 % K^{-1}, Kerr et al., 1988; Kerr, 2002). In addition, a 2% multiplicative bias was found between the Pandora and Brewer standard TCO products, which is due to the different ozone cross sections used in the retrievals.

- Are the TCO measurements by Brewer and Pandora meeting the GAW requirement? And what are these instruments' measurement precisions and accuracies?

In general, Pandora and Brewer instruments both have very low random uncertainty (< 2 DU) in the total column ozone measurements, with that for Pandora being ~0.5 DU lower than Brewer. This indicates that Pandora instruments could provide more precise measurements than the Brewer for the study of small-scale (temporal and magnitude) atmospheric changes. This work confirms the quality of the TCO data, with all eight instruments (used in this work) meeting the

GAW requirement for a precision better than 1% (WMO, 2014), however, the Brewer instruments have smaller ozone temperature dependence than the Pandoras.

- Can we improve the Pandora TCO data quality in a way that comparable to Brewer TCO data (given Brewer is designed to produce high-quality TCO data)?

By using the ERA-Interim and Brewer ozone data in a statistical method, this work successfully corrected the Pandora TCO to decrease its temperature dependence. After applying the corrections, the annual seasonal difference between Pandora and Brewer TCO measurements decreased from ±1.02 to ±0.25 % and the mean bias decreased from 2.92 to 0.04 %. In addition to using model ozone data (ERA-Interim for this case) to calculate the effective ozone temperature, it can also be estimated from Brewer or Pandora measurements (Kerr, 2002; Tiefengraber et al., 2016), however, at a cost of decreased TCO measurement precision. An effective ozone temperature algorithm is under development for the Pandora. The future operational Pandora ozone retrieval algorithm will use this derived effective ozone temperature to minimise the temperature dependence of the ozone product (Tiefengraber et al., 2016).

- How these differences (optical design, retrieval algorithm, etc.) in Brewer and Pandora instruments affect their precision and accuracy in TCO measurements?

The double Brewer has the advantage of very low internal stray light fraction (10^{-7}, stray light signal divided by total signal) compared to single Brewer (10^{-5}) in the 300-330 nm spectral range (Fioletov et al., 2000; Tzortziou et al., 2012). The Pandora instrument has low stray light fraction (~10^{-5}), which is comparable to the single Brewer. Due to stray light, Pandora ozone retrievals are accurate up to a slant column between 1400 and 1500 DU or 70 and 80° SZA, depending on the TCO amount (Herman et al., 2015). This work confirmed that the Pandora and Brewer TCO data have negligible airmass dependence when the ozone AMF < 3. The Pandora and BrT instruments have similar airmass dependence (relative airmass dependence < ±0.1%) up to 71° SZA (AMF < 3); the Pandora and BrT-D instruments have very good stray light control, and their AMF dependence is comparably low up to 81.6° SZA (within 1% up to AMF = 5.5 and within 1.5% up to AMF = 6).

6.2 Suggested Future Work

With the six years of measurements acquired during this work, the GBS zenith-sky dataset has been expanded to 17 years. Adams et al. (2012a) harmonised the GBS ozone and NO_2 dataset from 1999 to 2011 using the most up-to-date NDACC ozone and NO_2 LUTs at that time. I have performed NO_2 retrievals using 2011-2015 GBS zenith-sky data with both the latest version (v1.0) of the NDACC LUT and the version (v0.1) used by Adams et al. (2012a). In general, there are some offsets in the NO_2 VCDs retrieved by using these different LUTs. For example, the new LUT yields 1-3% higher spring-time NO_2 VCDs. But this offset decreased to only ~0.6% in the summer time. This is likely due to the new LUT using a climatological NO_2 profile from 12 to 60 km, whereas the old version uses an NO_2 profile from 18 to 60 km. Thus the latest version of the NDACC NO_2 LUT should be implemented in future GBS retrievals with caution (some comparison and validation work is necessary). The new GBS zenith-sky dataset should be harmonized, converted to HDF format (Kristof Bognar is working on this), and archived in the NDACC database. In addition, the NDACC LUTs have been found to have some bias for high-latitude sites (reported by the SAOZ group). Thus this work can be carried out as a more general scientific study, if more NDACC high-latitude sites are included. In addition, intercomparison between Brewer (even Pandora, in future) and NDACC UV-visible TCO should be performed for high-latitude sites.

The 2D MAX-DOAS measurement scheme was implemented and tested during the CINDI-2 campaign. The inhomogeneous horizontal distribution of BrO during bromine explosion events could be studied by using this technique. In addition, with the horizon scan method and implementation of a laser level, the accuracy of GBS viewing elevation could be improved. The almucantar scan is also potentially useful to improve aerosol retrievals. Ortega et al. (2016) proposed a new method of AOD and aerosol phase function retrievals based on RSP measurements (using almucantar scan spectra). They reported that this method has high sensitivity at low AOD and high SZA, potentially making it particularly useful for the Arctic. In general, the advanced 2D MAX-DOAS sequence and complementary scans should be implemented for the GBS Eureka measurements.

The horizontal level of the suntracker is critical for solar and lunar tracking. Direct-moon measurements were performed in winters of 2012-2015, but most of the measurements were poor due to the low accuracy of the passive tracking (approximately ±2°). Since the active tracking was successfully implemented during CINDI-2, it can now be used for GBS lunar polar-night measurements. Also, with the improved tracker levelling scheme (horizon scan and laser level), even the accuracy of passive tracking should be improved in the future. Since the active tracking scheme has also been implemented for the Bruker 125HR, comparison of polar-night measurements from the UV-visible and FTIR instruments could be undertaken.

As the UT-GBS has been upgraded to a MAX-DOAS instrument, the spring-to-summer time NO_2 tropospheric profile retrieval can be performed in Eureka (note PEARL-GBS is operating in the UV region, which can also be used to retrieve tropospheric NO_2). The snow-released NO_2 flux (Honrath et al., 1999; Grannas et al., 2007) can be studied using this approach.

A ten-year colour index dataset (2003-2013) was derived from UT-GBS zenith-sky spectra to study tropospheric clouds and PSCs. Future work including RTM simulation, comparison with radar and lidar for different cloud conditions, and comparison with sun photometer for aerosol loadings could be performed. For example, using the AHSRL and MMCR data, the colour ratio of lidar/radar can be compared with the GBS colour index, as ice cloud and ice crystals should have different colour index/ratio compared to water cloud.

A NOAA surface ozone analyser was installed in July 2016 at 0PAL (10 m above sea level), Eureka. There were two possible locations for this instrument, one was 0PAL, and the other was the PEARL Ridge Lab (610 m). The decision was made based on ozonesonde data from 2007 to 2015 (528 ozone profiles in total). I found 13 ozonesonde measurements with deep ODEs (ozone VMR < 10 ppbv from the surface to 610 m) and 18 ozonesonde measurements with shallow ODEs (ozone VMR < 10 ppbv for the surface, but > 10 ppbv at 610 m). This result suggested that only ~40% of all ODEs could be measured in Eureka, if the analyser was located at the Ridge Lab. Unlike ozonesondes, which have poor temporal resolution (daily during springtime, weekly at other times), this new ozone analyser can work 24 hr/day. Thus it will provide valuable continuous ground-level observations of ODEs, which can complement the MAX-DOAS tropospheric BrO measurements. However, the drawback of the ozone analyser is its lack of vertical resolution. Since the ozonesonde dataset revealed that ~40% of ODEs in Eureka could be deep depletion events, additional insights could be obtained by installing another ozone analyser at the PEARL Ridge Lab. With two ozone analysers located at different altitudes, ozone “profiles” with coarse vertical resolution but high temporal resolution could be acquired, providing additional information for ODE studies.

The GBS ozone and NO_2 data have previously been used to validate ACE-FTS, ACE-MAESTRO, and OSIRIS. This work could be updated using the last several years of GBS measurements. Additional satellite validation work could be done with the GBS BrO and OClO data. Potential target satellite instruments include GOME, GOME-2, OMI, and TROPOMI.

I have performed stratospheric and tropospheric BrO profile retrievals with two different OEM codes. Both OEM codes have limited DOFS in their retrieved profiles. As PEARL-GBS can perform good solar measurements now (due to the new filters and active tracking), a ZS-, DS-, and MAX-DOAS combined profile retrieval could be used to improve the quality of profile retrieval. This work will involve writing a new OEM that can work with a multiple scattering RTM. A possible approach is adapting/integrating Robin Schofield's ZS- and DS-OEM to work with the HeiPro.

The operational Pandora ozone retrieval algorithm is being modified to use the derived effective ozone temperature to minimise the temperature dependence of the ozone product (Tiefengraber et al., 2016). The performance of this new algorithm can be evaluated by making comparison with the statistical method in Section 5.3.1. In addition, Pandora and Brewer ozone measurements in the High Arctic should be compared for cold temperatures and low SZA.

Generally, this UV-visible project has contributed to long-term atmospheric measurements in the Canadian High Arctic. As this UV-visible dataset grows, it can continue to be used to quantify ozone depletion and recovery trends, studies of interannual and interseasonal variability of BrO and other trace gases, and to improve our understanding of chemistry-climate processes (by combining the measurements with atmospheric models).

References

Abbatt, J. P. D., Thomas, J. L., Abrahamsson, K., Boxe, C., Granfors, A., Jones, A. E., King, M. D., Saiz-Lopez, A., Shepson, P. B., Sodeau, J., Toohey, D. W., Toubin, C., von Glasow, R., Wren, S. N., and Yang, X.: Halogen activation via interactions with environmental ice and snow in the polar lower troposphere and other regions, Atmos. Chem. Phys., 12(14), 6237-6271, 2012.

Adams, C., McLinden, C. A., Strong, K., and Umlenski, V.: Ozone and NO_2 variations measured during the 1 August 2008 solar eclipse above Eureka, Canada with a UV-visible spectrometer, J. Geophys. Res., 115(D19), 10.1029/2010JD014424, 2010.

Adams, C., Strong, K., Zhao, X., Bassford, M. R., Chipperfield, M. P., Daffer, W., Drummond, J. R., Farahani, E. E., Feng, W., Fraser, A., Goutail, F., Manney, G., McLinden, C. A., Pazmino, A., Rex, M., and Walker, K. A.: Severe 2011 ozone depletion assessed with 11 years of ozone, NO_2, and OClO measurements at 80°N, Geophys. Res. Lett., 39(5), 10.1029/2011gl050478, 2012a.

Adams, C., Strong, K., Batchelor, R. L., Bernath, P. F., Brohede, S., Boone, C., Degenstein, D., Daffer, W. H., Drummond, J. R., Fogal, P. F., Farahani, E., Fayt, C., Fraser, A., Goutail, F., Hendrick, F., Kolonjari, F., Lindenmaier, R., Manney, G., McElroy, C. T., McLinden, C. A., Mendonca, J., Park, J. H., Pavlovic, B., Pazmino, A., Roth, C., Savastiouk, V., Walker, K. A., Weaver, D., and Zhao, X.: Validation of ACE and OSIRIS ozone and NO_2 measurements using ground-based instruments at 80°N, Atmos. Meas. Tech., 5(5), 927-953, 2012b.

Adams, C.: Measurements of atmospheric ozone, NO_2, OClO, and BrO at 80˚N using UV-visible spectroscopy, Ph.D. Thesis, University of Toronto, 2012.

Adams, C., Strong, K., Zhao, X., Bourassa, A., Daffer, W., Degenstein, D., Drummond, J., Farahani, E., Fraser, A., and Lloyd, N.: The spring 2011 final stratospheric warming above Eureka: anomalous dynamics and chemistry, Atmos. Chem. Phys., 13(2), 611-624, 2013.

Afe, O. T., Richter, A., Sierk, B., Wittrock, F., and Burrows, J. P.: BrO emission from volcanoes: A survey using GOME and SCIAMACHY measurements, Geophys. Res. Lett., 31(24), 10.1029/2004gl020994, 2004.

Aliwell, S., Van Roozendael, M., Johnston, P., Richter, A., Wagner, T., Arlander, D., Burrows, J., Fish, D., Jones, R., and Tørnkvist, K.: Analysis for BrO in zenith-sky spectra: An intercomparison exercise for analysis improvement, J. Geophys. Res., 107(D14), doi:10.1029/2001JD000329, 2002.

Andrews, D. G.: *An introduction to atmospheric physics*, Cambridge University Press, USA, 2010.

Antón, M., López, M., Vilaplana, J. M., Kroon, M., McPeters, R., Bañón, M., and Serrano, A.: Validation of OMI-TOMS and OMI-DOAS total ozone column using five Brewer spectroradiometers at the Iberian peninsula, J. Geophys. Res., 114(D14), 10.1029/2009jd012003, 2009.

Ariya, P. A., Dastoor, A. P., Amyot, M., Schroeder, W. H., Barrie, L., Anlauf, K., Raofie, F., Ryzhkov, A., Davignon, D., and Lalonde, J.: The Arctic: a sink for mercury, Tellus B, 56(5), 397-403, 2004.

Austin, J., and Wilson, R. J.: Ensemble simulations of the decline and recovery of stratospheric ozone, J. Geophys. Res., 111(D16), 10.1029/2005JD006907, 2006.

Austin, J., Scinocca, J., Plummer, D., Oman, L., Waugh, D., Akiyoshi, H., Bekki, S., Braesicke, P., Butchart, N., Chipperfield, M., Cugnet, D., Dameris, M., Dhomse, S., Eyring, V., Frith, S., Garcia, R. R., Garny, H., Gettelman, A., Hardiman, S. C., Kinnison, D., Lamarque, J. F., Mancini, E., Marchand, M., Michou, M., Morgenstern, O., Nakamura, T., Pawson, S., Pitari, G., Pyle, J., Rozanov, E., Shepherd, T. G., Shibata, K., Teyssèdre, H., Wilson, R. J., and Yamashita, Y.: Decline and recovery of total column ozone using a multimodel time series analysis, J. Geophys. Res., 115(D3), 10.1029/2010JD013857, 2010.

Bais, A., Zerefos, C., and McElroy, C.: Solar UVB measurements with the double- and single-monochromator Brewer ozone spectrophotometers, Geophys. Res. Lett., 23(8), 833-836, 1996.

Balis, D., Kroon, M., Koukouli, M., Brinksma, E., Labow, G., Veefkind, J., and McPeters, R.: Validation of Ozone Monitoring Instrument total ozone column measurements using Brewer and

Dobson spectrophotometer ground-based observations, J. Geophys. Res., 112(D24), 10.1029/2007JD008796, 2007.

Barrie, L. A., Bottenheim, J. W., Schnell, R. C., Crutzen, P. J., and Rasmussen, R. A.: Ozone destruction and photochemical-reactions at polar sunrise in the lower Arctic atmosphere, Nature, 334(6178), 138-141, 1988.

Barthlott, S., Schneider, M., Hase, F., Blumenstock, T., Kiel, M., Dubravica, D., García, O. E., Sepúlveda, E., Mengistu Tsidu, G., and Takele Kenea, S.: Tropospheric water vapour isotopologue data ($H_2{}^{16}O$, $H_2{}^{18}O$ and $HD^{16}O$) as obtained from NDACC/FTIR solar absorption spectra, Earth Syst. Sci. Data, 9(1), 15-29, 2017.

Bass, A., and Paur, R.: The ultraviolet cross-sections of ozone: I. The measurements, in: Atmospheric Ozone, Springer, Germany, 1985.

Bassford, M. R., Strong, K., and Rebello, J.: ARTICLES-An Automated Spectrometer for Monitoring Arctic Ozone Depletion-The authors discuss the construction of a portable spectrometer system developed for performing stand-alone measurements, Spectroscopy, 15(10), 42-46, 2000.

Bassford, M. R., McLinden, C. A., and Strong, K.: Zenith-sky observations of stratospheric gases: the sensitivity of air mass factors to geophysical parameters and the influence of tropospheric clouds, J. Quant. Spectrosc. Radiat. Transfer, 68(6), 657-677, 2001.

Bassford, M. R., Strong, K., McLinden, C. A., and McElroy, C. T.: Ground-based measurements of ozone and NO_2 during MANTRA 1998 using a Zenith-sky spectrometer, Atmos.-Ocean, 43(4), 325-338, 2005.

Batchelor, R. L., Strong, K., Lindenmaier, R., Mittermeier, R. L., Fast, H., Drummond, J. R., and Fogal, P. F.: A new Bruker IFS 125HR FTIR spectrometer for the Polar Environment Atmospheric Research Laboratory at Eureka, Nunavut, Canada: measurements and comparison with the existing Bomem DA8 spectrometer, J. Atmos. Ocean. Tech., 26(7), 1328-1340, 2009.

Bates, D. R., and Nicolet, M.: Atmospheric hydrogen, Publications of the Astronomical Society of the Pacific, 62(366), 106-110, 1950.

Begoin, M., Richter, A., Weber, M., Kaleschke, L., Tian-Kunze, X., Stohl, A., Theys, N., and Burrows, J. P.: Satellite observations of long range transport of a large BrO plume in the Arctic, Atmos. Chem. Phys., 10(14), 6515-6526, 2010.

Beine, H., Domine, F., Ianniello, A., Nardino, M., Allegrini, I., Teinilä, K., and Hillamo, R.: Fluxes of nitrates between snow surfaces and the atmosphere in the European high Arctic, Atmos. Chem. Phys., 3(2), 335-346, 2003.

Bhartia, P., and Wellemeyer, C.: OMI TOMS-V8 Total O_3 algorithm, algorithm theoretical baseline document: OMI ozone products, NASA God-dard Space Flight Cent, Greenbelt, Md., 2002.

Bhartia, P.: OMI/Aura TOMS-Like Ozone and Radiative Cloud Fraction Daily L3 Global 0.25x0.25 deg, NASA Goddard Space Flight Center, 10.5067/Aura/OMI/DATA3002, 2012.

Blechschmidt, A.-M., Richter, A., Burrows, J., Kaleschke, L., Strong, K., Theys, N., Weber, M., Zhao, X., and Zien, A.: An exemplary case of a bromine explosion event linked to cyclone development in the Arctic, Atmos. Chem. Phys., 16(3), 1773-1788, 2016.

Blossey, P. N., Kuang, Z., and Romps, D. M.: Isotopic composition of water in the tropical tropopause layer in cloud-resolving simulations of an idealized tropical circulation, J. Geophys. Res., 115(D24), 10.1029/2010jd014554, 2010.

Bogumil, K., Orphal, J., Homann, T., Voigt, S., Spietz, P., Fleischmann, O. C., Vogel, A., Hartmann, M., Kromminga, H., Bovensmann, H., Frerick, J., and Burrows, J. P.: Measurements of molecular absorption spectra with the SCIAMACHY pre-flight model: instrument characterization and reference data for atmospheric remote-sensing in the 230-2380 nm region, J. Photochem. Photobiol. A, 157(2), 167-184, 2003.

Bojkov, R. D., Bishop, L., and Fioletov, V. E.: Total ozone trends from quality-controlled ground-based data (1964-1994), J. Geophys. Res., 100(D12), 25867-25876, 1995.

Bosilovich, M., Lucchesi, R., and Suarez, M.: MERRA-2: File specification, NASA, Global Modeling and Assimilation Office, 2015.

Bottenheim, J. W., Gallant, A. G., and Brice, K. A.: Measurements of NO_y species and O_3 at 82° N latitude, Geophys. Res. Lett., 13(2), 113-116, 1986.

Bottenheim, J. W., Barrie, L. A., Atlas, E., Heidt, L. E., Niki, H., Rasmussen, R. A., and Shepson, P. B.: Depletion of Lower Tropospheric Ozone During Arctic Spring: The Polar Sunrise Experiment 1988, J. Geophys. Res., 95(D11), 18555-18568, 1990.

Bottenheim, J. W., Dibb, J. E., Honrath, R. E., and Shepson, P. B.: An introduction to the ALERT 2000 and SUMMIT 2000 Arctic research studies, Atmos. Environ., 36(15), 2467-2469, 2002.

Bourdages, L., Duck, T., Lesins, G., Drummond, J., and Eloranta, E.: Physical properties of High Arctic tropospheric particles during winter, Atmos. Chem. Phys, 9(18), 6881-6897, 2009.

Bovensmann, H., Burrows, J. P., Buchwitz, M., Frerick, J., Noël, S., Rozanov, V. V., Chance, K. V., and Goede, A. P. H.: SCIAMACHY: Mission Objectives and Measurement Modes, J. Atmos. Sci., 56(2), 127-150, 1999.

Box, J. E., Bromwich, D. H., and Bai, L. S.: Greenland ice sheet surface mass balance 1991-2000: Application of Polar MM5 mesoscale model and in situ data, J. Geophys. Res., 109(D16), 10.1029/2003JD004451, 2004.

Braesicke, P., Keeble, J., Yang, X., Stiller, G., Kellmann, S., Abraham, N. L., Archibald, A. T., Telford, P., and Pyle, J. A.: Consistent circulation differences in the Southern Hemisphere caused by ozone changes: a chemistry-climate model and observational study, Atmos. Chem. Phys. Discuss., 13(3), 8455-8487, 2013.

Breider, T. J., Chipperfield, M. P., Richards, N. A. D., Carslaw, K. S., Mann, G. W., and Spracklen, D. V.: Impact of BrO on dimethylsulfide in the remote marine boundary layer, Geophys. Res. Lett., 37(2), 10.1029/2009gl040868, 2010.

Brewer, A.: Evidence for a world circulation provided by the measurements of helium and water vapour distribution in the stratosphere, Q. J. Roy. Meteor. Soc., 75(326), 351-363, 1949.

Brewer, A.: A replacement for the Dobson spectrophotometer?, Pure Appl. Geophys., 106(1), 919-927, 1973.

Brion, J., Chakir, A., Daumont, D., Malicet, J., and Parisse, C.: High-resolution laboratory absorption cross section of O_3. Temperature effect, Chem. Phys. Lett., 213(5), 610-612, 1993.

Brion, J., Chakir, A., Charbonnier, J., Daumont, D., Parisse, C., and Malicet, J.: Absorption Spectra Measurements for the Ozone Molecule in the 350–830 nm Region, J. Atmos. Chem., 30(2), 291-299, 1998.

Budd, W.: *Studies in Antarctic Meteorology*, American Geophysical Union, USA, 1966.

Burrows, J. P., Weber, M., Buchwitz, M., Rozanov, V., Ladstätter-Weißenmayer, A., Richter, A., DeBeek, R., Hoogen, R., Bramstedt, K., and Eichmann, K.-U.: The global ozone monitoring experiment (GOME): Mission concept and first scientific results, J. Atmos. Sci., 56(2), 151-175, 1999.

Butchart, N., Scaife, A. A., Bourqui, M., de Grandpré, J., Hare, S. H. E., Kettleborough, J., Langematz, U., Manzini, E., Sassi, F., Shibata, K., Shindell, D., and Sigmond, M.: Simulations of anthropogenic change in the strength of the Brewer-Dobson circulation, Climate Dynamics, 27(7), 727-741, 2006.

Calvert, J. G., and Lindberg, S. E.: Potential influence of iodine-containing compounds on the chemistry of the troposphere in the polar spring. I. Ozone depletion, Atmos. Environ., 38(30), 5087-5104, 2004a.

Calvert, J. G., and Lindberg, S. E.: The potential influence of iodine-containing compounds on the chemistry of the troposphere in the polar spring. II. Mercury depletion, Atmos. Environ., 38(30), 5105-5116, 2004b.

Calvert, J. G., Orlando, J. J., Stockwell, W. R., and Wallington, T. J.: *The Mechanisms of Reactions Influencing Atmospheric Ozone*, Oxford University Press, USA, 2015.

Cavalieri, D., and Parkinson, C.: Arctic sea ice variability and trends, 1979-2010, Cryosphere, 6(4), 881-889, 2012.

Cede, A.: Manual for Pandora Software Suite Version 1.5, 72, 2012.

Chance, K. V., and Spurr, R. J. D.: Ring effect studies: Rayleigh scattering, including molecular parameters for rotational Raman scattering, and the Fraunhofer spectrum, Appl. Opt., 36(21), 5224-5230, 1997.

Chapman, S.: *A theory of upper-atmospheric ozone*, Edward Stanford, UK, 1930.

Choi, S., Wang, Y., Salawitch, R. J., Canty, T., Joiner, J., Zeng, T., Kurosu, T. P., Chance, K., Richter, A., Huey, L. G., Liao, J., Neuman, J. A., Nowak, J. B., Dibb, J. E., Weinheimer, A. J., Diskin, G., Ryerson, T. B., da Silva, A., Curry, J., Kinnison, D., Tilmes, S., and Levelt, P. F.: Analysis of satellite-derived Arctic tropospheric BrO columns in conjunction with aircraft measurements during ARCTAS and ARCPAC, Atmos. Chem. Phys., 12(3), 1255-1285, 2012.

Cleveland, W. S., and Devlin, S. J.: Locally weighted regression: an approach to regression analysis by local fitting, J. Am. Stat. Assoc. , 83(403), 596-610, 1988.

Comiso, J. C., Cavalieri, D. J., and Markus, T.: Sea ice concentration, ice temperature, and snow depth using AMSR-E data, IEEE Trans. Geosci. Remote Sens., 41(2), 243-252, 2003.

Comiso, J. C., Parkinson, C. L., Gersten, R., and Stock, L.: Accelerated decline in the Arctic sea ice cover, Geophys. Res. Lett., 35(1), 10.1029/2007gl031972, 2008.

Craig, H.: Standard for reporting concentrations of deuterium and oxygen-18 in natural waters, Science, 133(3467), 1833-1834, 1961.

Crutzen, P. J.: The influence of nitrogen oxides on the atmospheric ozone content, Q. J. Roy. Meteor. Soc., 96(408), 320-325, 1970.

Danckaert, T., Fayt, C., Van Roozendael, M., de Smedt, I., Letocart, V., Merlaud, A., and Pinardi, G.: QDOAS Software user manual version 2.109, Belgian Institute for Space Aeronomy, Brussels, Software user manual, 125, 2015.

Dastoor, A. P., Davignon, D., Theys, N., Van Roozendael, M., Steffen, A., and Ariya, P. A.: Modeling dynamic exchange of gaseous elemental mercury at polar sunrise, Env. Sci. Tech., 42(14), 5183-5188, 2008.

Dastoor, A. P., Ryzhkov, A., Durnford, D., Lehnherr, I., Steffen, A., and Morrison, H.: Atmospheric mercury in the Canadian Arctic. Part II: Insight from modeling, Sci. Total Env., 509–510(2015), 16-27, 2015.

Daumont, D., Brion, J., Charbonnier, J., and Malicet, J.: Ozone UV spectroscopy I: Absorption cross-sections at room temperature, J. Atmos. Chem., 15(2), 145-155, 1992.

de Vries, J., Laan, E. C., Deutz, A. F., Escudero-Sanz, I., Bokhove, H., Hoegee, J., Aben, I., Jongma, R., Landgraf, J., and Hasekamp, O. P.: Spectrograph dedicated to measuring tropospheric trace gas constituents from space, Proceedings of SPIE - The International Society for Optical Engineering, 59780O-59780O-59787, 2005.

Dee, D. P., Uppala, S. M., Simmons, A. J., Berrisford, P., Poli, P., Kobayashi, S., Andrae, U., Balmaseda, M. A., Balsamo, G., Bauer, P., Bechtold, P., Beljaars, A. C. M., van de Berg, L., Bidlot, J., Bormann, N., Delsol, C., Dragani, R., Fuentes, M., Geer, A. J., Haimberger, L., Healy, S. B., Hersbach, H., Hólm, E. V., Isaksen, L., Kållberg, P., Köhler, M., Matricardi, M., McNally, A. P., Monge-Sanz, B. M., Morcrette, J. J., Park, B. K., Peubey, C., de Rosnay, P., Tavolato, C., Thépaut, J. N., and Vitart, F.: The ERA-Interim reanalysis: configuration and performance of the data assimilation system, Q. J. Roy. Meteor. Soc., 137(656), 553-597, 2011.

Déry, S. J., and Yau, M.: A bulk blowing snow model, Boundary-Layer Meteorol., 93(2), 237-251, 1999.

Déry, S. J., and Yau, M.: Simulation of blowing snow in the Canadian Arctic using a double-moment model, Boundary-Layer Meteorol., 99(2), 297-316, 2001.

Dibb, J. E., Ziemba, L. D., Luxford, J., and Beckman, P.: Bromide and other ions in the snow, firn air, and atmospheric boundary layer at Summit during GSHOX, Atmos. Chem. Phys., 10(20), 9931-9942, 2010.

Dobson, G.: Origin and distribution of the polyatomic molecules in the atmosphere, Proceedings of the Royal Society of London. Series A, Mathematical and Physical Sciences, 187-193, 1956.

Dobson, G. M. B.: Forty Years' Research on Atmospheric Ozone at Oxford: a History, Appl. Optics., 7(3), 387-405, 1968a.

Dobson, G. M. B.: *Exploring the atmosphere*, 2nd ed., Clarendon Press, UK, 1968b.

Domine, F., Sparapani, R., Ianniello, A., and Beine, H. J.: The origin of sea salt in snow on Arctic sea ice and in coastal regions, Atmos. Chem. Phys., 4(9/10), 2259-2271, 2004.

Draxler, R., and Hess, G. D.: An overview of the HYSPLIT4 modeling system for trajectories, dispersion and deposition, Aust. Meteo. Mag., 47295-308, 1998.

Draxler, R., R. Draxler, B. Stunder, G. Rolph, A. Stein, and Taylor, A.: HYSPLIT4 user's guide, NOAA, Silver Spring, MD. (Available at http://www.arl.noaa.gov/documents/reports/hysplit_user_guide.pdf), 2014.

Dunkerton, T. J., and Delisi, D. P.: Evolution of Potential Vorticity in the Winter Stratosphere of January-February 1979, J. Geophys. Res., 91(D1), 1199-1208, 1986.

Dunn, G.: *Statistical evaluation of measurement errors: Design and analysis of reliability studies*, John Wiley & Sons, 2009.

Durnford, D., Dastoor, A., Ryzhkov, A., Poissant, L., Pilote, M., and Figueras-Nieto, D.: How relevant is the deposition of mercury onto snowpacks? Part 2: A modeling study, Atmos. Chem. Phys., 12(19), 9251-9274, 2012.

Ehhalt, D., Knott, K., Nagel, J., and Vogel, J.: Deuterium and oxygen 18 in rain water, J. Geophys. Res., 68(13), 3775-3780, 1963.

Ehn, J. K., Hwang, B. J., Galley, R., and Barber, D. G.: Investigations of newly formed sea ice in the Cape Bathurst polynya: 1. Structural, physical, and optical properties, J. Geophys. Res., 112(C5), 10.1029/2006JC003702, 2007.

Errera, Q., Daerden, F., Chabrillat, S., Lambert, J. C., Lahoz, W. A., Viscardy, S., Bonjean, S., and Fonteyn, D.: 4D-Var assimilation of MIPAS chemical observations: ozone and nitrogen dioxide analyses, Atmos. Chem. Phys., 8(20), 6169-6187, 2008.

Evans, M. J., Jacob, D. J., Atlas, E., Cantrell, C. A., Eisele, F., Flocke, F., Fried, A., Mauldin, R. L., Ridley, B. A., Wert, B., Talbot, R., Blake, D., Heikes, B., Snow, J., Walega, J., Weinheimer, A. J., and Dibb, J.: Coupled evolution of BrO_x-ClO_x-HO_x-NO_x chemistry during bromine-catalyzed ozone depletion events in the arctic boundary layer, J. Geophys. Res., 108(D4), 10.1029/2002jd002732, 2003.

Fan, S.-M., and Jacob, D. J.: Surface ozone depletion in Arctic spring sustained by bromine reactions on aerosols, Nature, 359(6395), 522-524, 1992.

Farahani, E.: Stratospheric composition measurements in the Arctic and at mid-latitudes and comparison with chemical fields from atmospheric models, Ph.D. Thesis, University of Toronto, Toronto, 2006.

Farman, J. C., Gardiner, B. G., and Shanklin, J. D.: Large losses of total ozone in Antarctica reveal seasonal ClO_x/NO_x interaction, Nature, 315(6016), 207-210, 1985.

Fayt, C.: QDOAS software user manual version 2.00, Belgian Institute for Space Aeronomy, Brussels, Software User Manual, 95, 2012.

Fernandez, R. P., Salawitch, R. J., Kinnison, D. E., Lamarque, J. F., and Saiz-Lopez, A.: Bromine partitioning in the tropical tropopause layer: implications for stratospheric injection, Atmos. Chem. Phys., 14(24), 13391-13410, 2014.

Fioletov, V., Kerr, J., Wardle, D., and Wu, E.: Correction of stray light for the Brewer single monochromator, Proceedings of the Quadrennial Ozone Symposium, Japan, 3-8, 2000.

Fioletov, V., Bodeker, G., Miller, A., McPeters, R., and Stolarski, R.: Global and zonal total ozone variations estimated from ground-based and satellite measurements: 1964-2000, J. Geophys. Res., 107(D22), 10.1029/2001JD001350, 2002.

Fioletov, V., Kerr, J., McElroy, C., Wardle, D., Savastiouk, V., and Grajnar, T.: The Brewer reference triad, Geophys. Res. Lett., 32(20), 10.1029/2005GL024244., 2005.

Fioletov, V., Tarasick, D., and Petropavlovskikh, I.: Estimating ozone variability and instrument uncertainties from SBUV (/2), ozonesonde, Umkehr, and SAGE II measurements: Short-term variations, J. Geophys. Res., 111(D2), 10.1029/2005jd006340, 2006.

Fioletov, V., McLinden, C., McElroy, C., and Savastiouk, V.: New method for deriving total ozone from Brewer zenith sky observations, J. Geophys. Res., 116(D8), 10.1029/2010JD015399, 2011.

Fish, D., and Jones, R.: Rotational Raman scattering and the ring effect in zenith-sky spectra, Geophys. Res. Lett., 22(7), 811-814, 1995.

Fleischmann, O. C., Hartmann, M., Burrows, J. P., and Orphal, J.: New ultraviolet absorption cross-sections of BrO at atmospheric temperatures measured by time-windowing Fourier transform spectroscopy, J. Photochem. Photobiol. A, 168(1-2), 117-132, 2004.

Fogal, P. F., LeBlanc, L. M., and Drummond, J. R.: The Polar Environment Atmospheric Research Laboratory (PEARL): Sounding the Atmosphere at 80˚ North, Arctic, 66(3), 337-386, 2013.

Franklin, J. E.: Solar absorption spectroscopy at the Dalhousie Atmospheric Observatory, Ph.D. Thesis, Dalhousie University, Halifax, 2015.

Fraser, A., Bernath, P., Blatherwick, R., Drummond, J., Fogal, P., Fu, D., Goutail, F., Kerzenmacher, T., McElroy, C., and Midwinter, C.: Intercomparison of ground-based ozone and NO_2 measurements during the MANTRA 2004 campaign, Atmos. Chem. Phys., 7(21), 5489-5499, 2007a.

Fraser, A., Goutail, F., McLinden, C., Melo, S., and Strong, K.: Lightning-produced NO_2 observed by two ground-based UV-visible spectrometers at Vanscoy, Saskatchewan in August 2004, Atmos. Chem. Phys., 7(6), 1683-1692, 2007b.

Fraser, A., Goutail, F., Strong, K., Bernath, P. F., Boone, C., Daffer, W. H., Drummond, J. R., Dufour, D. G., Kerzenmacher, T. E., Manney, G. L., McElroy, C. T., Midwinter, C., McLinden, C. A., Nichitiu, F., Nowlan, C. R., Walker, J., Walker, K. A., Wu, H., and Zou, J.: Intercomparison of UV-visible measurements of ozone and NO_2 during the Canadian Arctic ACE validation campaigns: 2004-2006, Atmos. Chem. Phys., 8(6), 1763-1788, 2008.

Fraser, A., Adams, C., Drummond, J. R., Goutail, F., Manney, G., and Strong, K.: The Polar Environment Atmospheric Research Laboratory UV-visible Ground-Based Spectrometer: First measurements of O_3, NO_2, BrO, and OClO columns, J. Quant. Spectrosc. Radiat. Transfer, 110(12), 986-1004, 2009.

Fraser, A. C.: Arctic and midlatitude stratospheric trace gas measurements using ground-based UV-visible spectroscopy, Ph.D. Thesis, University of Toronto, Toronto, 2008.

Frieß, U., Hollwedel, J., König-Langlo, G., Wagner, T., and Platt, U.: Dynamics and chemistry of tropospheric bromine explosion events in the Antarctic coastal region, J. Geophys. Res., 109(D6), 10.1029/2003jd004133, 2004.

Frieß, U., Sihler, H., Sander, R., Pöhler, D., Yilmaz, S., and Platt, U.: The vertical distribution of BrO and aerosols in the Arctic: Measurements by active and passive differential optical absorption spectroscopy, J. Geophys. Res., 116(D14), 10.1029/2011jd015938, 2011.

Fujiwara, M., Wright, J. S., Manney, G. L., Gray, L. J., Anstey, J., Birner, T., Davis, S., Gerber, E. P., Harvey, V. L., and Hegglin, M. I.: Introduction to the SPARC Reanalysis Intercomparison Project (S-RIP) and overview of the reanalysis systems, Atmos. Chem. Phys., 17(2), 1417-1452, 2017.

Gilman, J. B., Burkhart, J. F., Lerner, B. M., Williams, E. J., Kuster, W., Goldan, P. D., Murphy, P. C., Warneke, C., Fowler, C., and Montzka, S. A.: Ozone variability and halogen oxidation within the Arctic and sub-Arctic springtime boundary layer, Atmos. Chem. Phys, 10(21), 10,223-210,236, 2010.

Grainger, J., and Ring, J.: Anomalous Fraunhofer line profiles, Nature, 193762, 1962.

Grannas, A. M., Jones, A. E., Dibb, J., Ammann, M., Anastasio, C., Beine, H. J., Bergin, M., Bottenheim, J., Boxe, C. S., Carver, G., Chen, G., Crawford, J. H., Dominé, F., Frey, M. M., Guzmán, M. I., Heard, D. E., Helmig, D., Hoffmann, M. R., Honrath, R. E., Huey, L. G., Hutterli, M., Jacobi, H. W., Klán, P., Lefer, B., McConnell, J., Plane, J., Sander, R., Savarino, J., Shepson, P. B., Simpson, W. R., Sodeau, J. R., von Glasow, R., Weller, R., Wolff, E. W., and Zhu, T.: An overview of snow photochemistry: evidence, mechanisms and impacts, Atmos. Chem. Phys., 7(16), 4329-4373, 2007.

Grubbs, F. E.: On estimating precision of measuring instruments and product variability, J. Am. Stat. Assoc. , 43(242), 243-264, 1948.

Hay, T. D.: MAX-DOAS measurements of bromine explosion events in McMurdo Sound, Antarctica, Ph.D. Thesis, University of Canterbury, Canterbury, 2010.

Heintzenberg, J., Covert, D., and Van Dingenen, R.: Size distribution and chemical composition of marine aerosols: a compilation and review, Tellus B, 52(4), 1104-1122, 2000.

Helmig, D., Boylan, P., Johnson, B., Oltmans, S., Fairall, C., Staebler, R., Weinheimer, A., Orlando, J., Knapp, D. J., Montzka, D. D., Flocke, F., Frieß, U., Sihler, H., and Shepson, P. B.: Ozone dynamics and snow-atmosphere exchanges during ozone depletion events at Barrow, Alaska, J. Geophys. Res., 117(D20), 10.1029/2012jd017531, 2012.

Hendrick, F., Van Roozendael, M., Chipperfield, M. P., Dorf, M., Goutail, F., Yang, X., Fayt, C., Hermans, C., Pfeilsticker, K., Pommereau, J. P., Pyle, J. A., Theys, N., and De Mazière, M.: Retrieval of stratospheric and tropospheric BrO profiles and columns using ground-based zenith-sky DOAS observations at Harestua, 60°N, Atmos. Chem. Phys., 7(18), 4869-4885, 2007.

Hendrick, F., Pommereau, J. P., Goutail, F., Evans, R. D., Ionov, D., Pazmino, A., Kyrö, E., Held, G., Eriksen, P., Dorokhov, V., Gil, M., and Van Roozendael, M.: NDACC/SAOZ UV-visible total ozone measurements: improved retrieval and comparison with correlative ground-based and satellite observations, Atmos. Chem. Phys., 11(12), 5975-5995, 2011.

Hendrick, F., Pinardi, G., Roozendael, M. V., Apituley, A., Piters, A., Richter, A., Wagner, T., Kreher, K., Friess, U., and Lampel, J.: Fiducial Reference Measurements for Ground-Based

DOAS Air-Quality Observations (Intercomparison Campaign Planning Document), Cabauw, 118, 2016.

Herman, J., Cede, A., Spinei, E., Mount, G., Tzortziou, M., and Abuhassan, N.: NO_2 column amounts from ground-based Pandora and MFDOAS spectrometers using the direct-Sun DOAS technique: Intercomparisons and application to OMI validation, J. Geophys. Res., 114(D13), 10.1029/2009JD011848, 2009.

Herman, J., Evans, R., Cede, A., Abuhassan, N., Petropavlovskikh, I., and McConville, G.: Comparison of ozone retrievals from the Pandora spectrometer system and Dobson spectrophotometer in Boulder, Colorado, Atmos. Meas. Tech., 8(8), 3407-3418, 2015.

Hermans, C., Vandaele, A., Fally, S., Carleer, M., Colin, R., Coquart, B., Jenouvrier, A., and Merienne, M.-F.: Absorption cross-section of the collision-induced bands of oxygen from the UV to the NIR, in: Weakly Interacting Molecular Pairs: Unconventional Absorbers of Radiation in the Atmosphere, edited by: Camy-Peyret, C., and Vigasin, A. A., Springer, Germany, 2003.

Hollwedel, J., Wenig, M., Beirle, S., Kraus, S., Kühl, S., Wilms-Grabe, W., Platt, U., and Wagner, T.: Year-to-year variations of spring time polar tropospheric BrO as seen by GOME, Adv. Space Res., 34(4), 804-808, 2004.

Hönninger, G., and Platt, U.: Observations of BrO and its vertical distribution during surface ozone depletion at Alert, Atmos. Environ., 36(15-16), 2481-2489, 2002.

Hönninger, G., Leser, H., Sebastian, O., and Platt, U.: Ground-based measurements of halogen oxides at the Hudson Bay by active longpath DOAS and passive MAX-DOAS, Geophys. Res. Lett., 31(4), 10.1029/2003GL018982, 2004a.

Hönninger, G., von Friedeburg, C., and Platt, U.: Multi axis differential optical absorption spectroscopy (MAX-DOAS), Atmos. Chem. Phys., 4(1), 231-254, 2004b.

Honrath, R., Peterson, M. C., Guo, S., Dibb, J. E., Shepson, P., and Campbell, B.: Evidence of NO_x production within or upon ice particles in the Greenland snowpack, Geophys. Res. Lett., 26(6), 695-698, 1999.

Hopper, J. F., Barrie, L. A., Silis, A., Hart, W., Gallant, A. J., and Dryfhout, H.: Ozone and meteorology during the 1994 Polar Sunrise Experiment, J. Geophys. Res., 103(D1), 1481-1492, 1998.

Hoyle, C. R., Marécal, V., Russo, M. R., Allen, G., Arteta, J., Chemel, C., Chipperfield, M. P., D'Amato, F., Dessens, O., Feng, W., Hamilton, J. F., Harris, N. R. P., Hosking, J. S., Lewis, A. C., Morgenstern, O., Peter, T., Pyle, J. A., Reddmann, T., Richards, N. A. D., Telford, P. J., Tian, W., Viciani, S., Volz-Thomas, A., Wild, O., Yang, X., and Zeng, G.: Representation of tropical deep convection in atmospheric models - Part 2: Tracer transport, Atmos. Chem. Phys., 11(15), 8103-8131, 2011.

IPCC: Climate change 2013: The Physical Science Basis. Contribution of Working Group 1 to the Fifth Assessment Report of the Intergovernmental Panel on Climate Change, doi:10.1017/CBO9781107415324, 2013.

Johnson, C., Mann, G., Bellouin, N., and Dalvi, M.: Comparison between UKCAMODE and CLASSIC aerosol schemes in HadGEM3, Integrated Climate Programme MOHC Report M3. 2 to DECC, March 2010. Technical report, Met Office, 2010.

Johnston, H.: Reduction of stratospheric ozone by nitrogen oxide catalysts from supersonic transport exhaust, Science, 173(3996), 517-522, 1971.

Jones, A., Wolff, E., Salmon, R., Bauguitte, S.-B., Roscoe, H., Anderson, P., Ames, D., Clemitshaw, K., Fleming, Z. L., and Bloss, W.: Chemistry of the Antarctic Boundary Layer and the Interface with Snow: an overview of the CHABLIS campaign, Atmos. Chem. Phys., 8(14), 3789-3803, 2008.

Jones, A. E., Anderson, P. S., Begoin, M., Brough, N., Hutterli, M. A., Marshall, G. J., Richter, A., Roscoe, H. K., and Wolff, E. W.: BrO, blizzards, and drivers of polar tropospheric ozone depletion events, Atmos. Chem. Phys., 9(14), 4639-4652, 2009.

Jouzel, J., and Merlivat, L.: Deuterium and oxygen 18 in precipitation: Modeling of the isotopic effects during snow formation, J. Geophys. Res., 89(D7), 11749-11757, 1984.

Kaleschke, L., Richter, A., Burrows, J., Afe, O., Heygster, G., Notholt, J., Rankin, A. M., Roscoe, H. K., Hollwedel, J., Wagner, T., and Jacobi, H. W.: Frost flowers on sea ice as a source of sea salt and their influence on tropospheric halogen chemistry, Geophys. Res. Lett., 31(16), 10.1029/2004gl020655, 2004.

Kalnay, E., Kanamitsu, M., Kistler, R., Collins, W., Deaven, D., Gandin, L., Iredell, M., Saha, S., White, G., and Woollen, J.: The NCEP/NCAR 40-year reanalysis project, B. Am. Meteorol. Soc., 77(3), 437-471, 1996.

Keeling, C. D.: The concentration and isotopic abundances of atmospheric carbon dioxide in rural areas, Geochimica et cosmochimica acta, 13(4), 322-334, 1958.

Kerr, J., McElroy, C., and Olafson, R.: Measurements of ozone with the Brewer ozone spectrophotometer, Proceedings of the Quadrennial Ozone Symposium, Boulder, 74-79, 1981.

Kerr, J., Asbridge, I., and Evans, W.: Intercomparison of total ozone measured by the Brewer and Dobson spectrophotometers at Toronto, J. Geophys. Res., 93(D9), 11129-11140, 1988.

Kerr, J., Fast, H., McElroy, C., Oltmans, S., Lathrop, J., Kyro, E., Paukkunen, A., Claude, H., Köhler, U., and Sreedharan, C.: The 1991 WMO international ozonesonde intercomparison at Vanscoy, Canada, Atmos.-Ocean, 32(4), 685-716, 1994.

Kerr, J., McElroy, C., and Wardle, D.: The Brewer instrument calibration center 1984-1996, Proceedings of the Quadrennial Ozone Symposium, Italy, 915-918, 1998.

Kerr, J.: New methodology for deriving total ozone and other atmospheric variables from Brewer spectrophotometer direct sun spectra, J. Geophys. Res., 107(D23), 10.1029/2001JD001227, 2002.

Kerzenmacher, T. E., Walker, K. A., Strong, K., Berman, R., Bernath, P. F., Boone, C. D., Drummond, J. R., Fast, H., Fraser, A., and MacQuarrie, K.: Measurements of O_3, NO_2 and temperature during the 2004 Canadian Arctic ACE Validation Campaign, Geophys. Res. Lett., 32(16), 10.1029/2005GL023032, 2005.

Kitchin, C. R.: *Astrophysical techniques*, Taylor & Francis, UK, 2013.

Koo, J. H., Wang, Y., Kurosu, T. P., Chance, K., Rozanov, A., Richter, A., Oltmans, S. J., Thompson, A. M., Hair, J. W., Fenn, M. A., Weinheimer, A. J., Ryerson, T. B., Solberg, S., Huey, L. G., Liao, J., Dibb, J. E., Neuman, J. A., Nowak, J. B., Pierce, R. B., Natarajan, M., and Al-Saadi, J.: Characteristics of tropospheric ozone depletion events in the Arctic spring: analysis of the ARCTAS, ARCPAC, and ARCIONS measurements and satellite BrO observations, Atmos. Chem. Phys., 12(20), 9909-9922, 2012.

Kraus, S.: *DOASIS: A framework design for DOAS*, Shaker, Germany, 2006.

Kroon, M., Veefkind, J. P., Sneep, M., McPeters, R. D., Bhartia, P. K., and Levelt, P. F.: Comparing OMI-TOMS and OMI-DOAS total ozone column data, J. Geophys. Res., 113(D16), 10.1029/2007jd008798, 2008.

Kurtz, N., Studinger, M. S., Harbeck, J., Onana, V., and Farrell, S.: IceBridge Sea Ice Freeboard, Snow Depth, and Thickness, Boulder, Colorado USA: NASA DAAC at the National Snow and Ice Data Center, 2012.

Kurtz, N. T., Markus, T., Farrell, S. L., Worthen, D. L., and Boisvert, L. N.: Observations of recent Arctic sea ice volume loss and its impact on ocean-atmosphere energy exchange and ice production, J. Geophys. Res., 116(C4), 10.1029/2010jc006235, 2011.

Labow, G. J., McPeters, R. D., Bhartia, P. K., and Kramarova, N.: A comparison of 40 years of SBUV measurements of column ozone with data from the Dobson/Brewer network, J. Geophys. Res., 118(13), 7370-7378, 2013.

Legrand, M., Yang, X., Preunkert, S., and Theys, N.: Year-round records of sea salt, gaseous, and particulate inorganic bromine in the atmospheric boundary layer at coastal (Dumont d'Urville) and central (Concordia) East Antarctic sites, J. Geophys. Res., 121(2), 997-1023, 2016.

Lehrer, E., Hönninger, G., and Platt, U.: A one dimensional model study of the mechanism of halogen liberation and vertical transport in the polar troposphere, Atmos. Chem. Phys., 4(11/12), 2427-2440, 2004.

Leser, H., Hönninger, G., and Platt, U.: MAX-DOAS measurements of BrO and NO_2 in the marine boundary layer, Geophys. Res. Lett., 30(10), 10.1029/2002gl015811, 2003.

Levelt, P. F., Hilsenrath, E., Leppelmeier, G. W., Van den Oord, G. H., Bhartia, P. K., Tamminen, J., De Haan, J. F., and Veefkind, J. P.: Science objectives of the ozone monitoring instrument, IEEE Trans. Geosci. Remote Sens., 44(5), 1199-1208, 2006.

Levine, J., Yang, X., Jones, A., and Wolff, E.: Sea salt as an ice core proxy for past sea ice extent: A process-based model study, J. Geophys. Res., 119(9), 10.1002/2013JD020925, 2014.

Lewis, E. R., and Schwartz, S. E.: *Sea salt aerosol production: mechanisms, methods, measurements, and models-A critical review*, American Geophysical Union, USA, 2004.

Li, L., and Pomeroy, J. W.: Probability of blowing snow occurrence by wind, J. Geophys. Res., 102(21), 21955-21964, 1997.

Liao, J., Sihler, H., Huey, L. G., Neuman, J. A., Tanner, D. J., Friess, U., Platt, U., Flocke, F. M., Orlando, J. J., Shepson, P. B., Beine, H. J., Weinheimer, A. J., Sjostedt, S. J., Nowak, J. B., Knapp, D. J., Staebler, R. M., Zheng, W., Sander, R., Hall, S. R., and Ullmann, K.: A comparison of Arctic BrO measurements by chemical ionization mass spectrometry and long path-differential optical absorption spectroscopy, J. Geophys. Res., 116(D14), 10.1029/2010jd014788, 2011.

Liao, J., Huey, L. G., Scheuer, E., Dibb, J. E., Stickel, R. E., Tanner, D. J., Neuman, J. A., Nowak, J. B., Choi, S., Wang, Y., Salawitch, R. J., Canty, T., Chance, K., Kurosu, T., Suleiman, R., Weinheimer, A. J., Shetter, R. E., Fried, A., Brune, W., Anderson, B., Zhang, X., Chen, G., Crawford, J., Hecobian, A., and Ingall, E. D.: Characterization of soluble bromide measurements and a case study of BrO observations during ARCTAS, Atmos. Chem. Phys., 12(3), 1327-1338, 2012.

Lindenmaier, R., Strong, K., Batchelor, R., Chipperfield, M., Daffer, W., Drummond, J., Duck, T., Fast, H., Feng, W., and Fogal, P.: Unusually low ozone, HCl, and HN_3 column measurements at Eureka, Canada during winter/spring 2011, Atmos. Chem. Phys., 12(8), 3821-3835, 2012.

Lipson, A., Lipson, S. G., and Lipson, H.: *Optical physics*, Cambridge University Press, UK, 2010.

Loyola, D., Koukouli, M., Valks, P., Balis, D., Hao, N., Van Roozendael, M., Spurr, R., Zimmer, W., Kiemle, S., and Lerot, C.: The GOME-2 total column ozone product: Retrieval algorithm and ground-based validation, J. Geophys. Res., 116(D7), 10.1029/2010JD014675, 2011.

Lutsch, E., Dammers, E., Conway, S., and Strong, K.: Long-range transport of NH_3, CO, HCN, and C_2H_6 from the 2014 Canadian Wildfires, Geophys. Res. Lett., 43(15), 8286-8297, 2016.

Mackay, C. D.: Charge-coupled devices in astronomy, Annual Review of Astronomy and Astrophysics, 24(1), 255-283, 1986.

Manney, G. L., Zurek, R. W., Gelman, M. E., Miller, A. J., and Nagatani, R.: The anomalous Arctic lower stratospheric polar vortex of 1992-1993, Geophys. Res. Lett., 21(22), 2405-2408, 1994.

Manney, G. L., Daffer, W. H., Zawodny, J. M., Bernath, P. F., Hoppel, K. W., Walker, K. A., Knosp, B. W., Boone, C., Remsberg, E. E., Santee, M. L., Harvey, V. L., Pawson, S., Jackson, D. R., Deaver, L., McElroy, C. T., McLinden, C. A., Drummond, J. R., Pumphrey, H. C., Lambert, A., Schwartz, M. J., Froidevaux, L., McLeod, S., Takacs, L. L., Suarez, M. J., Trepte, C. R., Cuddy, D. C., Livesey, N. J., Harwood, R. S., and Waters, J. W.: Solar occultation satellite data and derived meteorological products: Sampling issues and comparisons with Aura Microwave Limb Sounder, J. Geophys. Res., 112(D24), 10.1029/2007jd008709, 2007.

Manney, G. L., Daffer, W. H., Strawbridge, K. B., Walker, K. A., Boone, C. D., Bernath, P. F., Kerzenmacher, T., Schwartz, M. J., Strong, K., Sica, R. J., Krüger, K., Pumphrey, H. C., Lambert, A., Santee, M. L., Livesey, N. J., Remsberg, E. E., Mlynczak, M. G., and Russell Iii, J. R.: The high Arctic in extreme winters: vortex, temperature, and MLS and ACE-FTS trace gas evolution, Atmos. Chem. Phys., 8(3), 505-522, 2008.

Manney, G. L., Santee, M. L., Rex, M., Livesey, N. J., Pitts, M. C., Veefkind, P., Nash, E. R., Wohltmann, I., Lehmann, R., and Froidevaux, L.: Unprecedented Arctic ozone loss in 2011, Nature, 478(7370), 469-475, 2011.

Maslanik, J. A., Fowler, C., Stroeve, J., Drobot, S., Zwally, J., Yi, D., and Emery, W.: A younger, thinner Arctic ice cover: Increased potential for rapid, extensive sea-ice loss, Geophys. Res. Lett., 34(24), 10.1029/2007gl032043, 2007.

Massom, R. A., Eicken, H., Hass, C., Jeffries, M. O., Drinkwater, M. R., Sturm, M., Worby, A. P., Wu, X., Lytle, V. I., and Ushio, S.: Snow on Antarctic sea ice, Rev. Geophys., 39(3), 413-445, 2001.

May, N., Quinn, P., McNamara, S., and Pratt, K.: Multiyear study of the dependence of sea salt aerosol on wind speed and sea ice conditions in the coastal Arctic, J. Geophys. Res., 121(15), 9208-9219, 2016.

McConnell, J. C., Henderson, G. S., Barrie, L., Bottenheim, J., Niki, H., Langford, C. H., and Templeton, E. M. J.: Photochemical bromine production implicated in Arctic boundary-layer ozone depletion, Nature, 355(6356), 150-152, 1992.

McElroy, C., and Fogal, P.: Ozone: From discovery to protection, Atmos.-Ocean, 46(1), 1-13, 2008.

McPeters, R. D., and Labow, G. J.: An assessment of the accuracy of 14.5 years of Nimbus 7 TOMS version 7 ozone data by comparison with the Dobson network, Geophys. Res. Lett., 23(25), 3695-3698, 1996.

McPeters, R. D., and Labow, G. J.: Climatology 2011: An MLS and sonde derived ozone climatology for satellite retrieval algorithms, J. Geophys. Res., 117(D10), 10.1029/2011JD017006, 2012.

Melo, S. M., Farahani, E., Strong, K., Bassford, M., Preston, K., and McLinden, C. A.: NO_2 vertical profiles retrieved from ground-based measurements during spring 1999 in the Canadian Arctic, Adv. Space Res., 34(4), 786-792, 2004.

Melo, S. M., Strong, K., Bassford, M., Preston, K., McElroy, C. T., Rozanov, E. V., and Egorova, T.: Retrieval of stratospheric NO_2 vertical profiles from ground-based zenith-sky

DOAS measurements: Results for the MANTRA 1998 field campaign, Atmos.-Ocean, 43(4), 339-350, 2005.

Merlivat, L., and Nief, G.: Fractionnement isotopique lors des changements d ‘état solide-vapeur et liquide-vapeur de l'eau à des températures inférieures à 0°C, Tellus, 19(1), 122-127, 1967.

Miller, J. B., and Tans, P. P.: Calculating isotopic fractionation from atmospheric measurements at various scales, Tellus B, 55(2), 207-214, 2003.

Molina, M. J., and Rowland, F. S.: Stratospheric sink for chlorofluoromethanes - chlorine atomic-catalysed destruction of ozone, Nature, 249(5460), 810-812, 1974.

Morgenstern, O., Braesicke, P., O'Connor, F. M., Bushell, A. C., Johnson, C. E., Osprey, S. M., and Pyle, J. A.: Evaluation of the new UKCA climate-composition model - Part 1: The stratosphere, Geosci. Model Dev., 2(1), 43-57, 2009.

Mount, G. H., Sanders, R. W., Schmeltekopf, A. L., and Solomon, S.: Visible spectroscopy at mcmurdo station, Antarctica .1. Overview and daily variations of NO_2 and O_3, Austral Spring, 1986, J. Geophys. Res., 92(D7), 8320-8328, 1987.

Moyer, E. J., Irion, F. W., Yung, Y. L., and Gunson, M. R.: ATMOS stratospheric deuterated water and implications for troposphere-stratosphere transport, Geophys. Res. Lett., 23(17), 2385-2388, 1996.

NDACC protocol: - Appendix VII - UV/Visible Instruments: http://www.ndsc.ncep.noaa.gov/organize/protocols/appendix7/, access date: 03/02/2017.

Neuman, J. A., Nowak, J. B., Huey, L. G., and Burkholder, J. B.: Bromine measurements in ozone depleted air over the Arctic Ocean, Atmos. Chem. Phys., 10(14), 6503-6514, 2010.

Nilsson, E., Rannik, Ü., Swietlicki, E., Leck, C., Aalto, P. P., Zhou, J., and Norman, M.: Turbulent aerosol fluxes over the Arctic Ocean: 2. Wind-driven sources from the sea, J. Geophys. Res., 106(D23), 32139-32154, 2001.

Noone, D.: Pairing measurements of the water vapor isotope ratio with humidity to deduce atmospheric moistening and dehydration in the tropical midtroposphere, J. Climate., 25(13), 4476-4494, 2012.

Noone, D., Risi, C., Bailey, A., Berkelhammer, M., Brown, D., Buenning, N., Gregory, S., Nusbaumer, J., Schneider, D., and Sykes, J.: Determining water sources in the boundary layer from tall tower profiles of water vapor and surface water isotope ratios after a snowstorm in Colorado, Atmos. Chem. Phys., 13(3), 1607-1623, 2013.

Noxon, J.: Nitrogen dioxide in the stratosphere and troposphere measured by ground-based absorption spectroscopy, Science, 189(4202), 547-549, 1975.

O'Connor, F., Carver, G., Savage, N., Pyle, J., Methven, J., Arnold, S., Dewey, K., and Kent, J.: Comparison and visualisation of high-resolution transport modelling with aircraft measurements, Atmos. Sci. Lett., 6(3), 164-170, 2005.

Obbard, R. W., Roscoe, H. K., Wolff, E. W., and Atkinson, H. M.: Frost flower surface area and chemistry as a function of salinity and temperature, J. Geophys. Res., 114(D20), 10.1029/2009JD012481, 2009.

Oltmans, S. J., and Komhyr, W. D.: Surface Ozone Distributions and Variations From 1973-1984 Measurements at the NOAA Geophysical Monitoring for Climatic Change Baseline Observatories, J. Geophys. Res., 91(D4), 5229-5236, 1986.

Ortega, I., Koenig, T., Sinreich, R., Thomson, D., and Volkamer, R.: The CU 2-D-MAX-DOAS instrument – Part 1: Retrieval of 3-D distributions of NO_2 and azimuth-dependent OVOC ratios, Atmos. Meas. Tech., 8(6), 2371-2395, 2015.

Ortega, I., Coburn, S., Berg, L. K., Lantz, K., Michalsky, J., Ferrare, R. A., Hair, J. W., Hostetler, C. A., and Volkamer, R.: The CU 2-D-MAX-DOAS instrument – Part 2: Raman scattering probability measurements and retrieval of aerosol optical properties, Atmos. Meas. Tech., 9(8), 3893-3910, 2016.

Perner, D., and Platt, U.: Detection of nitrous acid in the atmosphere by differential optical absorption, Geophys. Res. Lett., 6(12), 917-920, 1979.

Perrin, F. H.: Whose absorption law?, J. Opt. Soc. Am., 38(1), 72-74, 1948.

Peterson, P. K., Simpson, W. R., Pratt, K. A., Shepson, P. B., Frieß, U., Zielcke, J., Platt, U., Walsh, S. J., and Nghiem, S. V.: Dependence of the vertical distribution of bromine monoxide in the lower troposphere on meteorological factors such as wind speed and stability, Atmos. Chem. Phys., 15(4), 2119-2137, 2015.

Pinardi, G., Van Roozendael, M., Abuhassan, N., Adams, C., Cede, A., Clémer, K., Fayt, C., Frieß, U., Gil, M., Herman, J., Hermans, C., Hendrick, F., Irie, H., Merlaud, A., Navarro Comas, M., Peters, E., Piters, A. J. M., Puentedura, O., Richter, A., Schönhardt, A., Shaiganfar, R., Spinei, E., Strong, K., Takashima, H., Vrekoussis, M., Wagner, T., Wittrock, F., and Yilmaz, S.: MAX-DOAS formaldehyde slant column measurements during CINDI: intercomparison and analysis improvement, Atmos. Meas. Tech., 6(1), 167-185, 2013.

Piot, M., and von Glasow, R.: The potential importance of frost flowers, recycling on snow, and open leads for ozone depletion events, Atmos. Chem. Phys., 8(9), 2437-2467, 2008.

Piot, M., and Von Glasow, R.: Modelling the multiphase near-surface chemistry related to ozone depletions in polar spring, J Atmos Chem, 64(2-3), 77-105, 2009.

Piters, A. J. M., Boersma, K. F., Kroon, M., Hains, J. C., Van Roozendael, M., Wittrock, F., Abuhassan, N., Adams, C., Akrami, M., Allaart, M. A. F., Apituley, A., Beirle, S., Bergwerff, J. B., Berkhout, A. J. C., Brunner, D., Cede, A., Chong, J., Clémer, K., Fayt, C., Frieß, U., Gast, L. F. L., Gil-Ojeda, M., Goutail, F., Graves, R., Griesfeller, A., Großmann, K., Hemerijckx, G., Hendrick, F., Henzing, B., Herman, J., Hermans, C., Hoexum, M., van der Hoff, G. R., Irie, H., Johnston, P. V., Kanaya, Y., Kim, Y. J., Klein Baltink, H., Kreher, K., de Leeuw, G., Leigh, R., Merlaud, A., Moerman, M. M., Monks, P. S., Mount, G. H., Navarro-Comas, M., Oetjen, H., Pazmino, A., Perez-Camacho, M., Peters, E., du Piesanie, A., Pinardi, G., Puentedura, O., Richter, A., Roscoe, H. K., Schönhardt, A., Schwarzenbach, B., Shaiganfar, R., Sluis, W., Spinei, E., Stolk, A. P., Strong, K., Swart, D. P. J., Takashima, H., Vlemmix, T., Vrekoussis, M., Wagner, T., Whyte, C., Wilson, K. M., Yela, M., Yilmaz, S., Zieger, P., and Zhou, Y.: The

Cabauw Intercomparison campaign for Nitrogen Dioxide measuring Instruments (CINDI): design, execution, and early results, Atmos. Meas. Tech., 5(2), 457-485, 2012.

Platt, U., Perner, D., and Pätz, H.: Simultaneous measurement of atmospheric CH_2O, O_3, and NO_2 by differential optical absorption, J. Geophys. Res., 84(C10), 6329-6335, 1979.

Platt, U.: Differential optical absorption spectroscopy (DOAS), Air Monit. Spectro. Tech., 12727-84, 1994.

Platt, U., and Lehrer, E.: Arctic tropospheric ozone chemistry, ARCTOC, Final Report of the EU-Project No, EV5V-CT93-0318, Heidelberg, 1996.

Platt, U., and Stutz, J.: *Differential Optical Absorption Spectroscopy: Principles and Applications*, Springer, Germany, 2008.

Pomeroy, J. W., Marsh, P., and Gray, D. M.: Application of a distributed blowing snow model to the Arctic, Hydrol. Process., 11(11), 1451-1464, 1997.

Prados-Roman, C., Butz, A., Deutschmann, T., Dorf, M., Kritten, L., Minikin, A., Platt, U., Schlager, H., Sihler, H., Theys, N., Van Roozendael, M., Wagner, T., and Pfeilsticker, K.: Airborne DOAS limb measurements of tropospheric trace gas profiles: case studies on the profile retrieval of O_4 and BrO, Atmos. Meas. Tech., 4(6), 1241-1260, 2011.

Pratt, K. A., Custard, K. D., Shepson, P. B., Douglas, T. A., Pohler, D., General, S., Zielcke, J., Simpson, W. R., Platt, U., Tanner, D. J., Gregory Huey, L., Carlsen, M., and Stirm, B. H.: Photochemical production of molecular bromine in Arctic surface snowpacks, Nature Geosci., 6(5), 351-356, 2013.

Ramaswamy, V., Schwarzkopf, M. D., and Shine, K. P.: Radiative forcing of climate from halocarbon-induced global stratospheric ozone loss, Nature, 355(6363), 810-812, 1992.

Rankin, A. M., Wolff, E. W., and Martin, S.: Frost flowers: Implications for tropospheric chemistry and ice core interpretation, J. Geophys. Res., 107(D23), 10.1029/2002jd002492, 2002.

Rannik, U.: Turbulent aerosol fluxes over the Arctic Ocean 1. Dry deposition over sea and pack ice, J. Geophys. Res., 106(D23), 32,125-132,137, 2001.

Rayleigh, L., and Ramsay, W.: Argon, a New Constituent of the Atmosphere, Proceedings of the Royal Society of London, 57(340-346), 265-287, 1894.

Rayner, N., Parker, D. E., Horton, E., Folland, C., Alexander, L., Rowell, D., Kent, E., and Kaplan, A.: Global analyses of sea surface temperature, sea ice, and night marine air temperature since the late nineteenth century, J. Geophys. Res., 108(D14), 10.1029/2002JD002670, 2003.

Reader, M., and McFarlane, N.: Sea-salt aerosol distribution during the Last Glacial Maximum and its implications for mineral dust, J. Geophys. Res., 108(D8), 10.1029/2002JD002063, 2003.

Redondas, A., Evans, R., Stuebi, R., Köhler, U., and Weber, M.: Evaluation of the use of five laboratory-determined ozone absorption cross sections in Brewer and Dobson retrieval algorithms, Atmos. Chem. Phys., 14(3), 1635-1648, 2014.

Rhodes, B. C.: PyEphem, 2010.

Rhodes, R. H., Yang, X., Wolff, E. W., and McConnell, J. R.: Sea ice as a source of sea salt aerosol to Greenland ice cores: a model-based study, submitted to Atmospheric Chemistry and Physics, 2017.

Richter, A., Wittrock, F., Eisinger, M., and Burrows, J. P.: GOME observations of tropospheric BrO in northern hemispheric spring and summer 1997, Geophys. Res. Lett., 25(14), 2683-2686, 1998.

Rienecker, M. M., Suarez, M. J., Gelaro, R., Todling, R., Bacmeister, J., Liu, E., Bosilovich, M. G., Schubert, S. D., Takacs, L., and Kim, G.-K.: MERRA: NASA's modern-era retrospective analysis for research and applications, J. Climate., 24(14), 3624-3648, 2011.

Rodgers, C. D.: *Inverse Methods for Atmospheric Sounding: Theory and Practice*, *Series on Atmospheric, Oceanic and Planetary Physics*, vol. 2, World Scientific, 2000.

Roscoe, H. K., Van Roozendael, M., Fayt, C., du Piesanie, A., Abuhassan, N., Adams, C., Akrami, M., Cede, A., Chong, J., Clemer, K., Friess, U., Ojeda, M. G., Goutail, F., Graves, R., Griesfeller, A., Grossmann, K., Hemerijckx, G., Hendrick, F., Herman, J., Hermans, C., Irie, H., Johnston, P. V., Kanaya, Y., Kreher, K., Leigh, R., Merlaud, A., Mount, G. H., Navarro, M., Oetjen, H., Pazmino, A., Perez-Camacho, M., Peters, E., Pinardi, G., Puentedura, O., Richter, A., Schonhardt, A., Shaiganfar, R., Spinei, E., Strong, K., Takashima, H., Vlemmix, T., Vrekoussis, M., Wagner, T., Wittrock, F., Yela, M., Yilmaz, S., Boersma, F., Hains, J., Kroon, M., Piters, A., and Kim, Y. J.: Intercomparison of slant column measurements of NO_2 and O_4 by MAX-DOAS and zenith-sky UV and visible spectrometers, Atmos. Meas. Tech., 3(6), 1629-1646, 2010.

Rothman, L., Gordon, I., Barber, R., Dothe, H., Gamache, R., Goldman, A., Perevalov, V., Tashkun, S., and Tennyson, J.: HITEMP, the high-temperature molecular spectroscopic database, J. Quant. Spectrosc. Radiat. Transfer, 111(15), 2139-2150, 2010.

Rozanov, A., Rozanov, V., Buchwitz, M., Kokhanovsky, A., and Burrows, J. P.: SCIATRAN 2.0 – A new radiative transfer model for geophysical applications in the 175–2400 nm spectral region, Adv. Space Res., 36(5), 1015-1019, 2005.

Rozanski, K., Araguas-Araguas, L., and Gonfiantini, R.: Relation between long-term trends of oxygen-18 isotope composition of precipitation and climate, Science, 258(5084), 981-985, 1992.

Rubin, M. B.: The history of ozone. The Schönbein period, 1839-1868, Bull. Hist. Chem, 26(1), 40-56, 2001.

Russo, M. R., Marécal, V., Hoyle, C. R., Arteta, J., Chemel, C., Chipperfield, M. P., Dessens, O., Feng, W., Hosking, J. S., Telford, P. J., Wild, O., Yang, X., and Pyle, J. A.: Representation of tropical deep convection in atmospheric models - Part 1: Meteorology and comparison with satellite observations, Atmos. Chem. Phys., 11(6), 2765-2786, 2011.

Ruti, P., Williams, J., Hourdin, F., Guichard, F., Boone, A., Van Velthoven, P., Favot, F., Musat, I., Rummukainen, M., and Domínguez, M.: The West African climate system: a review of the AMMA model inter‐comparison initiatives, Atmos. Sci. Lett., 12(1), 116-122, 2011.

Salawitch, R. J., Canty, T., Kurosu, T., Chance, K., Liang, Q., da Silva, A., Pawson, S., Nielsen, J. E., Rodriguez, J. M., Bhartia, P. K., Liu, X., Huey, L. G., Liao, J., Stickel, R. E., Tanner, D. J., Dibb, J. E., Simpson, W. R., Donohoue, D., Weinheimer, A., Flocke, F., Knapp, D., Montzka, D., Neuman, J. A., Nowak, J. B., Ryerson, T. B., Oltmans, S., Blake, D. R., Atlas, E. L., Kinnison, D. E., Tilmes, S., Pan, L. L., Hendrick, F., Van Roozendael, M., Kreher, K., Johnston, P. V., Gao, R. S., Johnson, B., Bui, T. P., Chen, G., Pierce, R. B., Crawford, J. H., and Jacob, D. J.: A new interpretation of total column BrO during Arctic spring, Geophys. Res. Lett., 37(21), 10.1029/2010gl043798, 2010.

Sander, R., Keene, W. C., Pszenny, A. A. P., Arimoto, R., Ayers, G. P., Baboukas, E., Cainey, J. M., Crutzen, P. J., Duce, R. A., Hönninger, G., Huebert, B. J., Maenhaut, W., Mihalopoulos, N., Turekian, V. C., and Van Dingenen, R.: Inorganic bromine in the marine boundary layer: a critical review, Atmos. Chem. Phys., 3(5), 1301-1336, 2003.

Sanders, R. W., Solomon, S., Smith, J. P., Perliski, L., Miller, H. L., Mount, G. H., Keys, J. G., and Schmeltekopf, A. L.: Visible and Near-Ultraviolet spectroscopy at McMurdo station, Antarctica 9. Observations of OClO from April to October 1991, J. Geophys. Res., 98(D4), 7219-7228, 1993.

Scarnato, B., Staehelin, J., Peter, T., Gröbner, J., and Stübi, R.: Temperature and slant path effects in Dobson and Brewer total ozone measurements, J. Geophys. Res., 114(D24), 10.1029/2009JD012349, 2009.

Schmidt, R.: Vertical profiles of wind speed, snow concentration, and humidity in blowing snow, Boundary-Layer Meteorol., 23(2), 223-246, 1982.

Schneider, M., Wiegele, A., Barthlott, S., González, Y., Christner, E., Dyroff, C., García, O. E., Hase, F., Blumenstock, T., Sepúlveda, E., Mengistu Tsidu, G., Takele Kenea, S., Rodríguez, S., and Andrey, J.: Accomplishments of the MUSICA project to provide accurate, long-term, global and high-resolution observations of tropospheric {H2O,δD} pairs - a review, Atmos. Meas. Tech., 9(7), 2845-2875, 2016.

Schofield, R.: The Vertical Distribution of Atmospheric BrO from Ground-Based Measurements, Ph.D. Thesis, University of Auckland, Auckland, 2003.

Schofield, R., Connor, B. J., Kreher, K., Johnston, P. V., and Rodgers, C. D.: The retrieval of profile and chemical information from ground-based UV-visible spectroscopic measurements, J. Quant. Spectrosc. Radiat. Transfer, 86(2), 115-131, 2004a.

Schofield, R., Kreher, K., Connor, B. J., Johnston, P. V., Thomas, A., Shooter, D., Chipperfield, M. P., Rodgers, C. D., and Mount, G. H.: Retrieved tropospheric and stratospheric BrO columns over Lauder, New Zealand, J. Geophys. Res., 109(D14), 10.1029/2003jd004463, 2004b.

Schofield, R., Johnston, P. V., Thomas, A., Kreher, K., Connor, B. J., Wood, S., Shooter, D., Chipperfield, M. P., Richter, A., von Glasow, R., and Rodgers, C. D.: Tropospheric and stratospheric BrO columns over Arrival Heights, Antarctica, 2002, J. Geophys. Res., 111(D22), 10.1029/2005jd007022, 2006.

Schönbein, C.: On the Odour Accompanying Electricity, and on the Probability of Its Dependence on the Presence of a New Substrate, Proceedings of the Royal Society of London Series I, 4226, 1837.

Schroeder, W. H., Anlauf, K. G., Barrie, L. A., Lu, J. Y., Steffen, A., Schneeberger, D. R., and Berg, T.: Arctic springtime depletion of mercury, Nature, 394(6691), 331-332, 1998.

Seibert, P., and Frank, A.: Source-receptor matrix calculation with a Lagrangian particle dispersion model in backward mode, Atmos. Chem. Phys., 4(1), 51-63, 2004.

Serdyuchenko, A., Gorshelev, V., Weber, M., Chehade, W., and Burrows, J. P.: High spectral resolution ozone absorption cross-sections - Part 2: Temperature dependence, Atmos. Meas. Tech., 7(2), 625-636, 2014.

Shupe, M. D., Walden, V. P., Eloranta, E., Uttal, T., Campbell, J. R., Starkweather, S. M., and Shiobara, M.: Clouds at Arctic Atmospheric Observatories. Part I: Occurrence and Macrophysical Properties, J. Appl. Meteorol., 50(3), 626-644, 2010.

Sihler, H., Platt, U., Beirle, S., Marbach, T., Kühl, S., Dörner, S., Verschaeve, J., Frieß, U., Pöhler, D., Vogel, L., Sander, R., and Wagner, T.: Tropospheric BrO column densities in the

Arctic derived from satellite: retrieval and comparison to ground-based measurements, Atmos. Meas. Tech., 5(11), 2779-2807, 2012.

Simpson, W. R., Alvarez-Aviles, L., Douglas, T. A., Sturm, M., and Domine, F.: Halogens in the coastal snow pack near Barrow, Alaska: Evidence for active bromine air-snow chemistry during springtime, Geophys. Res. Lett., 32(4), 10.1029/2004GL021748, 2005.

Simpson, W. R., Carlson, D., Hönninger, G., Douglas, T. A., Sturm, M., Perovich, D., and Platt, U.: First-year sea-ice contact predicts bromine monoxide (BrO) levels at Barrow, Alaska better than potential frost flower contact, Atmos. Chem. Phys., 7(3), 621-627, 2007a.

Simpson, W. R., von Glasow, R., Riedel, K., Anderson, P., Ariya, P., Bottenheim, J., Burrows, J., Carpenter, L. J., Frieß, U., Goodsite, M. E., Heard, D., Hutterli, M., Jacobi, H. W., Kaleschke, L., Neff, B., Plane, J., Platt, U., Richter, A., Roscoe, H., Sander, R., Shepson, P., Sodeau, J., Steffen, A., Wagner, T., and Wolff, E.: Halogens and their role in polar boundary-layer ozone depletion, Atmos. Chem. Phys., 7(16), 4375-4418, 2007b.

Simpson, W. R., Brown, S. S., Saiz-Lopez, A., Thornton, J. A., and Glasow, R. v.: Tropospheric Halogen Chemistry: Sources, Cycling, and Impacts, Chem. Rev., 115(10), 4035-4062, 2015.

Sinreich, R., Merten, A., Molina, L., and Volkamer, R.: Parameterizing radiative transfer to convert MAX-DOAS dSCDs into near-surface box-averaged mixing ratios, Atmos. Meas. Tech., 6(6), 1521-1532, 2013.

Skamarock, W., Klemp, J., Dudhia, J., Gill, D., Barker, D., Duda, M., Huang, X., Wang, W., and Powers, J.: NCAR Technical Note NCAR/TN-475+ STR: A Description of the Advanced Research WRF Version 3, Boulder, CO, 2008.

Skov, H., Christensen, J. H., Goodsite, M. E., Heidam, N. Z., Jensen, B., Wåhlin, P., and Geernaert, G.: Fate of elemental mercury in the Arctic during atmospheric mercury depletion episodes and the load of atmospheric mercury to the Arctic, Env. Sci. Tech., 38(8), 2373-2382, 2004.

Smit, H. G., Straeter, W., Johnson, B. J., Oltmans, S. J., Davies, J., Tarasick, D. W., Hoegger, B., Stubi, R., Schmidlin, F., and Northam, T.: Assessment of the performance of ECC-ozonesondes under quasi-flight conditions in the environmental simulation chamber: Insights from the Juelich Ozone Sonde Intercomparison Experiment (JOSIE), J. Geophys. Res., 112(D19), 10.1029/2006JD007308, 2007.

Smith, J. A., Ackerman, A. S., Jensen, E. J., and Toon, O. B.: Role of deep convection in establishing the isotopic composition of water vapor in the tropical transition layer, Geophys. Res. Lett., 33(6), 10.1029/2005gl024078, 2006.

Solomon, S., Garcia, R. R., Rowland, F. S., and Wuebbles, D. J.: On the depletion of Antarctic ozone, Nature, 321(6072), 755-758, 1986.

Solomon, S., Schmeltekopf, A., and Sanders, R.: On the interpretation of zenith sky absorption measurements, J. Geophys. Res., 2(D7), 8311-8319, 1987.

Solomon, S., Garcia, R. R., and Ravishankara, A.: On the role of iodine in ozone depletion, J. Geophys. Res., 99(D10), 20491-20499, 1994.

Steffen, A., Douglas, T., Amyot, M., Ariya, P., Aspmo, K., Berg, T., Bottenheim, J., Brooks, S., Cobbett, F., and Dastoor, A.: A synthesis of atmospheric mercury depletion event chemistry in the atmosphere and snow, Atmos. Chem. Phys., 8(6), 1445-1482, 2008.

Stewart, M. K.: Stable isotope fractionation due to evaporation and isotopic exchange of falling waterdrops: Applications to atmospheric processes and evaporation of lakes, J. Geophys. Res., 80(9), 1133-1146, 1975.

Stohl, A., Forster, C., Frank, A., Seibert, P., and Wotawa, G.: Technical note: The Lagrangian particle dispersion model FLEXPART version 6.2, Atmos. Chem. Phys., 5(9), 2461-2474, 2005.

Stohl, A., Sodemann, H., Eckhardt, S., Frank, A., Seibert, P., and Wotawa, G.: The Lagrangian particle dispersion model FLEXPART version 8.2, FLEXPART user guide, 2011.

Stohl, A., Klimont, Z., Eckhardt, S., Kupiainen, K., Shevchenko, V., Kopeikin, V., and Novigatsky, A.: Black carbon in the Arctic: the underestimated role of gas flaring and residential combustion emissions, Atmos. Chem. Phys., 13(17), 8833-8855, 2013.

Stolarski, R. S., Krueger, A. J., Schoeberl, M. R., McPeters, R. D., Newman, P. A., and Alpert, J. C.: Nimbus 7 satellite measurements of the springtime Antarctic ozone decrease, Nature, 322(6082), 808-811, 1986.

Stolarski, R. S., Bloomfield, P., McPeters, R. D., and Herman, J. R.: Total Ozone trends deduced from Nimbus 7 Toms data, Geophys. Res. Lett., 18(6), 1015-1018, 1991.

Stroeve, J. C., Serreze, M. C., Holland, M. M., Kay, J. E., Malanik, J., and Barrett, A. P.: The Arctic's rapidly shrinking sea ice cover: a research synthesis, Clim. Chang., 110(3-4), 1005-1027, 2012.

Stutz, J., and Platt, U.: Problems in using diode arrays for open path DOAS measurements of atmospheric species, Proceedings of SPIE - Optical Methods in Atmospheric Chemistry, 329-340, 1993.

Stutz, J., Thomas, J. L., Hurlock, S. C., Schneider, M., von Glasow, R., Piot, M., Gorham, K., Burkhart, J. F., Ziemba, L., Dibb, J. E., and Lefer, B. L.: Longpath DOAS observations of surface BrO at Summit, Greenland, Atmos. Chem. Phys., 11(18), 9899-9910, 2011.

Tarasick, D. W., Davies, J., Smit, H. G. J., and Oltmans, S. J.: A re-evaluated Canadian ozonesonde record: measurements of the vertical distribution of ozone over Canada from 1966 to 2013, Atmos. Meas. Tech., 9(1), 195-214, 2016.

Tegtmeier, S., Rex, M., Wohltmann, I., and Krüger, K.: Relative importance of dynamical and chemical contributions to Arctic wintertime ozone, Geophys. Res. Lett., 35(17), 10.1029/2008GL034250, 2008.

Thalman, R., and Volkamer, R.: Temperature dependent absorption cross-sections of O_2-O_2 collision pairs between 340 and 630 nm and at atmospherically relevant pressure, Phys. Chem. Chem. Phys., 15(37), 15371-15381, 2013.

Theys, N., Van Roozendael, M., Dils, B., Hendrick, F., Hao, N., and De Mazière, M.: First satellite detection of volcanic bromine monoxide emission after the Kasatochi eruption, Geophys. Res. Lett., 36(3), 10.1029/2008gl036552, 2009.

Theys, N., Van Roozendael, M., Hendrick, F., Yang, X., De Smedt, I., Richter, A., Begoin, M., Errera, Q., Johnston, P. V., Kreher, K., and De Mazière, M.: Global observations of tropospheric BrO columns using GOME-2 satellite data, Atmos. Chem. Phys., 11(4), 1791-1811, 2011.

Tiefengraber, M., Cede, A., and Cede, K.: ESA Ground-Based Air-Quality Spectrometer Validation Network and Uncertainties Study: Report on Feasibility to Retrieve Trace Gases other than O_3 and NO_2 with Pandora, LuftBlick, 32, 2016.

Timco, G., and Weeks, W.: A review of the engineering properties of sea ice, Cold Reg. Sci. Technol., 60(2), 107-129, 2010.

Toohey, M., and Strong, K.: Estimating biases and error variances through the comparison of coincident satellite measurements, J. Geophys. Res., 112(D13), 10.1029/2006JD008192, 2007.

Toyota, K., McConnell, J. C., Lupu, A., Neary, L., McLinden, C. A., Richter, A., Kwok, R., Semeniuk, K., Kaminski, J. W., Gong, S. L., Jarosz, J., Chipperfield, M. P., and Sioris, C. E.: Analysis of reactive bromine production and ozone depletion in the Arctic boundary layer using 3-D simulations with GEM-AQ: inference from synoptic-scale patterns, Atmos. Chem. Phys., 11(8), 3949-3979, 2011a.

Toyota, K., McConnell, J. C., Staebler, R. M., and Dastoor, A. P.: Air-snowpack exchange of bromine, ozone and mercury in the springtime Arctic simulated by the 1-D model PHANTAS - Part 1: In-snow bromine activation and its impact on ozone, Atmos. Chem. Phys., 14(8), 4101-4133, 2014.

Toyota, T., Massom, R., Tateyama, K., Tamura, T., and Fraser, A.: Properties of snow overlying the sea ice off East Antarctica in late winter, 2007, Deep Sea Research Part II: Topical Studies in Oceanography, 58(9), 1137-1148, 2011b.

Tukey, J. W.: *Exploratory Data Analysis*, Addison-Wesley Pub. Co., 1977.

Tzortziou, M., Herman, J. R., Cede, A., and Abuhassan, N.: High precision, absolute total column ozone measurements from the Pandora spectrometer system: Comparisons with data from a Brewer double monochromator and Aura OMI, J. Geophys. Res., 117(D16), 10.1029/2012JD017814, 2012.

Van Roozendael, M., Peeters, P., Roscoe, H., De Backer, H., Jones, A., Bartlett, L., Vaughan, G., Goutail, F., Pommereau, J.-P., and Kyro, E.: Validation of ground-based visible measurements of total ozone by comparison with Dobson and Brewer spectrophotometers, J. Atmos. Chem., 29(1), 55-83, 1998.

Van Roozendael, M., and Hendrick, F.: Recommendations for total ozone retrieval from NDACC zenith-sky UV-VIS spectrometers, Belgian Institute for Space Aeronomy, Brussels, 7, 2009.

Van Roozendael, M., and Hendrick, F.: Recommendations for NO_2 retrieval from NDACC zenith-sky UV-VIS spectrometers, Belgian Institute for Space Aeronomy, Brussels, 7, 2012.

Vandaele, A. C., Hermans, C., Simon, P. C., Carleer, M., Colin, R., Fally, S., Mérienne, M. F., Jenouvrier, A., and Coquart, B.: Measurements of the NO_2 absorption cross-section from 42 000 cm^{-1} to 10 000 cm^{-1} (238 -1000 nm) at 220 K and 294 K, J. Quant. Spectrosc. Radiat. Transfer, 59(3-5), 171-184, 1998.

Vaughan, G., Roscoe, H. K., Bartlett, L. M., OConnor, F. M., Sarkissian, A., Van Roozendael, M., Lambert, J. C., Simon, P. C., Karlsen, K., Hoiskar, B. A. K., Fish, D. J., Jones, R. L., Freshwater, R. A., Pommereau, J. P., Goutail, F., Andersen, S. B., Drew, D. G., Hughes, P. A., Moore, D., Mellqvist, J., Hegels, E., Klupfel, T., Erle, F., Pfeilsticker, K., and Platt, U.: An intercomparison of ground-based UV-visible sensors of ozone and NO_2, J. Geophys. Res., 102(D1), 1411-1422, 1997.

Veefkind, J., Aben, I., McMullan, K., Förster, H., De Vries, J., Otter, G., Claas, J., Eskes, H., De Haan, J., and Kleipool, Q.: TROPOMI on the ESA Sentinel-5 Precursor: A GMES mission for global observations of the atmospheric composition for climate, air quality and ozone layer applications, Remote Sens. Environ., 12070-83, 2012.

Veefkind, J. P., Haan, J. F. d., Brinksma, E. J., Kroon, M., and Levelt, P. F.: Total ozone from the ozone monitoring instrument (OMI) using the DOAS technique, IEEE Trans. Geosci. Remote Sens., 44(5), 1239-1244, 2006.

Viscardy, S., Errera, Q., Christophe, Y., Chabrillat, S., and Lambert, J. C.: Evaluation of Ozone Analyses From UARS MLS Assimilation by BASCOE Between 1992 and 1997, IEEE J. Selec. Topics Appl. Earth Observ. Remote Sens., 3(2), 190-202, 2010.

Vogt, R., Crutzen, P. J., and Sander, R.: A mechanism for halogen release from sea-salt aerosol in the remote marine boundary layer, Nature, 383(6598), 327-330, 1996.

Volten, H., Brinksma, E. J., Berkhout, A. J. C., Hains, J., Bergwerff, J. B., Van der Hoff, G. R., Apituley, A., Dirksen, R. J., Calabretta-Jongen, S., and Swart, D. P. J.: NO_2 lidar profile measurements for satellite interpretation and validation, J. Geophys. Res., 114(D24), 10.1029/2009jd012441, 2009.

Voulgarakis, A., Yang, X., and Pyle, J.: How different would tropospheric oxidation be over an ice-free Arctic?, Geophys. Res. Lett., 36(23), 10.1029/2009GL040541, 2009.

Vountas, M., Rozanov, V. V., and Burrows, J. P.: Ring effect: impact of rotational Raman scattering on radiative transfer in Earth's atmosphere, J. Quant. Spectrosc. Radiat. Transfer, 60(6), 943-961, 1998.

Wagner, T., Otten, C., Pfeilsticker, K., Pundt, I., and Platt, U.: DOAS moonlight observation of atmospheric NO_3 in the Arctic winter, Geophys. Res. Lett. , 27(21), 3441-3444, 2000.

Wagner, T., Leue, C., Wenig, M., Pfeilsticker, K., and Platt, U.: Spatial and temporal distribution of enhanced boundary layer BrO concentrations measured by the GOME instrument aboard ERS-2, J. Geophys. Res., 106(D20), 24225-24235, 2001.

Wagner, T., Dix, B., Friedeburg, C. v., Frieß, U., Sanghavi, S., Sinreich, R., and Platt, U.: MAX-DOAS O_4 measurements: A new technique to derive information on atmospheric aerosols: Principles and information content, J. Geophys. Res., 109(D22), 10.1029/2004jd004904, 2004.

Wagner, T., Burrows, J. P., Deutschmann, T., Dix, B., von Friedeburg, C., Frieß, U., Hendrick, F., Heue, K. P., Irie, H., Iwabuchi, H., Kanaya, Y., Keller, J., McLinden, C. A., Oetjen, H., Palazzi, E., Petritoli, A., Platt, U., Postylyakov, O., Pukite, J., Richter, A., Van Roozendael, M., Rozanov, A., Rozanov, V., Sinreich, R., Sanghavi, S., and Wittrock, F.: Comparison of box-air-mass-factors and radiances for Multiple-Axis Differential Optical Absorption Spectroscopy (MAX-DOAS) geometries calculated from different UV/visible radiative transfer models, Atmos. Chem. Phys., 7(7), 1809-1833, 2007.

Wagner, T., Beirle, S., and Deutschmann, T.: Three-dimensional simulation of the Ring effect in observations of scattered sun light using Monte Carlo radiative transfer models, Atmos. Meas. Tech., 2(1), 113-124, 2009.

Wagner, T., Beirle, S., Brauers, T., Deutschmann, T., Frieß, U., Hak, C., Halla, J. D., Heue, K. P., Junkermann, W., Li, X., Platt, U., and Pundt-Gruber, I.: Inversion of tropospheric profiles of aerosol extinction and HCHO and NO_2 mixing ratios from MAX-DOAS observations in Milano during the summer of 2003 and comparison with independent data sets, Atmos. Meas. Tech., 4(12), 2685-2715, 2011.

Wagner, T., Apituley, A., Beirle, S., Dörner, S., Friess, U., Remmers, J., and Shaiganfar, R.: Cloud detection and classification based on MAX-DOAS observations, Atmos. Meas. Tech., 7(5), 1289-1320, 2014.

Wahner, A., Tyndall, G. S., and Ravishankara, A. R.: Absorption cross sections for symmetric chlorine dioxide as a function of temperature in the wavelength range 240-480nm, J. Phys. Chem., 91(11), 2734-2738, 1987.

Wang, Y., Li, A., Xie, P. H., Wagner, T., Chen, H., Liu, W. Q., and Liu, J. G.: A rapid method to derive horizontal distributions of trace gases and aerosols near the surface using multi-axis differential optical absorption spectroscopy, Atmos. Meas. Tech., 7(6), 1663-1680, 2014.

Wardle, D., McElroy, C., Kerr, J., Wu, E., and Lamb, K.: Laboratory tests on the double Brewer spectrophotometer, Proceedings of the Quadrennial Ozone Symposium, Italy, 997-1000, 1996.

Warwick, N. J., Pyle, J. A., Carver, G. D., Yang, X., Savage, N. H., O'Connor, F. M., and Cox, R. A.: Global modeling of biogenic bromocarbons, J. Geophys. Res., 111(D24), 10.1029/2006jd007264, 2006.

Weaver, D., Strong, K., Schneider, M., Rowe, P. M., Sioris, C., Walker, K. A., Mariani, Z., Uttal, T., McElroy, C. T., and Vömel, H.: Intercomparison of atmospheric water vapour measurements in the Canadian high Arctic, Atmos. Meas. Tech. Discuss.10.5194/amt-2016-330, in review, 2017.

Wennberg, P.: Atmospheric chemistry: Bromine explosion, Nature, 397(6717), 299-301, 1999.

WMO: Scientific Assessment of Ozone Depletion: 2014, Global Ozone Research and Monitoring Project-Report No. 552014.

Wofsy, S. C., McElroy, M. B., and Yung, Y. L.: The chemistry of atmospheric bromine, Geophys. Res. Lett., 2(6), 215-218, 1975.

Wren, S. N., Donaldson, D., and Abbatt, J.: Photochemical chlorine and bromine activation from artificial saline snow, Atmos. Chem. Phys., 13(19), 9789-9800, 2013.

Yang, X., Cox, R. A., Warwick, N. J., Pyle, J. A., Carver, G. D., O'Connor, F. M., and Savage, N. H.: Tropospheric bromine chemistry and its impacts on ozone: A model study, J. Geophys. Res., 110(D23), 10.1029/2005jd006244, 2005.

Yang, X., Pyle, J. A., and Cox, R. A.: Sea salt aerosol production and bromine release: Role of snow on sea ice, Geophys. Res. Lett., 35(16), 10.1029/2008gl034536, 2008.

Yang, X., Pyle, J. A., Cox, R. A., Theys, N., and Van Roozendael, M.: Snow-sourced bromine and its implications for polar tropospheric ozone, Atmos. Chem. Phys., 10(16), 7763-7773, 2010.

Yang, X., Abraham, N. L., Archibald, A. T., Braesicke, P., Keeble, J., Telford, P. J., Warwick, N. J., and Pyle, J. A.: How sensitive is the recovery of stratospheric ozone to changes in concentrations of very short-lived bromocarbons?, Atmos. Chem. Phys., 14(19), 10431-10438, 2014.

Yilmaz, S.: Retrieval of Atmospheric Aerosol and Trace Gas Vertical Profiles using Multi-Axis Differential Optical Absorption Spectroscopy, 2012.

Yokouchi, Y., Akimoto, H., Barrie, L., Bottenheim, J., Anlauf, K., and Jobson, B.: Serial gas chromatographic/mass spectrometric measurements of some volatile organic compounds in the Arctic atmosphere during the 1992 Polar Sunrise Experiment, J. Geophys. Res., 99(D12), 25379-25389, 1994.

York, D., Evensen, N. M., Martınez, M. L., and Delgado, J. D. B.: Unified equations for the slope, intercept, and standard errors of the best straight line, Am. J. Phys., 72(3), 367-375, 2004.

Yung, Y. L., Pinto, J. P., Watson, R. T., and Sander, S. P.: Atmospheric Bromine and Ozone Perturbations in the Lower Stratosphere, J. Atmos. Sci., 37(2), 339-353, 1980.

Zhao, X., Strong, K., Adams, C., Schofield, R., Yang, X., Richter, A., Friess, U., Blechschmidt, A. M., and Koo, J. H.: A case study of a transported bromine explosion event in the Canadian high arctic, J. Geophys. Res., 121(1), 457-477, 2016a.

Zhao, X., Fioletov, V., Cede, A., Davies, J., and Strong, K.: Accuracy, precision, and temperature dependence of Pandora total ozone measurements estimated from a comparison with the Brewer triad in Toronto, Atmos. Meas. Tech., 9(12), 5747-5761, 2016b.

Appendices

A. BrO Spectral Fitting Window Tests

Several BrO spectral fitting windows (Table A.1) were tested using PEARL-GBS MAX-DOAS spectra recorded from 1-5 April 2011. As shown in Figure A.1, these six fitting windows cover wavelengths from 332 to 370 nm. The DOAS spectral analyses were performed using the settings listed in Table 3.1 (the MAX-DOAS column). Figure A.2 is a colour-coded (by measurement date) scatter plot of BrO dSCD error vs. BrO dSCD, for fitting window #6. It shows that the measurements over these five days can be categorised into two regimes: non-BEE measurements and BEE measurements.

Table A.1: BrO fitting windows included in the sensitivity test.

Window #	Wavelength range [nm]	Number of BrO absorption features in the fitting window	Reference
1	340 – 370	5	Airborne DOAS, Prados-Roman et al. (2011)
2	345 – 360	2	Ground-based ZS-DOAS, Adams (2012)
3	336 – 352	3	Satellite DOAS, Theys et al. (2009)
4	332 – 359	5	Satellite DOAS, Theys et al. (2011)
5	341.5 – 357.6	3	Ground-based ZS-DOAS, Hay (2010)
6	337 – 361.9	5	Ground-based MAX-DOAS, Hay (2010)

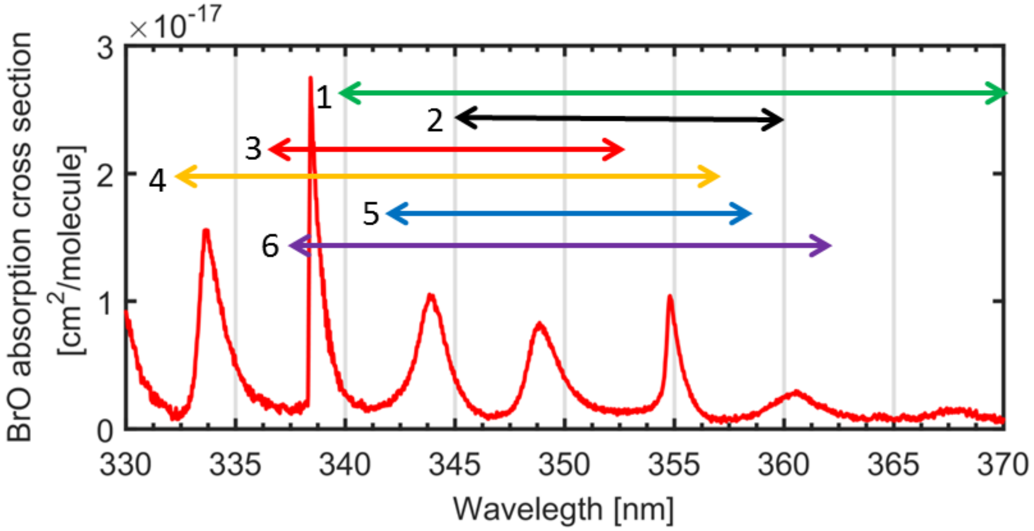

Figure A.1: BrO absorption cross section at 223 K (Fleischmann et al., 2004). The double-headed arrows represent the BrO DOAS fitting windows listed in Table A.1.

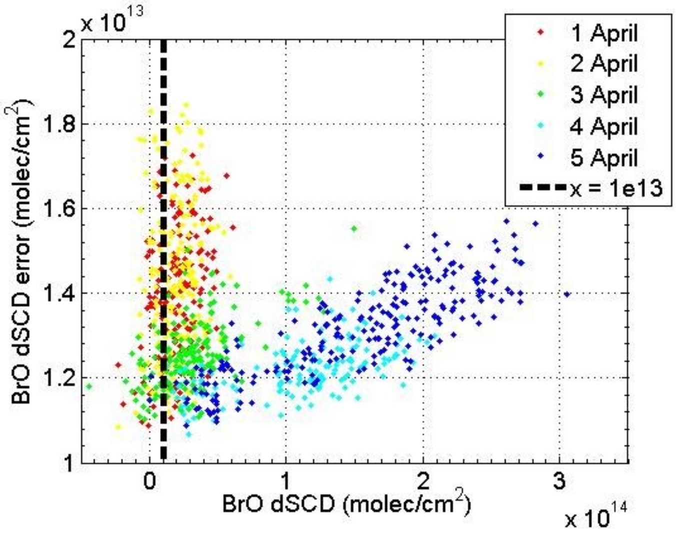

Figure A.2: BrO dSCD error vs. BrO dSCD (fitting window #6). The data points are colour coded by the date of the measurement. The black dashed line is the threshold of 1-sigma confidence level for BrO dSCDs.

Figure A.3 shows the fitted BrO dSCDs and RMS fitting residuals obtained using these six windows. Figure A.4 shows the histogram of the BrO dSCDs and RMS residuals. In general, the selection of fitting window was made based on the smoothness of the fitted BrO dSCDs, the RMS residual (e.g., low RMS, the shape of the histogram), and the correlation between the BrO cross section and the other cross sections used in the DOAS fitting. For example, in Figure A.3, BrO dSCDs on day 95 of 2011 (5 April) retrieved using windows #1, #2 and #5 show more scatter than those retrieved using the other windows. Thus they are not ideal for MAX-DOAS BrO fitting (if we assume that the concentration of BrO during a BEE does not change rapidly).

In Figure A.4, the two peaks of the BrO dSCD histogram represent measurements during low and high BrO conditions. Since a scanning reference (at 90°) is used, the fitted BrO dSCDs should not have negative values (for good quality spectra). Thus windows #3 and #6 performed better than the other windows. Figures A.5 and A.6 show the histogram of the BrO dSCDs and RMS residuals for elevation angles of 6° and 30° respectively. As expected, since the BrO plume extended from the surface up to ~2 km during the BEE days, the two peaks of the BrO dSCD histogram for 6° elevation angle are clearer than those for 30°. For measurements at both 6° and 30°, windows #3 and #4 have fewer negative BrO dSCDs than the other windows, with most of these corresponding to 30° (indicating the BrO detection limit). Figure A.7 shows the histogram of the BrO dSCD error and the scatter plots of BrO dSCD error vs. BrO dSCD. It shows that windows #3, #4, and #6 have lower BrO dSCD errors than the other windows. For non-BEE measurements, window #6 shows low correlation between the BrO dSCD error with BrO dSCDs, indicating the BrO detection limit.

In summary, both windows #3 and #6 provided good BrO results in this sensitivity test. Since window #6 shows two distinctive peaks in BrO dSCD histograms (Figures A.4 and A.5) and lower BrO dSCD error (Figure A.7), it was the window chosen for MAX-DOAS BrO fitting.

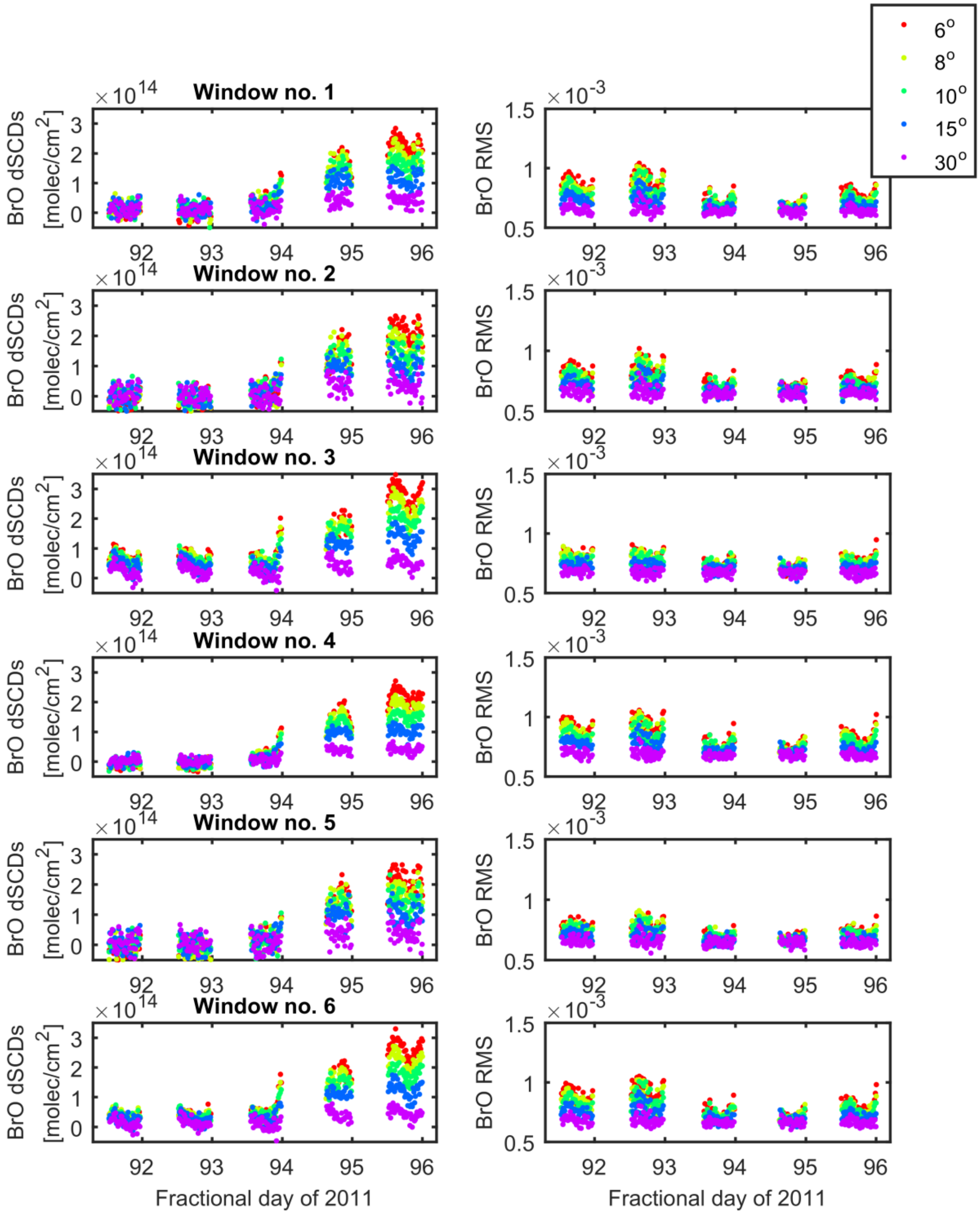

Figure A.3: MAX-DOAS BrO dSCDs and RMS fitting residuals at different elevation viewing angles (indicated in the legend) measured at Eureka from 1-5 April 2011. Each row represents results for one spectral fitting window (indicated by the title of the panels).

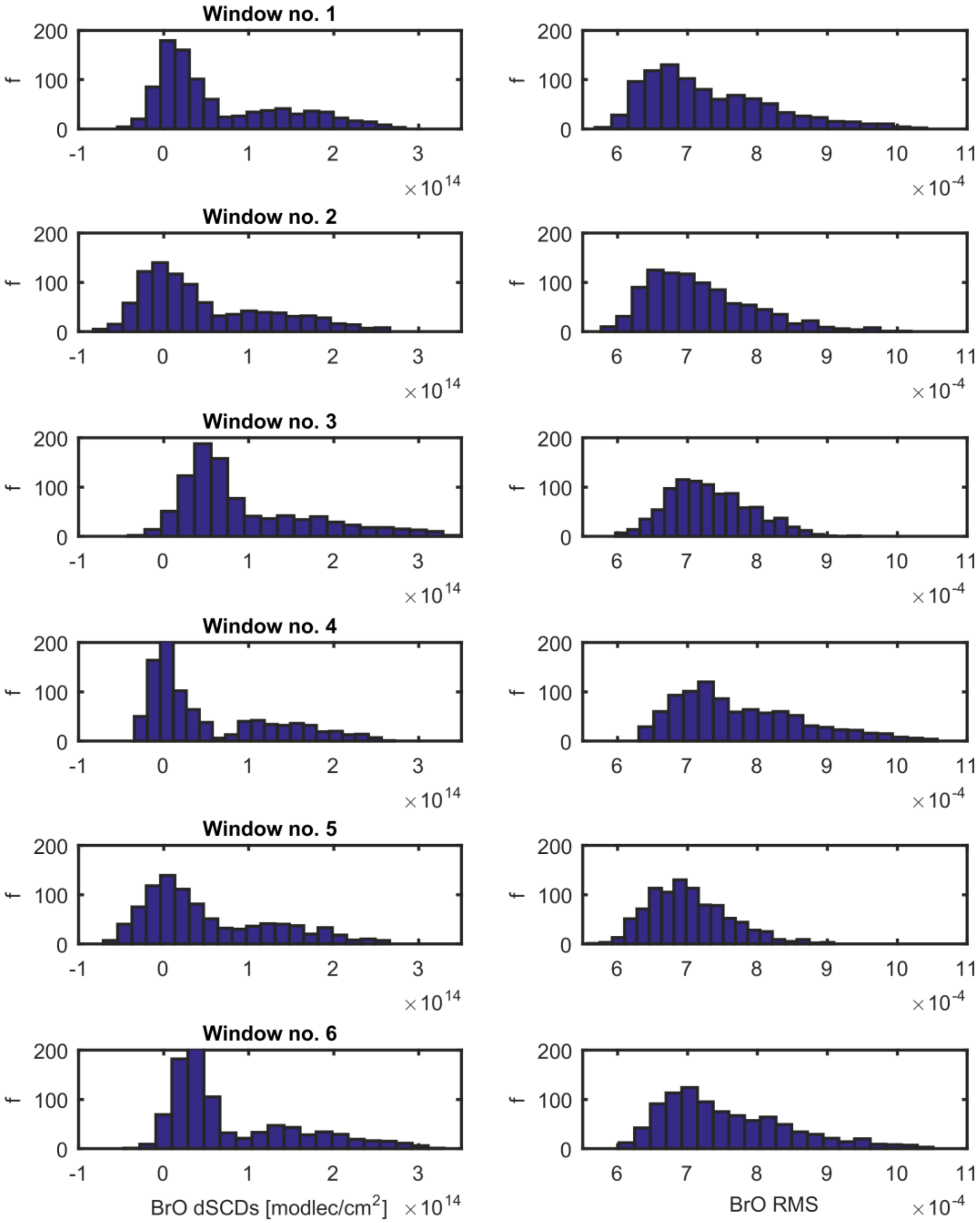

Figure A.4: Histograms of MAX-DOAS BrO dSCDs and RMS fitting residuals using results from all elevation viewing angles. Each row represents results for one spectral fitting window, as indicated.

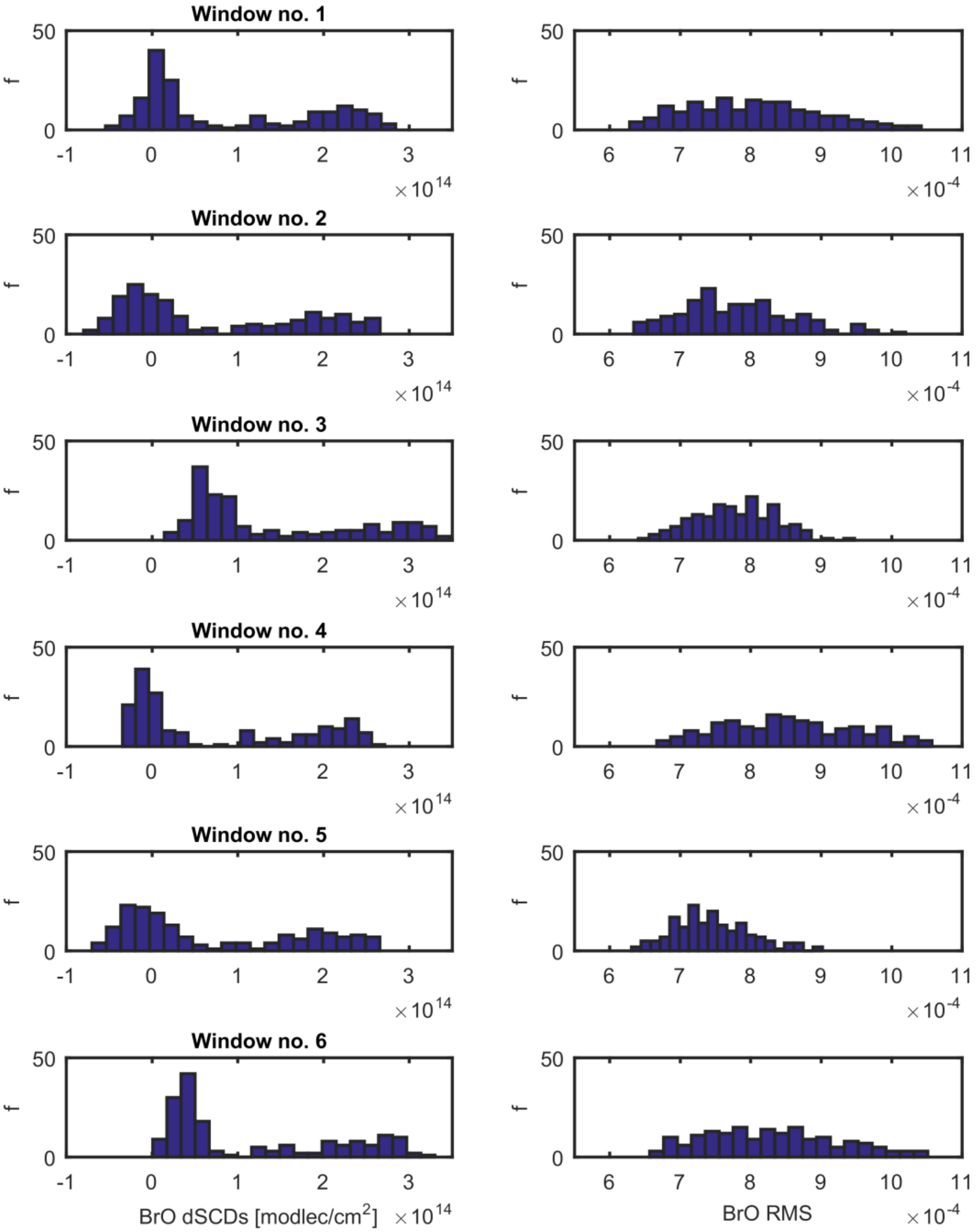

Figure A.5: Histograms of MAX-DOAS BrO dSCDs and RMS fitting residuals using results from 6° elevation viewing angle. Each row represents results for one spectral fitting window, as indicated.

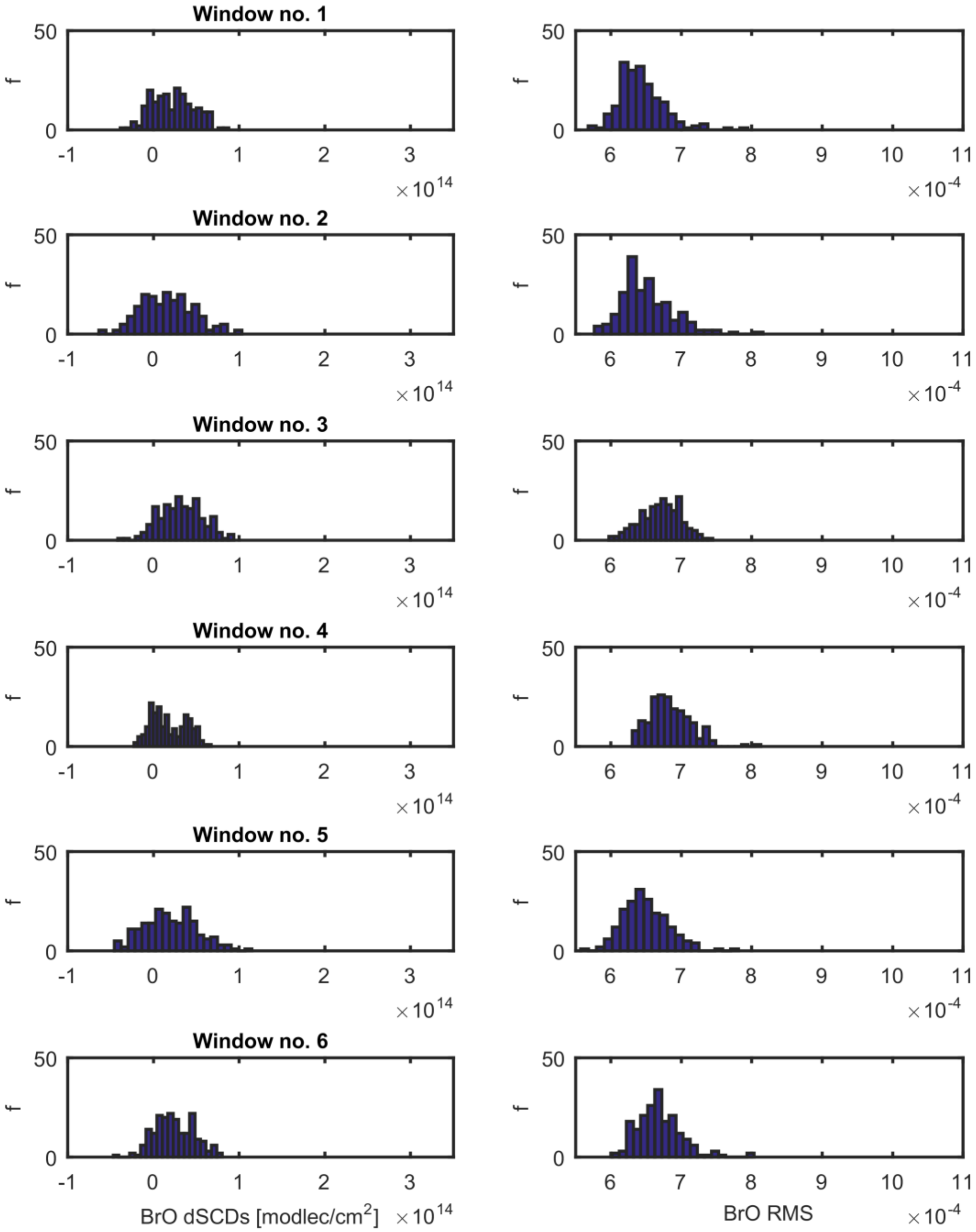

Figure A.6: Histograms of MAX-DOAS BrO dSCDs and RMS fitting residuals using results from 30° elevation viewing angle. Each row represents results for one spectral fitting window, as indicated.

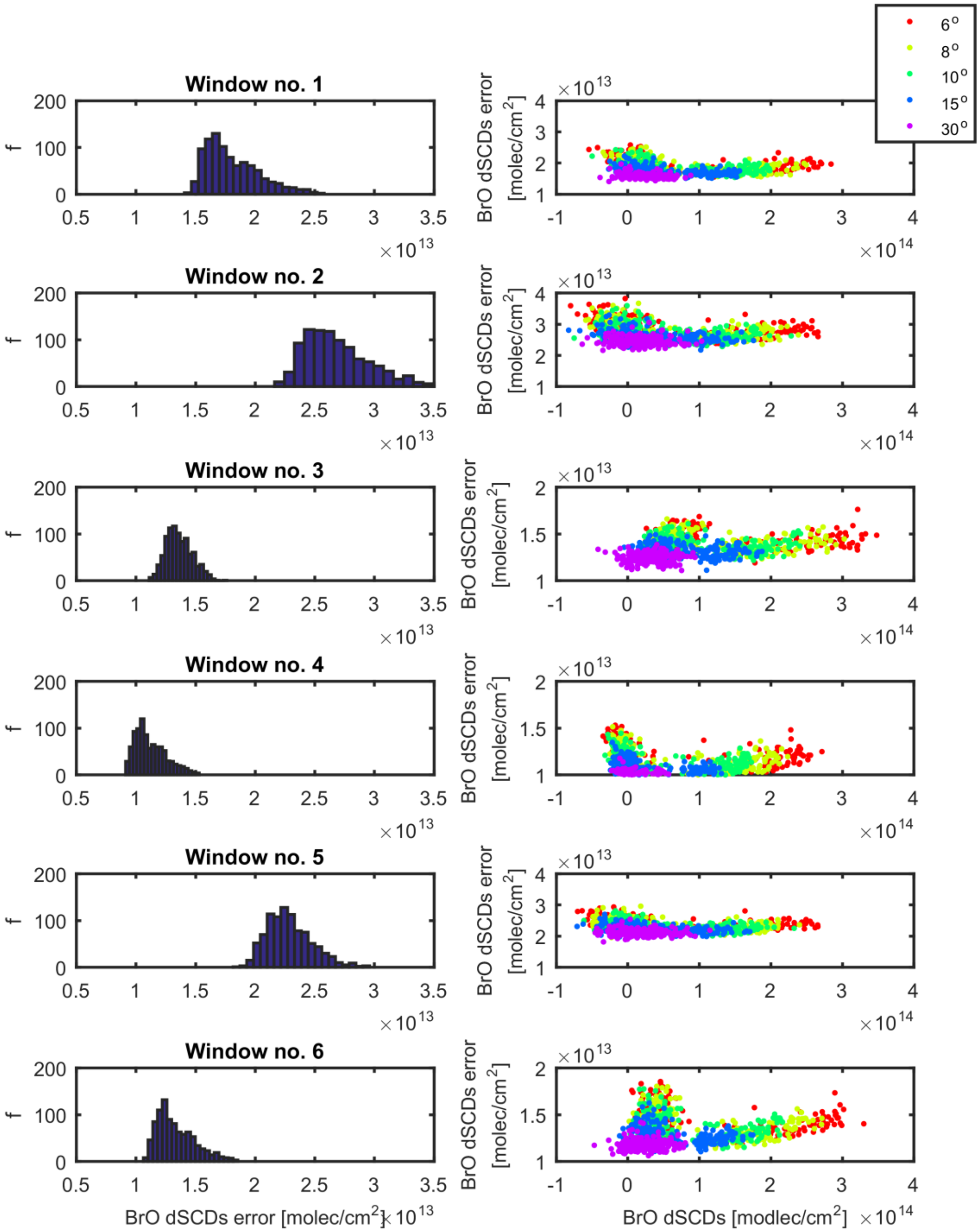

Figure A.7: Left panels: Histograms of MAX-DOAS BrO dSCD error for all elevation viewing angles. Right panels: Scatter plots of BrO dSCD error vs. BrO dSCD. Each row represents results for one spectral fitting window, as indicated. Note the y-axis scale in the scatter plots for windows #3, #4, and #6 is different from that for windows #1, #2, and #5.

B. MAXDOAS Box-AMFs

The sensitivity of MAX-DOAS measurements to surface layers depends strongly on the viewing geometry (Wagner et al., 2007). Following Wagner et al. (2007), height-resolved AMFs (or the so-called box-AMFs) were calculated for springtime Arctic conditions to compare the altitude sensitivity of the measurements at 1° and 6° elevation viewing angles. This simulation was performed using the SCIATRAN2 (Rozanov et al., 2005) RTM.

Figure B.1 shows the simulation results for two wavelengths (360 and 577 nm), with the SZA set to 80°, the RAA set to 180°, and the surface albedo set to 0.9. The temperature and pressure profiles from the US Standard Atmosphere were used. Three LOWTRAN7 aerosol scenarios were used in the simulation, with boundary layer (0-2 km) visibility ranging from 10 to 50 km.

Figure B.1a shows, in the no aerosol scenario, that the AMF for the 1° elevation angle (AMF_{100m} = 45.2) is ~3.6 times that for 6° (AMF_{100m} = 12.5) at 100 m altitude. For the 50 km visibility scenario, the AMF for the 1° elevation angle (AMF_{100m} = 30.1) is ~2.4 times that for the 6° (AMF_{100m} = 12.7) at 100 m altitude. For the 23 km visibility scenario, the AMF for the 1° elevation angle (AMF_{100m} = 19.1) is only ~1.6 times that for 6° (AMF_{100m} = 12.3) at 100 m altitude. Similar results can be seen in Figure B.1b for 577 nm. Thus, in general, the simulation results confirmed that measurements at low elevation viewing angles can greatly enhance the MAX-DOAS surface layer sensitivity; however, this enhanced sensitivity is strongly dependent on aerosol loading.

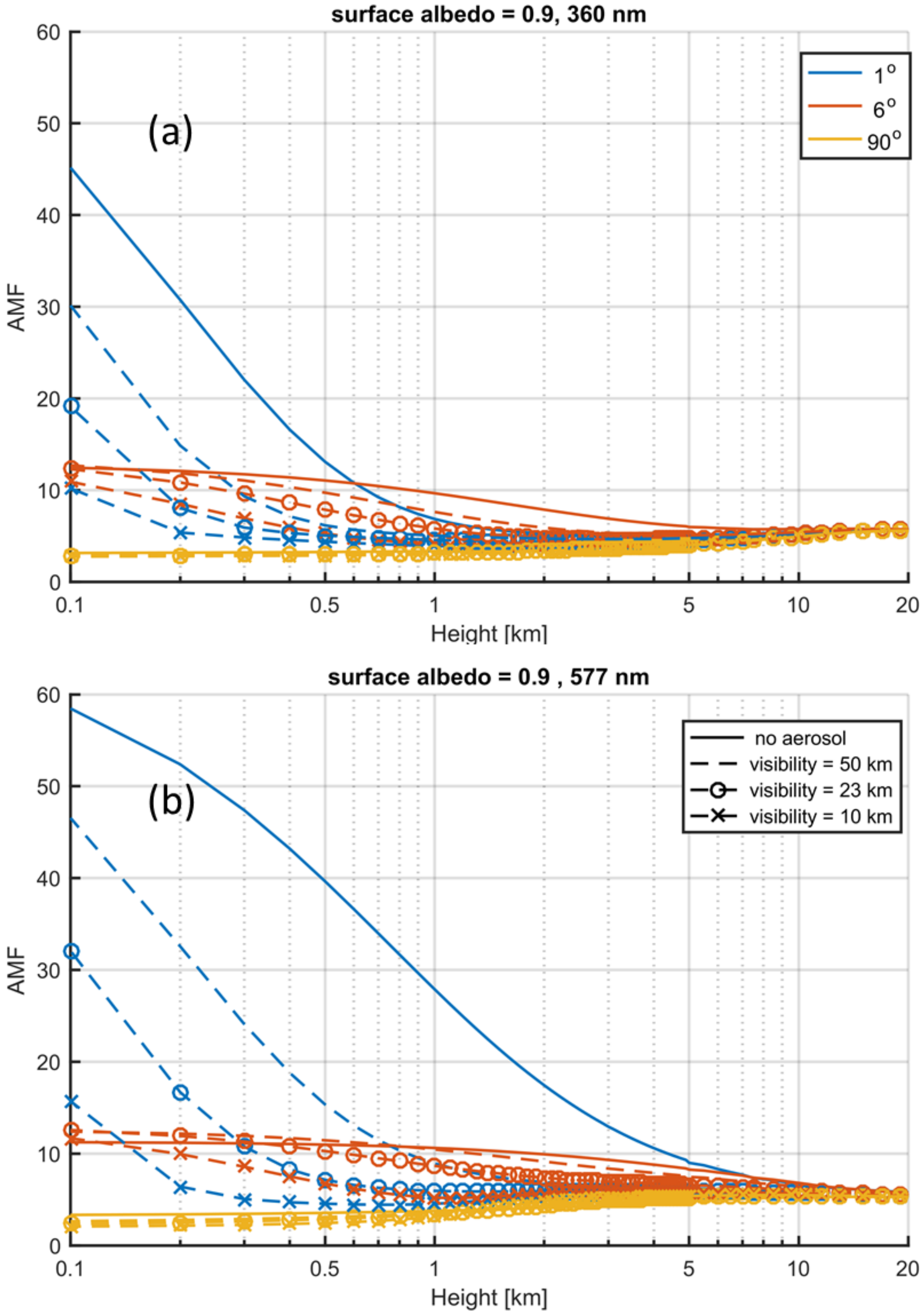

Figure B.1: Box-AMFs as a function of altitude (logarithmic scale), for different viewing elevations (coded by colour) and aerosol scenarios (coded by line shape and symbols) for: (a) 360 nm, (b) 577 nm.